THE UNIVERSITY *of* EDINBURGH

Innovative Bioactive Scaffold Technologies for Vascular Tissue Engineering:

Influences of Morphology and Composition

James Alexander Reid

A thesis submitted for the degree of Doctor of Philosophy

The University of Edinburgh

2020

Acknowledgements

This PhD would not have been possible without the help and support of many people.

My research was funded by an Engineering and Physical Sciences Research Council Doctoral Training Partnership Studentship (EP/N509644/1). I was also generously supported by several different groups for attendance at various conferences. These include: £150 from the Tissue and Cell Engineering Society; £175 from the British Heart Foundation; £300 from the Institute of Physics and Engineering in Medicine; and £641 from the Institute for Mechanical Engineers. Finally, I would like to thank Boehringer Ingelheim for kindly supporting me with €3680 for my exchange trip to Brown University under the supervision of Dr. Kareen Coulombe.

I would first like to thank my supervisor Dr. Anthony Callanan for the constant support and guidance throughout my studies. This PhD would have truly been impossible without your help. Your open door policy and time for all questions have made this work possible. I could not have asked for a better supervisor over the last three and a half years.

It has been a true joy working as part of the Callanan group. I would like to thank all members past and present for their support, both in the lab and as friends outside the lab. I would like to thank Dr. Nimrah Munir for the all the guidance she provided; the (hopefully!) excellent proof reading of this thesis; and of course for being a great friend! I would also like to thank Dr. Rhiannon Grant for teaching me approximately 95% of all lab based techniques I have learnt during my PhD; Dr. Todd Burton for teaching me electrospinning and for the advice during my Masters project; Thomas Bate and Alex Sturtivant for making PhD life a little bit less academic at times, going to several pub quizzes and on nights out; and Busra Baskapan, Yunxi Gao, Dr. Billy Shanahan and Dr. Maaaria Ginai for making life in the office a lot more enjoyable.

I would like to thank Dr. Alison McDonald for all the help imaging; the images she has provided me have been an asset to my PhD. I would also like to thank Dr. Helen Cope and Katalin Kis for the technical help in the lab.

Most importantly, I would like to thank my family and friends for their support and encouragement throughout my PhD; my parents and brothers who have been there supporting me through all the decisions I have ever made; and above all, I would like to thank Ruth Moffett for the love and care she has given me throughout this journey.

This achievement belongs to everyone mentioned in these acknowledgements.

Table of Contents

List of Figures

List of Tables

List of Abbreviations

2D: 2-dimensional

3D: 3-dimensional

A: area

ANOVA: Analysis of variance

ATR: attenuated total reflection

AV: atrioventricular

BSA: Bovine serum albumin

C: compliance

C:M: Chloroform: Methanol

CAD: Coronary artery disease

CARS: Coherent Anti-Stokes Raman

CD31: Platelet endothelial cell adhesion molecule

cDNA: Complementary Deoxyribonucleic acid

CT: computed tomography

DAPI: 4′,6-diamidino-2-phenylindole

diH_2O: Deionised water

DMEM: Dulbecco's Modified Eagle Medium

DMF: Dimethyl formamide

DNA: Deoxyribonucleic acid

E: Young's Modulus

ECM: Extracellular Matrix

EDC: (1-ethyl-3-(3-dimethylaminopropyl)carbodiimide)

eNOS: Nitric Oxide Synthase 3

F: Force

FBS: Fetal bovine serum

FDA: US Food and Drug Administration

FGF: Fibroblast growth factor

FTIR: Fourier-transform infrared spectroscopy

GAG: Glycosaminoglycans

GAPDH: Glyceraldehyde 3-phosphate dehydrogenase

H&E: Haematoxylin and Eosin

HAEC: Human aortic endothelial cells

HCAEC: Human coronary artery endothelial cells

HDMS: Hexamethyldisilazane

HFIP: Hexafluoroisopropanol

HGF: Hepatocyte growth factor

HIF1-α: Hypoxia-inducible factor 1-alpha

HUVEC: Human umbilical vein endothelial cell

HUVSMC: Human umbilical vein smooth muscle cell

ICAM1: Intercellular Adhesion Molecule 1

IL1-α: Interleukin 1 alpha

L: length

MEOX-2: Mesenchyme homeobox 2

MES: 2-(N-morpholino)ethanesulfonic acid

MMP1: Matrix metalloproteinase-1

MMP2: Matrix metalloproteinase-2

MSC: Mesenchymal stem cell

NHS: N-hydroxysuccinimide

P: Pressure

PAA: Polyacrylic acid

PAD: Peripheral artery disease

PBS: Phosphate buffer saline

PCL: Polycaprolactone

PEO: Polyethylene oxide

PET: Polyethylene terephthalate

PLA: polylactic acid

PLGA: polylactic-co-glycolic acid

PTFE: Polytetrafluoroethylene

PVA: Polyvinyl alcohol

RFU: Relative fluorescence units

RNA: Ribonucleic acid

RT-qPCR: Real-time polymerase chain reaction

S: Small

SDS: Sodium dodecyl sulfate

SEM: Scanning electron microscopy

TIMP2: Tissue inhibitor of metalloproteinases-2

TPEF: Two photon fluorescence

UTS: Ultimate tensile strength

V: Volume

VEGF: Vascular endothelial growth factor

VSMC: Vascular smooth muscle cell

XL: Extra-large

α-actin1: Actin alpha 1

Abstract

Vascular disease is currently the leading cause of mortality worldwide, with coronary heart disease, peripheral arterial disease and strokes accounting for upwards of 30% of all deaths in Europe. Bypass grafting is one of the major approaches utilised in the treatment of vascular disease. This technique involves diverting blood flow around an arterial blockage by grafting in an alternative path. This surgery is widely used in the treatment of coronary heart disease and peripheral arterial disease. This is either done with a synthetic material, such as PTFE, or by using an autologous vessel such as the saphenous vein or the internal thoracic artery. The grafting of autologous vessels is considered the gold standard for small diameter bypass grafts due to the higher patency rates compared to their synthetic counterparts. However, there are only a finite amount of vessels that can be harvested and in many cases the vessels are not of a high enough quality for use in surgery. Therefore, there is an urgent need for the development of novel biomaterials that can improve patency rates in bypass grafts. As a push for solutions to this problem, the field has placed a focus on improving the biofunctionality of materials in vitro as a means of testing the translatability of the material.

This thesis presents four different methods of improving the bioactivity of scaffolds for vascular tissue engineering through alteration of the morphology and composition of the scaffold: 1) Altering the fibre diameter of electrospun polycaprolactone (PCL) scaffolds to enhance the morphology for seeded cells. 2) Native aortic and heart bovine extracellular matrices (ECM) were incorporated into PCL scaffolds. 3) Cell secretome was bound to the PCL scaffolds to enhance the bioactivity of the scaffold. 4) Altering the cell's response through environmental factors such as hydrostatic pressure and hypoxia.

Scaffolds were either seeded with human umbilical vein endothelial cells (HUVECs) or human umbilical vein smooth muscle cells (HUVSMCs) and their response to their microenvironments were analysed. Gene expression analysis and immunohistochemical analysis showed that altering the fibre diameter of the scaffold had evident effects on cellular response. For example, increasing fibre diameter had the effect of increasing cellular infiltration for both cell types. HUVECs upregulated key phenotypic genes when seeded on the largest fibre diameter. On the contrary, the HUVSMCs

upregulated key genes when cultured on the smallest fibre diameter. Likewise, the incorporation of ECMs into the scaffold altered their mechanical properties and changed the biological response of the seeded cells. Incorporating ECM had the effect of decreasing stiffness and increasing scaffold elasticity. Furthermore, the incorporation of aortic ECM into the fibres led to higher cell viability for both cell types. Additionally, the binding of proteins released by cultured cells to the PCL scaffold was shown to alter gene expression and cell survival.

Each method undertaken altered cellular responses such as gene expression and cell viability, indicating that these methods provide a viable and translatable platform for vascular tissue engineering. These scaffold have great potential for vascular tissue engineering and offer translatability to other tissue types.

Lay Summary

Vascular disease is the leading cause of mortality worldwide and current treatments do not lead to long-term full functionality. Bypass grafting is a means of treating various vascular diseases by allowing blood to flow around a blockage in the vessel. The gold standard treatment option for bypass grafting is not available to all patients due to the finite resources within the body. Unfortunately, the synthetic grafts being made in the lab for these patients do not provide the patients with a long-term solution.

Vascular tissue engineering aims to provide hope for these patients by finding new treatments and materials to offer longer-term solutions. Bioengineers use a combination a materials science and biology to come up with novel solutions. Eventually, the hope is to provide scientist with platforms for the testing of new drugs and patients with artificial organs.

Electrospinning is a manufacturing technique that creates fibrous sheets of polymer with similar structural characteristics to that of the extracellular matrix (ECM). The extracellular matrix is composed of proteins and growth factors and provides the local cells with a framework to attach themselves to and grow around. This project focusses on ways to alter the structure and composition of these fibrous electrospun polymer sheets, to eventually use them as replacements for the native vascular ECM.

This research has looked at several ways to alter the morphology and composition of these electrospun polymer sheets. Firstly, the size of the individual fibres in the polymer sheet were changed to see how this aspect of the morphology influenced vascular cells (endothelial cells and smooth muscle cells). The second method looked at how altering the composition of these fibres influenced vascular cells. Decellularized native ECMs were incorporated into the fibres to provide the cells with some of the proteins and growth factors found in native tissue. The third method looked at how proteins and growth factors secreted by cells could be attached to the polymer fibre and how this would influence vascular cells. Cells were grown in the lab and their secreted proteins and growth factors were collected in media and then bound to the surface of the electrospun polymer fibres,

providing the vascular cells with the proteins and growth factors released by the cells in culture. Finally, environmental stimuli were used test how the electrospun sheets and vascular cells would respond to the native environment. Hydrostatic pressure was used to simulate the forces seen by the cells in the body, with the hope of altering the proteins and growth factors secreted so that different proteins could be bound to the electrospun sheet. Hypoxia (low oxygen) was used to assess the viability of these electrospun sheets for vascular cells when in a diseased state.

Each of the scaffolds designed in this thesis altered the biological behaviour of vascular cells. Altering the fibre diameter had positive effects on both cell types, with the larger fibre diameter leading to increased cell viability and gene expression of key phenotypic genes in the seeded HUVECs and the smallest fibre diameter having similar effects in the seeded HUVSMCs. The addition of ECM into the fibres altered their mechanical properties and had beneficial effects for both cell types. Higher cell viability was noted for both cell types when the aortic ECM was incorporated into the fibres. Furthermore, these scaffolds have a range of different mechanical properties that closely mimic those of the 'gold-standard' treatment for bypass grafting. These novel electrospun polymer sheets put us one step closer to finding a realistic solution to the gap between synthetic bypass grafts and the 'gold-standard' treatments.

Chapter 1: Introduction

1.1 Heart Anatomy

The heart muscle is composed of four main muscular chambers, two of which are associated with the pulmonary circuit and two with the systemic circuit [1]. Blood comes into the right atrium from the vena cava (systemic circuit). It is then passed on to the right ventricle through the tricuspid valve. This blood is then pumped into the pulmonary artery (pulmonary circuit) where it makes its way to the lungs, collecting oxygen to feed the organs. The blood comes back into the left atrium via the pulmonary veins. The blood then passes through the mitral valve into the left ventricle, before being pumped out via the aorta (systemic system). The heart is surrounded by the pericardial sac, which acts to stabilize the heart muscle within the body. It is composed of a network of collagen fibres and filled with approximately 20-60 ml of pericardial fluid in adult humans [2]. This fluid acts as a lubricant between the two internal surfaces of the pericardial sac.

The wall of the heart is made up of three distinct layers called the epicardium, the myocardium and the endocardium. The outer layer of the heart wall is called the epicardium and is composed of a mesothelium and areolar tissue [1]. This is connected to the myocardium which makes up the majority of the heart wall. The myocardium is a dense network of cardiac cells and connective tissues. The final inner layer of the heart wall is called the endocardium and is composed of areolar tissue and an endothelium lining the inner walls of the heart muscle [1]. The heart wall is supplied with blood from the coronary artery.

There are several different valves located within the heart muscle, all whose main purpose is to prevent the backflow of blood. The right atrioventricular (AV) tricuspid valve and left AV bicuspid valve are located between the right atrium and ventricle; and the left atrium and ventricle, respectively [3]. They are designed to prevent backflow form the ventricles to the atriums during ventricular contraction. These two valves are closed using the papillary muscles which connect the two valves to the inside wall of the ventricles [4]. The pulmonary valve and aortic valves are found between the right ventricle and the pulmonary artery and the left ventricle and aorta. Both of these valves are called semilunar valves and are designed to prevent the backflow of blood from the pulmonary artery and the aorta into the right and left ventricles, respectively [5].

1.2 Arterial Anatomy

1.2.1 Human Arterial Anatomy

Arteries are blood vessels within the body that take blood away from the heart to various parts of the body, such as organs and limbs. They are part of the circulatory system which is responsible for both carrying oxygenated nutrient filled blood to the cells, as well as removing carbon dioxide and waste [6]. As well as performing this transportation function, they also act as dampers to ensure the organs and tissues are receiving a steady flow and pressure of blood [6]. The pulmonary artery carries non-oxygenated blood to the lungs, whereby a network of bronchioles and capillaries transfers oxygen from the lung into the blood [7]. This oxygenated blood is then returned to the heart where it is pumped out of the aorta to all the subsequent arteries in the body. Major arteries that carry oxygenated blood are the coronary artery that supplies the heart muscle; the carotid artery that supplies the head and brain; the axillary arteries that supply the arms; the femoral artery that supplies the legs; the renal artery that supplies the kidneys; and the hepatic artery that supplies the liver [8]. There are many more arteries that supply other organs with oxygenated blood [8].

The walls of vessels consist of three distinct layers that all serve a unique function, as seen in Figure 1 [8]. Firstly, the inner most layer is called the tunica intima. This is the location of the blood wall barrier and consists of a thin layer called the endothelium that is made up of a monolayer of endothelial cells. Outside that (moving away from the central lumen of the vessel) there is a layer of elastic tissue called the internal elastic membrane, which separates the endothelial cells from the next core section of the vessel – the tunica media. Next, beyond the tunica intima is the tunica media which mostly consists of a dense network of smooth muscle cells interwoven amongst connective tissue. The tunica intima is bound to the tunica media by collagen fibres. The smooth muscle cells found in the tunica media are somewhat responsible for the contractile properties of the elastic arteries. Finally, at the outer extremity of the vessel there is the tunica externa. This region mostly consists of elastic fibres and connective tissue allowing for the vessel to stabilize itself against surrounding tissues [8].

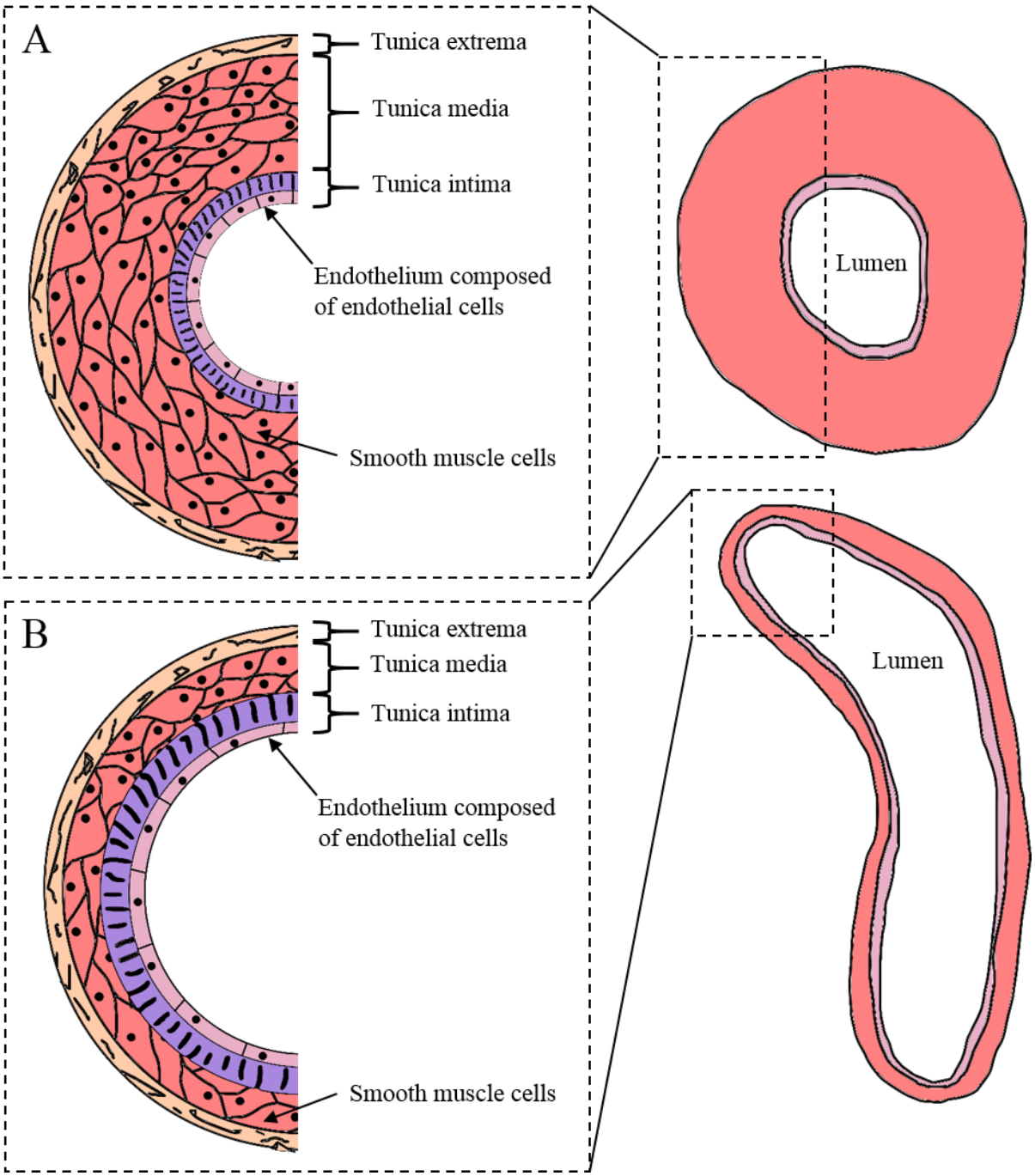

Figure 1: Structure of the vessels of the body: (A) arteries and (B) veins. Arteries have a thicker tunica media than veins, which helps them retain their shape.

Vessels and arteries may share a similar structure to each other but there are some clear differences between them, mostly due to the loading that they undergo [8]. Firstly, the vessel wall tends to be thicker in arteries, with the majority of this being in the tunica media, allowing the vessel to resist higher pressures (as seen in Figure 1). Secondly, the vessel lumen appears to be relatively smaller

compared to the vessel wall thickness due to the recoiling nature of the elastic fibres present in arteries. Finally, veins tend to contain valves, whereas arteries do not. This is because of the lower pressures associated with veins and the higher potential for backflow. Valves at regular intervals ensure the blood keeps flowing in the right direction [9].

Elastin and collagen are two of the major proteins that make up the extracellular matrix of arteries [10,11]. The quantity of each protein has a major effect on mechanical properties of the arteries [12,13]. This is described in more depth later on. The aorta is the largest artery in the body – it transports blood out of the heart to the entire body. The magnitude of the forces seen in the aorta change as you move down away from the heart [14]. The extracellular matrix (ECM) of the aorta changes in composition along its length to accommodate these differences in force.

Elastin and collagen have interesting mechanical properties that render them mechanically suitable for vascular tissue [12,13]. The major role of elastin is to allow the vessel to undergo repeated extension without resulting in tissue deformation [12]. As previously mentioned, elastin is found in higher quantity at the upper end of the aorta where pulsatile pressures are at their highest. This is because elastin is designed to maintain tissue shape under high repetitive forces [15]. During aging, the quantity of elastin within the arteries decreases significantly, resulting in an increase in arterial stiffness [16]. Elastin has a low propensity for turnover, therefore, the elastic fibres that were laid down during foetal development have to undergo large numbers of cyclic deformation without failure [17]. Like elastin, collagen does also offer a degree of elasticity [18]. However, its major role in the mechanical properties of vessels is to provide tensile strength. This stiffness comes from the intermolecular cross-links between each collagen molecule [13].

1.2.2 Animal Arterial Anatomy

The major animal of focus in this thesis is the Bovinae (cow). They were used as a source of vascular ECMs - aorta and myocardium to be precise. Interestingly, it was found that the aortic arch in young cows (similar in age to the cows used for ECM in this thesis) had elastin contents of 46.6% and collagen contents of 16.7% - a ratio of 2.79, which is lower than that found in the human aortic arch [19]. These elastin and collagen contents are similar to that found in pigs, goats and sheep [20].

1.3 Resident Cells of the Vasculature

1.3.1 Endothelial cells

1.3.1.1 Umbilical Vein Endothelial Cells

Human umbilical vein endothelial cells (HUVECs) are an endothelial cell line that is commonly used in vascular research as it is considered to be a robust cell line for the study of cell pathology and function [21]. They were first isolated from the umbilical cord in the early 1970s by *Jaffe, et al*. using a simple collagenase digestion method [22]. Since then, they have become a popular cell line for a variety of reasons including their low cost; simple isolation techniques; and their robustness during cell culture [23].

HUVECs have been widely used in vascular tissue engineering with a range of different studies being carried out [24–27]. Furthermore, *Liao, et al.* looked into the effect of passaging on HUVEC performance and whether or not any functionality losses were noted [28]. Their results suggest that P10 is the approximate point where functionality of the HUVECs is altered. Briefly, cell spreading percentage and actin filament length were both seen to drop after P10 and cell surface roughness (especially in the region around the nucleus) was seen to increase after P15 [28]. As changes were noted between different passage numbers, it is of crucial importance to use the same passage number between different studies.

1.3.1.2 Aortic Endothelial Cells

Human aortic endothelial cells (HAECs) are an endothelial cell line that is isolated from a segment of the ascending aorta [29]. This is a primary cell line that is directly obtained *ex vivo* through the use of endovascular surgery. HAECs have become more popular in recent times as they more accurately mimic the native vascular environment and are capable of substantially more doublings *in vitro* before undergoing senescence [29]. They have since been used in a variety of tissue engineering settings [30–32].

1.3.1.3 Coronary Artery Endothelial Cells

Human coronary artery endothelial cells (HCAECs) are a cell line that is isolated from a segment of the coronary artery. They can be isolated during angioplasty and stent surgery to open up a blocked

coronary artery [33]. They have been used for a range of tissue engineering applications and have shown positive results when cultured on 3D scaffolds [34–36].

1.3.2 Smooth Muscle Cells

Vascular smooth muscle cells (VSMCs) are an important component of vessel walls and are predominantly found in the tunica media [37]. Depending on the size of the vessel, the thickness in cell number of the tunica media can range from around 40 layers of VSMCs up to around 60 layers [37]. VSMCs differ slightly from other smooth muscle cell types that are often found in the walls of organs including the stomach, bladder and uterus, amongst others. Firstly, VSMCs have been found to contain high quantities of vimentin and low quantities of desmin, which is the opposite of the other conventional smooth muscle cell types [38]. Vimentin and desmin are both intermediate sized filament proteins that play crucial roles in supporting and anchoring various cell constituents such as the nucleus, mitochondria and endoplasmic reticulum [39,40]. A study by *Schwartz et al.* found that rat aortic smooth muscle cells contain 51% vimentin alone-positive cells, 48% positive for both vimentin and desmin, and 1% desmin alone-positive [41]. Both proteins differ in molecular weight but share similar biochemical properties such as low solubility [42]. In addition, VSMCs are predominantly composed of α-actin, whereas conventional smooth muscle cells are mostly made up of γ-actin [38,43]. Interestingly, the expression of α-actin is one of the earliest markers for VSMC differentiation [44].

1.3.3 Cardiomyocytes

Cardiomyocytes are the most abundant cell type found within the heart and are predominantly responsible for providing the contractile force necessary to pump the heart muscle and provide blood perfusion to the body [45]. Interestingly, once birth has occurred, cardiomyocytes reach maturity and lose their ability to divide [46]. At this point, any cardiac muscle growth is associated with the individual myocytes increasing in size and not due to proliferation and increase in cell number [45]. Therefore, any loss in cardiomyocyte number through adulthood has to be compensated for with increased workload from the remaining cardiomyocytes [45]. Cardiomyocytes for cell-study can be isolated from a variety of sources including rats, humans, and other animal sources. Furthermore, they can be isolated from neonatal sources or matured adult sources, providing a range of possibilities for the study of

cardiomyocytes [45]. Cardiomyocytes have been extensively used in tissue engineering, with work also being done on electrospun scaffolds [47–49].

1.3.4 Cardiac Pacemaker Cells

Cardiac pacemaker cells are responsible for creating the rhythmic electrical impulses that control the contraction of the cardiomyocytes, allowing for blood to be perfused around the body [50]. Without a controlled set of impulses, the heart would lose functionality, eventually leading to heart failure [51]. In this case, an artificial pacemaker can be used to synthetically produce the impulses required for heart muscle contraction [51]. These cells have not been extensively studied in tissue engineering, however, some work has been done on generating them from stem cell sources as a means of treating heart failure [50,52].

1.4 Growth Factors

Vascular endothelial growth factor (VEGF) is a major growth factor responsible for stimulating the formation of new vasculature, also known as angiogenesis [53]. The importance of VEGF in angiogenesis was discovered in 1983 by *Senger et al.* who originally called it vascular permeability factor [54]. They found that tumours from various rodents secreted VEGF, ultimately leading to increased cell permeability [54]. They noted similar findings with *in vitro* cell cultures [54]. Interestingly, it has since been suggested that the VEGF may in fact protect the tumour cells from chemotherapy and radiotherapy, ultimately hindering the effect of these treatments [55]. Furthermore, chemotherapy and radiotherapy have both been shown to increase the quantity of VEGF within the tumour cells [56]. While this suggests that increased VEGF expression is solely negative, there are situations where VEGF is required, most notably in the cardiovascular system. It has been shown that VEGF acts on the site of infarction, promoting tissue remodelling [57].

Fibroblast Growth Factor (FGF) is another growth factor responsible for angiogenesis and wound healing [58,59]. A lot of work has shown that FGF stimulates VEGF expression in both endothelial cells and stromal cells, along with accelerating tumour formation [60–62]. Likewise, increased FGF expression has been shown to synthesise hepatocyte growth factor (HGF), another angiogenic growth factor [63].

1.5 Vascular Extracellular Matrices

The ECM is a 3-dimensional network of proteins, cytokines and enzymes, that provide the structural support for surrounding cells to attach and grow into specific tissues [64]. Beyond its evident structural supporting functions, the ECM also provides cells with biochemical cues that can control the functionality of the local cells [64]. It has slightly different functions depending on the tissue type, but in most cases it is involved in cell adhesion and cell-cell communication that is crucial for successful proliferation and differentiation of local cells [65]. In vascular tissue, the ECM has the very important role of controlling the amount of stress and strain that the cells are exposed to, thus influencing cell metabolism [66].

The aorta is the largest artery in the human body, with average diameters ranging from about 3cm at the aortic arch down to approximately 1.8 cm in the abdomen [67]. As described in section 1.2.1, the arteries of the human body (including the aorta) are composed of various structural proteins that help give the artery its viscoelastic compliant properties [68]. The two major components that make up the majority of the aorta's ECM are collagen and elastin. The aortic arch (at the exit of the heart) is composed of approximately 38% elastin and 23% collagen (ratio of 1.65) [20]. The elastin content drops as you go along the aorta to about 21% at the sub-renal level (below the abdomen). In contrast, collagen levels increase to about 28% at this point along the aorta leading to a ratio of approximately 0.7, which is less than half of the ratio found at the artic arch [20]. Interestingly, the hydroxyproline content of the elastin was found to increase as the aorta descended [20]. A higher quantity of hydroxyproline is associated with increase elasticity [69].

In contrast to the aorta, the myocardium has a much lower collagen and elastin content. It has been found that the human left ventricle is composed of approximately 5% collagen, of which 85% is collagen type 1 and 11% collagen type 3 [70,71]. No values for human myocardium could be found in relation to elastin content, however, the ventricles of a rat were found to be composed of 3% collagen and 1.4% elastin, which is in the same realm as the human myocardium [70].

1.5.1.1 Collagen

Collagen is composed of a hierarchical structure which is somewhat responsible for its mechanical properties [67]. It is made of collagen fibrils that are approximately 50-200 nm in diameter that form the backbone of all collagenous tissues [72]. These collagen fibrils are formed of interlinked collagen triple helical molecules [73]. The fibrils are interlinked to each other by proteoglycan bridges (at 60 nm intervals along the fibrils) that allow for load transition between sequential fibrils [74]. Next in the hierarchical composition of collagen comes the collagen fibres that are made up of several collagen fibrils. Work by *O'Connell et al.* found that the average collagen fibre was made up of a bundle of approximately 24 parallel collagen fibrils, tightly enveloping the smooth muscle cells [75]. They also found that the fibrils run in parallel and were not woven together, and concluded that this was probably to improve its mechanical properties [75]. The hierarchical structure of collagen can be seen in Figure 2. Furthermore, collagen has a half-life of around 2 months meaning that it is constantly being turned over and deposited by the local cells [11]. The degradation of collagen is controlled by matrix metalloproteinase enzymes [11].

The collagen supplies strength and stiffness (bulk Young's moduli of approximately 3-10 GPa have been noted [69,76]) to the aorta wall, allowing it to resist the force of the blood being pumped around the body. Aortic stiffness increases as you descend from the aortic arch to the abdominal aorta, which correlates with an increasing quantity of collagen [77]. Furthermore, the spatial organisation of the collagen fibres has also been shown to greatly influence the mechanical properties of the aorta wall [72]. Collagen is described as having viscoelastic properties and this can be explained by the load sharing capabilities of collagen fibrils through the proteoglycan bridges [74]. More specifically, as the fibrils slide against each other the proteoglycan bridges deform allowing for the relative movement of each fibril [74]. Once the loading has finished the fibrils relax and return to their normal state [74].

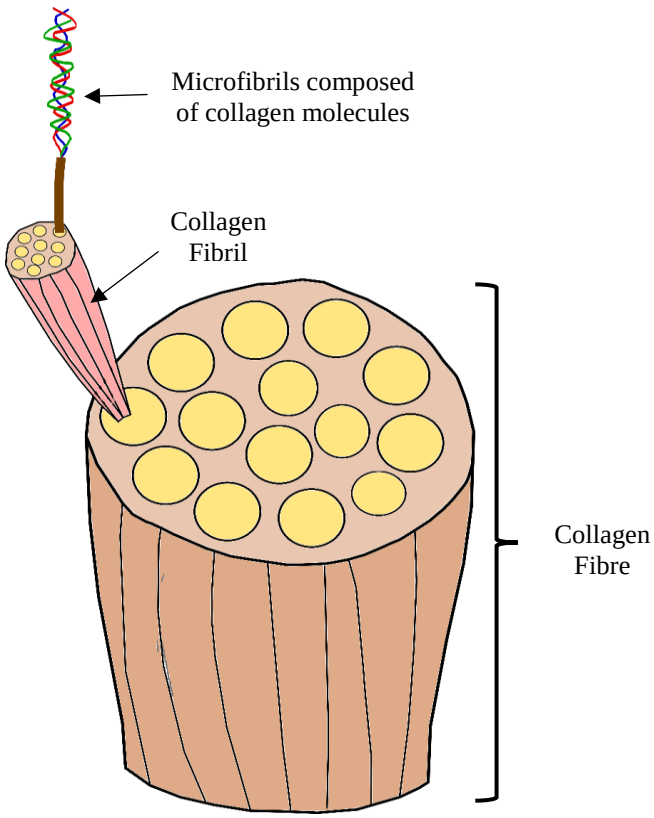

Figure 2: Hierarchical structure of collagen

1.5.1.2 Elastin

Elastin is one of the key proteins that makes up vascular ECM, especially in the case of arterial ECM where elastin can make upwards of 35% of the dry weight [20]. An elastic fibre is composed of both elastin and microfibrils – each making up around 90% and 10% of the elastic fibres weight, respectively [78]. The elastin forms the internal core of the elastic fibre, which is surrounded by a thin sheath of microfibrils. This elastic fibre has a diameter of approximately 10-12 nm [79]. These fibres align themselves along the axis of strain within the artery's wall, helping to counteract the effect of the pulsating blood, in turn protecting the organs downstream from the pulsating effect [6].

Elastin is an insoluble biopolymer with an estimate half-life of around 70 years [10]. Due to its inability to turn over, the total quantity of elastin in the human body drops over time [10]. Elastin is formed through the crosslinking of tropoelastin, a 60 kDa protein. Tropoelastin is found as a monomer in solution and is cross-linked using lysyl-oxidase, leading to the formation of long elastin fibres [80]. The

microfibril appears first and acts as a scaffold for the deposition of elastin [81]. It is mostly composed of two large (350 kDa) glycoproteins called fibrillins 1 and 2 [82,83].

The major property of elastin that makes it so prevalent in the body is its ability to extend and return to its original shape even after billions of cycles [17]. These fibres are capable of extensions in the range of 150% before fibre failure [84]. Furthermore, the Young's modulus of elastin has been found to be between 300 kPa and 1.2 MPa [84,85]

1.6 Cardiovascular Disease

1.6.1 Atherosclerosis

Atherosclerosis is a type of cardiovascular disease that narrows the arteries, restricting the amount of oxygenated blood that can reach beyond the narrowing [86]. Damage to the endothelium leads to a build-up of fat/cholesterol/calcium that over time expands causing a restriction in the vessel, as seen in Figure 3 [87]. This restriction itself causes issues as oxygenated nutrient filled blood can now no longer reach its destination, leading to diseases such as coronary artery disease and peripheral artery disease. Furthermore, if the blockage breaks away it can cause serious issues downstream as it can get stuck in narrower vessels leading to strokes and heart attacks [86].

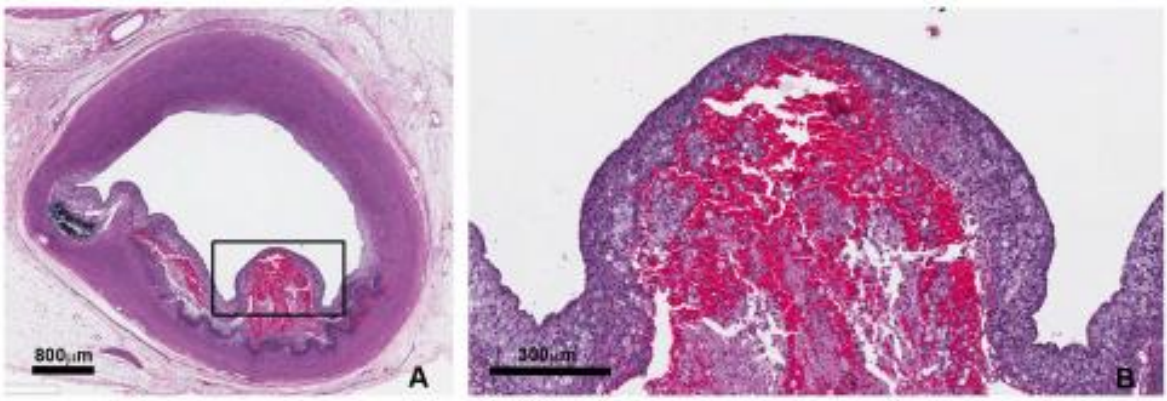

Figure 3: Coronary artery atherosclerosis in 11 month old pigs stained with haematoxylin, eosin and Verhoeff-van Gieson. (A) Overall image. (B) represents a zoomed in image of the black rectangle in image (A). Black = cell nuclei, purple = cell cytoplasm, red = elastic tissue. Image adapted from [87].

Interestingly, atherosclerosis first appears in childhood, whereby a small layer of plaque will line the endothelium of arteries [88]. From here on, atherosclerosis progresses into adulthood where the build-up

of plaque will become more pronounced in areas of damage. Treatment options for atherosclerosis vary depending on the severity of the blockage. For example, in cases where urgent intervention is not required the usual treatment options include lifestyle changes (weight management, physical activity, diet and reduction in smoking) or the use of antiplatelet medication and statins that prevent the build-up of more plaque and allow for smoother passage of blood [88]. In more serious cases where the blockage is deemed too severe for the aforementioned treatment options, surgery is often required [89]. This includes bypass grafting (grafting in an alternative path for the blood to flow around the blockage) and angioplasty (expansion of the artery to allow for smoother passage of blood) [90,91].

1.6.2 Fibromuscular Dysplasia

Fibromuscular dysplasia, also known as hyperplasia, is described as a non-atherosclerotic, non-inflammatory vascular disease that predominantly affects the renal and carotid arteries (60-75% and 25-30% frequency of involvement, respectively) [92]. The disease state is characterized by an increase in the number of cells within the organ or tissue beyond what is normal [93]. The difference between hyperplasia and dysplasia is that in hyperplasia the increased number of cells appear normal, whereas in dysplasia the cells appear abnormal. It can occur in any of the three layers of the vessel: intima, media and adventia; with medial dysplasia representing the most common type [92]. It is typically characterized as having the appearance of a "string of beads" [94]. These lesions can either present themselves as focal lesions (a single lesion) or multifocal lesions (several lesions), as seen in Figure 4. Briefly, Figure 4 shows an angiography of the affected vessel. Angiography is an imaging technique used to view the lumen of a vessel, so a narrowing in the lumen indicates hyperplasia may be occurring, causing the vessel walls to intrude in to the lumen [95].

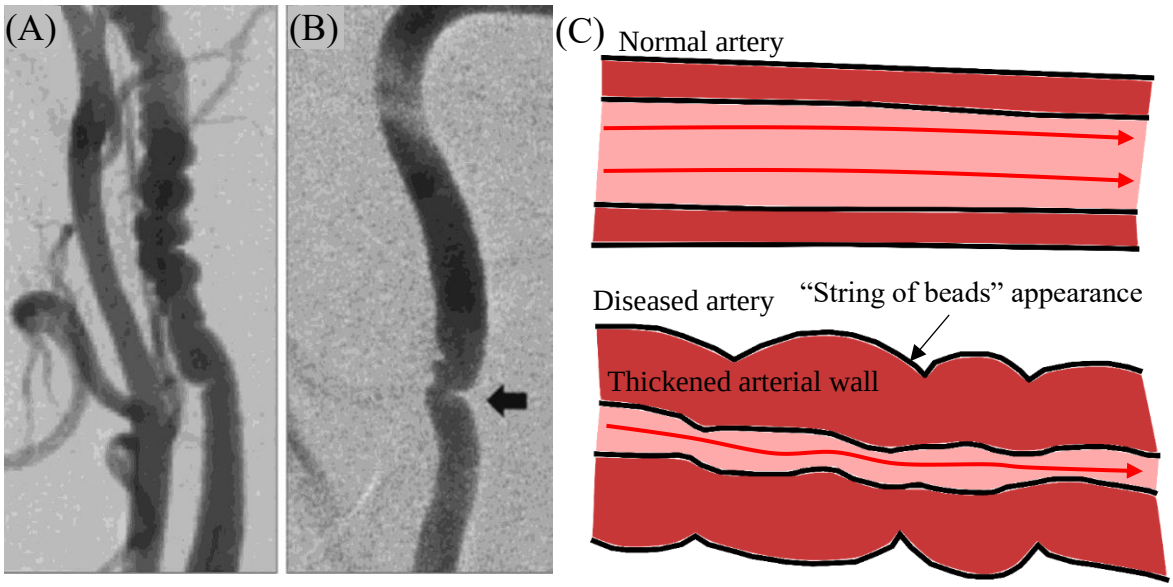

Figure 4: Angiographic subtypes: (A) Multifocal lesions in the carotid artery and (B) focal lesions in the carotid artery. Adapted from [96]*. (C) Diagram showing the "string of beads" appearance adopted by the artery due to fibromuscular dysplasia.*

1.6.3 Thrombosis

Thrombosis is a type of vascular disease that affects both arteries and veins. It occurs when a blood clot is formed inside the blood vessel, thus obstructing the flow of blood through the body [97]. When the vessel endothelium is breached/disrupted, the underlying ECM becomes exposed to the blood initiating the formation of a thrombus. The exposed ECM triggers an accumulation of platelets at the site of damage, and the exposed tissue factor signals for the creation of thrombin. These two signalling pathways occurring simultaneously lead to the creation of a solid thrombus [97]. Thrombosis can occur in almost every artery and vein in the body, with its location being a key factor in the severity of the disease [98]. When a thrombus breaks away from the endothelium it becomes an embolus that can now freely travel through the circulatory system [99].

1.6.4 Embolism

An embolism is a blockage caused by an embolus, which is a piece of material that has freely travelled around the circulatory system and lodged itself into a narrow vessel [99]. The embolus can come from a variety of sources: a dislodged blood clot called a thrombus [97]; a fat globule called a fat embolism [100]; a bubble of gas called a gas embolism [101]; and a foreign body/material [102].

There are two types of embolism: an arterial embolism and venous embolism. Arterial embolisms can occur anywhere in the body and often results in infarction, which is localised tissue death arising from a lack of oxygenated blood reaching that particular area [103]. A venous embolism will usually form inside the lungs (pulmonary embolism) after passing through the right side of the heart [104].

The most common treatment method employed for small scale embolisms is the use of an anticoagulant that stops blood from clotting, allowing time for the body to absorb the clot that has caused the embolism [105]. If the embolism is deemed to be more serious, the doctor might go in with a catheter to either remove the embolism directly or try to dissolve it [106]. Alternatively, a filter can be surgically placed into the Vena Cava, catching any embolus before it makes its way to the lungs [107].

1.6.5 Coronary Artery Disease

Coronary artery disease (CAD) starts to develop when the coronary artery that feeds the heart muscle with oxygen and nutrients starts to become blocked up due to atherosclerosis, thrombosis and hyperplasia, amongst other diseases [108]. This decrease in oxygenated blood flow to the heart muscle leads to angina (chest pain) and shortness in breath, and in serious cases, will lead to a heart attack (myocardial infarction). The severity of CAD is made evident by the fact that 45.7% of all UK cardiovascular disease related deaths in 2012 and 44% of all European cardiovascular disease related deaths in 2017 were attributed to CAD [109,110].

CAD treatments depend on what has actually caused the development of the disease. Once this has been concluded, a variety of treatment options are available. Briefly, if the CAD is in its early stages then a lifestyle change is the most common treatment method. This included changes in diet, reducing in alcohol intake and smoking, and more regular exercise [110]. In addition to this, a variety of drugs are available including: cholesterol-modifying medications (decreases low density/bad cholesterol); blood thinners such as aspirin; beta blockers (slow down heart rate, thus reducing oxygen demand from the heart muscle); and pain killers to help with angina [109]. If the CAD is deemed to be too severe and urgent intervention is required then angioplasty and stent placement or coronary artery bypass surgery are two options [111,112].

1.6.6 Myocardial Infarction

A myocardial infarction, more commonly known as a heart attack, is when blood flow is restricted or completely stopped to a particular part of the heart, causing damage to the heart muscle and reducing its functionality [113]. They are usually caused by a blockage in the coronary artery (atherosclerosis and hyperplasia) [113]. A myocardial infarction is often the first indicator of other vascular diseases, most often coronary artery disease. It can have a variety of effects on the patient, ranging from going unnoticed with no symptoms to sudden death [113]. Interestingly, myocardial infarctions can be predicted through the appearance of various proteins in the blood (myoglobin and cardiac troponin being examples) which are released by the dying myocardial cell population [114]. The favoured biomarkers for the assessment of myocardial infarction is troponin I or troponin T due to their high specificity to cardiac cells and their high sensitivity during testing [114].

1.6.7 Peripheral Artery Disease

Much like coronary artery disease, peripheral artery disease (PAD) starts to develop when a peripheral artery (renal and brachial) becomes blocked up due to atherosclerosis, thrombosis and hyperplasia, amongst other diseases [108]. These arteries feed the extremities with oxygen and nutrients. This can lead to a variety of issues such as numbness and weakness in the legs; blue/purple colouration of the legs; ulcers on the feet and hands; and muscle wastage [115]. In serious cases, PAD can lead to critical limb ischemia, which will eventually lead to necrosis of the extremities [116]. Treatment for PAD is very similar to CAD and includes the use of a variety of drugs, bypass surgery and angioplasty and stent placement [109].

1.6.8 Stroke

A stroke occurs when blood flow to the brain is restricted for various reasons, resulting in cell death [117]. They will often lead to disability and sometimes death of the patient. The majority of strokes are caused by atherosclerotic thrombi in the cranial arteries [92]. As the diameter of the artery decreases moving into the deeper parts of the brain, the thrombus (now called an embolus as it has broken away) can get stuck and block the artery, starving the downstream brain tissue of oxygen [118]. The other major type of stroke is a haemorrhagic stroke, which is caused by bleeding, often due to a ruptured

aneurysm [119]. Interestingly, the haemorrhagic stroke is usually more serious that the conventional ischemic stroke, with a significantly higher mortality noted (49.2% died during follow-up, compared to just 25.9%) [119].

1.6.9 Arterial Aneurysms

An arterial aneurysm is the dilatation of the artery to 50% larger than its normal size [120]. This 50% guideline is a loose definition as arteries will naturally change in size over the patient's lifetime [120]. They can be located in any artery, however, the most common and severe location is in the aorta, both abdominal and thoracic [121]. Aneurysms cause weaknesses in the arterial wall and create points of stress which increase the patient's risk of arterial rupture [122]. When a rupture does occur, large amounts of internal bleeding occur, often leading to death [121]. The mortality rate for patients whose abdominal aortic aneurysm has ruptures is as high as 85%, with half of deaths occurring before surgery was attempted [123,124]. In most cases, repair of large or symptomatic aneurysms (endovascular grafts) is recommended due to the higher risk associated with this type of aneurysm [121].

1.6.10 Heart Failure

Heart failure occurs when the heart muscle stops pumping blood efficiently, resulting in the muscle over working and ultimately leading to lower quantities of blood reaching the organs and limbs [125]. Heart failure can appear as either chronic or acute heart failure. Chronic heart failure is the more common of the two and presents itself with bouts of worsening symptoms (shortness of breath and fatigue, amongst many others) that may require hospitalisation [126]. In contrast to this, acute heart failure usually presents itself with severe symptoms (pulmonary oedema, cardiogenic shock and decompensation) and requires immediate attention [126]. Unfortunately, heart failure is hard to reverse, therefore most treatments focus on preventing the progression of the disease. The main methods of treatment are lifestyle changes (increased exercise, reduced smoking, etc.) and the use of beta-blockers and diuretics [127,128].

1.7 Treatment Options for Cardiovascular Disease

1.7.1 Bypass Grafting

Bypass grafting is a commonly used vascular intervention, whereby an alternative path is grafted onto a vessel to allow for oxygenated blood to travel around a damage or blockage in the vessel, as seen in Figure 5 [91]. This damage or blockage can be caused for a variety of reasons including, but not limited to, atherosclerosis and thrombosis, as mentioned above [86]. Bypass grafting is usually split into two different categories: small diameter grafts (< 6 mm) and large diameter grafts (> 6 mm). Small diameter grafts include the coronary arteries, infrainguinal arteries and infrageniculate arteries [129]. Large diameter grafts include aortoiliac substitutes (> 8 mm), carotid and femoral artery replacements (6 – 8 mm) [130,131].

The difference between the small and large diameter bypass grafts becomes stark when the type of graft being used is looked at [129]. Bypass grafting can be further subdivided into two more categories: synthetic grafts and vessel grafts (autologous vs allograft vs xenograft) [129]. Synthetic grafts are made from polymers such as Polytetrafluoroethylene (PTFE) and Polyethylene terephthalate (PET), also known as DACRON. They have shown very high patency (degree of openness) in large diameter bypass grafting, with values as high as 90% [130]. However, in small diameter vessels, they have shown to be fairly unsuccessful, with patency rates ranging from 32-75% after only 2 years depending on which vessel was being operated on, as seen in Figure 6 [111,132]. One of the major advantages of synthetic bypass grafts is the ability to bond medication to the surface of the polymer graft. Heparin is often bound to the inside layer of a graft, giving it direct contact with the flowing blood [133]. A study by *Devin et al.* found that 1, 2 and 3 year above-knee femoropopliteal bypass graft patency was increased by 22, 37 and 31%, respectively, when heparin was bound on the inside of the graft [133].

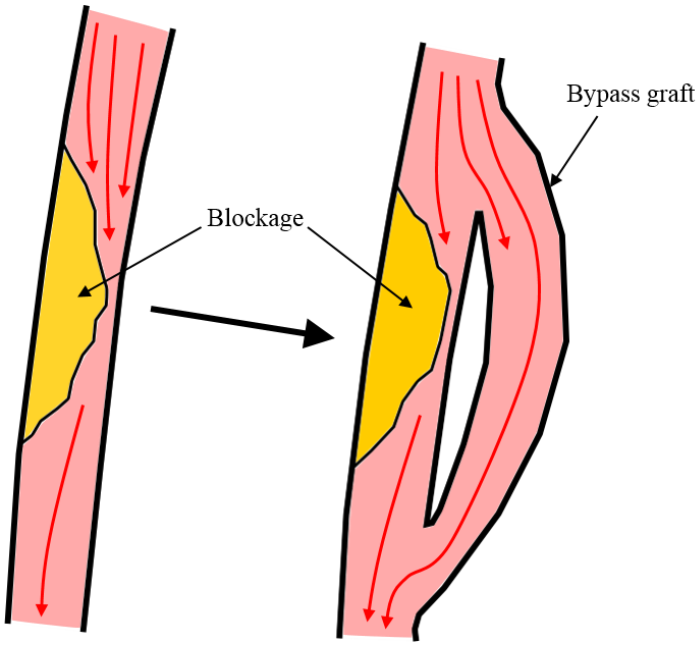

Figure 5: Schematic of how a bypass graft works. Bypass grafting allows for blood flow to be deviated around a blockage within an artery, allowing oxygenated blood to reach beyond the blockage.

The current 'gold standard' for bypass grafting is the use of an autologous vessel (one of the patients own vessels), in particular, the saphenous vein, internal thoracic artery and radial artery [134]. The use of autologous vessels is especially desirable in small diameter bypass graft where huge improvements in patency rates have been noted compared to their synthetic alternatives [129,135]. 5 year patency rates of approximately 75-85% have been noted in coronary artery bypass grafts, above-knee femoropopliteal bypass grafts and femoral popliteal distal bypass grafts, as seen in Figure 6 [129,136]. However, there is a limited availability of autologous vessels in the body due to there being a finite amount of vessels that can be used, and in some cases, the quality of the vessel is too low for transplantation, which means autologous vessel bypass grafting is not available for all patients [137,138]. Furthermore, in some cases the extraction of autologous vessels can be deemed to be too dangerous and can cause donor site morbidity [137].

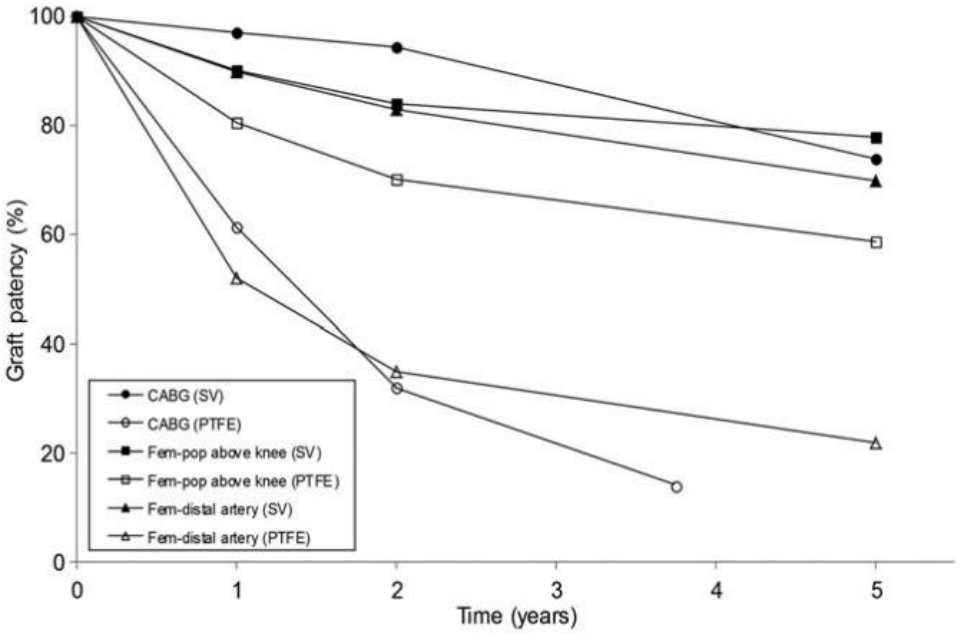

Figure 6: Patency rates for small diameter bypass grafts using the saphenous vein (SV) (gold standard) and PTFE conduits for three different surgeries. Patency rate is higher in all cases when using an SV conduit. CABG (coronary artery bypass grafts), Fem-pop above knee (above-knee femoropopliteal bypass grafts) and Fem-distal artery (femoral popliteal distal bypass grafts) [129].

Vessel bypass grafts can be further subdivided into three different categories: autologous grafts (patient and donor are the same); allograft (patient and donor are different) vs xenograft (patient and donor are different species) [139]. Autologous grafts and allografts are limited by the availability of the vessels within the body of the donor. The difference between the two is there is a higher chance of rejection in an allograft due to poor immune response [140]. Xenografts are the least desirable of the three as they suffer from much shorter lifespans depending on the source of the graft. For example, when using a xenograft sourced from a pig, the graft would have to be replaced approximately every 10-15 years [139].

1.7.2 Angioplasty and Stenting

Angioplasty and stenting are endovascular procedures designed to open up narrowed/obstructed vessels to allow for the free flow of blood [141]. They are often used to treat atherosclerosis and fibromuscular dysplasia [142,143]. An uninflated balloon carrying a stent is inserted into the blockage using a catheter before being inflated, causing the blockage to be opened up. This allows for the stent

(usually made of metal) to be placed into the now opened up blockage, ensuring it stays open and allows for the free passing of blood, as seen in Figure 7 [142,144]. The stent prevents arterial recoil and restenosis (the recurrence of arterial narrowing) after the balloon dilation [112].

Original stent designs were fairly simple and were usually manufactured from bare metal [112]. These devices successfully reduced restenosis compared to simple balloon angioplasty alone – mostly due to preventing arterial recoil [112]. However, a study by *Fischman, et al.* found that, even though rates of restenosis were lower than angioplasty alone, 31.6% of patients (67 of 159) who received stents still suffered from restenosis [145]. The next development in stent technology came in the early 2000s when the metallic stent was combined with a drug eluting polymer, allowing for pharmacological agents to be administered directly at the site of blockage [146]. The drugs used in these stents include immunosuppressants (stops stent rejection) and anti-proliferative agents (stops unwanted cell growth at the site of stenting [146,147]. As expected, the inclusion of these pharmacological agents had the effect of reducing restenosis rates down to approximately 5-8% (rate of restenosis reduced from 21% to 8.6% (N = 533 and 525) in the study by *Moses, et al.* and from 12% to 4.7% (N = 652 and 662) in the study by *Stone, et al.*) [146,147].

One of the common reasons for stent failure is a phenomenon called in-stent restenosis [148]. This can occur for a variety of reasons: firstly, there may be a hyperplasic response to the stent, resulting in excessive tissue proliferation causing the lumen of the vessel to grow over the stent causing a narrowing of the artery to reoccur [148]. Secondly, there may be neoatherosclerosis occurring which is the formation of a new fatty blockage within the stent [149,150]. Interestingly, the occurrence of neoatherosclerosis was significantly higher in drug-eluting stents than in simple bare metal stents (31% vs 16% (N = 81 and 76) beyond the 5 year mark) [150].

Stent technology is now moving towards the use of bioresorbable materials, whereby the stent still offers mechanical support for the artery in the short run (when arterial recoil is a key factor to consider) but can later be absorbed, thus avoiding the long run concerns of in-stent restenosis [151]. Materials used in bioresorbable drug eluting polymer stents include polylactic acid (PLA) and

polylactic-co-glycolic acid (PLGA), made by a variety of companies including Axxess®, BioMatrix®, MiStent® and SYNERGY®.

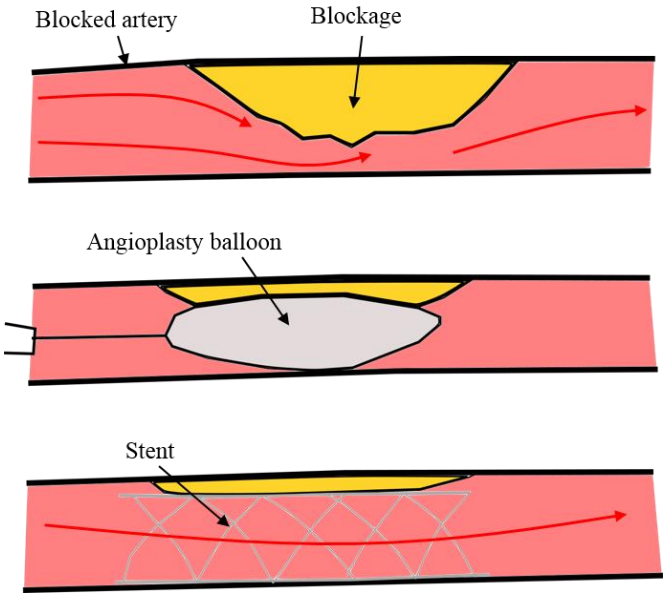

Figure 7: Schematic showing how angioplasty and stenting works. Blockage is opened up with an angioplasty balloon before a stent is placed to keep the blockage open.

1.7.3 Medication

Beta-blockers (medication that blocks the adrenergic β-receptors) are widely used in the treatment of different types of cardiovascular disease [152]. They act by blocking the binding of adrenaline and other stress hormones to these receptors, reducing the effect these stress hormones have on the cardiovascular system. They have been used to treat hypertension, abnormal heart rhythms and to protect the heart following myocardial infarction [153]. Interestingly, studies have shown that beta-blockers lead to lower negative outcomes in hypertensive patients compared to a placebo [154].

Diuretics are extensively used in the treatment and management of cardiovascular disease, most notably in the treatment of hypertension and heart failure [155,156]. Diuretics act on the kidney and inhibit the reabsorption of salts (chloride, sodium, potassium, etc.), increasing the amount of water taken out of your blood to increase the volume of urine. This in turn reduces the total volume of blood, helping reduce blood pressure and alleviate the symptoms of heart failure [155].

Immunosuppressants are drugs used during allograft transplantations to inhibit the activity of the immune system on what it deems as being a foreign body [157]. While immunosuppressants are a necessity for any patient undergoing a transplantation, they are associated with a variety of deleterious side effects [158]. For example, many have shown to increase the development of atherosclerosis and increased hypertension [159].

Anti-proliferative drugs are designed to prevent restenosis (narrowing of the blood vessel) after an endovascular medical procedure has been undertaken [160]. These drugs have been widely used in a range of different endovascular devices such as bioresorbable scaffolds, where they are grafted into the device and designed to elute out over time. This mechanism allows for the slow release of the drug, with the aim of preventing restenosis whilst the stent is in place [146,147].

Vasodilators are drugs designed to help widen the blood vessel, easing the perfusion of blood through the vascular system. They have been widely used to treat hypertension and heart failure [161,162]. The aim of vasodilators is to help reduce the pressure on the arteries and heart muscle without depressing the cardiac output [162]. Similarly, in heart failure, the most common symptom is an increased left ventricular filling pressure, which is alleviated through aortic dilation, in turn reducing the required pumping force [161]. Vasodilators are usually used in tandem with diuretics to treat hypertension and heart failure [155,161].

1.8 Cell Based Approaches for the Treatment of Vascular Disease

Cell based therapies for the treatment and management of cardiovascular disease are on the increase, with a particular focus on stem cell-based therapies [163–165]. Mesenchymal stem cell (MSC) localization in diseased hearts has been shown to improve cardiac function, reduce scar size and increase left ventricular ejection fraction [166,167]. This is achieved through the stimulation of a variety of repair mechanisms designed to either upregulate or downregulate abnormally expressed genes [168,169]. It is believed that the paracrinal secretion coming from the injected cells is providing growth factors and cytokines to the native cells [170]. Furthermore, umbilical cord MSCs have been shown to improve cardiac function in patients with heart failure and managed to increase the left ventricular ejection fraction [171]. The upside to using umbilical cord MSCs is they are easily obtained and cultured *in vitro.*

While stem cells alone have shown good results when used in cardiovascular therapies; the combination of two or more cell types has gained traction [172]. A study by *Patel, et al.* looking at the combination of MSCs and activated macrophages showed a significant reduction in negative cardiac events [172].

One of the major downfalls of conventional injection of cells is their poor engraftment [173]. To combat this, many studies have looked at cell seeded tissue engineered patches to ensure the cells are acting directly at the point where tissue regeneration is required [174].

1.9 Scaffolding Technologies for Vascular Tissue Engineering

A tissue engineering scaffold is a material that has been designed to promote a particular cellular response [175]. In many cases the scaffold is designed to mimic the native ECM, oftentimes proving to be the best structure for optimized cell growth [176]. Many different manufacturing methods exist and are listed in Table 1.

Table 1: Different techniques used to manufacture scaffolds for tissue engineering purposes.

Fabrication technique		Advantages	Disadvantages	References
Conventional methods	Electrospinning	• Nanofiber fabrication • Anisotropic or isotropic properties achievable • Good mechanical properties	• Use of hazardous solvents • Pore size can be too small for cell infiltration • Issues with repeatability	177–180
	Hydrogels	• Cell encapsulation • Easy inclusion of bioactive properties	• Poor mechanical properties	181–183
	Directional Freezing	• Anisotropic properties • Large pores and high porosity	• Dense base layer • No interconnection between pore columns	184–186
	Salt leaching	• High porosity • Cheap manufacturing technique • Can be used solvent free	• Time consuming manufacturing method	187,188
	Bioinks	• Carrier of cells and biologicals • Patient specific properties	• Limited by printer quality	189–191
	Gas foaming	• High porosity	• Can have low pore interconnectivity	192

Rapid prototyping	Stereolithography	• High resolution • Uniform pores with a high degree of interconnectivity	• Post-polymerization treatments required	193
	Selective laser sintering	• The use of ultra-high molecular weight polyethylene • High resolution and wide range of scaffolds can be manufactured	• Hard to remove the injected powder • High temperatures	194
	Solvent based extrusion freeforming	• Ceramics and metals can be manufactured • Micron level resolution	• Hard to achieve desired protocol	195
	Bioprinting	• Ability to print encapsulated cells • Wide range of scaffold architectures achievable	• Cell survival	196,197
Scaffold conditioning	Decellularized ECM	• Incorporation of native ECM components • Good use for unused tissue samples	• Decellularizing methods can damage ECM components • Full nuclear decellularization is crucial	198–200
	ECM proteins	• Mimic the native ECM • Easier to handle than decellularized ECM	• Don't fully recapitulate the native environment	201,202
	Conditioning media	• Functionalize a scaffold with a large range of cytokines	• Some cytokines may not be desirable	203,204
	Bioreactors	• Large range of mechanical stimuli	• Bulky • Issues with sterilization • Expensive	205,206

1.9.1 Electrospinning

Electrospinning is a method of fibre production that is widely used for a variety of applications including filtration, protective clothing, sensor, wound dressing and scaffolds for tissue engineering [207]. The technique works by applying a high voltage to a polymer/solvent solution. This increase in voltage charges the surface of the liquid solution droplet causing the droplet to stretch across from the spinning nozzle to the mandrel, as seen in Figure 8. The droplet at the spinning nozzle forms a Taylor cone before it starts stretching out. Once the critical point is reached, the droplet fires across towards the mandrel. This part of the flow is called Ohmic flow and is reliant on the difference in charge. Between the spinning nozzle and the mandrel the solvent phase of the solution evaporates

leaving behind thin fibres of polymer that are subsequently deposited onto the mandrel. This part of the flow is called convective flow and happens due to the charge within the fibre migrating towards the surface, as seen in Figure 8 [208].

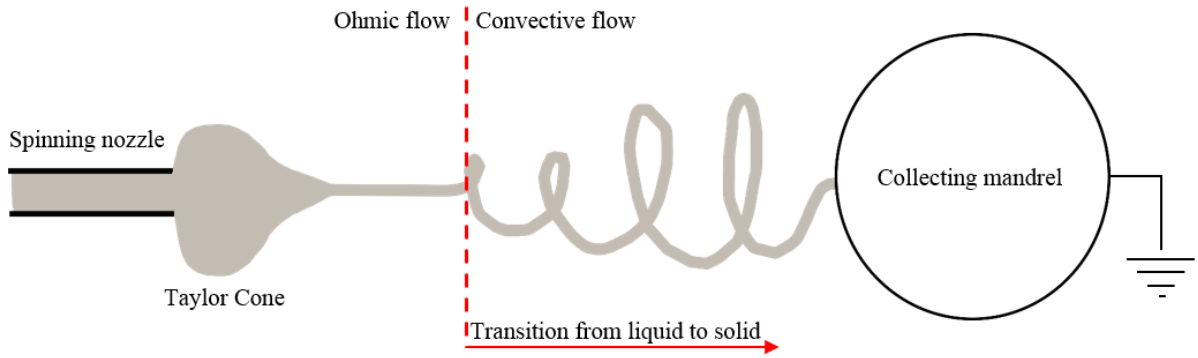

Figure 8: Electrospinning process. The high voltage charges the polymer/solvent solution causing it to fire across and deposit polymer fibres onto the mandrel. The transition from Ohmic flow to convective flow causes the solvent to evaporate from the solvent/polymer solution.

Electrospinning is a versatile technique that can manufacture a range of fibre morphologies and can use a variety of different polymers, proteins and solvents [177,209–211]. One of the major benefits of electrospinning is the ability to manufacture fibres in an array of sizes ranging from the nanoscale (30 nm) up to the micron scale (> 10 μm) [177,212–216]. This characteristic of electrospinning gives it the flexibility to be used for a variety of tissue engineering applications where local ECM morphologies may differ [217]. Beyond the control of the diameter of individual fibres, the orientation of the fibres can also be controlled by altering the rotational speed of the mandrel on which the fibres are collected [218]. This is only achievable using a rotating mandrel where the speed can be modified allowing the fibrous sheet to have anisotropic properties that may more closely mimic the properties of the tissue being studied [219]. Studies have also shown that certain cell types prefer aligned fibres where they can stretch out along the fibre [177]. Furthermore, the process of electrospinning can accommodate a variety of polymers, solvents and organic proteins allowing for a range of applications [217,220,221]. Polymers that have been widely researched in tissue engineering include polycaprolactone (PCL), polylactic acid (PLA), polylactic-co-glycolic acid (PLGA), Polyvinyl alcohol (PVA), amongst many other that will be discussed later [221]. Equally, the range of solvents/liquid phases that can be electrospun is large and

offers an assortment of possibilities. These include solvents such as hexafluoroisopropanol (HFIP), chloroform, dimethyl formamide (DMF), methanol and acetic acid, and in some cases deionised water [220,221]. Finally, a variety of other substances can be added to the electrospinning solution such as proteins, antibiotics/medication, growth factors, genes and cells [202,217,222,223]. The versatility in the substances used and different morphologies that can be created means electrospinning can be used for a large range of purposes.

1.9.2 Directional Freezing/Phase Separation

Phase separation, also known as directional freezing, is a scaffold manufacturing technique that relies on the liquid phase of the polymer/solvent solution freezing along a temperature gradient. During the controlled freezing process, the liquid phase solidifies into columnar structures pushing the polymer into the gaps between the ice crystals, as seen in Figure 9 [224]. Once the solution is frozen the liquid phase can be sublimated away in a freeze dryer leaving behind a scaffold with a distinct columnar structure [184]. A variety of parameters can be altered in the manufacturing process, allowing for a range of structures to be manufactured. These include the temperature at each end of the gradient; the polymers and solvents used; the polymer concentration; and the direction of the temperature gradient. Furthermore, this technique can incorporate a multitude of different proteins, growth factors and cells [184,186,225–227].

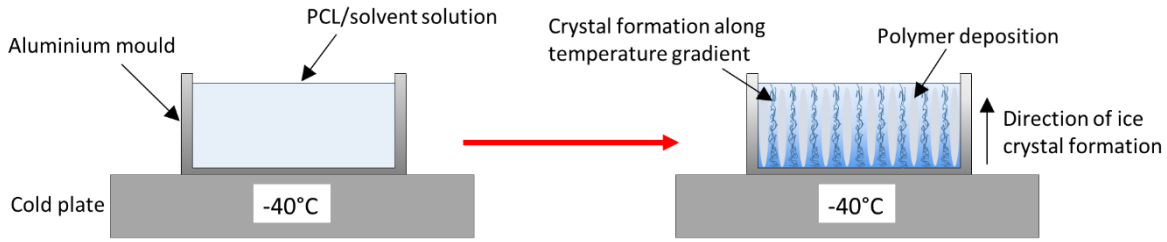

Figure 9: Schematic representation of the directional freezing process. Crystals form along the axis of temperature gradient. Once sublimated, a columnar structure is left behind [184].

1.9.3 Salt Leaching

Salt leaching is a sacrificial scaffold manufacturing technique that is used to create highly porous scaffolds [187]. The salt crystals are poured into a mold whereby the polymer solution is poured on top,

filling the voids left behind between the salt crystals (in some cases the salt can be mixed in with the polymer solution before being poured into the mold). Once the polymer solution has hardened, the salt particles are leached out through dissolution into a solvent, water often being the one used [228]. One of the major advantages of this technique is that it is easily used without cariogenic solvents, which are often the downfall of other techniques [187]. Furthermore, the scaffolds created can have large open pores that may be desirable for certain cell types [187]. Additionally, a variety of different salt crystals can be utilised allowing this method to generate an array of different porous structures, both in shape, regularity and size [188].

1.9.4 Gas Foaming

Gas foaming is a widely used technique in large scale industry that has moved its way towards the production of micro scale scaffolds for tissue engineering [192]. Examples of industrial uses include the manufacture of expanded polystyrene and various polymer based foams, where porosity and/or enclosed gases are desirable [192]. This method can be split up into two types of gas foaming structures: closed-cell and open-cell. Closed-cell structures do not have pore interconnectivity (gas bubbles) and tend to possess stronger mechanical properties; these structures are not common in tissue engineering. On the other hand, open-cell structures do have pore interconnectivity (gas tunnels) and allow for cell and nutrient transfer throughout the thickness of the structure [192]. Furthermore, these structures allow for vascularization, which is a key desirable feature for tissue engineering scaffolds [229].

The method works by gasifying a liquid phase through chemical decomposition or a thermal reaction. For example, an effervescent salt particle (ammonium bicarbonate) can be combined into a polymer gel and cast in a mold. The solution is heated up releasing ammonia and carbon dioxide gas resulting in the formation of pores (gas bubbles or gas tunnels) [230]. This technique has a range of applications in tissue engineering due to the different polymers, gases and proteins that can be developed into porous scaffolds [231].

1.9.5 Hydrogels

Hydrogels are a widely used scaffold manufacturing technique in tissue engineering; especially in soft tissues where the mechanical performance of the scaffold is not as important. They are a 3D structure

composed of a network of hydrophilic polymers cross-linked together via either covalent bonding or physical interactions [232]. They get their hydrophilicity from the presence of hydrophilic moieties (amine groups, carboxyl groups, etc.) along the backbone of the polymer chain [232]. Their highly porous structures combined with the high hydrophilicity of the polymers allow these hydrogel structures to absorb a large amount of fluid, often several times more mass than the polymer itself [232]. Furthermore, this methods lends itself to the use of a wide range of biocompatible polymers such as the natural polymers chitosan, alginate and collagen; and the synthetic polymers Polyethylene oxide (PEO), Polyvinyl acetate and Polyacrylic acid (PAA). In addition to this, a wide array of proteins, growth factors and cell types have been encapsulated into the hydrogel structure as a means of improving the bioactivity of the scaffold [181,182,232–234].

The encapsulation of native ECMs has gained traction in recent years due to the improving methods of decellularization along with the bioactive potential associated with these materials [235]. Retaining the full biochemical complexity of the native ECM is of crucial importance and has been done with a variety of different decellularized tissue types [235–237].

1.9.6 Rapid Prototyping

Rapid prototyping is a blanket term used to describe a range of manufacturing techniques that use models made from 3D computer aided design or computed tomography (CT). The scaffold is designed on a computer and then manufactured using 3D printing or additive layer manufacturing [196]. While this method is heavily used in industry for manufacturing objects from metals and polymers, it has only recently started being used to design scaffolds for tissue engineering applications. One of the major advantages of rapid prototyping is the ability to accurately tailor the morphology of the scaffold [238]. Bioprinting is a new rapid prototyping method which uses bioinks (see section 1.9.6) to create 3D scaffolds [197]. The method combines biomaterials with cells and growth factors to fabricate scaffolds which maximise mimicry with the native tissues. These rapid prototyping techniques have shown success in the tissue engineering realm [239,240]. Studies by *Bibb, et al.* and *Liew, et al.* have demonstrated the efficacy of bioprinting at developing 3D scaffolds with predefined vascular networks. Furthermore, selective laser sintering (another rapid prototyping method) has been used to

develop scaffolds for 'soft tissue' engineering [194]. They manufactured a scaffold with optimized mechanical properties capable of maintaining cell viability.

1.9.7 Bioinks

A bioink is a substance that carries cells and other bioactive substances and can be printed into a 3D scaffold for tissue engineering purposes [241]. These bioinks are the major component of bioprinting and need to carry the correct characteristics in order to function properly during the printing process and once the structure is complete. They are designed to mimic the native ECM structure in order to create a habitable environment for the support of cells at all developmental stages (adhesion, proliferation and differentiation) [191]. Due to the presence of biological components and cells within the bioinks, they tend to be processed and printed under very mild conditions to preserve the living cells and ensure no degradation of bioactive molecules occurs [242]. Bioinks have a huge potential in tissue engineering due to the wide array of cells and biological components that can be incorporated into the ink [243]. These include natural polymers such as collagen, chitosan, gelatin, or in some cases native ECMs that are made up of a mixture of different natural polymers [189,243,244]. Furthermore, these bioinks can be tailored for each individual patient through the use of autologous cells and tissues [190].

Printability is the major characteristic of the bioink that requires intricate design and study. They need to form filaments when they are deposited allowing the bioink to be printed into the desired shape [244]. A variety of bioink and printer characteristics can be altered to allow for the successful printing of the bioink. These include the print pressure and velocity; volume flow rate; viscosity; and bioink concentration [242]. Furthermore, flow rate needs to be kept minimal to ensure the cells undergo low shear stress as this can induce apoptosis [245]. The mechanical properties of bioprinted bioinks are often too low for most tissues [244]. Recent advancement of the field of bioinks has led to a combinational approach to bioprinting, whereby the mechanical properties are increased by embedding the bioink around a polymer lattice [244].

1.9.8 Decellularized Tissues

Decellularization is the process by which a tissue is stripped of its cellular population leaving behind the tissue's ECM [200]. This ECM is composed of a variety of different proteins and enzymes that are

tissue specific and is responsible for cell adhesion, cell-to-cell communication and cell differentiation into new functional tissue [64]. These decellularized ECMs can either be used as scaffolds or can be combined with other manufacturing techniques to create composite scaffolds [235,246]. They provide the new seeded cells with a native biochemical environment and therefore have the effect of increasing the bioactivity of the scaffold [217].

There are a variety of different decellularization methods which tend to fall under three different categories including physical methods, chemical methods and enzymatic methods, as seen in Table 2 [200]. Physical methods tend to rely on mechanical force or external environmental change. These include snap freezing, pressurization, sonication, agitation and shear stress via perfusion and have been successfully applied to a variety of tissues including vascular tissues [247–251]. Snap freezing relies on ice crystal formation causing cell lysis, however, this needs to be highly controlled as the ice can damage the ECM, rendering it unusable [252]. Furthermore, while this method does cause cell lysis, it doesn't remove the cells from the tissue, therefore a further cell removal method is required [253]. The pressurization method is a fairly simple method that relies on mechanical force to burst and remove the cells. It is an effective method when trying to decellularize a loosely packed tissue such as liver tissue, and has also been successfully implemented for decellularization of vessels [254,255]. Pressurization, agitation and sonication are methods that are often combined with chemical and enzymatic methods [256].

There are a wide range of different chemical methods that are used for decellularization [257]. One chemical method is the use of detergents such as sodium dodecyl sulfate (SDS) and Triton X-100. These detergents solubilize the cell's membranes and separate DNA from the cell's proteins allowing the cellular material to be removed from the tissue [258,259]. These methods are very effective at removing cellular material from the tissue and their efficacy increases with exposure time [260]. However, with increasing exposure time and detergent concentration, increased ECM protein degradation is also noted [246]. Over-exposure has been shown to decrease the ECM's GAG content and also leads to a reduced quantity of native growth factors within the decellularized tissue, therefore, finding a fine balance between concentration, exposure time and final DNA content is of crucial

importance [261,262]. As previously mentioned, combining physical methods and chemicals methods is fairly common practice when decellularizing tissues. An example of this is combining an SDS chemical method with a perfusion based pressurization method. By holding a pressure through the tissue, quicker and more effective decellularization is achieved [256].

Finally, enzymatic methods are available for decellularization and rely on the breakdown of the bonds holding the nucleic acids onto their neighbouring proteins [263]. Enzymes that have been widely used in literature for the purpose of vascular decellularization include collagenase, nuclease and trypsin [250,259,264]. Nucleases, for example, are designed to cleave onto the nucleic acid sequence after cell lysis, facilitating the removal of nucleic material from the tissue being decellularized [265]. While collagenase is an effective means of decellularization, it has a major drawback due to its collagen digesting properties, one of the major components of most ECMs. This means that collagenase can only be used when the collagen structure of the ECM is not required post-decellularization [266]. Finally, trypsin acts by breaking down the cell-matrix bonds and is often used to facilitate decellularization [267]. It has been shown to accelerate the decellularization process when used alongside other methods but can also damage the ECM [267,268].

Table 2: Different decellularization techniques used in tissue engineering.

Decellularization technique		Mode of action	Noted effect on tissue	References
Physical methods	Temperature/snap freezing	• Ice crystal formation disrupts cell membrane	• Damage to the local ECM due to freezing • Lysed cells need to be removed from tissue using an alternative method	253,269
	Pressurization	• High pressure can burst the cells • High pressure used to strip cells away from the ECM	• Effective with loosely packed ECM • Over-pressurization can damage the ECM	254,255,270
	Perfusion/shear stress	• Shear stress facilitates the removal of cellular material from the tissue	• Helps disrupt the cells • Can damage the ECM	251,256

Chemical methods	Detergents	• Detergent solubilizes the cell's membrane and separates DNA from protein	• Over-exposure can damage the ECM • Lysed cells need to be removed from the tissue using an alternative method	256,258,261
	Acids and bases	• Solubilizes the cytoplasm and disrupts the DNA	• Damages the ECM and removes GAG • Alters mechanical properties	268,271,272
	Alcohols	• Dehydration of cells causing lysis	• Damage ECM structure	273,274
Enzymatic methods	Nucleases	• Cleave onto nucleic acid post-lysis	• Lysed cellular content needs to be removed with an alternative method	250,265
	Trypsin	• Breaks down the cell-matrix bonds	• Speeds up the decellularization process • Damages the ECM	267,268,275
	Collagenase	• Digests collagen which breaks down bonds with cells	• Damages the ECM's collagen	266

1.10 Summary

To summarise, cardiovascular disease is the leading cause of death globally and can present itself in many different ways, requiring a range of different treatment options. While great progress is being made to find novel solutions, there is still a shortfall in the quality of treatment available. Patients requiring small diameter bypass grafts still find themselves without long-term solutions due to the inadequacies of the current materials being used. Tissue engineering is presenting itself as a promising avenue for the development of new treatments to treat cardiovascular disease. This project aims to look at novel biomaterials as a means of influencing the behaviour of two vascular cell types: endothelial cells and smooth muscle cells.

Aims and Objectives

The hypothesis of this thesis is that the morphology and composition of electrospun scaffolds can influence vascular cells – human umbilical vein endothelial cells (HUVECs) and human umbilical vein smooth muscle cells (HUVSMCs). Many studies have shown that vascular cells can be influenced by their environment, therefore there is rationale to studying scaffold morphology and composition.

The aims of this thesis are:

I. Manufacture electrospun scaffolds with differing morphologies and assess their impact on HUVECs and HUVSMCs. The morphological characteristic focussed on in this thesis is fibre diameter, which has been shown in past literature to affect other cell types.
II. Incorporate decellularized vascular ECMs (aortic and myocardial ECM) into polymer scaffolds and assess their impact on HUVECs and HUVSMCs. Aortic and myocardial ECM from a bovine source were used as these two ECMs are physiologically relevant to the two cell types being studies. Past literature has shown that ECMs from other tissue types can be incorporated into polymer scaffold and do have beneficial effects on other cell types.
III. Bind vascular cell secretome to polymer scaffolds to further biofunctionalized them and assess their impact on HUVECs and HUVSMCs. The pre-functionalization of scaffolds using proteins has shown promise in the field of tissue engineering. Therefore, there is rationale in trying to create a scaffold that is functionalized with proteins that have been directly secreted by vascular cells.
IV. Use physiologically relevant environmental conditions to alter cell secretome and cell functionality. Hydrostatic pressure was used to try and create an altered secretome profile for binding onto the scaffold and hypoxia was used to assess the ECM scaffolds in an *in vitro* representation of the diseased vascular state.

Chapter 2: Materials and Methods

2.1 Electrospinning

The electrospinning set up used during this thesis is an EC-DIG electrospinning platform from IME Technologies (Netherlands). The electrospinner had a wide range of settings allowing from a variety of solutions to be used and morphologies to be created [1]. Briefly, the range of potential set ups are: needle to mandrel distances ranging from 0 to 23 cm; mandrel rotational velocities ranging from 0 to 2500 RPM; needle bore sizes ranging from 0.1 to 0.9 mm; positive voltages ranging from 0 to 25 kV; negative voltages ranging from -4 to 0 kV; and a range of different needle motions.

All fibres during this study were collected on a rotating mandrel covered in aluminium foil at room temperature. The rotational velocity of the mandrel can be altered depending on the alignment being sought from the fibres. This thesis predominantly uses randomly orientated fibres which were collected at 150-250 RPM depending the solution being used. Polycaprolactone (PCL) (Mn=80000 Da) (Sigma-Aldrich, UK) was either dissolved into 1,1,1,3,3,3-hexafluoro-2-isopropanol (HFIP) (Manchester Organics, UK) or a 5:1 ratio solution of chloroform to methanol (both Sigma-Aldrich, UK), or a 10:1 ratio of the same two solvents. Solutions were mixed at 30 RPM overnight at room temperature using an SRT9D roller mixer (Stuart, UK). The finalised electrospun scaffold sheet was left overnight to dry in a fume hood before being removed for use as a scaffold. Electrospinning of ECM-PCL blends was achieved using the same protocol. Individual electrospinning protocols for each study are listed in their respective chapters. All scaffolds were punched out from the sheet using a 10 mm diameter punch.

2.2 Decellularization

Decellularization was achieved with a closed-loop perfusion based chemical detergent protocol using a bespoke decellularization device [2]. Bovine aorta and heart tissue samples were harvested from a 2 year old cows and frozen within 4 hours. First, approximately 2 g of native tissue was chopped up into 5x5x5 mm pieces to create a larger surface area for decellularization as this has been shown to facilitate the process [3]. The pieces were then placed into the device and perfusion decellularized using 0.5% w/v sodium dodecyl sulfate (SDS) (Sigma-Aldrich, UK) in 1 L of ultrapure deionised water (diH_2O). The SDS solution was swapped over to a new batch after 12 h of decellularization. In total,

decellularization lasted approximately 36 h. Subsequently, the SDS was flushed out of the decellularized tissue using 10 L of deionised water for a total of 1 h in the same system with the device exit attached to separate vessel to ensure flushed out SDS is not put back into the tissue. It is imperative that SDS is removed from the tissue as SDS residue has been shown to lead to several unwanted outcomes including foreign body response *in vivo* [4]. The decellularized tissue was then frozen and lyophilized to remove all liquid for the milling process.

2.2.1 Milling

Milling of decellularized tissue was achieved using a PM100 plenary ball mill (Retsch, Germany) with approximately 300 stainless steel balls with a diameter of 2 mm. Pieces of lyophilized decellularized tissue were cut up to be smaller than the individual balls before being placed into the ball mill. Milling was achieved using a 4 minute 500 RPM protocol (3min clockwise, 1min counter-clockwise). The protocol was run 8 times to achieve full milling. Between each run the set up was put on dry ice to make sure the decellularized tissue was kept as cold as possible, simulating cryomilling. This increases the brittleness of the ECM, leading to the creation of a finer powder and ensures the ECM does not overheat during the process [5–7]. Milled ECM was collected in water, frozen and then lyophilized leaving behind a fine powder.

2.3 Cell culture

2.3.1 Culture of Human Umbilical Vein Endothelial Cells

The human umbilical vein endothelial cell (HUVEC) line is a primary cell line that was first isolated in the 1970s by *Jaffe, et al*. using a collagenase digestion method [8]. They are widely used to study the pathology and functionality of endothelial cells, and have shown to be robust, cheap and easy to isolate, making them an ideal cell type for preliminary *in vitro* cell studies [9].

The HUVECs used were isolated from the umbilical cord of an infant male Caucasian donor (PromoCell GmbH). This study abides by all criteria of the UK Human Tissue Act. The HUVECs arrived at P1 and were cultured to P7 in a humidified atmosphere of 5% CO_2 and 37°C. HUVECs were cultured in MCDB131 medium (Life Technologies™) supplemented with 5% v/v FBS (ThermoFisher Scientific) + 1% v/v L-glutamine + 100 U/mL penicillin + 100 μg/mL streptomycin

(all Gibco) + 1 mg/L hydrocortisone + 50 mg/L of ascorbic acid (Sigma) + 2 mg/L fibroblast growth factor + 10 mg/L epidermal growth factor + 2 mg/L insulin-like growth factor + and 1 mg/L VEGF (all PeproTech). Cells were passaged once 80% confluency was reached using Trypsin-EDTA (Gibco). All cell studies were run with HUVECs at either passage 7 or 8.

2.3.2 Culture of Human Umbilical Vein Smooth Muscle Cells

The human umbilical vein smooth muscle cell (HUVSMC) line is a primary cell line that is isolated from one or two of the arteries found within the human umbilical cord [10]. They are usually isolated in a similar manner to HUVECs, often using a form of enzymatic digestion that was first introduced by *Jaffe, et al*. in the 1970s [8]. They are a robust cell line for the study of vascular diseases and have been widely used in tissue engineering for preliminary *in vitro* and *in vivo* studies [11–13].

The HUVSMCs used were isolated from the umbilicus of a neonatal Caucasian male (Merck). Briefly, the HUVSMCs arrived at P1 and were cultured to P5 in a humidified atmosphere of 5% CO_2 and 37°C. Cells were cultured and banked using smooth muscle cell culture medium (Merck) up to P4. Cells were passaged at 80% confluence using Trypsin-EDTA (Gibco) at room temperature and were split 1:3. Subsequent cell studies were run using P5 HUVSMCs and cultured using DMEM supplemented with 10% v/v FBS + 100 U/mL penicillin + 100 µg/mL streptomycin + 1% Non-essential amino acids.

2.4 Histology

2.4.1 Paraffin Wax Embedding and Sample Processing

All tissue samples undergoing immune histological staining were fixed and embedded into paraffin wax before being cut down using a microtome for staining. Firstly, the tissue sample was cut down to approximately 5 mm of thickness and then fixed in 10% v/v formalin for 24 h. This ensured that the samples were thoroughly fixed but not damaged due to over-fixation. Formalin fixation followed by paraffin wax embedding has been shown to lead to sample shrinkage by up to 30%, therefore, it is imperative that the sample is adequately processed [14]. The sample was then moved over to 70% v/v ethanol before the next step is performed.

Once fixed, the sample went through a series of ethanol based dehydration steps and xylene washes to displace the water and subsequently allow for paraffin wax infiltration. Once the tissue sample had been completely cleared with xylene, the sample was placed into paraffin to allow for the paraffin wax to infiltrate the tissue. The paraffin used had a melting point of 54-58°C, therefore the oven should be set at no more than 60°C. This melted the wax whilst limiting any damage that overheating may cause on the fixed tissue. Over-exposure to hot wax can lead to brittle samples [14]. The tissue goes through two soakings in paraffin lasting 1-2 h each. This ensures that the paraffin has fully penetrated the fixed sample.

The sample was then ready to be embedded into solid paraffin wax in a microtome cassette. This was all done at 60°C to ensure the wax does not solidify during processing. Approximately 1-2 mm of molten wax was placed onto the base of the cassette. The sample was then placed on top of this wax in the desired orientation for trimming. The cassette backing was then added before the whole cassette was filled with paraffin wax. Once the wax had solidified the whole embedded block could be placed into the freezer for later use.

The embedded blocks were then be sectioned into thin slices for staining using a microtome. Before sectioning, the blocks were placed on ice to keep the paraffin wax cold as this facilities the sectioning process [15]. The microtome blade was set at approximately 5° and the slice thickness was set to anywhere between 3-10 μm. The sections were sliced and floated in 37°C water before being picked up by glass slides. The slides were then heated up to 60°C (slightly above the wax's melting temperature) to allow for the tissue slices to bond onto the glass slide. Samples were then stored at room temperature.

Once the sample had been sectioned and bound onto a glass slide, they were read to undergo dewaxing so they could be stained. First, the samples was thoroughly dewaxed using three 2 min washes of xylene or histoclear. The sample was then rehydrated in a series of ethanol and water washes.

2.4.2 Haematoxylin and Eosin

The haematoxylin and eosin (H&E) stains are commonly used stains for microscopic examination of cellular based tissues and are widely used in medical diagnosis, where they are regarded as the gold standard [16]. Examples of this include the diagnosis of many cancers that can be easily identified using H&E staining [17]. Likewise, H&E staining are widely used in tissue engineering for a variety of reason. For example, the stain is often used to confirm decellularization or to evaluate the success of *in vivo* experiments [18,19]. Haematoxylin has a dark blue/black colour that stains anything that can be considered basophilic (anything with an affinity for the base dye). In this case that includes the cell nuclei, rough endoplasmic reticulum and the ribosomes[20]. In contrast, the eosin stain has a light pink colour that stains anything that can be considered to be eosinophilic. This includes the cell membrane, cell cytoplasm and most ECM proteins such as collagen, elastin and many more [20]. It is imperative that the protocol used is tailored to each tissue type as overstaining and understaining can be misleading. Both haematoxylin and eosin are light sensitive stains and require varying exposure times to different tissues [21].

Once the tissue had been dewaxed and rehydrated it can be stained with H&E. Briefly, the sample was placed in haematoxylin solution for 6min, allowing enough time for the haematoxylin stain to penetrate the cell nucleus. This was followed by a 5 min rinse under tap water to ensure the haematoxylin is completely removed. At this point the sample will darken in colour as the haematoxylin starts to bind to the basophilic substances. The sample was then placed in eosin for 90 s allowing enough time for the eosin to penetrate. The eosin was then removed using 95% ethanol. The sample was placed in acidified water (0.5% v/v acetic acid in diH_2O) for 15 s before undergoing a series of dehydration steps.

2.4.3 Picrosirius Red

The picrosirius red stain is a widely used stain for the characterisation of collagen I and III fibres within embedded tissue samples [22,23]. The stain possess a red colour and reacts with the sulfonic acid and base groups present in collagen molecules and can easily be visualized under conventional light microscopy, although cross-polarized light has also been used [24]. Furthermore, the cell substances

such as the nucleus and cytoplasm are stained a dull yellow colour, helping to create contrast between the cellular material and the collagenous substances [23].

Once the tissue had been dewaxed and rehydrated it could be stained with Picrosirius red. Briefly, the sample was placed into the 0.1% w/v Picrosirius red stain (Sirius red in saturated aqueous picric acid) for 1 h. This gave near equilibrium staining which does not increase over time. Shorter times should be avoided as this may lead to incomplete staining. Sample was then washed in two changes of acidified water (0.5% v/v acetic acid in diH_2O) for 1 min. The sample was then dehydrated through a series of ethanol washes and cleared:

2.5 Plasma Coating

Plasma coating is a surface modification technique that is often used in biomaterials engineering as a means of altering the hydrophilicity of a material [25,26]. The process is usually performed under a low pressure oxygen environment, however, argon and conventional air compositions can also be used. Ionization of these elements is achieved by applying a high frequency voltage to the central coil of the chamber containing the gas. This creates highly reactive free radicals that will bind themselves to the material within the chamber. In an oxygen environment, this leads to the formation of oxygen containing groups on the surface of the material, increasing its hydrophilicity [27]. Furthermore, the process of plasma coating has the additional benefit of sterilizing the material [27].

Polymer scaffolds were plasma coated directly before use to avoid the effect of hydrophobic recovery taking place [28]. Briefly, a Harrick Plasma cleaner and a PPC-FMG-2 PlasmaFlo gas flow mixer (Harrick Plasma) were used to plasma coat the scaffolds before cell seeding. This process was done after the scaffolds were punched out of their respective electrospun sheets. Oxygen was introduced into the system and the pressure was stabilised at approximately 500mTorr. Plasma coating was undertaken at 10.2 W for 60 s. Scaffolds were immediately removed and placed into sterilized PBS containing antibiotic/antimycotic treatment solution.

2.6 Mechanical Testing

The mechanical properties of the scaffolds in this thesis were undertaken in tension, the predominant direction of force observed by vascular tissue [29]. Studying and understanding the mechanical properties of any scaffold or device that is designed for implantation is of crucial importance. The mechanical properties of the host and implant need to fall within a tight band or else the unmatched loads can lead to complications down the line, and ultimately, failure of the implant and further damage to the native tissue [30,31]. Synthetic materials have great difficulty in matching the mechanical properties of native vessels due to the native tissue's unique mechanical features including non-linearity (steep increase in Young's modulus as pressure is increased), viscoelasticity (viscous time-dependent strain response) and compliance (ability of the vessel to extend under pressure) [32]. Compliance is of particular interest as this mechanical feature is very hard to mimic with synthetic materials. In clinical practice, arterial compliance is defined as how much the cross-sectional area of the artery distends when internal blood pressure increases [33]. Designing scaffolds with mechanical properties that fall within the realm of native tissues is the first step to designing a successful scaffold. In vascular tissue engineering, this involves designing scaffolds with properties similar to the arteries that are either being healed or replaced. *Strekelenburg et al.* found that the saphenous vein has longitudinal and circumferential elastic moduli of 23.7 MPa and 4.2 MPa, and longitudinal and circumferential ultimate tensile strengths of 6.3 MPa and 1.8 MPa [34].Similarly, *Soletti et al.* noted a circumferential elastic modulus of 2.25 MPa for the saphenous vein [35].

An Instron 3367 tensile testing machine (Instron, UK) was used for all mechanical characterization. The device was set up with a 50 N load cell. For the majority of studies a gauge length of 20 mm was used with an extension rate of 10 mm/min (50% strain per minute was always used to ensure consistency between studies and to ensure high resolution of data capture). Samples were fixed to a 'C' shaped paper template to improve handleability of the samples and ensure the same gauge length was used every time. The width of each sample was measured using digital callipers and the thickness measured using a DMK 41 AU02 monochrome 1280 x 960 camera.

An incremental Young's modulus method was used [1,36,37]. Young's modulus is a measure of the materials ability to withstand deformation when under tension or compression. Briefly, incremental Young's modulus was calculated using the formula

$$E_{incremental} = \frac{\sigma}{\varepsilon} = \frac{(F_1 - F_0)L_0}{A(L_1 - L_0)}$$

where $E_{incremental}$ is the Young's modulus between two strain bands (denoted as 1 and 0 in the subscripts), σ is stress, ε is strain, F_1 is the applied force at the upper strain band, F_0 is the applied force at the lower strain band, A is the cross-sectional area of the scaffold perpendicular to the direction of elongation, L_0 is the original length at the lower strain band, and L_1 is the final length at the upper strain band. Young's modulus is calculated over a range of strains to show the evolving properties of the scaffold under extension.

The ultimate tensile strength was calculated as the highest stress withstood by the scaffold. This was also used as the point at which the scaffold was deemed to have failed (failure strain).

An incremental compliance method was used to characterise the different ECM concentration blended scaffolds. Compliance was measured using the following equation

$$C = \frac{\Delta V}{\Delta P}$$

where C is the compliance, ΔV is the change in volume and ΔP is the change in pressure. Values for ΔP and ΔV between 0 and 5% strain were deduced from thin-wall pressure vessel theory. Briefly, the equation for circumferential stress was reorganized to give an equation that told us the representative pressure (P_n) at a given stress value σ_n (subscript n denoting that the value is at % strain).

$$\sigma_n = \frac{P_n d_n}{2t}$$

$$P_n = \frac{\sigma_n \times 2t}{d_n}$$

where σ_n is stress, d_n is the diameter of the representative cylinder, and t is the thickness of the scaffold. Representative volume (V_n) was calculated by treating the strip of scaffold as a cylinder and the strain as a volume increase to this cylinder (subscript n denoting that the value is at n% strain)

$$V_n = \pi \times \left(\frac{d_n}{2}\right)^2 \times w$$

where d_n is the diameter of the representative cylinder and w is the width of the scaffold.

2.7 Contact Angle Measurement

The term wettability refers to the ease at which a liquid will spread itself across or through a solid substrate and how easily it will adhere itself to the substrate [38]. Water contact angle measurement is a common method of assessing the wettability of a material [39]. The water contact angle is defined as the angle formed at the intersection of the liquid–solid interface. In this case, the liquid is a water droplet and the solid is the polymer scaffold being tested. A lower contact angle is indicative of a more hydrophilic substrate, whereas a higher contact angle is indicative of a hydrophobic substrate [40,41]. Furthermore, studies have shown that altering the contact angle of a scaffold can have interesting effects on cell adhesion [25,42].

Briefly, all contact angles were measured using the sessile drop method. This is the most commonly used method and relies on measuring the advancing contact angle between a water droplet and the substrate [43,44]. All contact angles were measured on dry scaffolds. A 5 μL droplet of water was placed onto the scaffold using a pipette tip, and images were captured using a DMK 41 AU02 monochrome camera at a frequency of 5 Hz. Analysis of the scaffolds was done on ImageJ (NIH) using the LBADSA plugin at varying times after the water droplet made contact with the scaffold, as seen in Figure 10 [45].

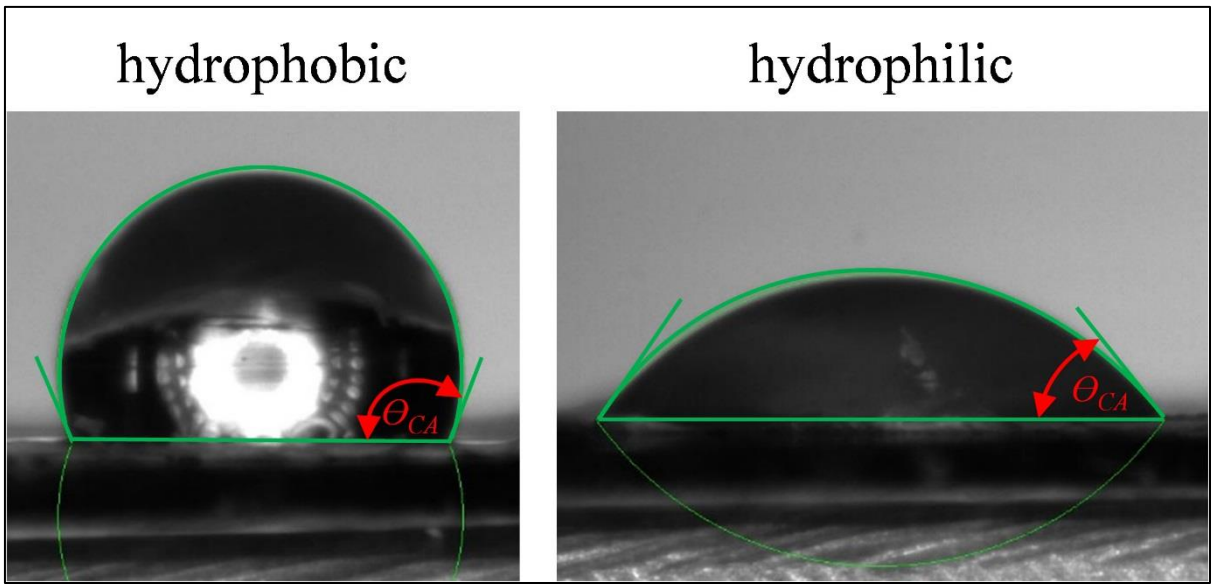

Figure 10: LBASDA plugin for ImageJ measuring the contact angle of a hydrophobic and a hydrophilic substrate. The contact angle being measured is denoted by θ_{CA}.

2.8 Scaffold Fibre Alignment/Orientation

The fibre alignment and orientation of various biological substrates have been shown to have a drastic effect on cell survival, performance and morphology for a range of cell types [1,46–49]. Furthermore, a scaffolds mechanical properties can be altered through the modulation of fibre orientation [50]. Aligning fibres in parallel leads to a highly anisotropic scaffold with high stiffness along the axis of its fibres and low stiffness perpendicularly. On the contrary, a highly random fibre orientation will lead to an isotropic scaffold with similar mechanical properties along all its axes [1].

The alignment/orientation of the fibres within each scaffold were assessed using the OrientationJ plugin for ImageJ [51]. Briefly, SEM images of the scaffold's fibres were imported into ImageJ and thresholded for analysis.

2.9 Scaffold Porosity

Scaffold porosity is a measure of the amount of empty space found within the scaffold. A high porosity suggests that there is a lot of empty space within the scaffold, and vice versa for a low porosity. In some cases the pores are highly interconnected (often the case with electrospun scaffolds), whereas sometimes the pore interconnectivity will be low even with a high porosity

(occurs more often in directional freezing). Studies have suggested that there is a connection between the scaffolds porosity and pore interconnectivity with overall cell survival, proliferation and migration [36,52–54]. These studies tend to follow the trend that high pore interconnectivity and porosity are beneficial for cellular performance [55]. In addition, the size of each pore is also very important, with most cells and tissue types having an optimal middle ground. Pores that are too small don't allow for sufficient cell infiltration and nutrient transfer, whereas pores that are too large do not allow for adequate cell-cell interactions [54]. Therefore it is very important to modulate the scaffold's porosity for the particular cell type being studied.

Scaffold porosity (%) was calculated using a DMK 41AU02 monochrome camera with the following equation:

$$Porosity = 100 \times \left(1 - \frac{m_{scaffold}/V_{scaffold}}{\rho_{polymer}}\right)$$

where V is volume, m is mass and ρ is density.

2.10 Fourier Transform Infrared Spectroscopy

Fourier Transform Infrared spectroscopy (FTIR) is a commonly used technique that obtains either an absorbance or emission spectrum from a substance [56]. This method allows for the collection of a range of data over a wide spectral range, which is advantageous compared to traditional dispersive spectrometers as they only measure the intensity of a narrow range of wavelengths. FTIR has been widely used in tissue engineering to confirm the presence of various substances within biomaterials and tissues [42,57–60]. They have been used to show that decellularization techniques do not destroy the native components of the tissue [61]; ECM has been incorporated into polymeric scaffolds [42,60]; and that specific substances have been successfully grafted onto polymeric scaffolds [58,59]. The absorbance spectrum collected for a particular material can give a wide range of information regarding the types of bonds and substances present. Each peak along the spectrum is associated to a particular bond type which in turn is associated to a particular substance [62]. For example, the peaks at 1655 cm^{-1} and

1550 cm^{-1} are associated with the amide I and amide II bonds, respectively [63]. These bonds are found with collagen I and other ECM related proteins [63].

FTIR spectra were recorded using a Nicolet iS10 spectrometer with a Smart iTX diamond attenuated total reflector (all from Thermo Fisher Scientific). Measurements were taken over a wave range of 400-4000 cm^{-1} at a 1 cm^{-1} resolution using the OMNIC Spectra software (Thermo Fisher Scientific). FTIR spectra were used to ensure the integrity of the ECM was maintained during decellularization and to ensure the ECM was properly integrated into the electrospun fibres.

2.11 Scaffold Seeding

Scaffolds used for experiments were punched out using a 10 mm punch and soaked in 70% ethanol to remove them from the aluminium foil that they were collected on and to sterilize the scaffolds. Scaffolds are then transferred to a bio hood to ensure they remain sterilized. Scaffolds that were treated with plasma are soaked in PBS + 1% antibiotic/antimycotic before being transferred across to the bio hood. The scaffolds were then placed into a 48 well plate and soaked in serum free medium overnight to help with hydrophilicity. The medium was then removed prior to cell seeding.

Cells were drip seeded at the required cell density in 20 μL of medium. This medium volume was kept as small as possible as it has been shown that scaffold seeding efficiency is increased when the seeding volume to scaffold volume ratio is kept as small as possible [64]. The drop of medium was placed in the middle of the scaffold and allowed to soak through the scaffold for 30 mins. This ensures the cells are caught within the fibrous structure of the scaffold. An additional 30 μL of medium was added after 30 mins to ensure the cells are provided with sufficient medium. The volume of media is kept minimal and the incubation time until topping of up of media is kept long enough to help with cell binding as this has shown to lead to more efficient cell seeding [64]. After another 90 mins, the medium was topped up to 500 μL. Seeded scaffolds were fed every 48 hours.

2.12 CellTiter-Blue Assay

The CellTiter-Blue® (Promega, UK) assay is a fluorescence based method for measuring cell metabolic activity and thus cell viability. The assay works by the living cells converting a redox dye

called resazurin into a fluorescent end product called resorufin [65]. Any non-viable cell will rapidly lose metabolic capacity and will therefore not produce a fluorescent signal [65]. The resazurin is dark blue in colour and has very little fluorescence until it is changed to resorufin, which is pink and highly fluorescent at 579/584 nm. For most cells, there is a highly linear correlation between cell number and fluorescence, meaning that changes in cell viability can be considered as the same percentage change in cell number [65].

The assay was run as per manufacturer's protocol. Briefly, scaffolds were removed from their well-plates, were washed thrice in PBS and then placed in new well-plates. A 1:4 ratio of CellTiter-Blue assay to cell culture medium was mixed together. This solution was added to the cell seeded scaffold and cultured for between 3 and 3.5 hours (this time should not be exceeded as it leads to assay saturation [65]) . The reduced solution was then added to a black microplate in 100 µL samplings. Measurements were taken using a Modulus™ II microplate reader at excitation wavelength of 525 nm and emission wavelength of 580-640 nm.

2.13 BCA Assay – Protein Quantification

The Pierce™ BCA Protein Assay (Thermo Scientific) is a quantification method for measuring the total protein content of a solution. The assay works by the peptide bonds found within the protein reducing the cupric ions from the copper sulfate down to copper [66,67]. There is a direct correlation between the amount of reduced copper ions and the amount of protein present. These copper ions then bind to the bicinchonic acid forming a purple complex that absorbs light at the 562 nm wavelength [66]. The assay works through absorption and quantification is achieved by comparing the results with known protein standards. This assay has been widely used in tissue engineering, where it can be used to confirm the successful engraftment of proteins onto a polymeric scaffold and the rate of release of a protein from a scaffold [68–71].

This assay was used to quantify the amount of protein being released during the media functionalizing experiments and the amount of protein being bound to the scaffolds during the soaking phase that followed on after the EDC/NHS treatment of scaffolds. All experiments were run as per manufacturers' protocol. Briefly, 25 µL of unknown protein solution is pipetted into a clear bottomed

96-well plate along with 200 μL of BCA assay working reagent. This is done alongside known standards ranging from 0 to 2000 μg/mL. The well plate is mixed on shaking plate for 30 s before being incubated at 37°C for 30 mins. Absorbance is then measured at 560 nm using a Modulus™ II microplate reader.

2.14 EDC/NHS Binding Method

The EDC NHS surface activation method is an effective technique of activating the surface of a polymer to aide with the immobilisation of biomolecules [68]. The method works by the 1-Ethyl-3-(3-dimethylaminopropyl)-carbodiimide (EDC) activating the carboxyl groups on the polymer for reaction with the primary amines [72]. This creates an unstable intermediate that can react with another amine. The N-hydroxysuccinimide (NHS) is then added to stabilize this intermediate by converting the unstable amine-reactive O-acylurea into a stable amine-reactive NHS ester. This process allows one side of the carboxyl group to be free for coupling with a ligand that already contains a free aldehyde group [68]. The process is shown in Figure 11 [68]. The EDC/NHS surface activation method has been widely used to help with the grafting of proteins onto various different surfaces [73–75].

The EDC/NHS method was used to help with the binding of proteins and cytokines found in the cell-secretome functionalized media. Briefly, 5 mM of EDC and 5 mM of NHS were dissolved into 0.5 M of MES buffer at a pH of 5.7. The pH of the solution and the molarity of the EDC and NHS are both critical. The pH directly affects the half-life of the activation period of the EDC and NHS and the molarity of the solution affects whether or not complete activation of the surface is achieved or if by-products are left on the scaffold [73]. A lower pH (< 6.5) has been shown to drastically reduce the activity half-life of EDC and NHS from above 4 hours to below 30 minutes [76]. Furthermore, it has also been found that over-treatment in EDC/NHS can lead to lower quantity of amide bonds being formed and that a pH of approximately 5-6 leads to a higher rate of amide bond formation [76]. Therefore, selecting an appropriate pH is of crucial importance when trying to ensure an optimal amount of amide bonds are formed to increase the quantity of protein binding. On that note, scaffolds were bathed in the EDC/NHS solution for 30mins and were then washed thrice in PBS to remove all

remnant EDC/NHS. The scaffolds were then bathed in the protein solution (media in this instance) for 4h to maximise the quantity of protein being bound to the scaffold.

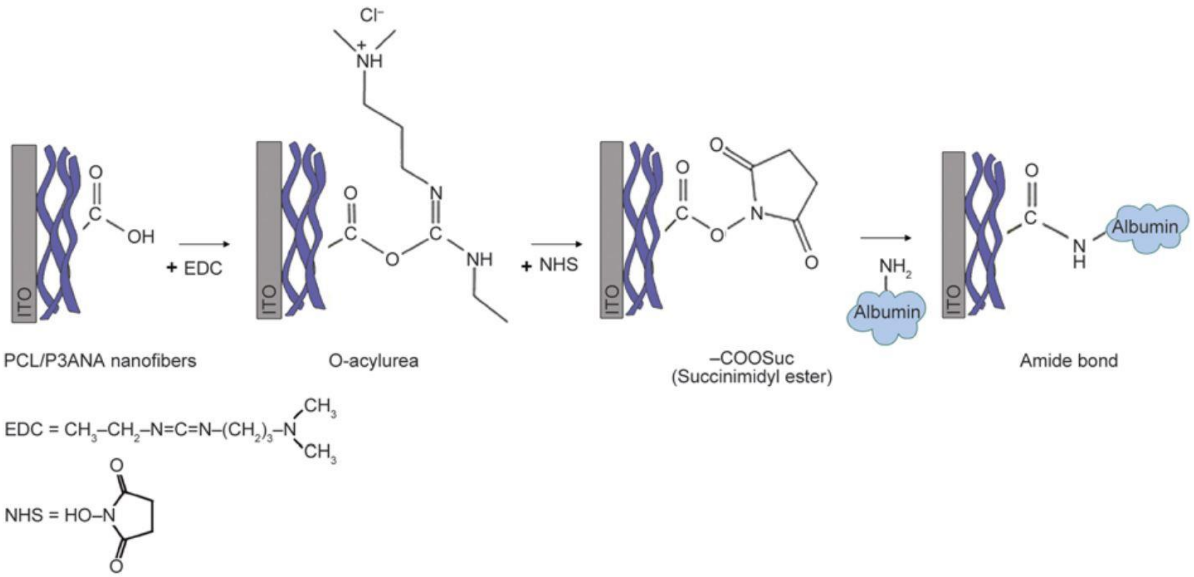

Figure 11: Schematic of how the 1-Ethyl-3-(3-dimethylaminopropyl)-carbodiimide (EDC)/ N-hydroxysuccinimide (NHS) process creates binding opportunities for proteins. In this case the protein is albumin. The EDC activates the carboxyl group for a reaction with a primary amine. This creates an unstable intermediate which is stabilized using the NHS. This process creates a stable amide bond for binding with a free aldehyde group [68].

2.15 DNA Quantification

DNA quantification was performed using the Quant-IT™ Picogreen® dsDNA assay (Promega). The assay has become popular for biological applications as it about 1000 times more sensitive than traditional absorbance methods [77]. For most biological applications where sample sizes are quite small, a more sensitive method is required that can read below 250 ng/mL. This fluorescent nucleic acid stain is used to quantify double-stranded DNA and has a sensitivity as low as 0.25 ng/mL. All unknowns were compared to known DNA standards to give a numerical quantity of DNA in each sample [78].

Samples were lyophilized and then digested in a papain solution containing 2.5 U of papain, 5 mM cysteine HCL and 5 mM EDTA in DNA free water (all Sigma-Aldrich, UK). Digestion lasted 24 h at

60°C with periodic vortexing to disrupt the samples to aide with digestion. The assay was run as per manufacturer's protocol. Samples were measured for fluorescent intensity in a Modulus™ II microplate reader at an excitation wavelength of 490 nm and emission of 510-570 nm.

2.16 Cell Staining

2.16.1 Fluorescence Staining

Fluorescence staining is a technique used with a fluorescent microscope to visualize particular biomolecules within the cell. The process works by targeting the antigens of these specific biomolecules with antibodies that bind to them at specific sites called epitopes. These antibodies are then targeted by specific fluorescent dyes that allow for the specific biomolecule to be visualized using a fluorescence microscope. Phalloidin is used to visualize the F-actin filaments found with the cell cytoplasm [79]. Phalloidin-iFluor™ 514 Conjugate was purchased from Sigma and used on all cell types in this thesis. (The Phalloidin comes conjugated with a fluorescent dye meaning that the antibody has already been dyed and no second step of attaching a dye to the antibody is required). Likewise, 4',6-diamidino-2-phenylindole (DAPI) was purchased from Sigma and used to areas within the cell that contain DNA. Specifically, DAPI binds to the AT regions of dsDNA and notes a 20 fold increase in fluorescence upon binding [80]. DAPI (blue) is excited at 405 nm making it an ideal counterstain for phalloidin (green) or anything stained with a yellow, orange or red stain. Other fluorescently conjugated antibodies were used to visualize parts of the cell specific to the particular cell line.

Briefly, cell seeded scaffolds were removed from their media and washed thrice in PBS, before being fixed in 10% v/v formalin solution in PBS for 30 mins. This was followed by three further PBS washes. Cells were then permeabilized in a 0.2% v/v Triton X-100 solution in PBS for 5 mins and then washed thrice in PBS. Cells were then placed in 1 µL/Ll of primary antibody in 1% v/v BSA in PBS overnight at 4ºC to allow for the antibodies to bind to the targeted antigens. This was followed by three PBS washes. Cells were then placed in 1 µL/mL of secondary fluorescent conjugate in 1% v/v BSA in PBS for 30 mins to allow the fluorescent dye to bind to the antibody. This was followed by a further three washes in PBS.

Cells were then stained with conjugated phalloidin at 1 µL/mL in 1% v/v BSA in PBS for 30 mins at room temperature. This was followed by three 5 min PBS washes to ensure no phalloidin remains unbound. Cells were then stained with conjugated DAPI at 300 nM in deionized water for 20 mins, then washed thrice in PBS for 5 mins per wash. Scaffolds were then imaged using a Coherent Anti-Stokes Raman scattering microscope.

2.16.2 Fluorescence Imaging

Cell seeded fluorescently stained scaffolds were visualized using one of two microscopes.

The first set up was a custom built multiphoton microscope [81]. Coherent anti-stokes Raman scattering (CARS) imaging at 2911cm-1 was used to image the PCL scaffold fibres, whilst simultaneously exciting two photon fluorescence (TPEF) from Phalloidin and DAPI stained cells. CARS excitation was performed by overlapping the 1064 nm stokes beam with the 812.6 nm pump beam on to the sample using excitation power of 85 mW and 110 mW respectively. The 812.6 nm beam simultaneously excited TPEF, the signals were collected in the backscattered detection and spectrally separated using custom filter cubes. For CARS and Phalloidin a 649 nm long pass (LP) dichroic cube with a 660/13 nm and 542/50 nm bandpass filter was used. The DAPI signal was acquired consecutively using a 454/50 nm bandpass filter and a 570 nm Dichroic. All images were acquired using a 25x/1.05 N.A water immersion lens (XLPlanN, Olympus), providing a maximum field of view of 509 µm on the sample.

The second set up is a Zeiss Axio Imager fluorescent microscope. This was used to image fluorescently stained cells through a variety of different filters. While this set up doesn't allow for visualization of the scaffold fibres, it does allow for the several different fluorescent wavelengths to be imaged simultaneously. Images were processed using ICY or ImageJ.

2.16.3 Osmium Staining for SEM

Osmium staining is used to condition the cells so that they can be visualized using SEM. Osmium staining follows directly on from glutaraldehyde fixation. This allows for clear viewing of the cellular membrane and ECM components on the scaffold. Glutaraldehyde fixation causes rapid crosslinking of the proteins within the cells [82]. Osmium tetroxide is then used as a lipid stain by embedding a heavy

metal directly into the cell membrane, thus creating a high electron scattering rate allowing for clear visualization of the cell membrane [83]. Interestingly, osmium staining has been widely used to visualize cells in many tissue engineering applications [8,84–86].

Briefly, cell seeded scaffolds were fixed overnight in 4% glutaraldehyde. A 1% osmium solution was diluted into deionised water and cell seeded scaffolds were stained for 30mins. The samples were then rinsed thrice in deionised water and then put through a set of dehydration steps and then left overnight in Hexamethyldisilazane (HDMS). The cell seeded scaffolds are now ready to be sputter coated and visualized using SEM.

2.17 Scanning Electron Microscopy

Scanning electron microscopy (SEM) is a method of microscopy that produces an image by scanning the surface of an object with a beam of electrons. The electrons interact with the atoms located on the surface of the object which releases various signals that can be picked up by a detector. This allows for nanoscale topographies to be imaged [87]. Many materials, such as polymers, absorb electrons which can change the trajectory of the electrons that are being sent towards the specimen. This can create blurred images, therefore, most objects need to be sputter coated in order to visualize them using SEM.

Briefly, two different SEM set ups were used for this thesis. The first set up used was a Hitachi S4700 fuelled emission scanning electron microscope (SEM, Hitachi) with a 5 kV accelerating voltage and a working distance of 12 mm. This set up was used for the ECM blended scaffold studies utilising endothelial cells. The second set up used was a Hitachi TM4000 tabletop SEM (Hitachi) with a 15 kV accelerating voltage and a 10 mm working distance. This set up was used for the remainder of the studies.

2.17.1 Sputter Coating

Sputter coating is a sample preparation method employed to improve the quality of the information gathered by the SEM [88]. Many materials, such as a range of non-conductive polymers and biological materials will lead to charging in certain areas of the sample, influencing the image information.

Therefore, applying a thin layer (< 10 nm) of conductive material such as gold, platinum or palladium reduces the effect of charging and increases the quality of information captured by the SEM.

Two different sputter coating methods were used. One method used an Elmscope SC500A splutter coater with gold–palladium (60:40). The second method used an Elmscope FLM-007 with gold.

2.18 Reverse Transcription Polymerase Chain Reaction

Reverse transcription polymerase chain reaction (RT-qPCR) is a method used to quantify the genes expressed by cells. Firstly, the RNA is extracted from the cells using standard Tri-Reagent (Invitrogen, ThermoFisher) methods and purified using a Qiagen RNeasy spin column system (Qiagen). This RNA is then reverse-transcribed into complementary DNA (cDNA) using a reaction based around reverse transcriptase (Promega). The cDNA is then used with real-time polymerase chain reaction using a LightCycler® 480 Instrument II (Roche Life Science) and Sensifast™ SYBR® High-ROX system (Bioline). This final step uses a specific primer sequence to target a particular area along the DNA strand associated with that primer. As each cycle passes, the quantity of DNA associated to that particular primer is doubled, binding itself to SybrGreen. This continues until the fluorescence reaches a threshold value, whereby the number of cycles required to reach this value is recorded (C_t). This C_t value is then used to quantify the amount of RNA present in the original sample using the $2^{-\Delta\Delta C_t}$ method [89,90]. This method is a means of relative quantification of a target gene in the group of interest to that of the same gene in a control group, whilst normalizing it to a housekeeping reference gene, in this case GAPDH.

Briefly,

$$\Delta\Delta C_t = \Delta C_{tS} - C_{tR} = (STG_{Ct} - STHKG_{Ct}) - (RTG_{Ct} - RTHKG_{Ct})$$

where STG_{Ct} is the is the C_t value of the subject target gene, $STHKG_{Ct}$ is the C_t value of the subject housekeeping gene, RTG_{Ct} is the is the C_t value of the reference target gene, and $RTHKG_{Ct}$ is the C_t value of the reference housekeeping gene.

This value for $\Delta\Delta C_t$ is then used to find the fold difference in gene expression between the two samples:

$$Relative\ expression = 2^{-\Delta\Delta C_t}$$

This works out as any value below 1 representing a relative downregulation of that gene and anything above 1 a relative upregulation. All RT-qPCR data is plotted on a log axis as to ensure all downregulations are represented equally in size to upregulations.

A variety of different primer sequences were used to target specific genes in both endothelial cells and smooth muscle cells. In all studies, gene expression levels were normalised to the expression of the housekeeping gene Glyceraldehyde 3-phosphate dehydrogenase (GAPDH). These primer sequences can be seen in

Table 3.

Table 3: Primer sequences used for gene analysis of HUVECs and HUVSMCs.

Gene	**Primer**	**Sequence**
Glyceraldehyde 3-phosphate dehydrogenase	GAPDH (forward)	GTCTCCTCTGACTTCAACAG
	GAPDH (reverse)	GTTGTCATACCAGGAAATGAG
Matrix metalloproteinase-1	MMP1 (forward)	CGGTTTTTCAAAGGGAATAAGTACT
	MMP1 (reverse)	TCAGAAAGAGCAGCATCGATATG
Matrix metalloproteinase-2	MMP2 (forward)	CGCTCAGATCCGTGGTGAG
	MMP2 (reverse)	TGTCACGTGGCGTCACAGT
Tissue inhibitor of metalloproteinases-2	TIMP2 (forward)	AATGCAGATGTAGTGATCAGG
	TIMP2 (reverse)	TCTATATCCTTCTCAGGCCC
Vascular endothelial growth factor	VEGF (forward)	AGACCAAAGAAAGATAGAGCAAGACAAG
	VEGF (reverse)	GGCAGCGTGGTTTCTGTATCG
Platelet endothelial cell adhesion molecule	CD31 (forward)	ACTGGACAAGAAAGAGGCCATCCA
	CD31 (reverse)	TCCTTCTGGATGGTGAAGTTGGCT
Actin alpha 1	α-actin1 (forward)	CCGCCCAGAAACTAGACACA
	α-actin1 (reverse)	CAGCGATCCCAGGGTACATC
Myocardin	Myocardin (forward)	GGGTCTGAGCATTCCTTGCT
	Myocardin (reverse)	CTGGACGTTTCAGTGGTGGT
Mesenchyme homeobox 2	MEOX-2 (forward)	AAAAGCGACAGCTCAGACTC

	MEOX-2 (reverse)	TTGCTGTCCACCCTTTACCC
Interleukin 1 alpha	IL1-α (forward)	GCGTTTGAGTCAGCAAAGAAG
	IL1-α (reverse)	GCCGTGAGTTTCCCAGAAGA
Intercellular Adhesion Molecule 1	ICAM1 (forward)	CCTTCCTCACCGTGTACTGG
	ICAM1 (reverse)	AGCGTAGGGTAAGGTTCTTGC
Basic Fibroblast Growth Factor	FGF2 (forward)	CACCTATAATTGGTCAAAGTGGTTG
	FGF2 (reverse)	AAACGAGGGAGAAAGGATGGA
Hypoxia-inducible factor 1-alpha	HIF1-α (forward)	ACTTGGCAACCTTGGATTGG
	HIF1-α (reverse)	GTGCAGTGCAATACCTTCCA
Nitric Oxide Synthase 3	eNOS (forward)	AGATGTTCCAGGCTACAATCCGCT
	eNOS (reverse)	TGTATGCCAGCACAGCTACAGTGA

2.19 Statistical Analysis

Statistical analysis was performed using Minitab software. For all data sets, the mean and standard deviation were calculated. The number of biological replicates are displayed under the graphs in each individual chapter, with a minimum of 3 biological replicates being used for statistical analysis. The tests used in this thesis include the one-way analysis of variance (ANOVA) with Tukey's or Fisher's post hoc tests. Statistical significances are shown as $*p < 0.05$, $**p < 0.01$ and $***p < 0.001$, unless stated otherwise.

Chapter 3: Optimizing Scaffold Morphology for Vascular Tissue Engineering

Introduction

Currently, vascular diseases (a subcategory of cardiovascular disease which looks at the vessels) such as coronary heart disease, peripheral arterial disease and strokes account for upwards of 30% of all deaths in Europe [1]. To treat this, approaches such as bypass grafting are implemented. Bypass grafting is a surgery that involves diverting flow around an arterial blockage by grafting in an alternative path for the blood to flow [2]. This surgery is often used in the treatment of coronary heart disease (blockage in the coronary artery) and peripheral arterial disease (blockage in arteries in the arms and legs). This is either done with a synthetic material, such as PTFE, or by using an autologous vessel such as the saphenous vein or the internal thoracic artery [3]. These autologous vessels represent the gold standard for bypass grafting, especially for smaller vessel bypasses (< 6mm), as they are associated with much higher patency rates compared to their synthetic counterparts (80-90% for the saphenous vein after 5 years compared to 20-70% for the PTFE conduit) [3]. However, there are only a finite amount of vessels that can be harvested for bypass grafting, and patients who are in need of a bypass graft will often have damaged autologous vessels that are not of the standard required for surgery [4]. Therefore, there is a clear need for an easily manufacturable synthetic alternative that can achieve higher patency rates.

Currently, a wide array of strategies are being investigated to come up with novel treatment methods for vascular disease. These include mechanical cues, biochemical cues (incorporation of native ECM, protein binding, etc.) and bioelectric cues (electrical stimulation) [3,5–10]. An optimized environment can be created by providing the correct physical cues to the cells through altering the topographical features of the scaffold [11,12]. For example, it has been shown with a human kidney primary epithelial cell line that fibre diameter and fibre orientation have dramatic effects on cell morphology and the expression of key genes [13]. Likewise, a study looking at the effect of fibre diameter on seeded chondrocytes found that a reduction in fibre diameter increased collagen II and integrin expression, two key phenotypic markers [14]. Furthermore, recent work has shown that including nano-topographical features onto a PCL mesh had the effect of promoting endothelial cell proliferation and adhesion compared to the smooth PCL mesh [15].

Electrospinning is an exciting avenue that allows for a wide range of scaffold morphologies to be created [13,16]. This method has been used in many aspects of tissue engineering to mimic the structure of the native ECM, providing the cells with the correct mechanical cues, allowing for improved environments for cell adhesion, migration and proliferation [17]. Herein, the present study proposes altering the fibre size of PCL electrospun scaffolds to study how this aspect of the scaffold morphology affects the performance of two vascular cell types: human umbilical vein endothelial cells (HUVECs) and human umbilical vein smooth muscle cells (HUVSMCs).

Part A: Optimizing Scaffold Morphology for Endothelial Cells

3A.1 Introduction

Angiogenesis is a process by which endothelial cell proliferation and remodelling leads to the formation of new blood vessels [18]. This is the aim of vascular tissue engineering, whereby an area of damaged or degenerated tissue can be healed through vascularization. One of the major components of the vessel is the endothelium, which is made up of a monolayer of endothelial cells [19]. This is one of the main constituents of the vessel that affects bypass graft patency due to its direct contact with the flowing blood. This is where thrombosis, blood clotting and hyperplasia occur, and to some extent infection as well [19]. Therefore, one of the major aims when developing new bypass grafts is to create a healthy layer of endothelial cells organized into a tubular network [20]. This can happen under the correct environmental conditions, whereby endothelial cells communicate with each other through the release of angiogenic paracrinal factors [21].

As previously mentioned, it has been shown that adding topographical features of the nanometre scale onto smooth electrospun PCL fibres had the effect of increasing endothelial cell adhesion and proliferation [17]. This suggests that endothelial cells are very sensitive to their local topographical features and strengthens the case for studying the effect that scaffold fibre diameter has on seeded endothelial cells. Therefore, the present study has looked at how altering the diameter of the individual fibres within an electrospun scaffold affects seeded endothelial cells.

3A.2 Methods and Materials

3A.2.1 Electrospinning

Polycaprolactone (Mn = 80,000 Da) was either dissolved into HFIP or a 5:1 mixture of Chlorofrom:Methanol (C:M) (Sigma Aldrich) at varying concentrations to achieve four different solutions (Table 4). Briefly, the electrospun fibres were spun as one continuous fibre onto an aluminium foil covered 8 cm diameter rotating mandrel. Scaffolds were subsequently stored at 4°C. All scaffold analysis was performed on ImageJ. A schematic of the experimental process is shown in Figure 12. More details can be seen in Section 2.1.

Table 4: Electrospinning parameters used to manufacture scaffolds with four different fibre diameters.

Fibre size	Polymer concentration (%)	Solvent used	Needle bore (mm)	Flow rate (ml/h)	Total volume (ml)	Distance between needle tip and mandrel (cm)	Positive voltage (kV)	Negative Voltage (kV)	Mandrel rotational speed (RPM)
S – 1.64 µm	8	HFIP	0.4	1	6	11	+10.6	-2	250
M – 2.95 µm	12	HFIP	0.4	1.7	8.5	15	+14	0	250
L – 3.37 µm	14	5:1 C:M	0.8	3	18	19	+15	-4	250
XL – 4.83 µm	19	5:1 C:M	0.8	4	20	23	+18	-4	250

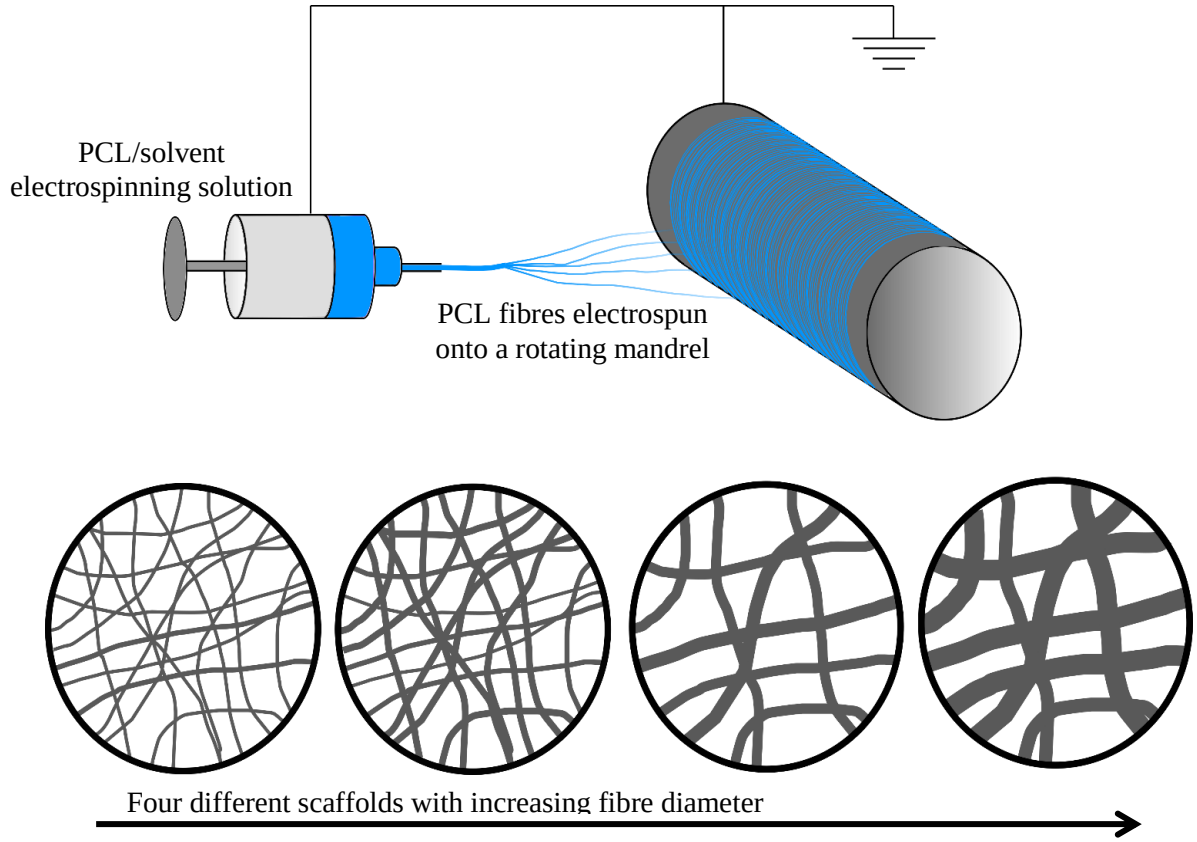

Figure 12: Schematic representation of the electrospinning process with increasing fibre diameters. Four different electrospinning set-ups were used to achieve the four different fibre diameters.

3A.2.2 Scanning Electron Microscopy

Scaffolds were imaged using a Hitachi TM4000 tabletop SEM (Hitachi) with a 15 kV accelerating voltage and a 10 mm working distance. These scaffolds were sputter coated with an Elmscope FLM-007 using gold. More details can be found in Section 2.5.

3A.2.3 Fibre and Pore Properties

Scanning electron images were analysed using ImageJ software (NIH). Images were imported into the software and thresholded. They were then analysed using the DiameterJ plugin (fibre diameter analysis) and the OrientationJ plugin (fibre orientation analysis) [22]. More details can be found in Section 2.9.

3A.2.4 Mechanical Testing

Tensile properties were measured using an Instron 3367 testing rig. Measurements were performed on 40 x 5 mm strips of electrospun scaffold with a starting gauge length of 20 mm. Scaffolds were stretched at 10 mm/min until failure. Incremental Young's moduli were calculated. More details can be found in Section 2.7.

3A.2.5 Contact Angle Measurement

Contact angle was measured on each scaffold using a DMK 41AU02 monochrome camera at a frequency of 5 Hz. Briefly, a 5 µL droplet of water was placed on the scaffold whilst images were being taken. Analysis was performed on ImageJ using the LBADSA plugin [23]. More details can be found in Section 2.8.

3A.2.6 Scaffold Porosity

Scaffold porosity was calculated using the density of PCL, weight of the scaffold and volume of the scaffold. Volume was measured using a DMK 41AU02 monochrome camera. All scaffolds were punched out using a 10 mm diameter punch. More details can be found in Section 2.10.

3A.2.7 Cell Culture and Scaffold Seeding

HUVECs were expanded to passage 7 in a 5% CO_2/37°C atmosphere. HUVECs were expanded using MCBD 131 medium supplemented with 5% v/v FBS; 1% v/v L-glutamine; 1% v/v penicillin/streptomycin; 1 mg/L hydrocortisone; 50 mg/L ascorbic acid; 2 µg/L fibroblast growth factor; 10 µg/L epidermal growth factor; 2 µg/L insulin-like growth factor; and 1 µg/L vascular endothelial growth factor. HUVECs were lifted for scaffold seeding at 80% confluence. Briefly, 10 mm diameter scaffolds were punched out and sterilized in 70% ethanol before being soaked in

basal medium overnight. Scaffolds were then placed in a 48-well plate. 20,000 cells/cm^2 were drip seeded in 30 µL of medium onto the middle of the scaffold. After 30 mins a further 20µL of medium was added to stop the cells from drying out. After a further 30mins, medium in each well was topped up to 500 µL. Medium was replaced every 48 h. More details can be found in Sections 2.3 and 2.12.

3A.2.8 CellTiter-Blue® Cell Viability Assay

The assay was performed at 1, 6 and 12 days as per manufacturer's instructions. Measurements were taken at ex: 525 nm and em: 580-640 nm. More details can be found in Section 2.13.

3A.2.9 Cell Staining

Scaffolds used for cell staining were washed thrice in PBS and fixed in 10% v/v formalin solution in PBS overnight. Cells were permeabilized in 0.2% v/v TritonX-100 solution in PBS for 5mins, followed by three PBS washes. Scaffolds were then stained in 0.1% v/v 1000X Phalloidin-iFluor-^{TM}514 conjugate and in DAPI. More details can be found in Section 2.17.

Cell seeded scaffolds were visualized after 12 days using a previously described osmium based method [24]. Briefly, samples were stained in 0.1% osmium tetroxide and visualized using a Hitachi TM4000 tabletop SEM with a 15 kV accelerating voltage and a 10 mm working distance. More details can be found in Section 2.17.

3A.2.10 Measuring Cell Infiltration

Cell infiltration was measured using DAPI and phalloidin stained Z-stack images on ImageJ (NIH) whereby depth of cell intravasasion was measured.

3A.2.11 Reverse Transcription Quantative Polymerase Chain Reaction (RT-qPCR)

RNA was extracted from the cell seeded scaffolds using a Tri-Reagent method and purified using Qiagen's RNeasy spin colum system. Real-time polymerase chain reaction was performed using a LightCycler® 480 Instrument II and Sensifast™ SYBR® High-ROX system. Forward and reverse sequences were taken from literature and are displayed in Table 5. Relative quantification of RT-PCR results was carried out using the $2^{-\Delta\Delta ct}$ method [25]. Gene expression levels were expressed relative to

GAPDH (housekeeping gene) and normalised to 70% confluent HUVECs on tissue culture plastic. More details can be found in Section 2.18.

Table 5: Primer sequences used for RT-qPCR to measure gene expression from the seeded HUVECs

Gene	Primer	Sequence	Reference
Glyceraldehyde 3-phosphate dehydrogenase	GAPDH (forward)	GTCTCCTCTGACTTCAACAG	20
	GAPDH (reverse)	GTTGTCATACCAGGAAATGAG	
Matrix metalloproteinase-1	MMP1 (forward)	CGGTTTTTCAAAGGGAATAAGTACT	20
	MMP1 (reverse)	TCAGAAAGAGCAGCATCGATATG	
matrix metalloproteinase-2	MMP2 (forward)	CGCTCAGATCCGTGGTGAG	20
	MMP2 (reverse)	TGTCACGTGGCGTCACAGT	
Tissue inhibitor of metalloproteinases-2	TIMP2 (forward)	AATGCAGATGTAGTGATCAGG	20
	TIMP2 (reverse)	TCTATATCCTTCTCAGGCCC	
Vascular endothelial growth factor	VEGF (forward)	AGACCAAAGAAAGATAGAGCAAGACAAG	20
	VEGF (reverse)	GGCAGCGTGGTTTCTGTATCG	
Platelet endothelial cell adhesion molecule	CD31 (forward)	ACTGGACAAGAAAGAGGCCATCCA	26
	CD31 (reverse)	TCCTTCTGGATGGTGAAGTTGGCT	

3A.2.12 Statistical Analysis

Data was expressed as mean ± 1 standard deviation. Statistical analysis was performed using one-way ANOVA with post-hoc Tukey test [27].

3A.3 Results

3A.3.1 Scaffold Properties

By altering the electrospinning parameters, four different fibre morphologies were achieved. Firstly, increasing fibre diameters of 1.64 ± 0.18 µm, 2.95 ± 0.16 µm, 3.37 ± 0.27 µm and 4.83 ± 0.49 µm were noted across the four scaffolds ($p < 0.001$ between each group). This meant that all the morphologies could be considered as being different. The four different fibre morphologies can be seen in Figure 13.

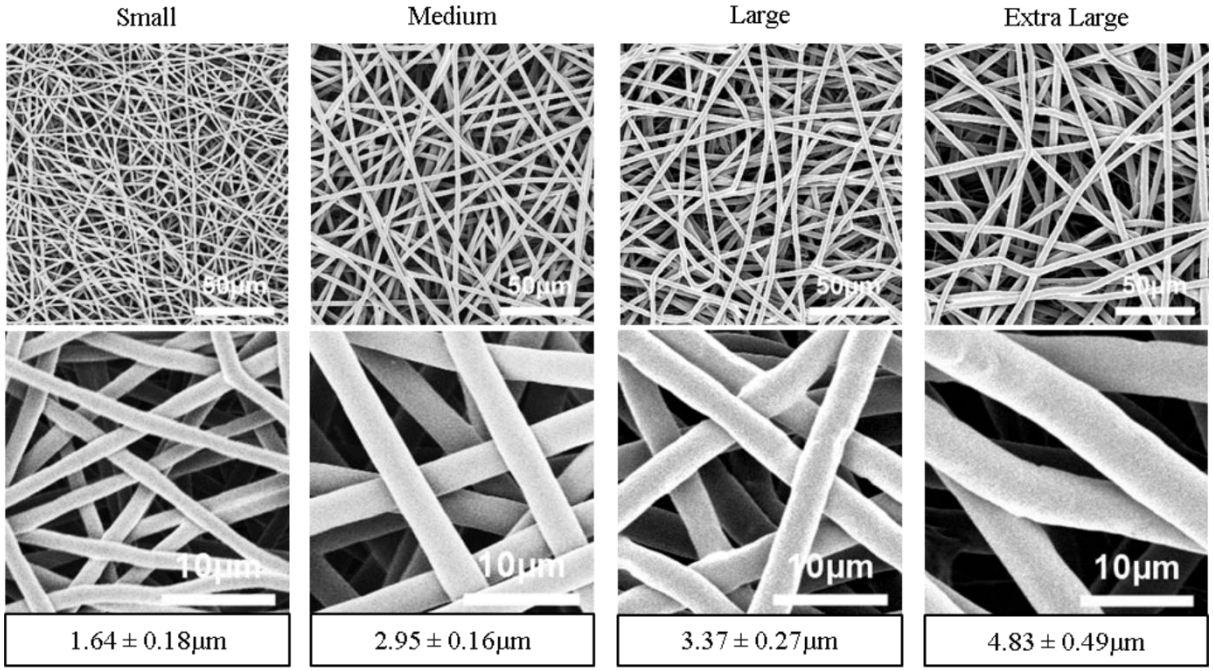

Figure 13: The four different scaffold morphologies with increasing fibre diameters. Scaffold thickness ranged from approximately 0.2 mm in the small fibre diameter to 0.5 mm in the extra-large fibre diameter.

Secondly, the fibre orientation of all four scaffolds appeared to be very similar. Likewise all four scaffolds had a uniform random alignment. These can be seen in Figure 14. The electrospinning parameters were set up so that the mandrel rotational speed was low enough to ensure that the fibres did not adopt an aligned morphology.

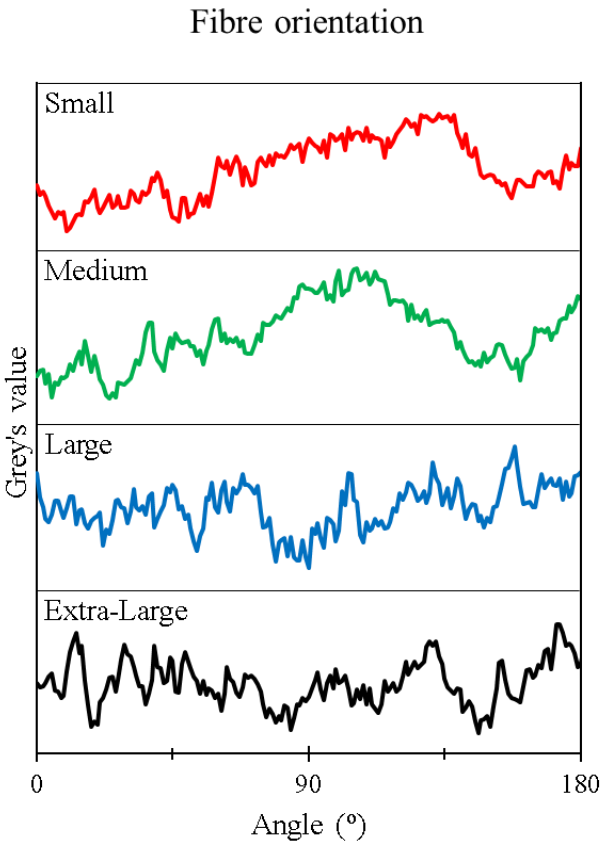

Figure 14: Fibre orientation of all four scaffold morphologies. All four scaffolds appear to have a random orientation with no clear peaks at any angle.

Finally, a very strong correlation between fibre diameter and pore width was noted between the four scaffold morphologies (R^2 =0.9997). These can be seen in Figure 15. Pore diameter ranged from

8.4 ± 3.7µm in the small fibre scaffold up to 23.3 ± 9.0µm in the extra-large fibre scaffold (Table 6). This high correlation between fibre diameter and pore width was expected.

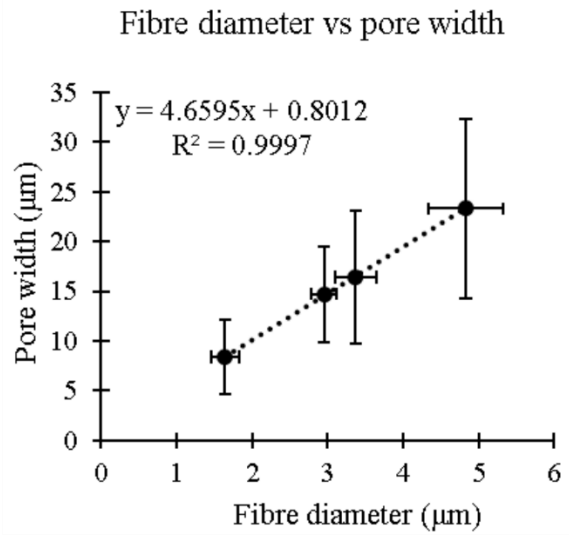

Figure 15: Correlation between fibre diameter and pore width. A strong correlation with an R^2 = 0.9997 noted. Error bars = SD.

Furthermore, it was noted that scaffold porosity decreased as fibre diameter increased. The small fibre had a porosity of 91.0 ± 1.6%, decreasing all the way down to 83.3 ± 0.9% in the extra-large fibre scaffold (Table 6).

Table 6: Physical and tensile mechanical properties of the four different scaffold morphologies.

	Fibre diameter (µm)	**Ultimate tensile strength (MPa)**	**Failure strain (%)**	**Porosity (%)**	**Contact angle at 0.2s (°)**	**Pore diameter (µm)**	**Stiffness (MPa)**	
							0-5%	**5-10%**
S	1.64 ± 0.18	1.08 ± 0.17$^{\&\#}$	843 ± 143$^{\&\#}$	91.0 ± 1.6	110.8 ± 7.7$^{\$}$	8.4 ± 3.7	4.10 ± 0.33$^{\$}$	2.17 ± 0.25$^{\$}$
M	2.95 ± 0.16	1.50 ± 0.09$^{\#}$	1202 ± 62$^{\#}$	89.6 ± 2.4	128.2 ± 4.0	14.7 ± 4.8	6.50 ± 0.72	2.99 ± 0.46
L	3.37 ± 0.27	1.55 ± 0.16$^{\&}$	1071 ± 21$^{\&}$	83.9 ± 1.1	129.1 ± 2.5	16.4 ± 6.7	5.80 ± 0.36	3.16 ± 0.48
XL	4.83 ± 0.49	1.26 ± 0.06$^{\&\#}$	855 ± 120$^{\&\#}$	83.3 ± 0.9	131.5 ± 1.1	23.3 ± 9.0	5.77 ± 0.39	3.66 ± 0.28

*Results with matching symbols (# and &) are significantly different to each other ($p<0.05$). Results with the $ symbol are significantly different ($p<0.05$) to all other results.

3A.3.2 Scaffold Mechanical Properties

Mechanical characterization of the scaffolds led to some interesting results. Firstly, the ultimate tensile strength (UTS) of the scaffold was highest in the medium and large fibres, but significantly

dropped in the small fibre and extra-large fibre (p values ranging from 0.001 to 0.068) (as seen in Table 6). Representative stress-strain curves can be seen in Figure 16.

Similarly, scaffold failure strain was highest in the medium and large fibre scaffold, but dropped significantly in the small and extra-large scaffold (p values ranging from 0.001 to 0.019) (as seen in Table 6).

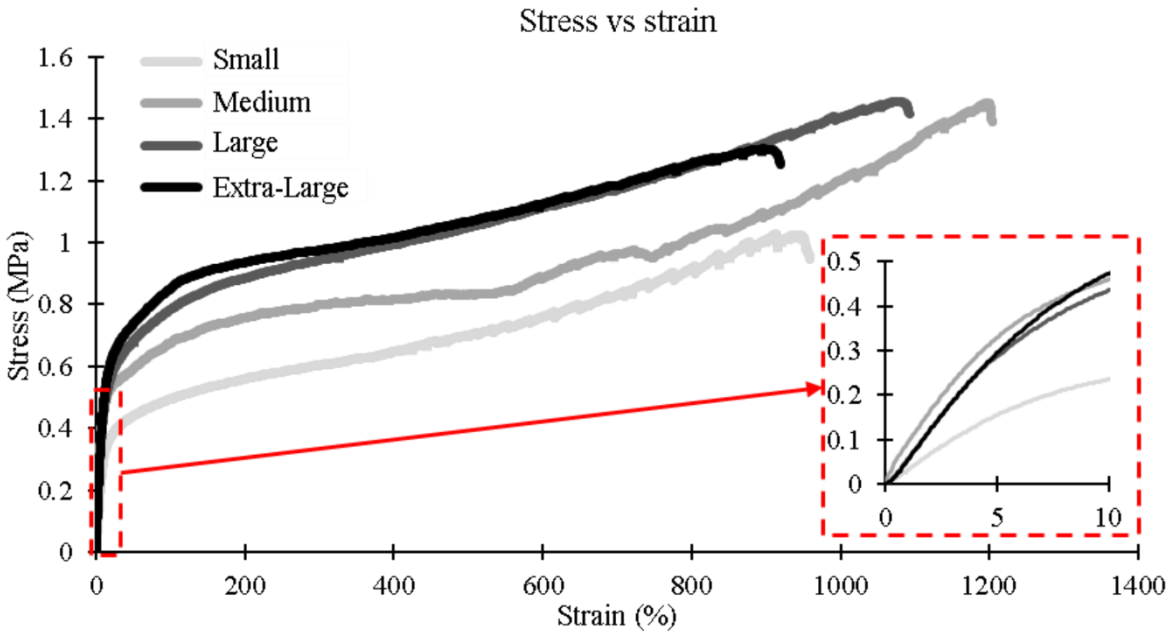

Figure 16: Representative stress vs strain curves for all four scaffold morphologies. Failure strain and ultimate tensile strength were highest in the medium and large fibre diameters.

The stiffnesses at the 5-10% strain band were 2.17 ± 0.25, 2.99 ± 0.46, 3.16 ± 0.48 and 3.66 ± 0.28 MPa for the small, medium, large and extra-large scaffolds, respectively. This represents an increase in stiffness at each subsequently larger fibre diameter with a strong correlation between the two results ($R^2 = 0.9667$). Furthermore, the small fibre scaffold had significantly lower stiffness at both the 0-5% ($p < 0.001$) and 5-10% ($p < 0.017$) strain bands compared to the three other fibre diameters. Interestingly, the larger the fibre diameter, the more stiffness/elasticity the scaffold maintained as the strain band was increased (Table 6). For example, the relative drop in stiffness between the two strain bands was lowest in the largest fibre and increased as fibre size became smaller.

Contact angle measurements lead to some interesting findings. There was a general trend in increasing contact angle as fibre size increased – ranging from 110.8 ± 7.7° in the small fibre up to 131.5 ± 1.1° in the extra-large fibre. A significant difference was noted between the contact angles on the small fibre scaffold compared to the three other scaffolds ($p < 0.001$) (as seen in Table 6).

3A.3.3 Cell Imaging

SEM images of osmium stained HUVECs growing on all four scaffold morphologies showed that the cells were spreading across the fibres and had several binding sites (as seen in Figure 17). The images also show that the cells were starting to adopt a slightly more elongated HUVEC like morphology when bound onto the largest fibre diameter scaffold.

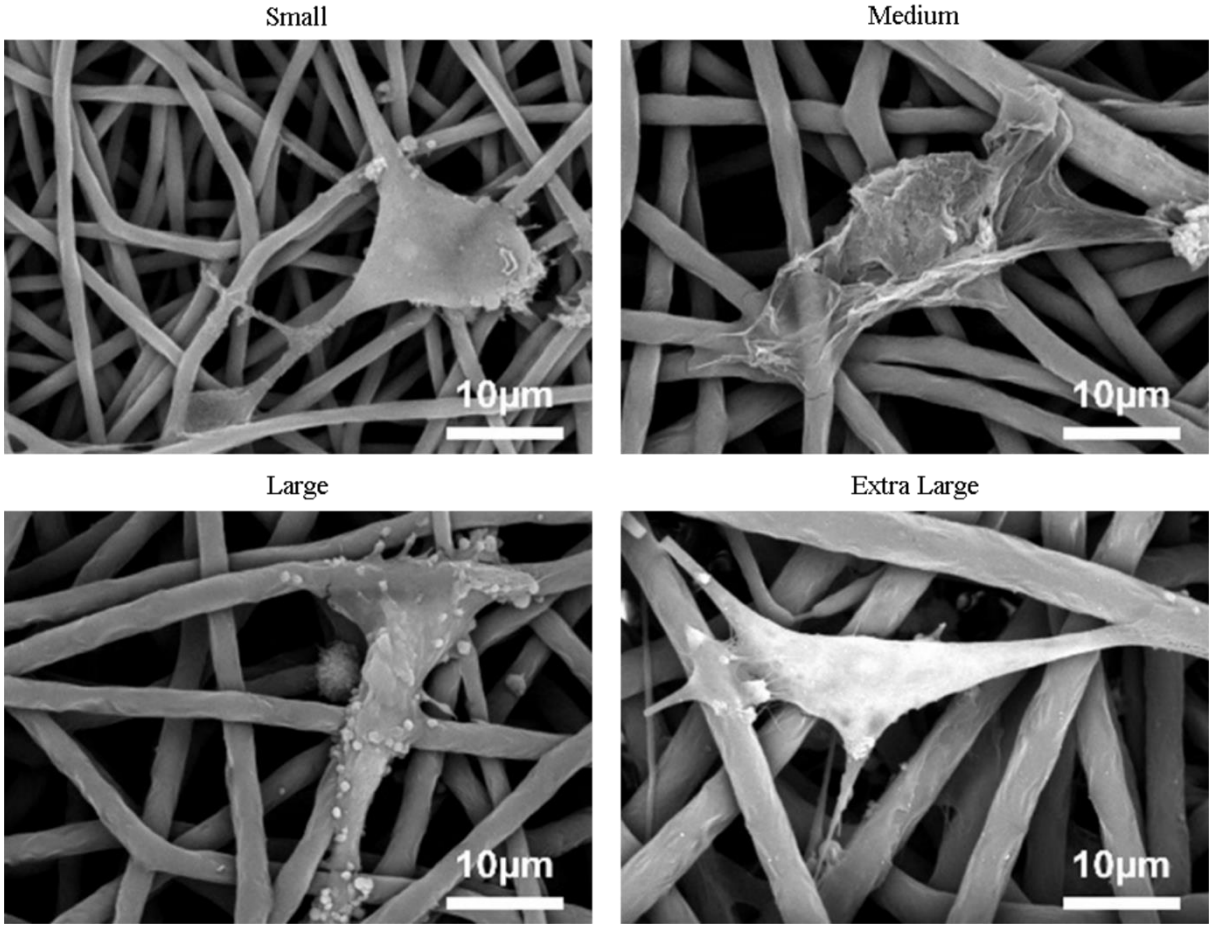

Figure 17: SEM images of osmium stained HUVECs bound to the four scaffold morphologies. HUVECs have binding sites on several fibres.

Likewise, nuclei and f-actin staining (Figure 18) showed that the larger fibres led to the HUVECs spreading out across the fibre, adopting a more desirable elongated shape. This spreading became more evident in the later time points. In contrast, the small fibre showed a more rounded cell shape, which may indicate apoptosis [28].

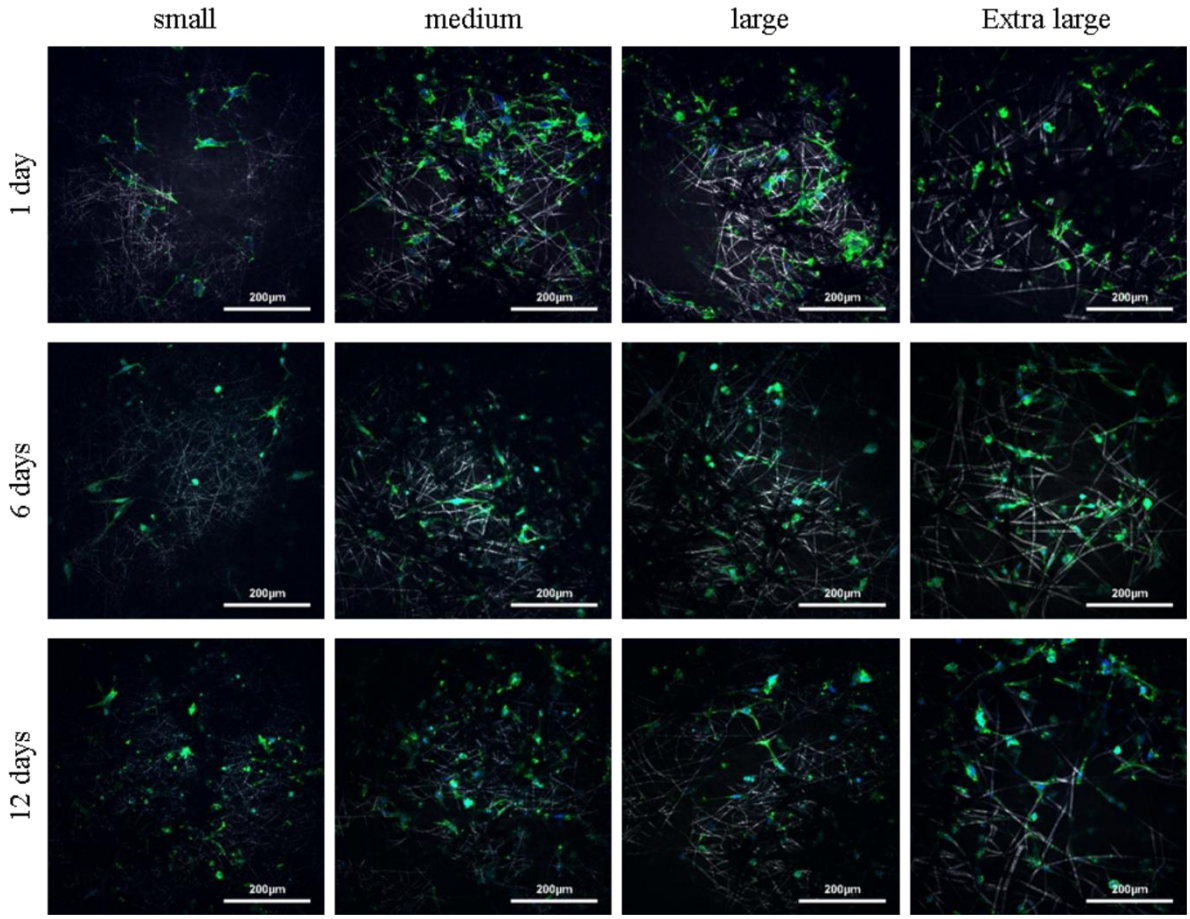

Figure 18: DAPI (nuclei) and phalloidin (f-actin) stained HUVECs on all four scaffolds after 1, 6 and 12 days of culture. HUVECs appear more elongated (phenotypic morphology) on the Extra-large fibre scaffold.

Further analysis of nuclei and f-actin stained scaffolds was achieved using Z-stack imaging. This allowed for cell infiltration to be assessed. The larger fibre scaffold with larger pores showed infiltration up to approximately 80 µm, compared to approximately 25-30 µm of infiltration for the other three scaffolds (Figure 19).

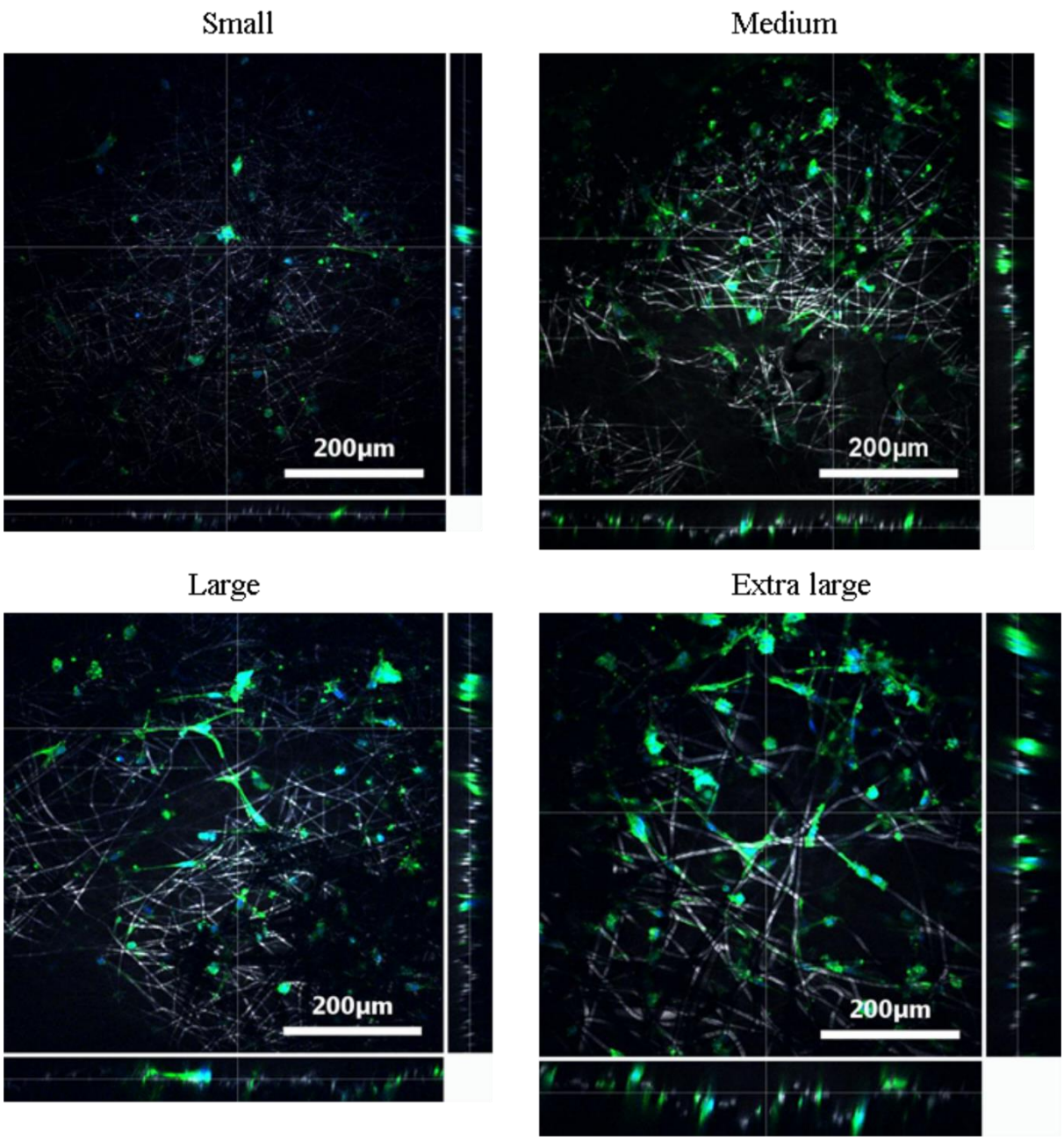

Figure 19: Z-stack images of DAPI (nuclei) and phalloidin (f-actin) stained HUVECs on all four morphologies. The largest fibre diameter showed deeper cellular infiltration compared to three smaller fibre morphologies. Infiltration depths of approximately 80µm were noted for the extra-large fibre scaffold compared to 25-30 µm for the three smaller fibre diameter scaffolds.

3A.3.4 Cell Viability

Results showed that the extra-large fibre led to significantly higher cell viability after 12 days compared to the three other scaffolds ($p < 0.001$). Relative fluorescence units (RFU) values were

approximately 200% to 300% higher (Figure 20). Furthermore, higher viabilities were also noted in the medium and extra-large scaffolds after 24h compared to the small scaffold.

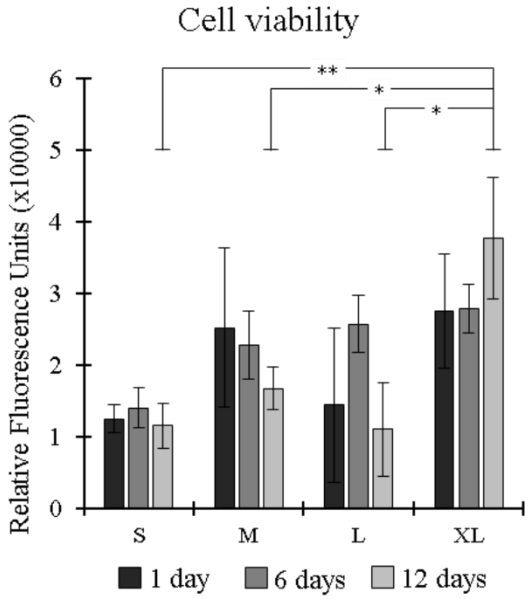

*Figure 20: Cell viability of HUVECs on all four scaffolds after 1, 6 and 12 days of culture. Significantly higher cell viability was noted in the XL scaffold after 12 days compared to the three other fibre diameters. S=small, M=medium, L=large and XL=extra-large. N=4, error bars = SD. *p < 0.05, **p < 0.01*

3A.3.5 Reverse Transcription Quantitative Polymerase Chain Reaction

Interesting trends in gene expression were noted across the four scaffold morphologies (Figure 21). Most notably, CD31 expression was significantly higher in the extra-large fibre scaffold after 6 days compared to the medium fibre diameter. While no other significance was noted in the CD31 expression, there was an evident trend with the extra-large scaffold having higher relative expression than the three other fibre sizes at both 6 days and 12 days of culture. MMP1, MMP2 and TIMP2 all showed very similar results to each other. In all cases the small fibre diameter showed a significantly lower relative expression at 12 days compared to 6 days. Furthermore, MMP1 expression at 12 days on the small fibre scaffold was significantly lower than the 3 other fibre diameters. The other three morphologies did show downregulations between 6 and 12 days, however, none of these were significant. No trends were noted in VEGF relative expression across the four scaffolds.

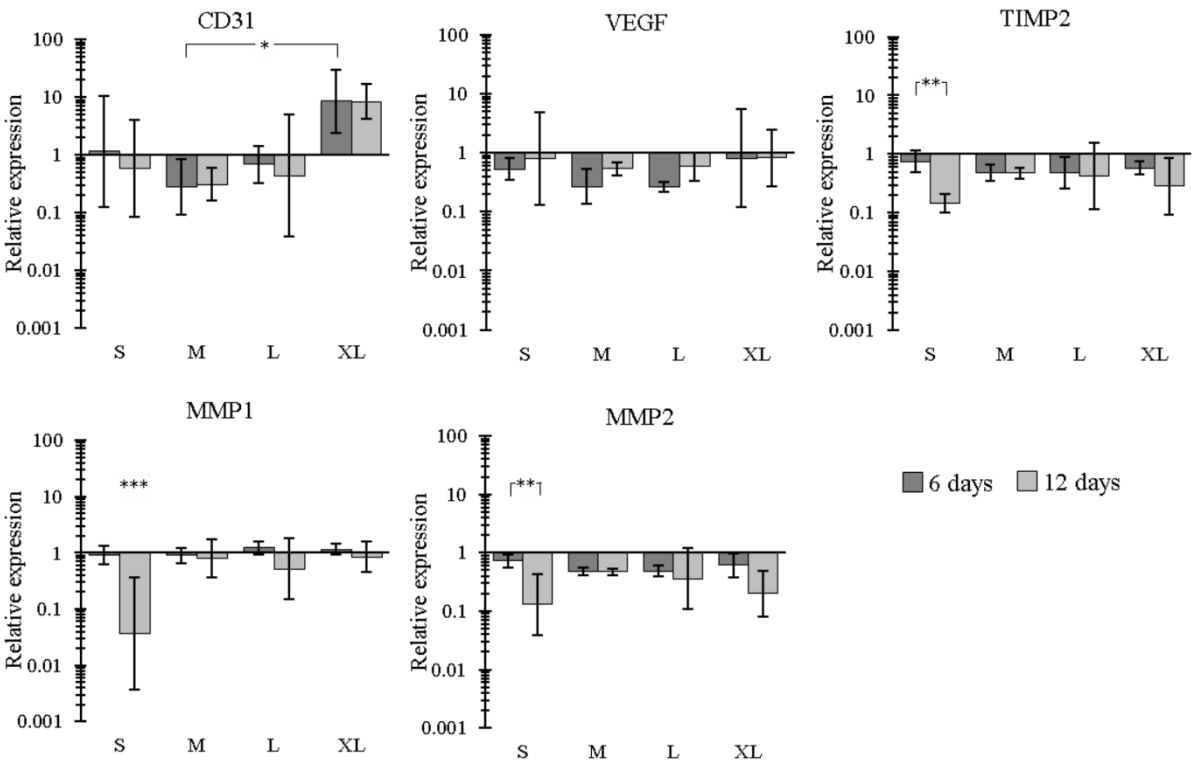

*Figure 21: RT-qPCR results for five different genes on all four scaffold morphologies. All results were normalised to 70% confluent HUVECs on tissue culture plastic. The expression of CD31 was significantly higher in the XL scaffold after 6 and 12 days compared to the three other morphologies. N=5, error bars = SD. *p < 0.05, **p < 0.01, ***p < 0.001.*

3A.4 Discussion

When studying endothelial cells in combination with novel materials for vascular tissue engineering, it is of crucial importance that the concept of angiogenesis is considered. As previously mentioned, angiogenesis is a process by which endothelial cell proliferation and remodelling leads to the formation of new blood vessels [18]. In this study, electrospinning was shown to offer a flexible solution for the manufacture of scaffolds for vascular tissue engineering. Four scaffold morphologies were created with increasing fibre diameters: 1.64 ± 0.18 µm, 2.95 ± 0.16 µm, 3.37 ± 0.27 µm and 4.83 ± 0.49 µm, with significant differences noted between all four scaffolds. They were manufactured using PCL, which has FDA approval for various uses *in vivo* due to its biocompatibility and tailorable bioresorption properties [29,30].

Fluorescence imaging of cell seeded scaffolds led to some interesting results. Firstly, in the conventional fluorescence images (Figure 18), a clear cellular elongation and spreading of the cell's morphology can be noted on the extra-large and large scaffolds, becoming more obvious after 6 and 12 days. In contrast to this, the small fibre (and to some extent the medium fibre) appears to show more rounded cells, especially after 12 days, which may indicate apoptosis [28]. This phenomenon may be caused by the fibre size and/or pore size, with evidence shown in other studies examining the effect of electrospun scaffold topography on cellular performance [13,15,31]. Secondly, Z-stack imaging showed that the extra-large scaffold morphology aided cell infiltration after 12 days of culture. Cells were seen to at depths of approximately 80 µm, compared to 25 µm for the three other scaffolds. A HUVEC is approximately 20-30 µm in diameter, meaning that the extra-large scaffold is the only one with pore sizes 'large enough' to allow for a full sized HUVEC to pass through without altering its shape [32]. Furthermore, a large fibre dimeter and pore size means the HUVEC can grow perpendicular to the top of the scaffold. While this may seem counterintuitive as previous studies have typically tried to grow a monolayer of endothelial cells on the surface; this infiltration and 3D cell culture could be helping with cell survival (higher cell viability, Figure 20) and with the quantity of angiogenic genes being actuated (PCR results, Figure 21). It has been shown in many cases that a 3D cell culture is favourable in relation to gene expression as it more accurately captures the morphological characteristics of the native ECM [33]. This has also been shown when using human coronary artery endothelial cells, where 3D culture showed a significant increase in the expression of key proteins compared to 2D culture [34].

On this note, gene expression results showed some interesting trends. While none of the VEGF gene expression results showed any significance, all four scaffold morphologies showed a relative increase in gene expression between 6 and 12 days, suggesting that VEGF expression is predominantly driven by the cell's maturity, as opposed to scaffold morphology. This trend has been noted before when studying HUVECs. *Zhang et al*. noted a doubling in the relative gene expression of VEGF from HUVECs between 7 and 14 days, which falls within the values noted in this study [35].

The same applies for MMP1, MMP2 and TIMP2, whereby all four morphologies showed a relative decrease in gene expression after 12 days compared to 6 days. This, like the results for VEGF, suggest that the expression of these particular genes is mediated more by the cell's maturity rather than the scaffold's morphology. However, some trends were noted between the four scaffold morphologies. Most notably, all three genes were significantly downregulated in the small fibre scaffold between 6 and 12 days, as opposed to the other morphologies whereby a relative downregulation was still noted, albeit without significance. This suggests that while cell maturity is playing a role in the expression of these genes, the smaller fibre morphology is also having an effect. MMP1 and MMP2 are two genes associated with the remodelling of ECM proteins (collagen and gelatin, respectively). Their downregulation means the cells are not trying to turnover ECM, suggesting homeostasis within the cell microenvironment [36]. Furthermore, an upregulation of these genes is associated with a variety of degenerative diseases [37].

Additionally, an upregulation in CD31 was noted in the extra-large scaffold compared to the three other scaffolds. CD31, also known as PECAM1 is an angiogenic gene that is heavily involved in endothelial cell motility and endothelial cell-cell association that is required for their reorganization into a tubular network [21]. Therefore, a relative upregulation of this gene is desirable in the short run where cellular reorganization is one of the main aims. However, overexpression of this gene, like many other angiogenic genes, is associated with cancer and tumour formation [38,39]. Therefore, finding a point whereby endothelial cell modulation leads to the creation of new vasculature without leading to tumour formation is of crucial importance. A significant relative upregulation in CD31 was noted in the extra-large scaffold after 6 days compared to the medium scaffold and the 70% confluent HUVECs on tissue culture plastic. Relative increases were also noted between the extra-large scaffold and the three other morphologies at both 6 and 12 days, albeit not significant. This can either be explained by the larger fibres creating a more favourable environment for the cells, or by the increase in pore size leading to infiltration of cells, creating a more '3D-like' microenvironment. No trend in data could be noted between the three other morphologies suggesting that the increase from 3.37 µm to 4.83 µm (with an increase in pore size too) ultimately led to this increase in CD31 expression.

Therefore, with the final aim of creating an environment most suited for endothelial cells to proliferate into a healthy endothelium, the results suggest that a fibre and pore diameter similar to that of the extra-large scaffold is the best candidate.

The tensile testing results exposed intriguing findings in how fibre diameter modified the mechanical properties of the four scaffolds. Firstly, the ultimate tensile strength (UTS) was found to be significantly lower in the small and extra-large scaffolds when compared to the medium and large scaffold. It is interesting to note that the middling fibre diameters had the effect of increasing UTS. Similarly, the failure strain was significantly higher in the medium and large fibre diameter compared to the small and extra-large fibre diameters. This finding may be linked to the increase in UTS noted in these same scaffolds and warrants further study. Furthermore, it was noted that the stiffness of the small diameter fibre was significantly lower than that of the three larger fibres for both the 0-5% and 5-10% strain bands. Moreover, the larger the fibre diameter the more stiffness it maintained as it was stretched into the 5-10% strain band. This particular phenomena may be a result of the lower porosity, leading to increased bulk properties and therefore merits further research.

Additionally, all four scaffolds had stiffnesses that were found to fall within the range of values noted in native vessels, such as the saphenous vein. For example, *Stekelenburg et al.* found that the saphenous vein had longitudinal and circumferential elastic moduli of 23.7 MPa and 4.2 MPa [40]. Similarly, *Soletti et al.* noted a circumferential elastic modulus of 2.25 MPa for the saphenous vein [41]. These circumferential elastic moduli are in a similar realm to the four elastic moduli noted in this study at the 0-5% and 5-10% strains; with values ranging from 2.17 ± 0.25 MPa up to 6.50 ± 0.72 MPa depending on strain range and fibre diameter.

A further interesting finding was that as fibre diameter was increased, the scaffold's porosity decreased. This finding has been noted before when electrospinning PCL, *Pham et al.* noted that as fibre diameter increased from 2 μm to 8 μm, the porosity of the scaffold decreased from approximately 89% down to 83%, which is in line with the results found in this study [42].

One of the major limitations of this study is the inability to differentiate between whether fibre diameter or pore width was having the major effect on the seeded HUVECs. A very strong correlation between fibre diameter and pore width was noted ($R^2 = 0.9997$). One issue with electrospinning is that these two morphological characteristics are somewhat interconnected, with a study by *Pham et al.* showing a linear correlation between the two characteristics [42]. While this in itself is an interesting finding, it makes it difficult to distinguish between which aspect had the effect on cellular performance. A further limitation is that the full spectrum of fibre diameters was not analysed. Only a limited number of scaffold morphologies could be studied and the apparatus only allowed for fibre diameters of up to approximately 5 μm. While these limitations merit further study in an attempt to gain an overarching image of exactly how scaffold morphology is affecting the seeded endothelial cells; the present study has shown that cellular performance can be influenced through altering the scaffold's fibre diameter.

3A.5 Conclusions

In this study, four different scaffolds with incrementally larger fibre diameters ranging from 1.64 μm to 4.83 μm were successfully manufactured. The largest fibre diameter led to greater HUVEC infiltration and significantly greater cell viability after 12 days of culture. Furthermore, the largest fibre diameter also had interesting effects on gene expression. Most notably, CD31 expression was higher in the largest fibre after 6 and 12 days compared to the three other fibre diameters. CD31 is a gene associated with angiogenesis and is required for endothelial cell reorganization into vasculature, therefore and upregulation in the short run is desirable. These findings suggest that the largest fibre diameter (4.83 μm) is most suitable for the seeding of endothelial cells with the final aim of creating a vascularized functional bypass graft.

Part B: Optimizing Scaffold Morphology for Smooth Muscle Cells

3B.1 Introduction

Vascular smooth muscle cells (VSMC) are an important component of the vessel wall and are predominantly located in the largest part of the vessel; the tunica media [43]. The tunica media on average consists of between 40 and 60 layers of smooth muscle cells depending on the size and location of the vessel [43]. This part of the vessel wall provides mechanical force and the vasoactive responsive properties that allow blood vessels to function effectively [44]. Due to the thickness of the tunica media, it has been suggested that it would be beneficial to create a scaffold that allows for sufficient VSMC infiltration to mimic the functionality of the native tunica media [45]. It has been well documented with several cell types that increasing infiltration can affect cell morphology and phenotype [16,46,47]. Furthermore, work focussing on creating optimal environments for VSMCs has shown that both scaffold morphology and pore size can have a drastic effect on the performance of VSMCs [12,16,48,49]. These studies suggest that there is merit to studying the effect of electrospun fibre diameter on VSMC performance. Therefore, the present study has looked at how fibre diameter of an electrospun polymer scaffold affects seeded VSMCs.

3B.2 Methods and Materials

3B.2.1 Electrospinning

PCL was either dissolved into HFIP; a 5:1 mixture of Chlorofrom:Methanol (C:M) or a 10:1 mixture of C:M at varying concentrations to achieve four different solutions (Table 7). Briefly, the electrospun fibres were spun as one continuous fibre onto an aluminium foil covered 8 cm diameter rotating mandrel. All scaffold analysis was performed on ImageJ. A schematic of the experimental process is shown in Figure 12. More details can be found in Section 2.1.

Table 7: Electrospinning parameters used to manufacture four different fibre diameter scaffolds for seeding with HUVSMCs.

Fibre size	Polymer concentration (%)	Solvent used	Needle bore (mm)	Flow rate (ml/h)	Total volume (ml)	Distance between needle tip and mandrel (cm)	Positive voltage (kV)	Negative Voltage (kV)	Mandrel rotational speed (RPM)
S	8	HFIP	0.4	1.2	8	12	+12	0	250
M	12	HFIP	0.4	1.7	8.5	15	+12	0	250
L	20	5:1 C:M	0.8	5	18	23	+15	-4	250
XL	20	10:1 C:M	0.8	6	18	21	+23.5	0	250

3B.2.2 Scanning Electron Microscopy

Scaffolds were imaged using a Hitachi TM4000 tabletop SEM. More detail can be found in Section 2.5.

3B.2.3 Fibre and Pore Properties

Scanning electron images were analysed using ImageJ software. Images were imported into the software and thresholded. They were then analysed using the DiameterJ plugin (fibre diameter analysis) and the OrientationJ plugin (fibre orientation analysis) [22]. More details can be found in Section 2.9.

3B.2.4 Mechanical Testing

Tensile properties were measured using an Instron 3367 testing rig. Measurements were performed on 40 x 5 mm strips of electrospun scaffold with a starting gauge length of 20 mm. Scaffolds were stretched at 10mm/min until failure. The incremental Young's Moduli were calculated using the stress strain curve. More details can be found in Section 2.7.

3B.2.5 Contact Angle Measurement

Contact angle was measured on each scaffold using a DMK 41AU02 monochrome camera at a frequency of 5 Hz. Briefly, a 5 µL droplet of water was placed on the scaffold whilst images were being taken. Analysis was performed on ImageJ using the LBADSA plugin [23]. More details can be found in Section 2.8.

3B.2.6 Scaffold Porosity

Scaffold porosity (%) was calculated using the density of PCL, weight of the scaffold and volume of the scaffold. The thickness of the scaffold was measured in order to calculate the volume of the scaffold. This was done using a DMK 41AU02 monochrome camera. All scaffolds were punched out using a 10 mm diameter punch. More details can be found in Section 2.10.

3B.2.7 Cell Culture and Scaffold Seeding

HUVSMCs were expanded to passage 4 in a 5% CO_2/37°C atmosphere. HUVSMCs were expanded using smooth muscle cell growth medium and then cultured using DMEM supplemented with 10% v/v FBS; 1% v/v penicillin/streptomycin; and 1% v/v non-essential amino acids. HUVSMCs were lifted for scaffold seeding at 80% confluence. Briefly, 10 mm diameter scaffolds were punched out and sterilized in 70% ethanol before being soaked in basal medium overnight (non-supplemented DMEM). Scaffolds were then seeded in a 48-well plate. 25,500 cells/cm^2 were drip seeded in 20 µL of culture medium (supplemented DMEM) onto the middle of the scaffold. After 30 mins a further 30 µL of medium was added to stop the cells from drying out. After a further 30 mins, medium in each well was topped up to 500 µL. Medium was replaced every 48 h. More details can be found in Section 2.3 and Section 2.11.

3B.2.8 CellTiter-Blue® Cell Viability Assay

The assay was performed at 1, 6 and 12 days as per manufacturer's instructions (Promega). Briefly, cell seeded scaffolds were removed and placed in new wells. Each well was topped up with 300 µL of media and 75 µL of CellTiter-Blue assay (4:1 ratio). The plate was lightly shaken for 1 min and then wrapped in aluminium foil and incubated for 3.5 h. After incubation, 100 µL samples (x3) of the media/assay were taken from each scaffold and pipetted into a black well plate. The plate was measured in a Modulus™ II microplate reader at excitation: 525 nm and emission: 580-640 nm.

3B.2.9 Cell Staining

Scaffolds used for cell staining were washed thrice in phosphate buffer saline (PBS) and fixed in 10% v/v formalin solution in PBS overnight. Cells were permeabilized in 0.2% v/v TritonX-100 solution

then stained in 0.1% v/v 1000X Phalloidin-iFluor™514 conjugate and in DAPI. Fluorescent images were taken using a bespoke coherent anti-stokes Raman (CARS) system. More details can be found in Section 2.17.

SEM images were taken of cell seeded scaffolds after 12 days using a previously described osmium based method [24]. Briefly, samples were stained in 0.1% osmium tetroxide and visualized using a Hitachi TM4000 tabletop SEM. More details can found in Section 2.17.

3B.2.10 Measuring Cell Infiltration

Cell infiltration was measured using DAPI and phalloidin stained Z-stack images on ImageJ (NIH) whereby depth of cell intravasation was measured.

3B.2.11 Reverse Transcription Quantative Polymerase Chain Reaction (RT-qPCR)

RNA was extracted from the cell seeded scaffolds using a Tri-Reagent method and purified using Qiagen's RNeasy spin colum system. Real-time polymerase chain reaction was performed using a LightCycler® 480 Instrument II and Sensifast™ SYBR® High-ROX system. Forward and reverse sequences were either designed or used from literature and are displayed in Table 8. Relative quantification of RT-PCR results was carried out using the $2^{-\Delta\Delta ct}$ method [25]. Gene expression levels were expressed relative to GAPDH (housekeeping gene) and normalised to 70% confluent HUVECs on tissue culture plastic. More details can be found in Section 2.18.

Table 8: Primer sequences used for RT-qPCR to analyse gene expression from the seeded HUVSMCs.

Gene	Primer	Sequence	Reference
Glyceraldehyde 3-phosphate dehydrogenase	GAPDH (forward)	GTCTCCTCTGACTTCAACAG	[20]
	GAPDH (reverse)	GTTGTCATACCAGGAAATGAG	
Smooth muscle actin alpha 1	A-actin1 (forward)	CCGACCGAATGCAGAAGGA	[50]
	A-actin1 (reverse)	ACAGAGTATTTGCGCTCCGAA	
Myocardin	Myocardin (forward)	GGGTCTGAGCATTCCTTGCT	Self-designed
	Myocardin (reverse)	CTGGACGTTTCAGTGGTGGT	
Mesenchyme homeobox 2	MEOX-2 (forward)	AAAAGCGACAGCTCAGACTC	[51]
	MEOX-2 (reverse)	TTGCTGTCCACCCTTTACCC	
Interleukin 1 alpha	IL1-α (forward)	GCGTTTGAGTCAGCAAAGAAG	Self-designed
	IL1-α (reverse)	GCCGTGAGTTTCCCAGAAGA	

3B.2.12 Statistical Analysis

Data was expressed as mean ± 1 standard deviation. Statistical analysis was performed using one-way ANOVA with post-hoc Tukey test.

3B.3 Results

3B.3.1 Scaffold Properties

Four different fibre morphologies were achieved through altering the electrospinning parameters. Firstly, increasing fibre diameters of 0.77 ± 0.14 µm, 2.06 ± 0.26 µm, 3.91 ± 0.40 µm and 5.91 ± 0.56 µm were noted for the four scaffolds ($p < 0.001$ between each group) (Figure 22 and Figure 23). This significance between each scaffold means that all the morphologies can be considered as being different.

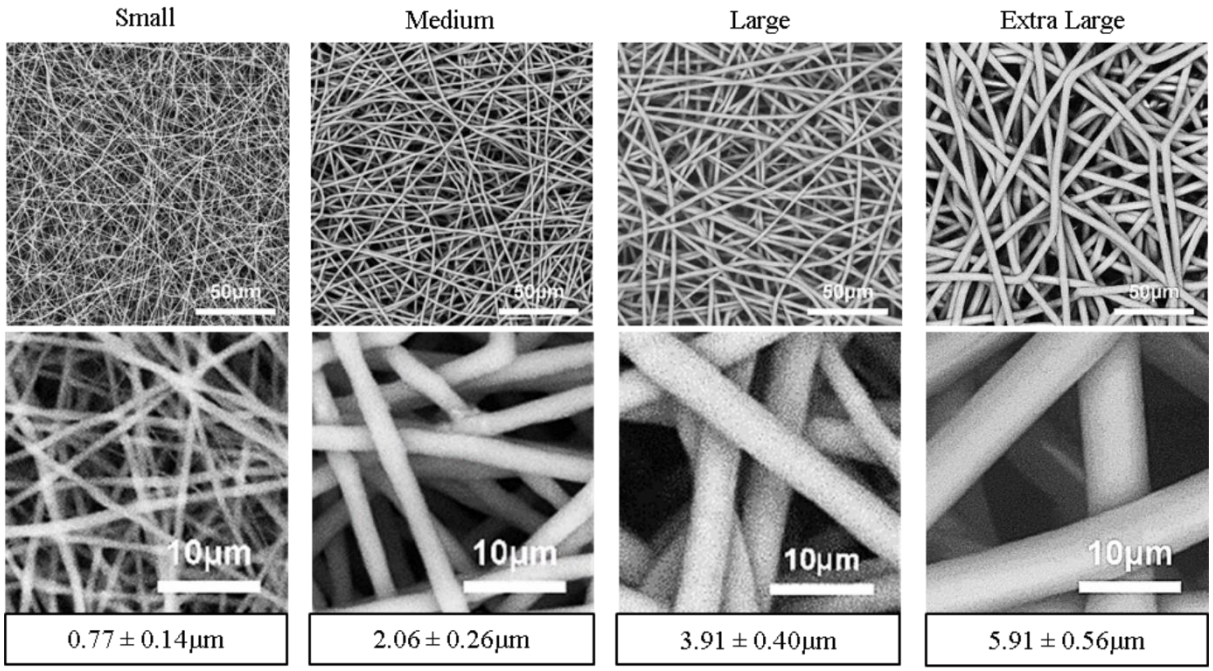

Figure 22: Representative SEM images of four different PCL scaffold morphologies with increasing fibre diameters for seeding with HUVSMCs. Fibre diameters ranged from 0.77 µm in the smallest fibre scaffold to 5.91 µm in the largest fibre scaffold.

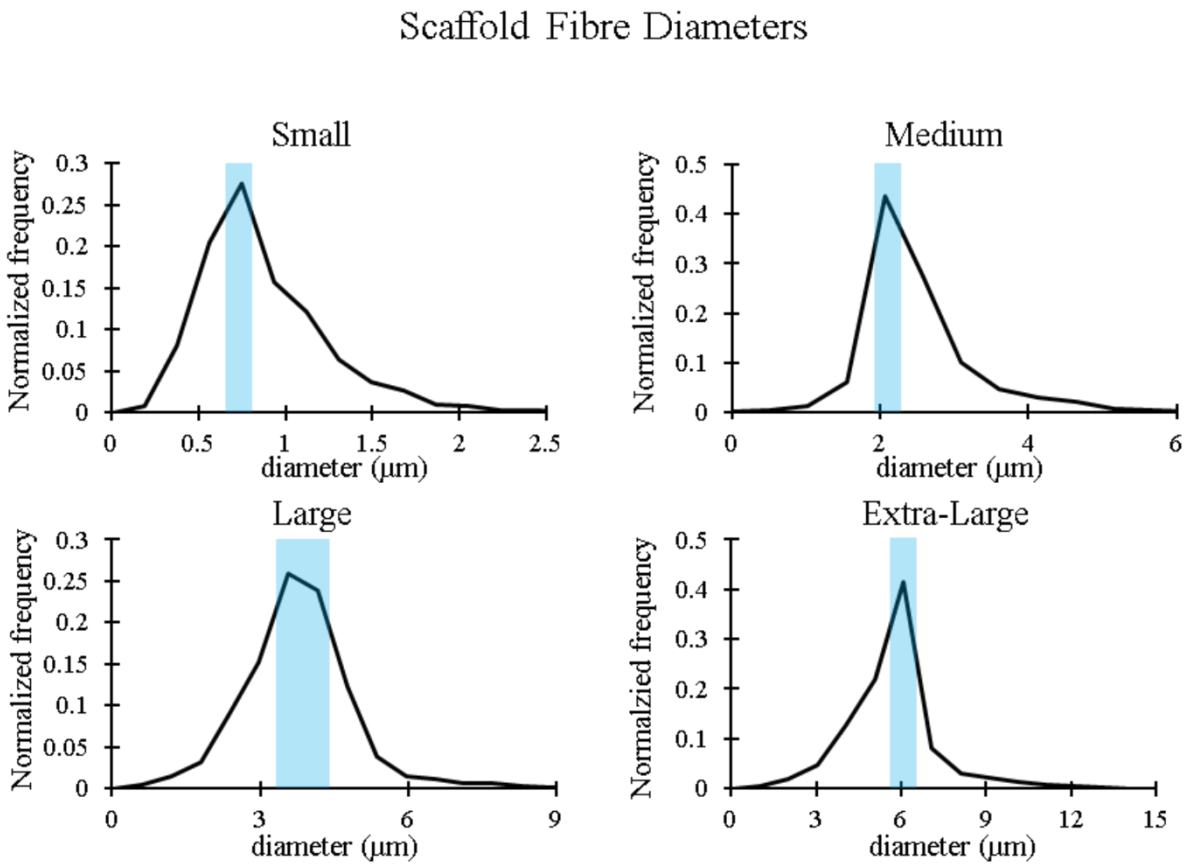

Figure 23: Fibre diameter histograms showing frequency of sizes for each scaffold. All four scaffolds show a peak in frequency of fibre diameter at different values.

Additionally, the fibre alignment of each scaffold appeared to be fairly random and displayed no alignment in a particular direction. This can be seen in the SEM images in Figure 22 and the fibre orientation analysis done using the OrientationJ plugin on ImageJ in Figure 24.

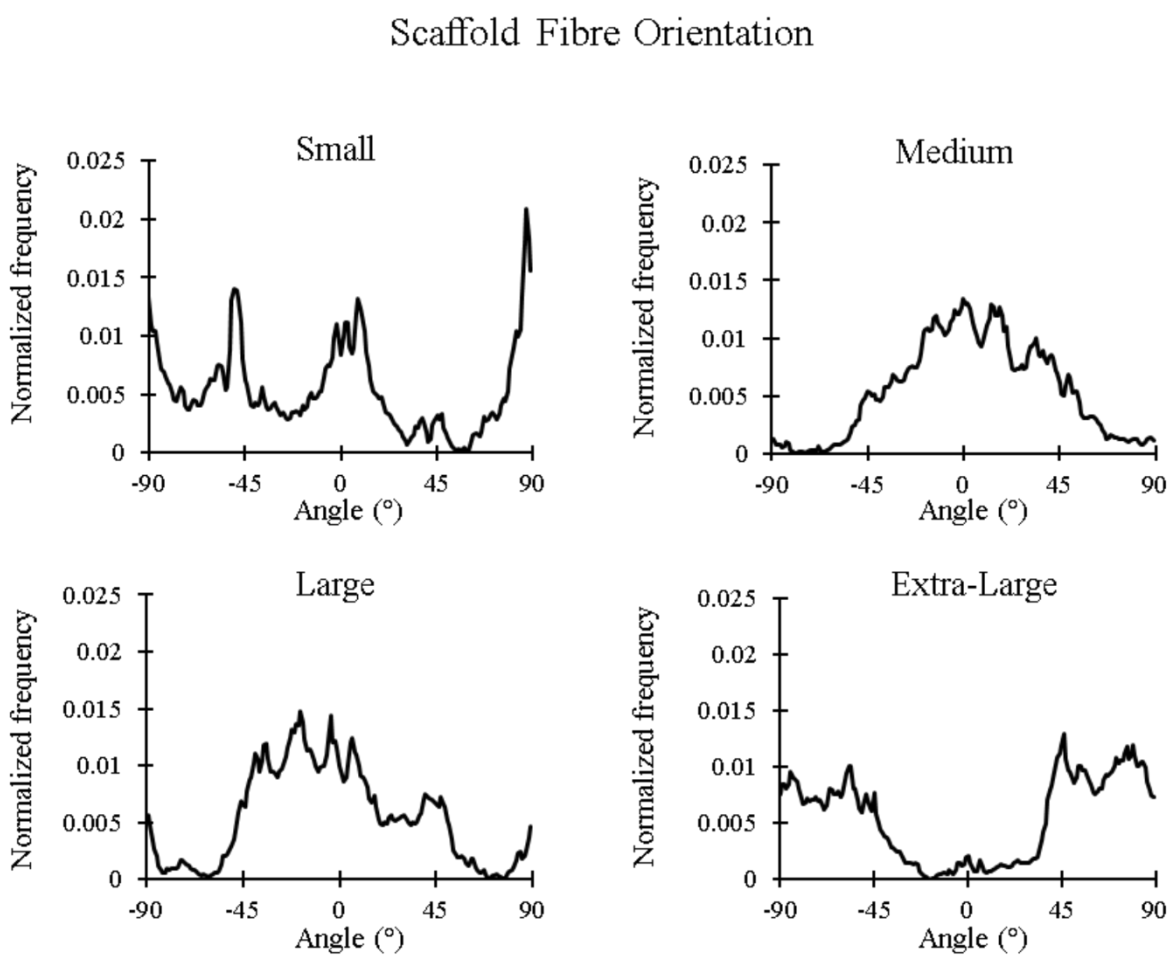

Figure 24: Fibre orientations for all four scaffold morphologies showing no clear sharp peak at any angle.

Furthermore, a very strong correlation between fibre diameter and pore width was noted for all four scaffold morphologies, with an R^2 value of 0.9918. Pore widths ranged from 4.37 ± 1.29 μm for the small fibre morphology up to 33.41 ± 13.37 μm for the largest fibre diameter. These correlations can be seen in Figure 25.

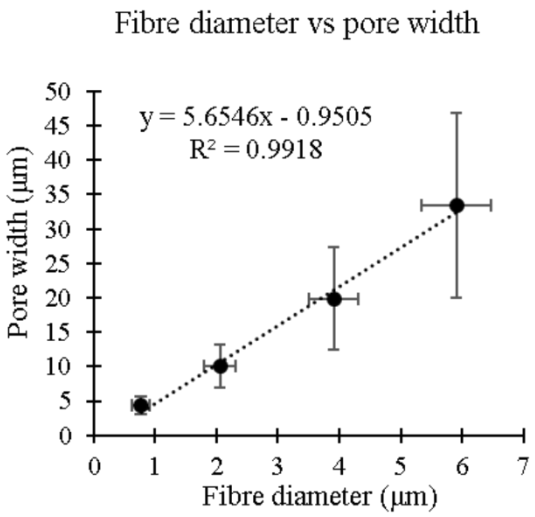

Figure 25: Correlation between fibre diameter and pore width of all four scaffold morphologies. A strong correlation was noted (R^2 = 0.9918).

3B.3.2 Scaffold Mechanical Properties

Firstly, it was noted that the medium scaffold morphology has the highest ultimate tensile strength (UTS), highest failure strain and the highest stiffness at all 5 strain bands measured (Table 9). The UTS for these scaffolds dropped either side of the medium sized fibre diameter with the medium fibre diameter showing a significantly higher UTS ($p < 0.012$ for all 3 comparisons). While the failure strain was higher in the medium fibre diameter compared to the three other morphologies, it was only significantly higher than the small fibre diameter ($p = 0.000$ for the small, $p = 0.164$ and 0.168 for the large and extra-large, respectively). Furthermore, the small scaffold morphology not only had a significantly lower failure strain than the medium fibre diameter, as previously mentioned, it also had significantly lower failure strains than the large and extra-large fibre diameters ($p = 0.011$ for both). These values can all be seen in Table 9.

Likewise, the stiffness of each scaffold at the five different strain bands followed a similar pattern. The medium scaffold morphology showed a higher stiffness at all five strain bands (see Table 9) compared to the three other fibre diameters, and the extra-large fibre diameter showed a lower stiffness at all five strain bands. Significance was noted at all 5 strain bands between the medium fibre diameter and the large and extra-large fibre diameters ($p < 0.05$ in all cases) and in some cases

significance between the medium fibre and small fibre (p = 0.053 for the 0-1% strain band; p = 0.042 for the 1-2% strain band).

Table 9: Physical and tensile mechanical properties of all four scaffold fibre diameters for seeding with HUVSMCs.

	Ultimate tensile strength (MPa)	Failure strain (%)	Contact angle at 0.2s (°)	Pore diameter (μm)	Stiffness (MPa) at given strain bands				
					0-1 %	1-2 %	2-3 %	3-4 %	4-5 %
S	1.41 ± 0.09	357 ± 79	130.7 ± 0.9	4.3 ± 1.3	3.77 ± 1.75	6.49 ± 1.64	7.35 ± 0.66	7.09 ± 0.64	6.31 ± 0.67
M	1.98 ± 0.31	1090 ± 283	130.6 ± 5.0	10.1 ± 3.2	5.77 ± 0.53	9.04 ± 1.62	8.76 ± 1.78	7.88 ± 1.77	6.76 ± 1.56
L	1.45 ± 0.21	819 ± 117	134.2 ± 3.9	19.8 ± 7.4	3.51 ± 0.55	5.97 ± 0.25	6.05 ± 2.05	5.64 ± 0.25	4.77 ± 0.62
XL	1.22 ± 0.07	821 ± 127	130.1 ± 2.2	33.4 ± 13.4	2.07 ± 0.16	3.53 ± 0.39	3.63 ± 0.43	3.43 ± 0.53	3.14 ± 0.39

3B.3.3 Cell Imaging

Conventional 2D epifluorescence imaging showed that on the smaller fibre diameter a layer of SMCs were formed showing the phenotypic characteristics of healthy SMCs. Furthermore, while no clear monolayer could be noted on the three other morphologies, they were all able to maintain the elongated phenotypic characteristics of SMCs like the small fibre diameter scaffold.

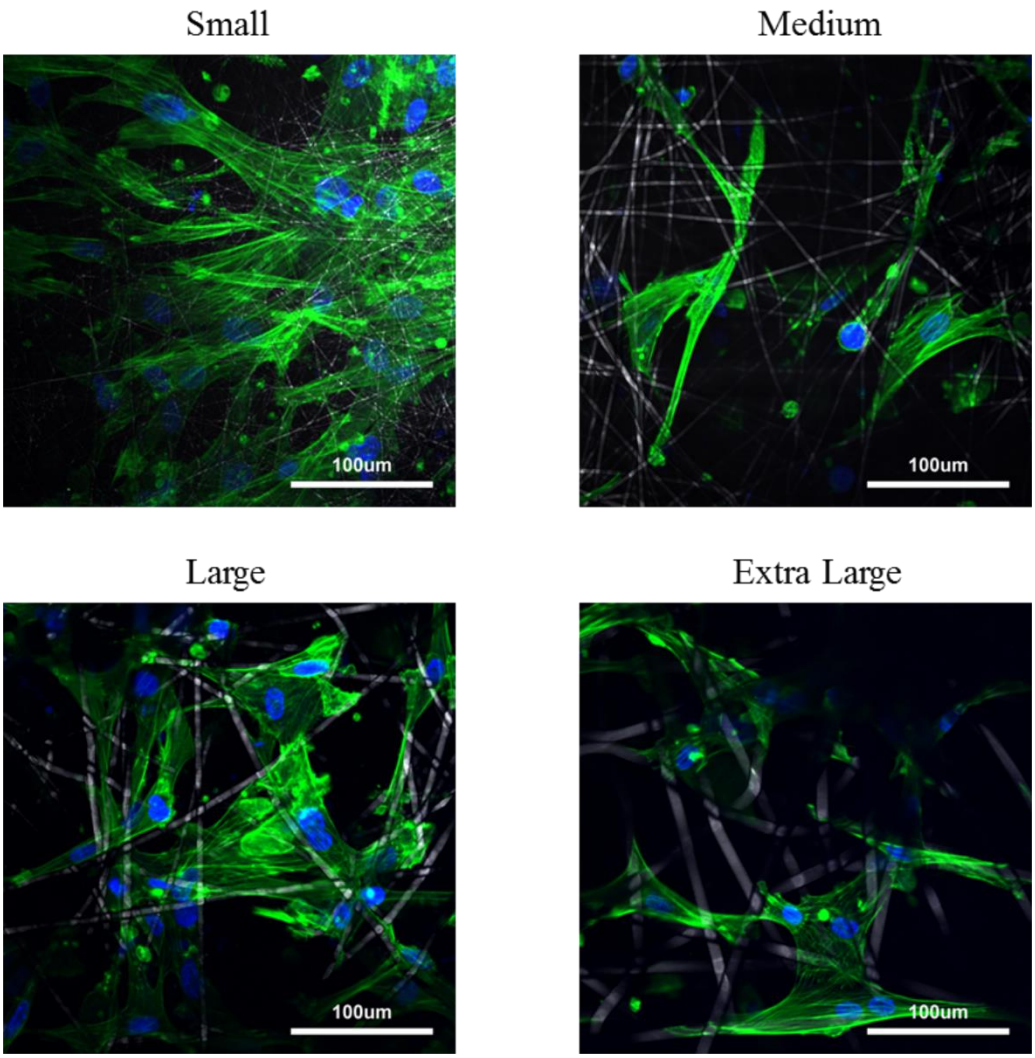

Figure 26: Representative DAPI (nuclei) and phalloidin (f-actin) stained HUVSMCs seeded onto all three scaffold morphologies. HUVSMCS showed a phenotypic morphology on all four fibre diameters.

Z-stacks of phalloidin stained SMCs showed how increasing fibre diameter had the effect of increasing cell infiltration into the scaffold. Cell infiltrations of approximately 40 µm, 42 µm, 61 µm and 82 µm were noted for the four scaffolds, as seen in Figure 27.

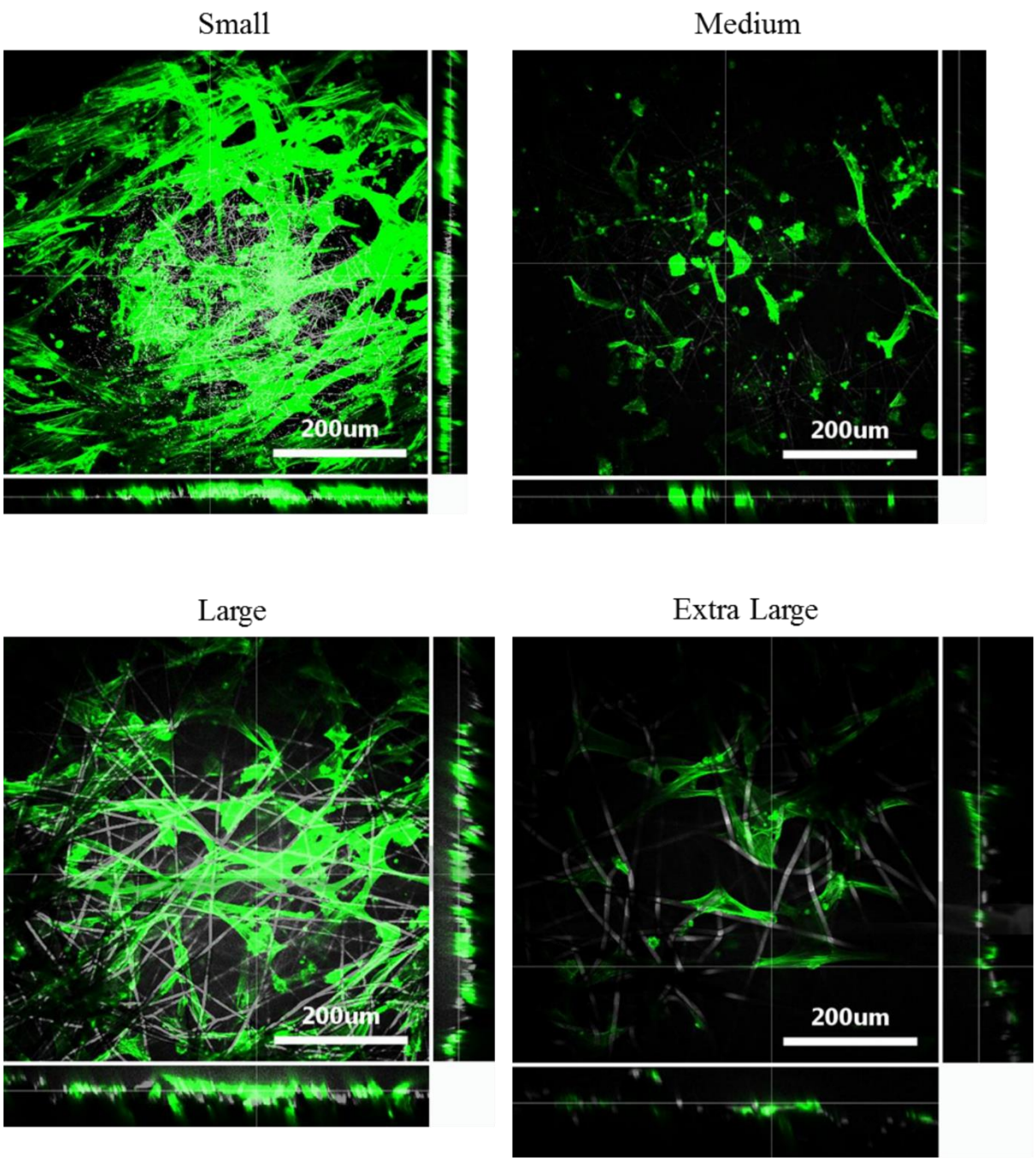

Figure 27: Representative Z-stacks of phalloidin (f-actin) stained HUVSMCs showing depth of cell infiltration into the scaffold. As expected, infiltration was deepest on the extra-large scaffold. HUVSMCs spread and elongated on the smallest fibre diameter.

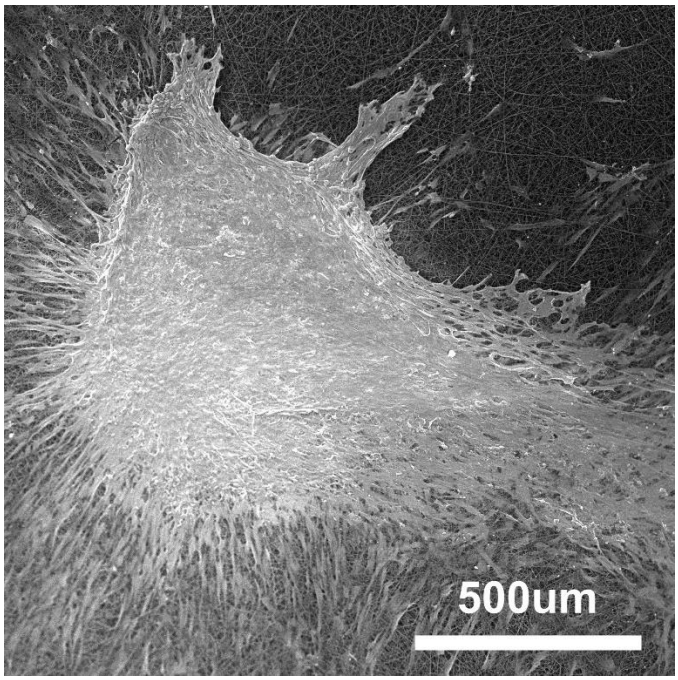

Figure 28: Representative SEM image of the HUVSMCs on the small fibre scaffold showing the hill and valley cell morphology.

3B.3.4 Cell Viability

Cell viability was measured using a CellTiter-Blue® Cell Viability Assay and showed some interesting results, as seen in Figure 29. Firstly, cell viability in the small electrospun fibre morphology after 12 days of culture was significantly higher than in the three other morphologies, suggesting that a smaller fibre morphology may be more suited for the growth of SMCs. On the contrary, the medium fibre diameter and XL fibre diameter both had reductions in cell viability, whereas the large fibre diameter showed no real change in cell viability over the 12 days of culture.

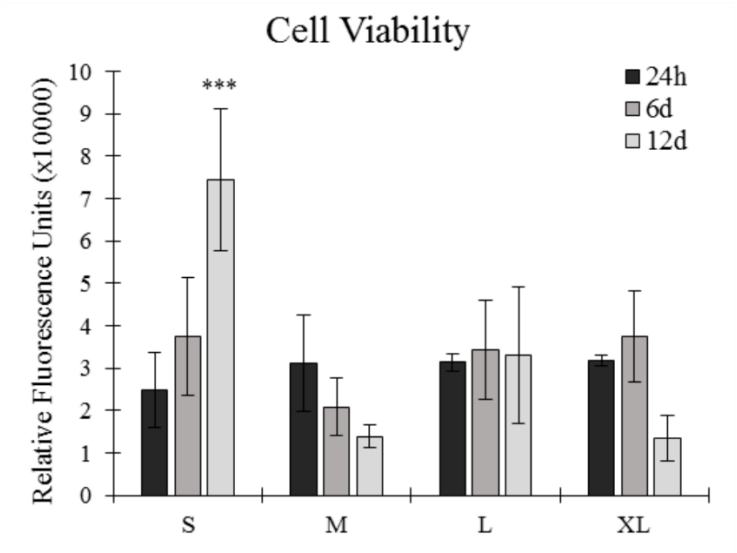

*Figure 29: Cell viability of HUVSMCs on all four scaffolds after 1, 6 and 12 days of culture. Cell viability was significantly higher in the smallest fibre morphology compared to the three larger fibre morphologies. N=4, error bars = SD. ***p < 0.001*

3A.3.5 Reverse Transcription Quantitative Polymerase Chain Reaction

RT-PCR results showed some interesting trends in HUVSMC gene expression between the four scaffold morphologies over the 12 days of culture, as seen in Figure 30. Myocardin is a key phenotypic gene in smooth muscle cells and is heavily involved in their contractile functionality, with upregulations being associated with cell maturity [52–55]. In this study, the smallest fibre diameter lead to an upregulation in myocardin between 6 and 12 days of culture, whereas in the three larger fibre diameters, a downregulation was noted between the same two timepoints. Likewise, smooth muscle alpha actin 1 is associated with maturing smooth muscle cells and their contractile functionality [50]. This study found an upregulation of smooth muscle alpha actin 1 on the small fibre between 24 h and 12 days of culture. On the contrary, all three other scaffolds showed a downregulation.

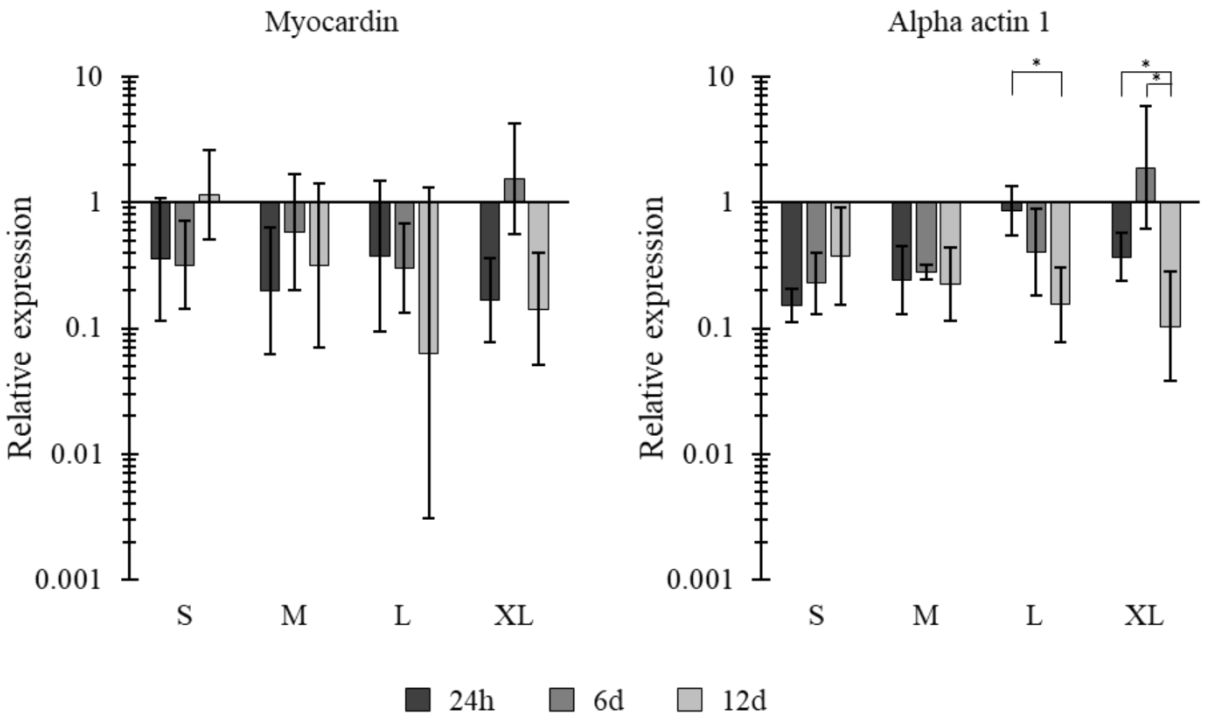

*Figure 30: RT-qPCR results for three different genes on all four scaffolds. All results were normalised to 70% confluent HUVSMCs on tissue culture plastic. N=4, error bars = SD. *p < 0.05.*

3B.4 Discussion

In this study PCL was used as the polymer source for electrospinning. PCL is a widely used polymer in tissue engineering applications due to its versatility and its FDA approval for certain applications *in vivo* [15,56]. It has been extensively used to manufacture different types of scaffolds, especially electrospun fibrous scaffolds which require a polymer that can be easily used with different solvents [11,57–59]. Electrospinning is a flexible scaffold manufacturing technique that allows for a range of different morphologies to be created [13]. Four different scaffolds were manufactured with increasing fibre diameters ranging from 0.77 ± 0.14 µm to 5.91 ± 0.56 µm with relatively equal increments between each scaffold. Interestingly, a very strong correlation was noted between the fibre diameter and the average pore width found on all four scaffolds ($R^2 = 0.9918$). This allowed for the effect of fibre diameter/pore width and cellular infiltration on seeded SMCs to be studied in an attempt to find an optimum fibre diameter for the culture of SMCs.

As expected, an increase in infiltration depth was noted as fibre diameter and pore width were increased. Depths of approximately 40 µm, 42 µm, 61 µm and 82 µm for the small, medium, large and extra-large scaffolds, respectively. This phenomena is expected and has been seen in previous studies where increasing the pore size of a scaffold has led to increased cellular infiltration [60,61]. *Phipps et al.* noted a 6 to 7 fold increase in mean cellular infiltration of mesenchymal stem cells when average pore area was increased from approximately 400 μm^2 to 1800 μm^2 [61]. Likewise, *Whited et al.* found that increasing pore diameter from less than 10 µm to 89 µm lead to significant increases in osteoblasts infiltrating to depths greater than 600 µm after 6 days of culture [60]. While these cell types are different to the ones used in this study, the same principle applies whereby a larger pore size offers more space for cell infiltration.

Fluorescence images of nuclei and f-actin stained cells showed a monolayer of SMCs on the small and large fibre scaffolds. In contrast, the extra-large scaffold appears to show cells infiltrating into pores and growing into the scaffold. While the medium fibre diameter scaffold may not have a full monolayer of cells growing, it does show cells growing along the same plane of the scaffold, which suggests that no infiltration is occurring. *In vivo*, VSMCs adopt an elongated morphology and are found interwoven around the ECM in thick layers of 40 to 60 cells [44]. This would suggest that the extra-large scaffold would be optimal for the growth of VSMCs. However, the results suggest that the smallest fibre scaffold lead to increased cell performance. VSMCs tend to grow in very compact formations *in vivo* and therefore the extra-large fibre scaffold may not have allowed for adequate cell-cell interactions due to the increase in space on offer for cell growth. This in turn may have decreased the amount of paracrine communication between the cells, reducing their proliferative performance. Studies have shown that decreased cell-cell communication in seeded scaffolds can lead to reduced cell growth and altered phenotypic gene expression in various cell types [62,63].

The small scaffold morphology lead to the formation of VSMC bundles, whereby the cells realign themselves and adopt the phenotypic ‘hill and valley’ morphology commonly seen in *in vitro* 2D cultures [64,65]. While this shows that the scaffold is well suited to the culture of VSMCs, it does not necessarily mean that this scaffold is optimal for the long-term 3D culture of VSMCs.

A relative upregulation of myocardin was noted in the smallest fibre diameter scaffold compared to the three larger fibre diameter scaffolds between 6 and 12 days of culture. Myocardin is a major phenotypic gene present in SMCs and is responsible for their contractile functionality [52–55]. As SMCs proliferate and mature, an upregulation of myocardin would be expected. Furthermore, smooth muscle alpha actin 1 is associated with maturing smooth muscle cells and their contractile functionality [50]. This study found that the small fibre diameter increased the expression of this gene over a 12 day culture period, whereas the three other scaffolds lead to a decrease in the expression of this gene over 12 days. These results would suggest that the smallest fibre diameter scaffold helped facilitate SMC maturing and improved their functionality compared to the larger fibre diameters.

3B.5 Conclusions

In conclusion, four different electrospun scaffolds were manufactured with increasing fibre diameters ranging from 0.77 μm to 5.91 μm. The largest fibre diameter led to increased cell infiltration compared to the three other morphologies. However, the smallest diameter fibre lead to a monolayer of HUVSMCs growing, showing significantly higher cell viability after 12 days of culture compared to the three other morphologies. Furthermore, altering the fibre diameter had the effect of changing the levels of gene expression from the HUVSMCs. Most notably, the cells seeded onto the smallest fibre had elevated expressions of myocardin and smooth muscle actin-α 1 (two genes associated with mature SMCs) compared to the three other morphologies. These results show how altering the fibre diameter of the scaffold has clear effects on the seeded HUVSMCs. These findings suggest that the smallest fibre diameter (0.77 μm) is most suitable for the seeding of SMCs with the aim of aiding cell maturity.

Chapter 4: Incorporation of Vascular Extracellular Matrices into Polymer Scaffolds

Introduction

In 2015 cardiovascular disease killed around 630,000 people in the United States, accounting for 23.4% of all deaths [391]. Approximately 80% of those deaths fell in the category of over 65 year olds [391]. One of the major reasons for the increase in people requiring sophisticated and complex cardiac interventions is the ever increasing average life expectancy across the world's population [392].

There are currently a variety of tissue engineering strategies utilized in the treatment of arterial disease, including scaffold materials that mimic the native ECM [393,394]. Materials used in vascular tissue engineering include decellularized extracellular matrices, biopolymers, bioabsorbable polymers and collagen [200,394–399]. There are many scaffold manufacturing methods utilised in vascular tissue engineering including electrospinning, which has been widely used due to its ability to mimic the nano and micro scale structure of tissues [214,338,375,400]. While utilising polymers does give good control over architecture, they lack some of the unique biomolecular cues found in native tissue, which is why in recent years there has been an increase in demand for utilising decellularized ECMs in tissue engineering [24,246,401,402]. The ECM is the pivotal factor in the intracellular microenvironment, thus it plays a major role in maintaining and regulating tissue function [403]. Therefore, incorporating components of the ECM into a scaffold to more closely mimic the native environment is an effective way to promote tissue regeneration [404]. On this note, hybrid electrospun scaffolds that incorporate ECM into a spun fibre have shown improved cellular performance when using meniscus and cartilage [198,199].

Herein, the present study proposes electrospinning PCL/ECM composites with two different ECM sources: bovine aorta and bovine myocardium, to study how the inclusion of these biological substances affects the performance of human umbilical vein endothelial cells HUVECs and HUVSMCs.

Part A: Vascular ECMs and Endothelial Cells

4A.1 Introduction

One of the major aims of vascular tissue engineering is to create a functional layer of endothelial cells, which can happen under the correct environmental conditions [359]. Current treatments are not keeping up with the increased demand for surgery and transplantation [392,405], therefore it is imperative that new treatments are developed.

It has been shown that the inclusion of native biochemical factors can have beneficial effects on a variety of different cell types, including endothelial cells [199,394]. Herein, the present study proposes incorporating the native vascular ECM into the electrospun polymer fibres via solubilisation of the ECM. By combining heart and aorta ECM with PCL, the aim is to manufacture an improved platform for the attachment and growth of endothelial cells, with the goal of improving vascular regeneration

4A.2 Methods and Materials

4A.2.1 ECM Production

Bovine aorta and heart were collected from a 2 year old female cow. Samples were frozen at -80ºC upon collection. The heart tissue was sliced into 5 mm thick slices, whilst the aorta was cut open and laid flat. Samples approximately 40 mm in diameter were punched out and cut up into 2x2x2 mm cubes to aide with decellularization. Samples were perfusion decellularized with 0.5% w/v SDS in deionised water for 36 h, before being washed out with 10 L of water to ensure all the remnant SDS and DNA was removed from the sample. Decellularized samples were then frozen at -80°C before being lyophilized and milled into a fine powder. More detail on decellularization and ECM processing can be seen in Section 2.2.

4A.2.2 Histology

Histology was performed on native and decellularized samples to confirm the decellularization process has been successful. Samples were fixed in 10% v/v formalin for 24 h, and embedded in

paraffin wax, before being trimmed down to 5 µm thicknesses and mounted onto glass slides. Before staining all samples were cleared with xylene to remove the paraffin wax.

Haematoxylin and Eosin staining was performed to see the remnant DNA in the tissue. Briefly, samples were cleared and then rehydrated before being stained in haematoxylin for 6 mins and eosin for 90 s. This lead to a vivid pink colour for all eosinophilic substances such as the cell cytoplasm and all ECM proteins; and a dark blue colour for the nuclear substances such as the cell nucleus.

Picrosirius Red staining was performed to ensure the collagenous structure of the tissue had not been damaged during decellularization. Briefly, samples were cleared and then rehydrated before being stained in 0.1% w/v Sirius Red for 1h, leading to a red colour for the collagen fibres and a dull yellow colour for the cellular substances [293].

More detail on histology can be seen in Section 2.4.

4A.2.3 Electrospinning

Powdered ECM (either heart or aorta) was dissolved into HFIP at 0.25% w/v. PCL was then added to this same solution at 8% w/v and dissolved overnight on a roller, resulting in ECM and PCL in solution with HFIP. A PCL only electrospun scaffold was used as a control. The solutions were electrospun using an EC-DIG electrospinning system. The parameters used for all three spins are seen in Table 10. Once finished, the electrospun sheet was left to dry overnight in the hood before being stored at 4°C. Scaffolds were punched out with a diameter of 10 mm and left in ethanol for 30 mins to sterilise. This resulted in two different ECM:PCL scaffolds with ECM:PCL ratios of approximately 3:97 and a pure PCL control. More information on the electrospinning process can be seen in Section 2.1.

Table 10: Electrospinning parameters

Needle bore (mm)	Flow rate (ml/h)	Total volume (ml)	Distance between needle tip and mandrel (cm)	Positive voltage (kV)	Negative Voltage (kV)	Mandrel rotational speed (RPM)
0.4	0.8	6	12	+14	-4	250

4A.2.4 Scanning Electron Microscopy

Scaffolds were visualized before and after cell seeding using a Hitachi S4700 fuelled emission scanning electron microscope (SEM (Hitachi) with a 5 kV accelerating voltage and a working distance of 12 mm. Scaffolds after 10 days of cell culture were stained with osmium tetroxide to allow for clear viewing of the cellular membrane and ECM components. Briefly, scaffolds were fixed in 4% v/v glutaraldehyde overnight and then stained in 0.1% v/v osmium for 30 mins. More details on SEM imaging and osmium staining can be seen in Sections 2.5 and 2.17.

4A.2.5 Mechanical Analysis

The Young's modulus of the scaffolds was assessed on unseeded scaffolds and on scaffolds after 10 days of culture. Samples with a gauge length of 14 mm were tested until 200% strain was reached. Data was analysed using a previously described analysis method [31,177,184,406]. More detail can be found in Section 2.7.

4A.2.6 Contact Angle Measurement

Contact angles were measured on dry scaffolds. A 5 µL droplet of deionised water was placed onto the scaffold and images were captured at 5Hz using a DMK 41AU02 monochrome 1280 x 960 camera. Analysis was done using ImageJ software with a previously developed plugin: LBADSA [309]. More detail can be found in Section 2.8.

4A.2.7 Fourier Transform Infrared Spectroscopy

Fourier transform infrared spectroscopy (FTIR) was used to confirm the successful inclusion of vascular ECMs into the electrospun PCL fibres. All spectra were obtained using a Nicolet™ iS™10 spectrometer with a Smart™ iTX diamond attenuated total reflection (ATR) detector. Spectra were acquired between 4000 and 400 cm^{-1} with a resolution of 1 cm^{-1} using OMNIC™ Spectra software (Thermo Fisher Scientific). More details can be found in Section 2.11.

4A.2.8 Cell Growth

HUVECs from an infant male Caucasian donor were obtained cryopreserved at passage 1 and expanded to passage 7 in a 5% CO_2/37°C atmosphere. This study abides by all criteria of the UK

Human Tissue Act. HUVECs were expanded using MCBD 131 medium supplemented with 5% v/v FBS; 1% v/v L-glutamine; 1% v/v penicillin/streptomycin; 1mg/L hydrocortisone; 50 mg/L ascorbic acid; 2 μg/L fibroblast growth factor; 10 μg/L epidermal growth factor; 2 μg/L insulin-like growth factor; and 1 μg/L vascular endothelial growth factor [31,407,408]. More details can be found in Section 2.3.

4A.2.9 Cell Seeding and Culture

Scaffolds were incubated in serum free MCDB 131 medium overnight to increase hydrophilicity and help with cell attachment. Cells were seeded at approximately 45,000 cells/cm^2 in 20 μL of culture medium (MCDB 131 + supplements as mentioned in 4A.2.8) and left for 30 mins to allow for attachment. Another 30 μL of medium was added and left for a further 30 mins before total medium was increased to 500 μL. Medium was replaced every 2 days. More details can be found in Section 2.3 and 2.12.

4A.2.10 Cell Viability

The CellTiter-Blue® assay was performed after 1, 5 and 10 days of culture as per the manufacturer's instructions [328]. Measurements were made with a Modulus™ II microplate reader at Excitation 525 nm and Emission 580-640 nm. More details can be found in Section 2.13.

4A.2.11 DNA Quantification

Cell seeded scaffolds cultured for 1, 5 and 10 days were frozen and tested for total DNA content of using a Quant-iT™PicoGreen® assay kit as per the manufacturers' instructions [341]. Fluorescence was read using a Modulus™ II microplate reader at Excitation 490 nm and Emission 510–570 nm. More detail can be found in Section 2.14.

4A.2.12 Cell Imaging

Scaffolds for imaging were fixed in 4% v/v formalin in PBS for 24 h. Scaffolds were then washed and stored in PBS. Permeabilization for cell imaging was achieved using 0.2% v/v TritonX-100 in PBS for 5 mins. Scaffolds were stained with 0.1 mL of 0.1 μL 1000X Phalloidin-iFluor™514 conjugate in 0.1 mL PBS with 1% v/v bovine serum albumin for 60 min. Scaffolds were washed thrice in PBS for

10 mins. Scaffolds were then stained with 0.1 mL of 300 nM 4',6-diamidino-2-phenylindole (DAPI) in PBS for 10 mins followed by three 10 min PBS washes. All scaffolds were imaged using a Coherent Anti-Stokes Raman scattering microscope. More details can be found in Section 2.17.

4A.2.13 Reverse Transcription Quantative Polymerase Chain Reaction (RT-qPCR)

RNA was extracted from the scaffolds using standard Tri-Reagent methods and purified using Qiagen's RNeasy spin column system. Real-time polymerase chain reaction was performed using a LightCycler® 480 Instrument II (Roche Life Science) and Sensifast™ SYBR® High-ROX system (Bioline). Forward and reverse sequences were designed with Sigma-Aldrich and are displayed in Table 11 [31,361]. Relative quantification of RT-PCR results was carried out using the $2^{-\Delta\Delta ct}$ method [350]. Gene expression levels were expressed relative to GAPDH (housekeeping gene) and normalised to expression on the day 1 PCL control. More details can be found in Section 2.18.

Table 11: Primer sequences used in RT-PCR amplification of genes from the seeded HUVECs.

Gene	Primer	Sequence	Sequence Length	Reference
Glyceraldehyde 3-phosphate dehydrogenase	GAPDH (forward)	GTCTCCTCTGACTTCAACAG	20	[31]
	GAPDH (reverse)	GTTGTCATACCAGGAAATGAG	21	
Matrix metalloproteinase-1	MMP1 (forward)	CGGTTTTTCAAAGGGAATAAGTACT	25	[31]
	MMP1 (reverse)	TCAGAAAGAGCAGCATCGATATG	23	
matrix metalloproteinase-2	MMP2 (forward)	CGCTCAGATCCGTGGTGAG	19	[31]
	MMP2 (reverse)	TGTCACGTGGCGTCACAGT	19	
Vascular endothelial growth factor	VEGF (forward)	AGACCAAAGAAAGATAGAGCAAGACAAG	28	[31]
	VEGF (reverse)	GGCAGCGTGGTTTCTGTATCG	21	

Platelet endothelial cell adhesion molecule	CD31 (forward)	ACTGGACAAGAAAGAGGCCATCCA	24	[361]
	CD31 (reverse)	TCCTTCTGGATGGTGAAGTTGGCT	24	

4A.2.14 Statistical Analysis

Data was expressed as mean ± 1 standard deviation, unless stated otherwise. Statistical analysis was preformed using one-way ANOVA with post-hoc Fisher test unless otherwise stated.

4A.3 Results

4A.3.1 Decellularization

Bovine heart and aorta tissue were both successfully decellularized using 0.5% w/v SDS as seen in Figure 31. DNA content was significantly reduced in both tissues and the Haematoxylin and Eosin staining showed that the nuclear content of the cells had been removed from both tissues. Furthermore, Picrosirius Red staining showed that the collagenous composition of the tissue was maintained during the decellularization process.

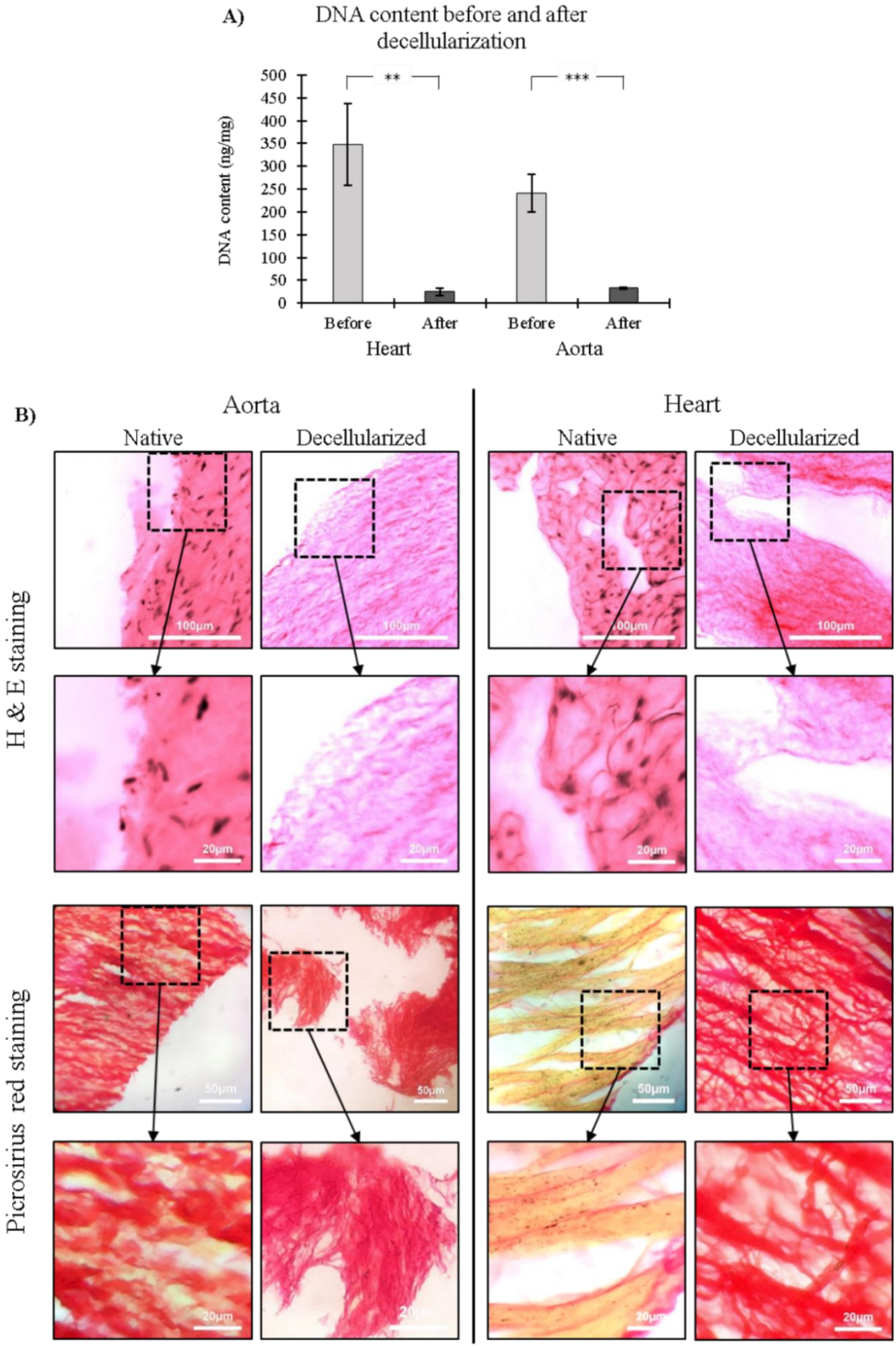

Figure 31: Decellularization of bovine aorta and myocardium was successfully achieved using a 0.5% SDS protocol. (A) DNA content of tissue before and after decellularization. (B) H&E and Picrosirius red staining of tissue before and after decellularization

4A.3.2 Electrospinning

Electrospun fibrous sheets were successfully manufactured, as seen in Figure 32. All three scaffolds are made up of randomly orientated fibres with fairly uniform fibre sizes. The three scaffolds have average fibre diameters of 0.97 ± 0.19 μm, 1.20 ± 0.09 μm and 0.94 ± 0.12 μm for the PCL control, heart ECM and aorta ECM scaffolds, respectively. The heart ECM and aorta ECM scaffolds comprise of 97% PCL and 3% ECM (aorta or heart depending on the scaffold), whereas the PCL control is 100% PCL.

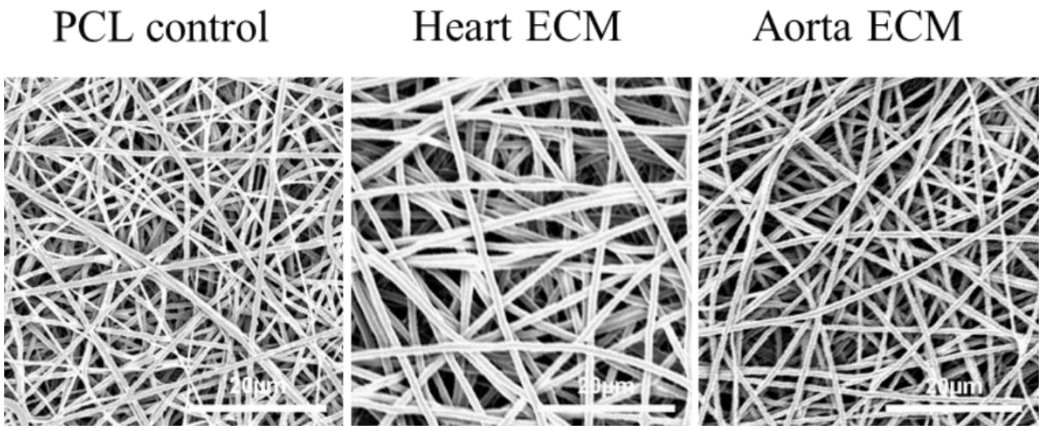

Figure 32: SEM images of the three electrospun scaffolds for seeding with HUVECs. The heart ECM and aorta ECM scaffold comprise of approximately 97% PCL and 3% ECM. The PCL control is entirely made up of PCL (100%).

4A.3.3 Mechanical Characterisation

Mechanical testing performed using an Instron tensile tester showed no statistically significant difference between cell seeded and unseeded scaffolds for each scaffold at all the strain bands. However, the general trend for the PCL scaffold and the heart ECM scaffold (3% ECM) is a slightly higher Young's modulus in the seeded scaffolds then the unseeded scaffold, as seen in Figure 33 and Table 12. Furthermore, it was noted that the two ECM scaffolds had consistently higher Young's moduli at all strain brackets compared to the PCL only scaffold (Table 12), with significance noted at the 0-1% strain bracket between the ECM scaffolds and the PCL scaffold; and in the 1-2% strain brackets between the aorta ECM scaffold and the PCL only scaffold.

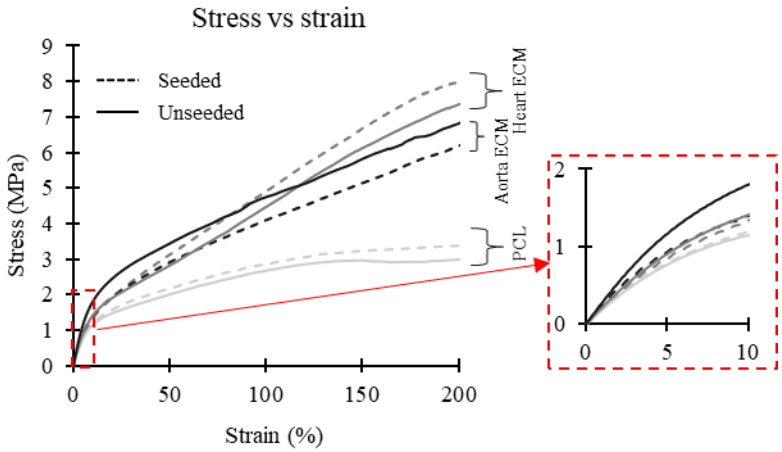

Figure 33: Representative stress vs strain curves for each scaffold – seeded and unseeded and after 10 days of culture. The incorporation of ECM led to steeper curves.

Table 12: The incremental Young's moduli of all three scaffolds and different strain bands along the stress strain curve. Incremental Young's moduli were taken on both unseeded scaffolds and seeded scaffold after 10 days of culture.

		Scaffold type					
		PCL		Heart ECM		Aorta ECM	
		Unseeded	Seeded	Unseeded	Seeded	Unseeded	Seeded
Young's Modulus at % strain, MPa	0-1	17.05 ± 1.81$	19.48 ± 2.14	21.00 ± 1.87$	22.58 ± 2.13	21.90 ± 2.93$	21.60 ± 1.91
	1-2	16.80 ± 1.27&	18.10 ± 2.21	20.87 ± 2.60	20.68 ± 2.37	22.00 ± 3.11&	18.76 ± 1.95
	2-3	15.03 ± 1.89	15.25 ± 2.47	16.27 ± 2.22	18.18 ± 1.62	18.04 ± 2.29	15.82 ± 1.12
	3-4	13.93 ± 1.53	14.55 ± 3.00	15.96 ± 1.69	15.84 ± 1.60	17.34 ± 1.95	14.30 ± 0.85
	4-5	12.45 ± 1.75	13.08 ± 2.80	12.64 ± 1.40	14.16 ± 1.18	14.90 ± 1.76	12.92 ± 0.64
	0-5	15.05 ± 1.54	16.09 ± 2.49	17.35 ± 1.83	18.29 ± 1.72	18.84 ± 2.28	16.68 ± 1.26

*Results with matching symbols (&) are significantly different to each other ($p<0.05$) across the same strain band. Results with the $ symbol are significantly different to all other results in that same strain band ($p<0.05$).

4A.3.4 Fourier Transform Infrared Spectroscopy

The FTIR results confirmed that the aorta ECM and heart ECM had both been successfully incorporated into the electrospun PCL scaffolds. A range of spectra were taken for PCL alone, PCL/ECM blended scaffolds and ECM alone. Figure 34 shows the peaks in intensity at 1720, 1654, and 1,541 cm^{-1} for both the aorta ECM and heart ECM. The peaks can be attributed to the stretching of the carbonyl in the PCL, the amide I bond in the ECM, and the amide II bond in the ECM,

respectively [326,409]. The differences in intensities for each peak were quantified to show that the ECM has been integrated and can be seen in

Table 13 and Table 14. Briefly, increases of 84.3 ± 8.0% ($p < 0.01$) and 109.2 ± 18.6% ($p < 0.01$) were seen at 1654 and 1,541 cm^{-1}, respectively, for the aorta ECM, with a decrease of 19.4 ± 15.5% ($p < 0.05$) at 1720 cm^{-1}. The heart ECM showed increases of 35.2 ± 6.7% ($p < 0.01$) and 26.8 ± 10.7% and a decrease of 10.5 ± 15.2% for the three wave- lengths.

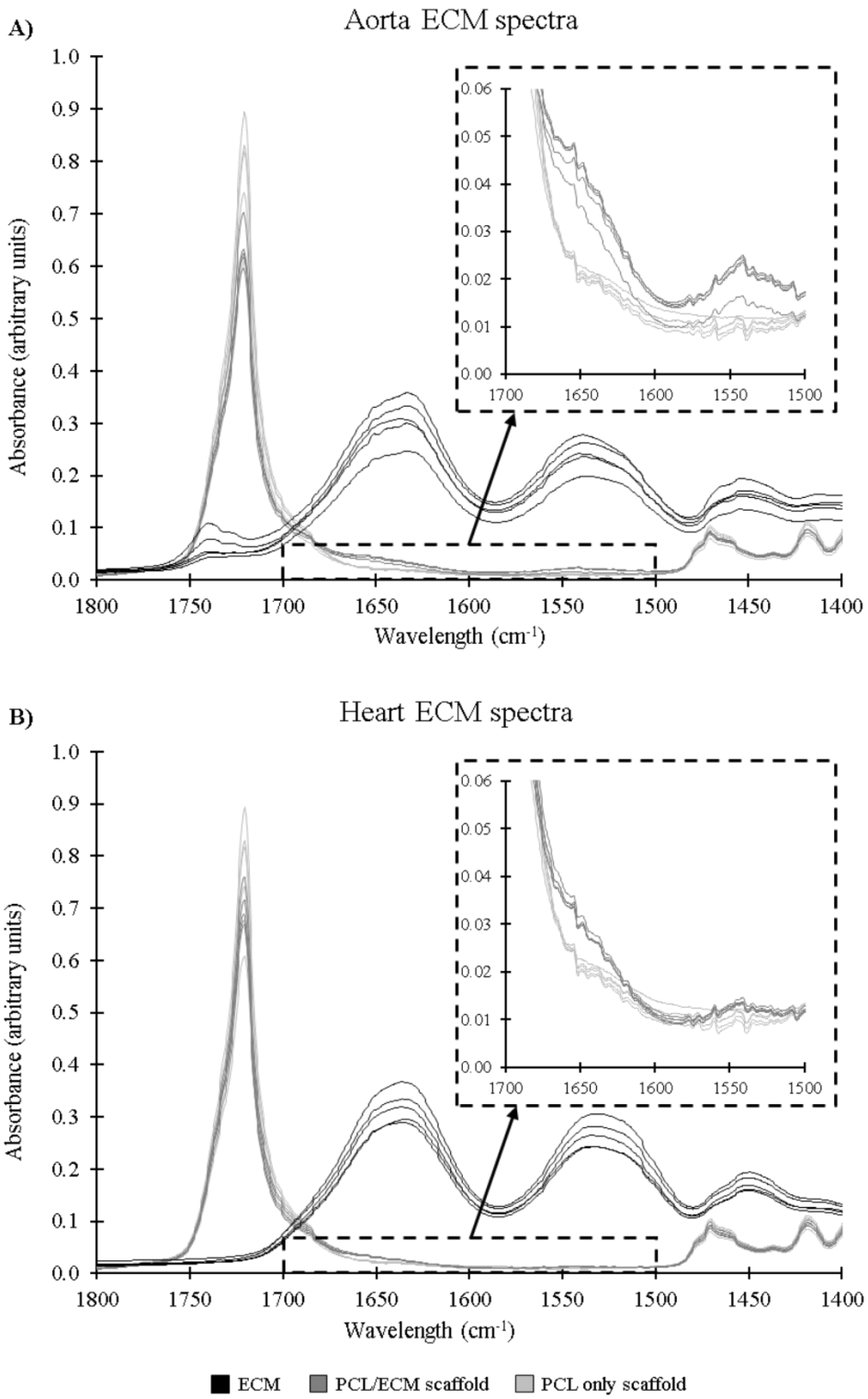

Figure 34: FTIR absorbance spectra for A) aorta ECM scaffolds and B) heart ECM scaffolds compared to PCL alone and ECM alone. Absorbance spectra show peaks in intensity at Amide I and Amide II bonds in both ECM blended scaffolds, suggesting that the ECM had been successfully incorporated into the fibre. N=5. Each individual line represents a separate measurement from a separate scaffold.

Table 13: Absorbance values for each peak on all three scaffolds.

Wavelength of peak (cm^{-1})	Absorbance values		
	PCL	Aorta ECM	Heart ECM
1720	0.774 ± 0.110	0.624 ± 0.040	0.693 ± 0.039
1654	0.025 ± 0.001	0.046 ± 0.004	0.034 ± 0.002
1541	0.011 ± 0.001	0.023 ± 0.004	0.014 ± 0.001

Table 14: Wavelengths of peaks noted in FTIR absorbance spectra and their associated intensity changes between each scaffold.

Wavelength of peak (cm^{-1})	Assignment	Caused by	Change in absorbance between PCL fibre and ECM/PCL fibre	
			Aorta ECM	Heart ECM
1720	Carbonyl group stretching	PCL	- 19.4 ± 15.5%	- 10.5 ± 15.2%
1654	Amide I bond	ECM (collagen and elastin)	+ 84.3 ± 8.0%	+ 35.2 ± 6.7%
1541	Amide II bond	ECM (collagen and elastin)	+ 109.2 ± 18.6%	+ 26.8 ± 10.7%

4A.3.5 Contact Angle Measurement

The addition of aorta ECM had the effect of increasing the hydrophilicity of the scaffold compared to the conventional PCL scaffold and heart ECM scaffold, as seen in Table 15. These results were significant when comparing the aorta ECM scaffold to the heart ECM scaffold: 26.9% lower ($p < 0.05$) after 0.2s and 38.7% lower ($p < 0.05$) after 1s, but not when comparing either to the PCL scaffold. Furthermore, the percentage drop in contact angle between 0.2 s post contact and 5 s post contact was higher for the aorta ECM scaffold than the two others (23.2% drop compared to 13.7% and 13.2%).

Table 15: Contact angle measurements for all three scaffolds after 0.2, 1 and 5 seconds.

	Scaffold type		
	PCL	Heart ECM	Aorta ECM
Contact angle after 0.2s, °	114.4 ± 8.9	122.5 ± 3.5[&]	89.6 ± 37.7[&]
Contact angle after 1s, °	103.6 ± 19.6	118.8 ± 10.7[#]	72.8 ± 43.9[#]
Contact angle after 5s, °	98.7 ± 25.2	106.3 ± 27.2	68.8 ± 43.6
Percentage drop in contact angle between 0.2s and 1s	9.44%	3.02%	18.75%
Percentage drop in contact angle between 0.2s and 5s	13.7%	13.2%	23.2%

*Results with matching symbols (& and #) are significantly different to each other ($p<0.05$).

4A.3.6 Cell Viability

Cell viability was assessed using a CellTitre-Blue® fluorescence assay. After 10 days, the aorta ECM scaffold and heart ECM scaffold both showed a significant increase in cell viability compared to their viabilities after 1 day ($p < 0.05$), as seen in Figure 35. Furthermore, the aorta ECM scaffold also showed a significant increase between 5 and 10 days of culture ($p < 0.01$). Conversely, the PCL scaffold showed no significant increase between all three timepoints, although an upward trend was noted.

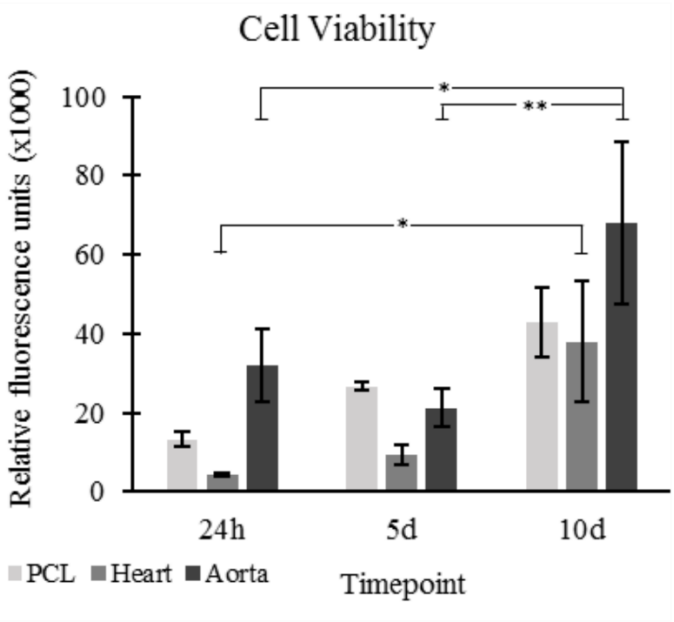

*Figure 35: Cell viability using the CellTitre-Blue assay for all three scaffolds after 1, 5 and 10 days of culture. HUVECs on the aorta ECM scaffold showed higher viability after 10 days compared to the heart ECM scaffold and PCL control. N=5, error bars = SD. *p < 0.05, **p < 0.01.*

4A.3.7 DNA Quantification

DNA quantification was performed using a Picogreen assay. The DNA content of the aorta ECM scaffold was significantly higher after 10 days than all other scaffolds at all three timepoints, as seen in Figure 36. While this was the only significance noted, a trend of increasing DNA content was noted across all three scaffolds as culture time increased.

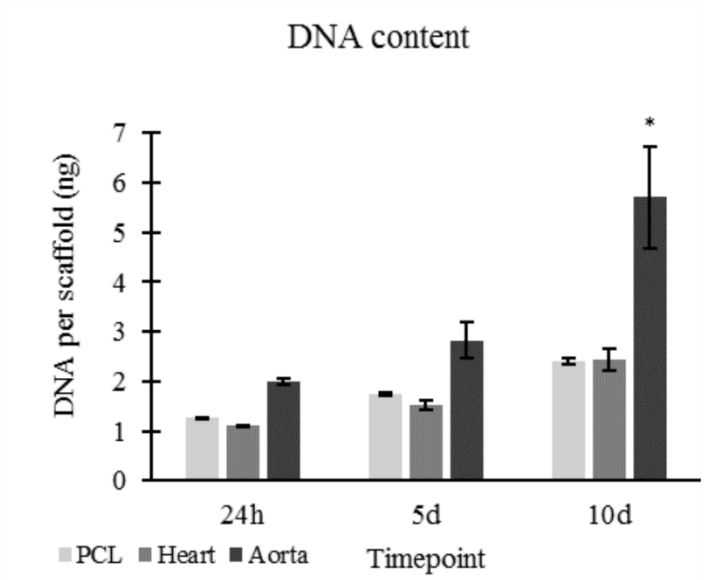

*Figure 36: DNA quantification using the Picogreen assay for all three scaffolds. The aorta ECM blended scaffold showed significantly higher DNA content after 10 days of culture compared to the two other scaffolds. N=5, error bars = SD. *p<0.05.*

4A.3.8 Cell Imaging

Representative SEM images taken using a scanning electron microscope show the functional cell layers on scaffolds after 10 days of culture (Figure 7A). Interestingly, the aorta ECM scaffold appears to be 100% confluent with HUVECs, compared to approximately 30% for the PCL scaffold and 50% for the heart ECM scaffold. These results validate the cell viability and DNA quantification results, suggesting that the incorporation of aorta ECM into the scaffold improved HUVEC proliferation. Furthermore, all three scaffolds show similar HUVEC morphology.

Representative images taken using CARS further confirm that the incorporation of aorta ECM into the scaffold had a favourable effect on HUVECs (Figure 7B). After 1 day of growth, the cells on the aorta ECM scaffold already appear greater in number and have a higher quantity of visible actin filaments. The heart ECM scaffolds show very poor cell attachment after 1 day, which matches the cell viability and DNA quantification results. Furthermore, cell number appears to increase for all scaffolds between day 1 and day 10. Interestingly, the actin filaments appear more characterized after 10 days, which is a sign of maturing cells [410].

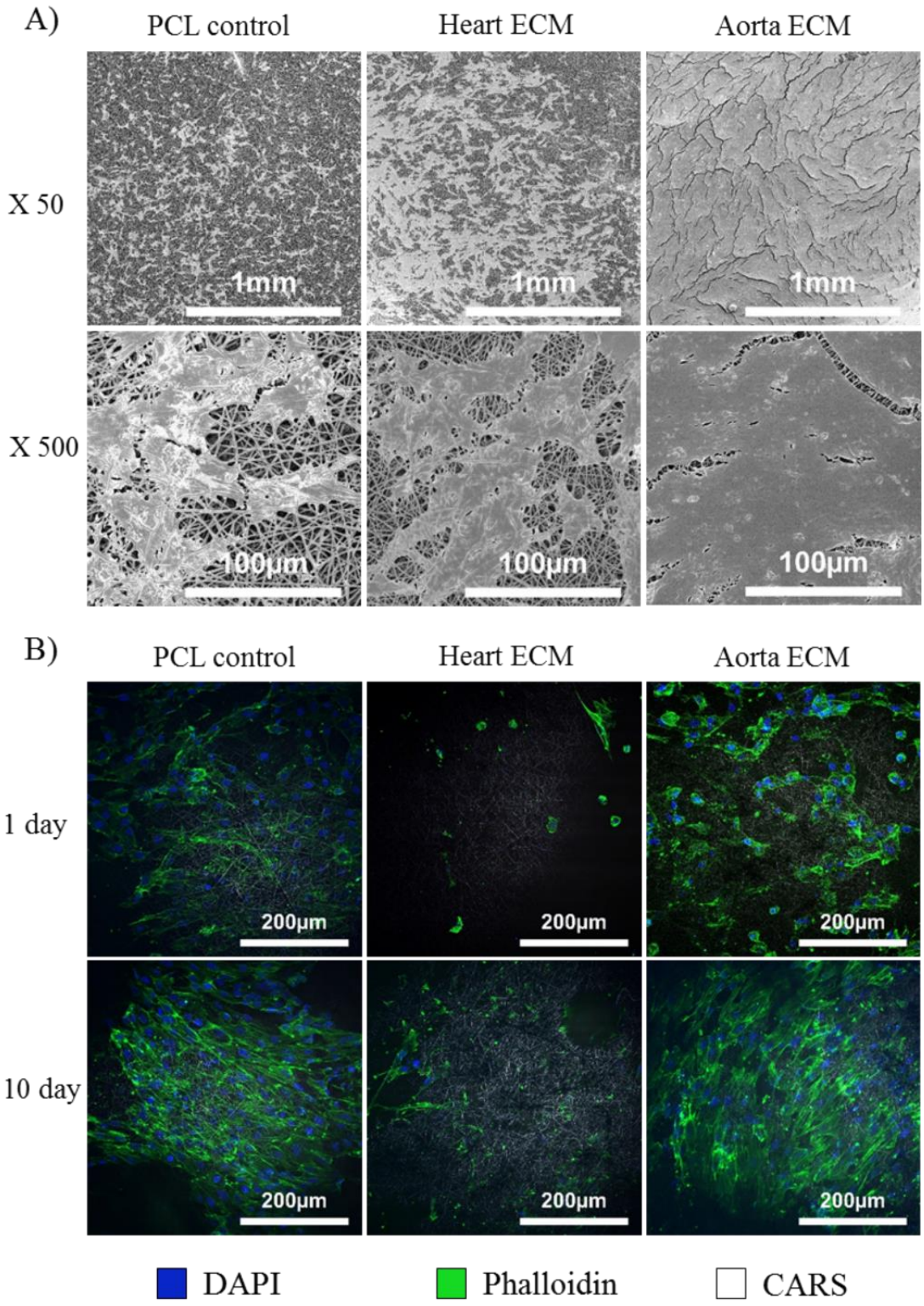

Figure 37: A) Representative SEM images of osmium stained HUVECs on the three scaffolds after 10 days. B) Representative CARS images of HUVECs on all three scaffolds after 1 and 10 days of culture. Blue = cell nuclei, green = f-actin filaments.

4A.3.9 Gene Analysis

Multiple genes associated with vascular function were assayed for their expression, including cluster of differentiation (CD31), matrix metalloproteinase-1 (MMP1), matrix metalloproteinase-2 (MMP2) and vascular endothelial growth factor (VEGF), as seen in Figure 38. All three scaffolds noted a downregulation in CD31 over the three timepoints. The day 1 heart ECM showed significantly higher expression compared to all other scaffolds at all timepoints. MMP1 expression showed downregulation over time for all three scaffolds, with the biggest reduction in expression seen for the aorta ECM scaffold. Significantly lower expressions were also noted for the aorta ECM scaffolds at 5 and 10 days when compared to the two other scaffolds.

Conversely, MMP2 expression was seen to increase over time, with significant increases for the PCL and heart ECM scaffolds. Furthermore, the aorta ECM scaffold had a significantly higher expression at day 1 compared to the PCL and heart ECM scaffolds. VEGF showed no real trend over time, with the only exception being that aorta ECM scaffold had a significantly higher expression than the heart ECM scaffold at day 1.

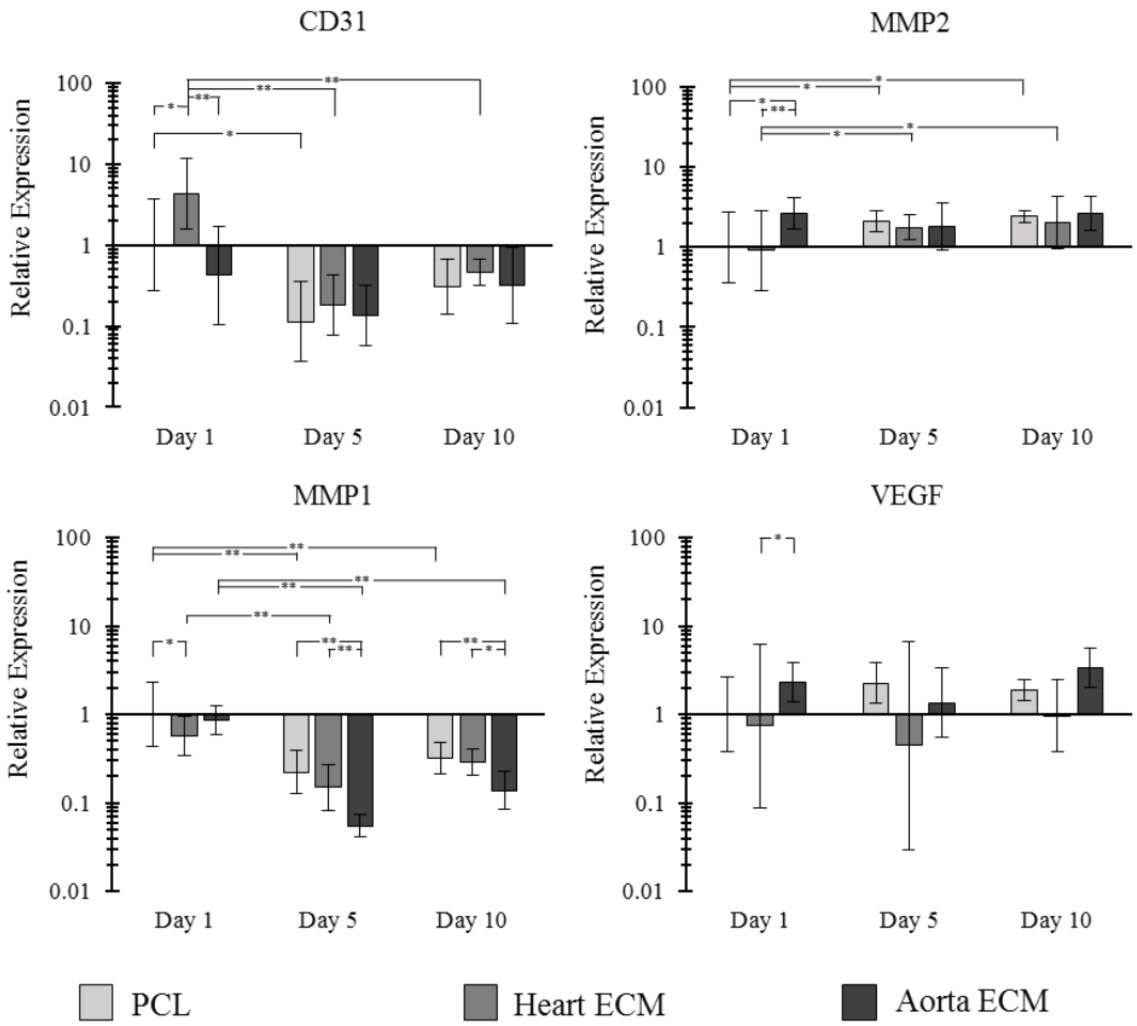

*Figure 38: RT-qPCR data showing the HUVEC gene expression of MMP1, MMP2, CD31 and VEGF relative to the house keeping gene: GAPDH. All results have been normalized to day 1 PCL. N=5, error bars = SD. *p < 0.05, **p < 0.01.*

4A.4 Discussion

Polymer scaffolds have long been utilised in tissue engineering as a platform for tissue regeneration [363,411,412]. Physical characteristics can be designed into the scaffold to support cellular activity and promote differentiation, proliferation and deposition of new functional ECM [412]. Furthermore, PCL offers a range of degradation profiles that can be tailored based on the tissue type its being designed for [413]. PCL is widely used as the polymer component of electrospun bioscaffolds due to these properties [198,414,415]. Alongside polymers, decellularized tissue has been used in tissue engineering due to its cell supporting physical and chemical characteristics [246,399]. The aim when decellularizing is to maintain the physical and chemical characteristics of the remnant ECM [200]. This

study utilized SDS, a commonly used ionic detergent for decellularizing tissues and successfully reduced the DNA content to below the 50ng/mg standard [249,257,271,416]. SDS is a very effective means of decellularization and has been used at varying concentrations ranging from 0.1% to 4%, with DNA removal and maintenance of structural integrity observed [417–421]. H&E staining confirmed the removal of the DNA content from the two tissue types after decellularization and the Picrosirius red staining confirmed that the collagenous structure of the ECM was maintained during decellularization. The FTIR results for the two ECMs showed peaks in the areas associated with structural proteins such as collagen and elastin, suggesting that the decellularizing process maintained the protein's integrity [422].

Polymers and ECM both have their advantages when used as scaffolds for tissue engineering [246,363]. In this study, the two were combined in an attempt to harness the beneficial characteristics from each to create a bioscaffold more suited for vascular tissue engineering. Recently, work has focussed on combining the two to take advantage of these characteristics, in a similar vein to this study [198,394,396,397,423]. For example, coating decellularized vascular ECMs with polymers has been implemented before, with the aim of improving biochemical and mechanical performance [396,423]. These studies both noted improved mechanical properties. However, the final structure of the scaffold is limited by the size and architecture of the ECM. By integrating the ECM directly into the polymer fibres, as has been done in this study using electrospinning, highly tailored and physically repeatable structures were created that include both the biochemical cues found in native ECM; and have the mechanical strength of the electrospun polymer. Moreover, as found in this study and previous, there are mechanical and biochemical benefits to combining ECM with polymers [396,423].

The method of solubilising ECMs into a PCL/HFIP solution has been used before with decellularized meniscus and cartilage ECM [198,199]. *Gao et al.* found that the addition of meniscus ECM had a positive effect in reducing contact angle, a phenomena also noted with the inclusion of aorta ECM in this study [198]. Similarly, *Garrigues et al.* dissolved decellularized cartilage ECM into a solution of PCL and HFIP and found gene expression changes, in similar vein to this study [199].

A downward trend in CD31 expression was seen for all three scaffolds. CD31, also known as PECAM1 (platelet endothelial cell adhesion molecule 1) is a protein found on the surface of many

cells and is involved in angiogenesis and integrin activation. Over-expression of CD31 can inhibit morphogenesis in cells [424]. Its downregulation suggests that: the HUVECs are struggling to adhere to each other [425], which SEM and fluorescence microscopy images disprove, or the HUVECs are not attempting to create new vasculature (angiogenesis) [426]. This is the most likely reason that can be attributed to the issue of poor cellular infiltration which is required in order to achieve full tissue regeneration. A lack of infiltration in this study resulted in a monolayer of cells growing on the surface of the scaffold. Studies have shown the contribution of porosity and pore interconnectivity on cell survival and HUVEC angiogenesis, similar to the findings in the fibre diameter study with HUVECs (Chapter 3.1) [227,315]. On the other hand, no real trend in VEGF expression was noted. VEGF is a signal protein that stimulates the formation of new blood vessels (angiogenesis) in tissue regeneration [53]. Its overexpression is also associated with tumour growth and intraocular neovascular disorders [53]. During cellular proliferation, an upregulation of VEGF would be expected [427]. It has been suggested that HUVECs 'overexpress' VEGF in the first 24h, which may explain this down regulation over time compared to the day 1 scaffolds [26].

A trend of decreasing MMP1 expression for all three scaffolds was noted. MMP1 is an enzyme involved in the breakdown and remodelling of collagen (one of the major components of vascular ECMs) [428]. Its downregulation suggests the cells are not trying to breakdown the collagen within the ECM, suggesting they are in a position of homeostatic equilibrium with their scaffold. In contrast, a significant upregulation of MMP2 was noted in all three scaffolds after 5 and 10 days. Furthermore, after 1 day a significantly higher expression was seen in the aorta ECM scaffold compared to the two other scaffolds. This enzyme is involved in the breakdown and remodelling of gelatin (another major component of vascular ECMs) [429]. Its upregulation suggests the presence of gelatin in the ECM scaffolds. An upregulation was noted across both ECM scaffolds, as well as the PCL only scaffold after 10 days of culture, with no significant differences noted between the three scaffolds. This suggests that this upregulation is unlikely to be caused by the presence of gelatin in the ECM scaffolds and is probably a result of something other than the constituents of the two native ECMs, such as scaffold architecture, as previously mentioned.

4A.5 Conclusions

This study showed that integrating two different sources of decellularized vascular ECMs into electrospun polymer scaffolds has promise for vascular tissue engineering. The ECMs were successfully decellularized and combined into the scaffolds. The inclusion of ECM had effects on the performance of seeded HUVECs and on the mechanical properties of the scaffold. Furthermore, the mechanical properties of the scaffold could easily be altered through including ECM into the scaffold. The inclusion of aorta ECM resulted in a stiffer scaffold that had improved biomechanical properties for the attachment of cells – leading to the increased cell adherence noted in this study. The method described combines the controllable physical properties of the polymer (PCL) with the biochemical and mechanical properties of the ECM (aorta and myocardium wall) to create a tailored hybrid bioscaffold. The combination of a natural ECM and a synthetic polymer to generate a hybrid bioscaffold has many potential applications in vascular tissue engineering.

Part B: Vascular ECMs and smooth muscle cells

4B.1 Introduction

Vascular smooth muscle cells (VSMCs) are an important component of the vessel, making up the bulk of the cells in the tunica media [37]. They are responsible for the mechanical properties and vasoactive responsive properties that allow blood vessels to function properly [372]. Vascular ECMs, especially aortic ECM contain a variety of different proteins and GAGs that have shown benefit to VSMCs. Furthermore, VSMCs are found integrated amongst a network of ECM, mostly made up of collagen and elastin and are strongly interconnected in their functions. Studies have looked at how smooth muscle cells interact with electrospun polymer/protein combinations [376], however, none have investigated the effect of electrospinning decellularized vascular ECMs on VSMCs.

Herein, this study proposes incorporating decellularized vascular ECMs into electrospun polymer fibres to see how they affect the performance of seeded HUVSMCs.

4B.2 Methods and Materials

4B.2.1 ECM Production

Aorta and heart samples were collected from a 2 year old female cow and decellularized using previously described methods. More detail on decellularization and ECM processing can be seen in Section 2.2.

4B.2.2 Histology

Histology was performed on native and decellularized samples. Samples were fixed in 10% v/v formalin for 24 h, embedded in paraffin wax and then trimmed down to 5 µm thicknesses and mounted onto glass slides. Before staining all samples were cleared with xylene to remove the paraffin wax.

Haematoxylin and Eosin staining was performed to see the remnant DNA in the tissue.

More detail on histology can be seen in Section 2.4.

4B.2.3 Electrospinning

Powdered ECM was dissolved into HFIP at 0.25% w/v. PCL was added at 8% w/v and dissolved resulting in ECM and PCL in solution with HFIP. A PCL only electrospun scaffold was used as a control. Electrospinning parameters used for all three spins are seen in Table 16. Scaffolds were punched out with a diameter of 10mm and left in ethanol for 30 mins to sterilize. This resulted in two different ECM:PCL scaffolds with ECM:PCL ratios of approximately 3:97 and a pure PCL control. More information on the electrospinning process can be seen in Section 2.1.

Table 16: Electrospinning parameters used to manufacture the three different scaffolds: PCL control; aorta ECM blended scaffold; and heart ECM blended scaffold.

Needle bore (mm)	Flow rate (ml/h)	Total volume (ml)	Distance between needle tip and mandrel (cm)	Positive voltage (kV)	Negative Voltage (kV)	Mandrel rotational speed (RPM)
0.4	1	6	12	+14	-4	250

4B.2.4 Scanning Electron Microscopy

Scaffolds were visualized before and after cell seeding using a scanning electron microscope. Scaffolds after 10 days of cell culture were stained with osmium tetroxide. Briefly, scaffolds were fixed in 4% v/v glutaraldehyde overnight and stained in 0.1% v/v osmium tetroxide for 30mins. More details on SEM imaging and osmium staining can be found in Sections 2.5 and 2.17.

4B.2.5 Mechanical Analysis

Samples were stretched using an Instron 3367 tensile testing machine with a 50 N load cell. Samples with a gauge length of 14mm were tested until failure. The incremental Young's modulus was deduced using the following formula:

$$E = \frac{FL_0}{A\Delta L}$$

where E is Young's modulus, F is the applied force, A is the cross sectional area, ΔL is change in length and L_0 is the original length. More details can be seen in Section 2.7.

4B.2.6 Contact Angle Measurement

Contact angles were measured on dry scaffolds. A 5 µL droplet of deionised water was placed onto the scaffold and images were captured at 5 Hz using a DMK 41AU02 monochrome 1280 x 960 camera. Analysis was done using ImageJ software with a previously developed plugin: LBADSA [309]. More details can be found in Section 2.8.

4B.2.7 Fourier Transform Infrared Spectroscopy

FTIR was used to confirm the successful incorporation of vascular ECMs into the electrospun PCL fibres. All spectra were obtained using diamond attenuated total reflection detector. Spectra were acquired between 4000 and 400 cm^{-1} with a resolution of 1 cm^{-1}. More details can be found in Section 2.11.

4B.2.8 Cell Growth

HUVSMCs from an infant male Caucasian donor were obtained cryopreserved at passage 1 (Sigma Aldrich) and expanded to passage 4 in a 5% CO_2/37°C atmosphere. HUVSMCs were expanded using Smooth Muscle Cell Growth Medium (Sigma Aldrich). More details can be found in Section 2.3.

4B.2.9 Cell Seeding and Culture

Scaffolds were soaked in serum free DMEM medium overnight to increase hydrophilicity and help with cell attachment. Cells were seeded at approximately 20,000 cells/cm^2 in 20 µL of culture medium (Smooth Muscle Cell Growth Medium as mentioned in 4B.2.8) and left for 30 mins to allow for attachment. The medium was topped up with another 30 µL of medium and left for a further 90 mins before total medium was topped up to 500 µL. Medium was replaced every 2 days. More details can be found in Section 2.3 and 2.12.

4B.2.10 Cell Viability

The CellTiter-Blue® assay was performed after 1, 5 and 10 days of culture as per the manufacturer's instructions [328]. Measurements were made at Excitation 525 nm and Emission 580-640 nm. More details can be found in Section 2.13.

4B.2.11 DNA Quantification

HUVSMC seeded scaffolds were cultured for 1, 5 and 10 days and tested for total DNA content using a Quant-iT™PicoGreen® assay kit as per the manufacturers' instructions [341]. Fluorescence was read at Excitation 490 nm and Emission 510–570 nm. More details can be found in Section 2.14.

4B.2.12 Cell Imaging

Scaffolds for imaging were fixed in 4%v/v formalin. Scaffolds were permeabilized using 0.2% v/v TritonX-100 in PBS for 5 mins. Scaffolds were stained with 0.1 mL of 0.1 µL 1000X Phalloidin-iFluor™514 conjugate and then stained with 0.1 mL of 300 nM DAPI in PBS for 10 mins. All scaffolds were imaged using a Coherent Anti-Stokes Raman scattering microscope. More details can be found in Section 2.17.

4B.2.13 Reverse Transcription Quantative Polymerase Chain Reaction

RNA was extracted from the scaffolds using standard Tri-Reagent methods and purified using Qiagen's RNeasy spin column system. Real-time polymerase chain reaction was performed using a LightCycler® 480 Instrument II and Sensifast™ SYBR® High-ROX system. Forward and reverse sequences were designed with Sigma-Aldrich and are displayed in Table 17. Relative quantification of RT-PCR results was carried out using the $2^{-\Delta\Delta ct}$ method [350]. Gene expression levels were expressed relative to GAPDH (housekeeping gene) and normalised to the expression of 70% confluent HUVSMCs. More details can be found in Section 2.18.

Table 17: Primer sequences used in RT-PCR amplification

Gene	Primer	Sequence	Sequence Length
Glyceraldehyde 3-phosphate dehydrogenase	GAPDH (forward)	GTCTCCTCTGACTTCAACAG	20
	GAPDH (reverse)	GTTGTCATACCAGGAAATGAG	21
Myocardin	Myocardin (forward)	GGGTCTGAGCATTCCTTGCT	20
	Myocardin (reverse)	CTGGACGTTTCAGTGGTGGT	20
Interleukin 1 alpha	IL1-α (forward)	GCGTTTGAGTCAGCAAAGAAG	21
	IL1-α (reverse)	GCCGTGAGTTTCCCAGAAGA	20

4B.2.14 Statistical Analysis

Data was expressed as mean ± 1 standard deviation, unless stated otherwise. Statistical analysis was preformed using one-way ANOVA with post-hoc Fisher test unless otherwise stated.

4B.3 Results

4B.3.1 Decellularization

To confirm the decellularization process, the DNA content of the decellularized tissue samples was assessed using a Picogreen DNA assay. Both tissues were found to have significant reductions in DNA content after decellularization, with the remnant values being lower than the 50 ng/mg standard [257] (Figure 39A). Furthermore, decellularization efficacy was assessed using H&E staining as seen in Figure 39B. Nuclear content is stained in dark blue and in both the aorta and heart tissues the DNA content appears to be removed after decellularization.

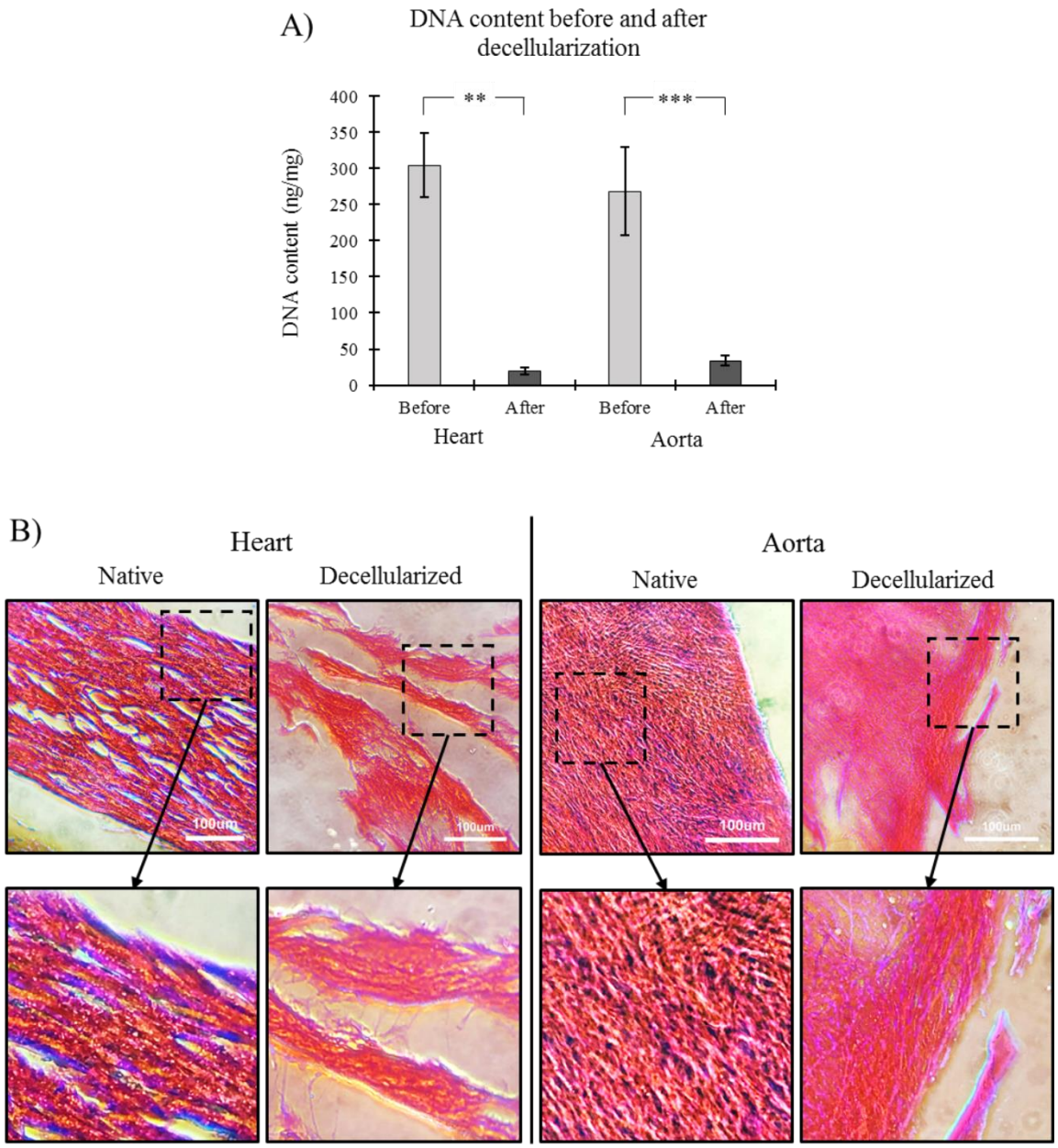

*Figure 39: Decellularization of bovine aorta and heart ECM was successfully achieved using a 0.5% SDS protocol. A) DNA content of the aorta and heart tissue before and after decellularization. B) H & E staining of the aorta and heart tissue before and after decellularization. N=4, error bars = SD. **p < 0.01, ***P < 0.001.*

4B.3.2 Electrospinning

All three scaffolds were successfully electrospun and showed very similar randomly orientated morphologies, as seen in Figure 40. The three scaffolds showed similar fibre orientations and had fibre diameters of 0.77 ± 0.14 µm, 0.69 ± 0.26 µm and 0.73 ± 0.27 µm for the PCL scaffold, aorta ECM scaffold and heart ECM scaffold, respectively. These similarities in the morphology of the

scaffolds ensures that all results noted can be attributed to the inclusion of ECM and not due to differences in morphology.

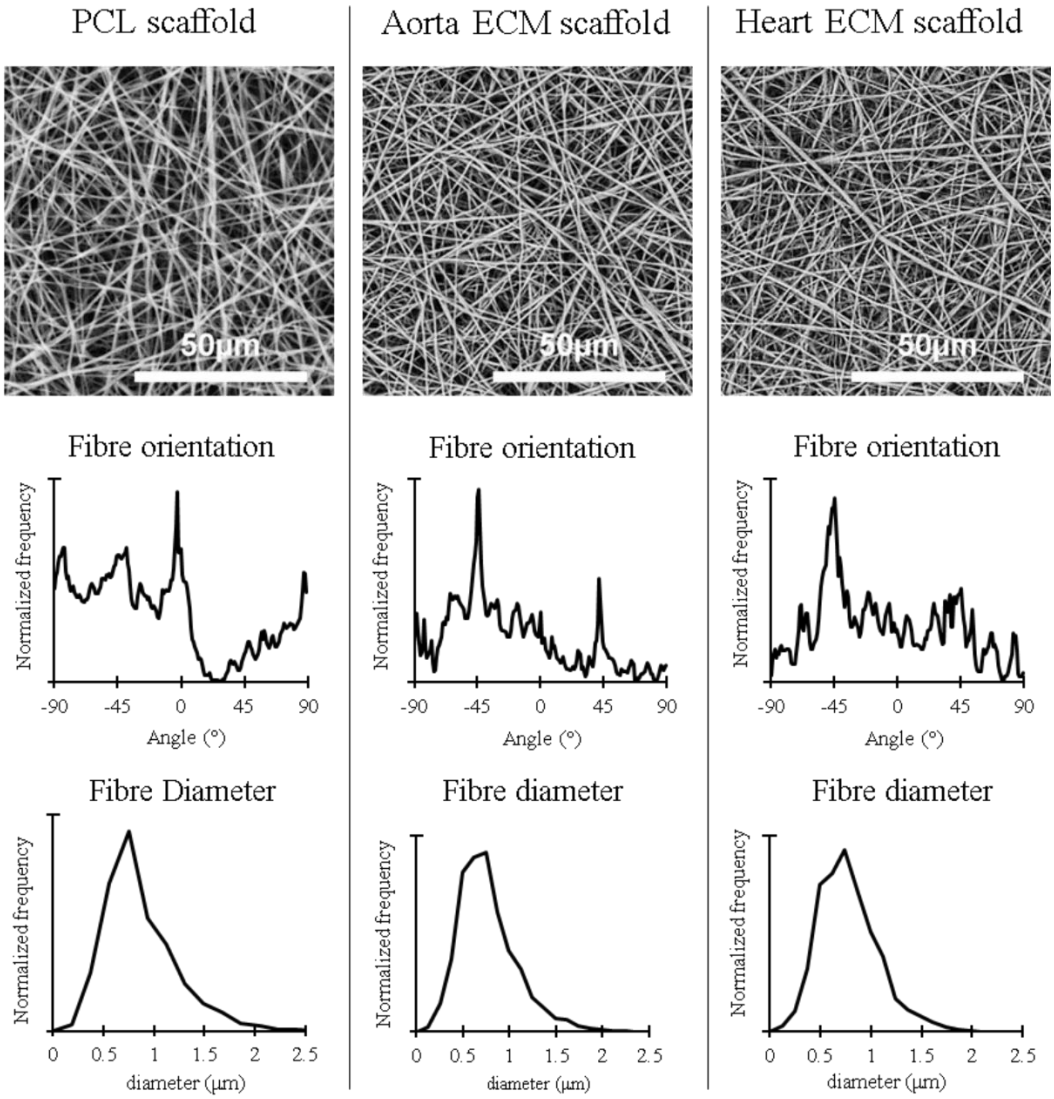

Figure 40: SEM images, fibre orientation and fibre diameter of all three scaffolds manufactured for seeding with HUVSMCs. SEM images show that the scaffold appear to all have uniform fibre morphologies. Fibre orientation shows similar peaks across all three scaffolds.

4B.3.3 Mechanical Characterisation

Mechanical characterisation led to some interesting results. Firstly, the PCL scaffolds were significantly stiffer than the two ECM scaffolds at all strain bands, as seen in Table 18. The ECM scaffolds were both relatively similar and were between 40 to 60% of the stiffnesses noted in the PCL scaffold, depending on the strain band measured. Secondly, the PCL scaffold had a significantly

higher failure strain than both ECM scaffolds: 159% higher than the heart ECM scaffold, and 55% higher than the aorta ECM scaffold. Moreover, the PCL scaffold also had a significantly higher ultimate tensile strength than the two ECM scaffolds: 27% and 34% higher than the heart ECM and aorta ECM scaffolds, respectively.

Table 18: Mechanical properties (Incremental Young's moduli, failure strain and ultimate tensile strength) of the three scaffolds (PCL, heart ECM and aorta ECM). The PCL scaffold had significantly higher values for all measured properties.

		Scaffold type		
		PCL	Heart ECM	Aorta ECM
Young's Modulus at each strain band, MPa	0-1%	3.78 ± 1.75*	1.42 ± 0.59	1.78 ± 0.73
	1-2%	6.49 ± 1.64*	2.57 ± 0.69	2.89 ± 0.75
	2-3%	7.35 ± 0.66*	3.40 ± 0.32	3.27 ± 0.68
	3-4%	7.09 ± 0.63*	3.70 ± 0.19	3.31 ± 0.59
	4-5%	6.31 ± 0.67*	3.55 ± 0.41	3.09 ± 0.44
	0-5%	6.20 ± 0.65*	2.93 ± 0.23	2.87 ± 0.58
Failure strain (%)		357 ± 79*	138 ± 5	231 ± 44
Ultimate tensile strength (MPa)		1.41 ± 0.09*	1.11 ± 0.09	1.05 ± 0.18

*The PCL scaffold showed significantly higher Young's modulus at all strain bands, failure strain and ultimate tensile strength compared to the two blended ECM scaffolds. No significance was noted between the two aorta ECM and heart ECM scaffolds

4B.3.4 Fourier Transform Infrared Spectroscopy

The FTIR results showed that the aorta and heart ECMs were both successfully incorporated into the electrospun PCL scaffold. A range of spectra were taken from PCL and ECM samples alone, alongside the PCL/ECM scaffolds, as seen in Figure 41. The spectra showed that characteristic peaks from the ECM and PCL could be seen in the combined scaffold, showing that the electrospinning process did successfully integrate the ECM into the fibres. Peaks were observed at wavelengths of 1720, 1654 and 1541cm^{-1} for both ECM scaffolds which can be attributed to the carbonyl bond in the PCL and the amide I and amide II bonds in the ECM, respectively [326,409,430].

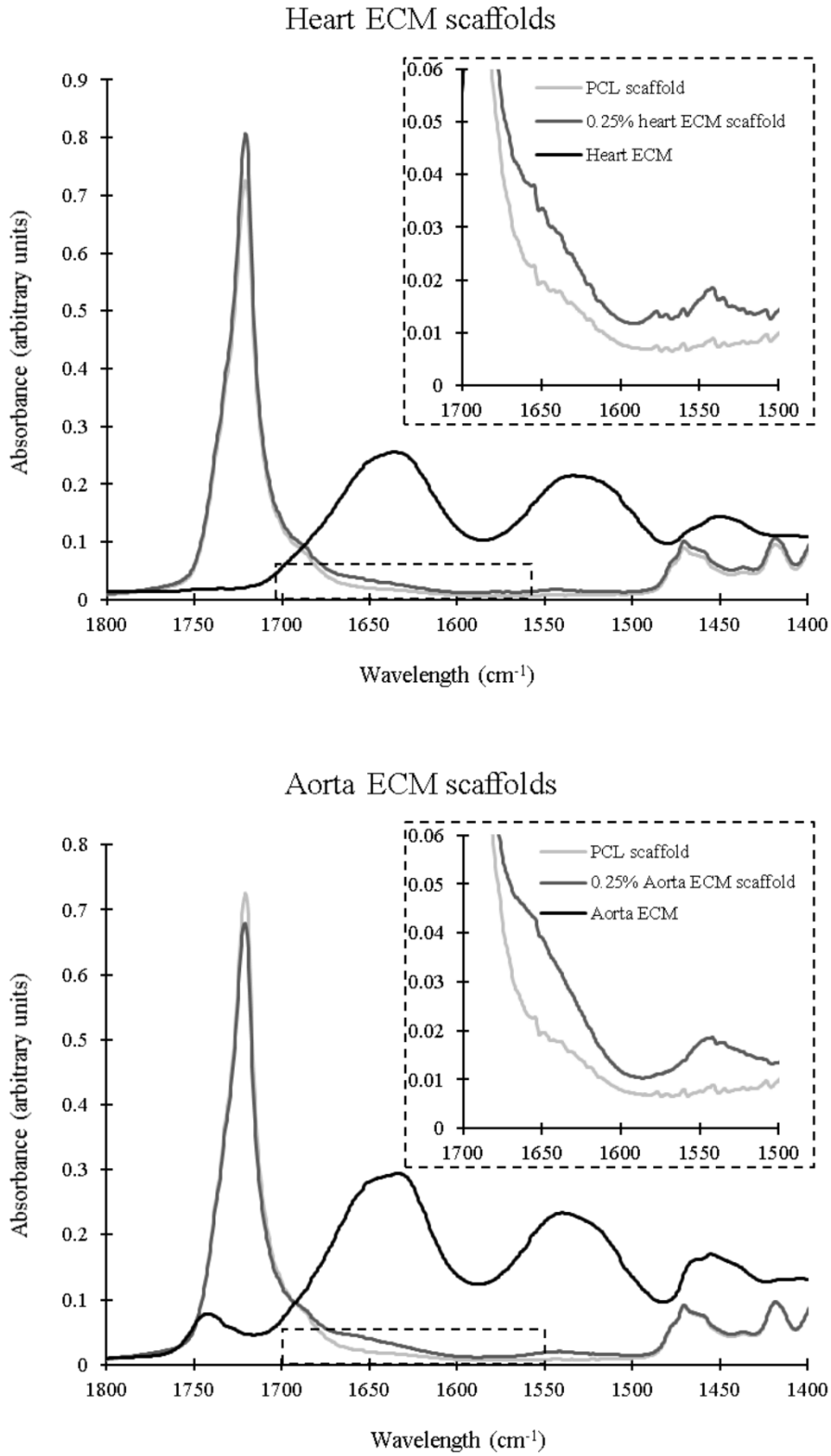

Figure 41: Representative FTIR spectra for the two ECM scaffolds (aorta and heart ECM blended scaffolds) compared to the PCL control and the native decellularized ECM. FTIR spectra of the blended scaffolds show peaks at the Amide I and Amide II bonds which are indicative of ECM proteins.

4B.3.5 Contact Angle Measurement

Contact angle measurements led to some interesting results as seen in Table 19. Firstly, the PCL had a significantly higher contact angle than the two ECM scaffolds after 0.2, 1 and 5 seconds of elapsed time. After 0.2 seconds, the PCL scaffold had a contact angle of 130.7 ± 0.9º, compared to 94.4 ± 39.6º and 93.1 ± 39.6º for the heart ECM and aorta ECM scaffolds, respectively. Interestingly, the PCL scaffold maintained its hydrophobicity over the 5 seconds, with a small reduction in contact angle of 2.59% noted. In contrast the heart ECM scaffold and aorta ECM scaffold had reductions in contact angle of 36.31% and 62.13% over the 5 seconds, respectively. This suggest that the two ECM scaffolds are much more hydrophilic than the PCL scaffold.

Table 19: Contact angle measurements for all three scaffolds

	Scaffold type		
	PCL	Heart ECM	Aorta ECM
Contact angle after 0.2s, °	130.7 ± 0.9*	94.4 ± 39.6	93.1 ± 39.6
Contact angle after 1s, °	131.3 ± 2.3*	85.3 ± 44.4	68.8 ± 33.4
Contact angle after 5s, °	127.3 ± 6.9*	60.1 ± 44.2	35.3 ± 7.4
Percentage drop in contact angle between 0.2s and 1s	- 0.44%	9.72%	26.11%
Percentage drop in contact angle between 0.2s and 5s	2.59%	36.31%	62.13%

*The PCL scaffold showed significantly higher contact angles than both ECM scaffolds after 0.2, 1 and 5 seconds.

4B.3.6 Cell Viability

Cell viability was assessed using a CellTitre-Blue® fluorescence assay. Results are displayed in Figure 42 and show a significant increase in HUVSMC cell viability on the two ECM scaffolds compared to the PCL scaffold after 10 days of culture. Furthermore, the two ECM scaffolds showed significantly higher cell viability after 10 days of culture compared to 1 and 5 days of culture, whereas the PCL only scaffold did not have a significant increase in cell viability over time. Interestingly, while the

PCL only scaffold did not show a significant increase in viability like the two ECM scaffolds, it did maintain cell viability over the 10 days of culture.

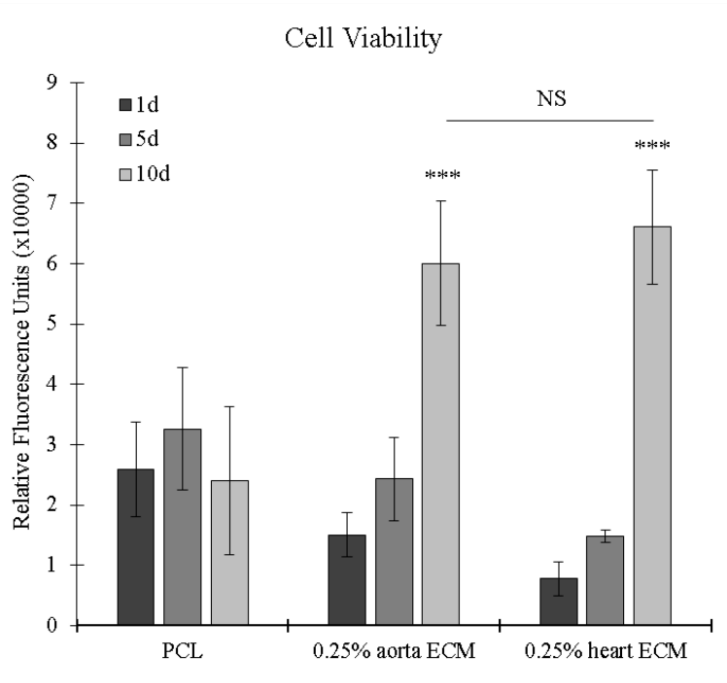

*Figure 42: Cell viability of HUVSMCs cultured on PCL, aorta ECM and heart ECM scaffolds after 1, 5 and 10 days of culture. N=4, error bars = SD. ***p < 0.001.*

4B.3.7 DNA Quantification

DNA quantification per scaffold was assessed using a Quant-iT™PicoGreen® assay kit. Results showed that DNA content per scaffold significantly increased in the aorta ECM and heart ECM scaffolds after 10 days of culture compared to the PCL only scaffold, as seen in Figure 43. Furthermore, the PCL only scaffold appeared to have a higher DNA content after 24 h of culture than the other two scaffolds, however, its DNA content stayed fairly constant over the 10 days of culture, whereas the two ECM scaffolds showed increases in DNA content as culture time increased.

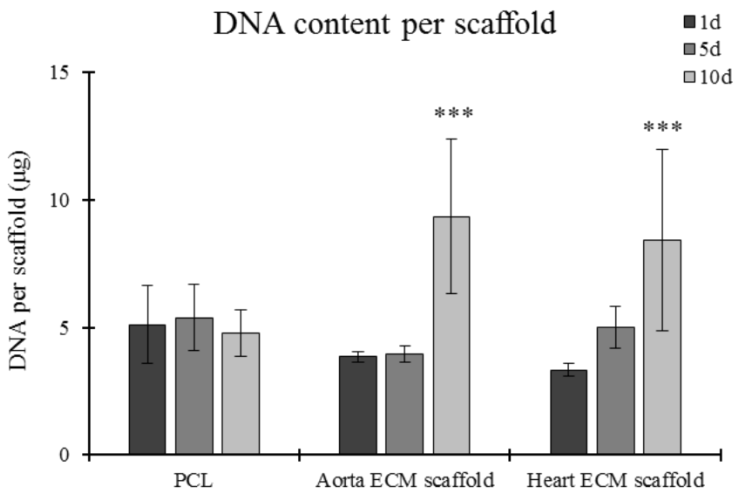

*Figure 43: DNA content of HUVSMCs on all three scaffolds after 1, 5 and 10 days. The HUVSMCs on the two ECM scaffolds showed significantly higher DNA content after 10 days of culture compared to the two other scaffolds. N=4, error bars = SD. ***p < 0.001.*

4B.3.8 Cell Imaging

Representative SEM images show the functional cell layers on scaffolds after 10 days of culture (Figure 44). The PCL only scaffold and aorta ECM scaffold both show cell alignment, which is a phenotypic characteristic of VSMCs. The heart ECM scaffold did not show alignment. Interestingly, the aorta ECM scaffold showed the typical 'hill and valleys' morphology seen with VSMCs when cultured *in vitro*.

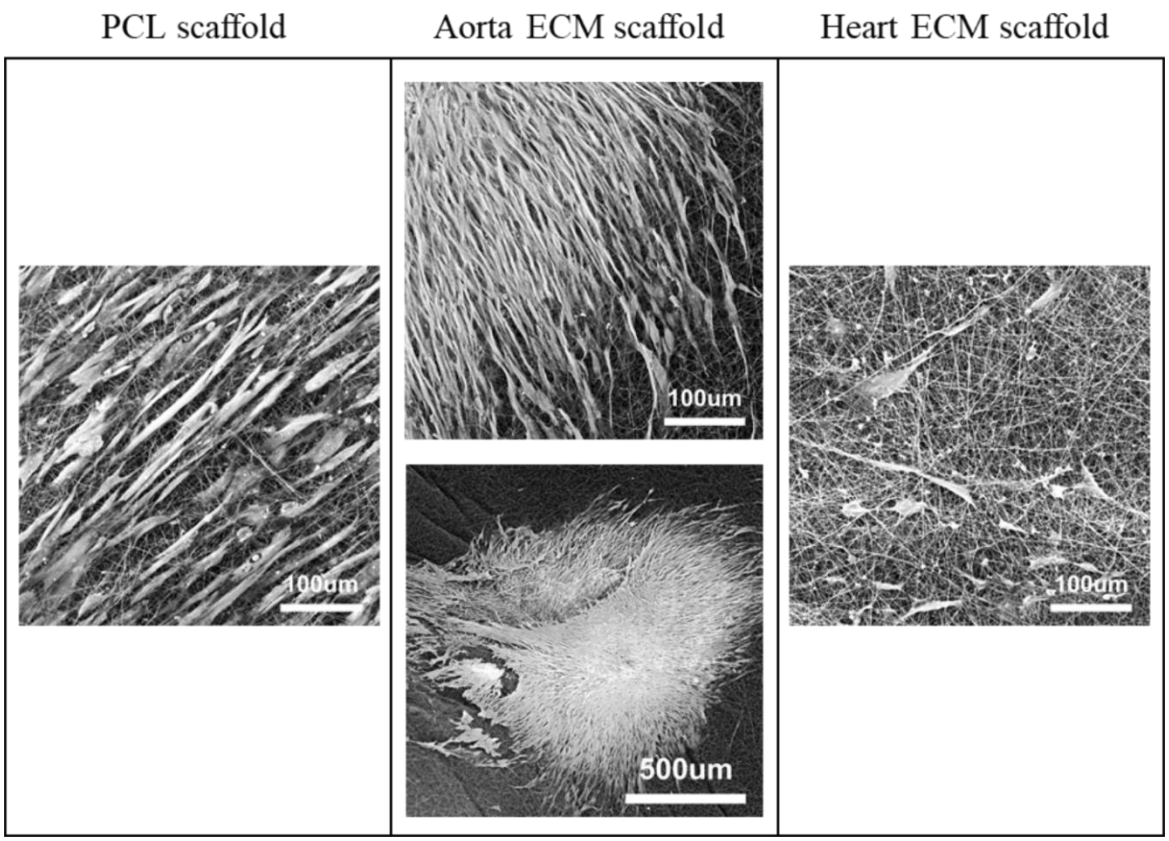

Figure 44: Representative osmium stained SEM images showing seeded HUVSMCs on all thee scaffolds (PCL, aorta ECM and heart ECM) after 10 days of culture.

Representative DAPI (nuclei) and phalloidin (f-actin) stained images taken using CARS show that all three scaffolds were capable of maintaining healthy HUVSMCs (Figure 45). All images show an elongated cell shape, which is a phenotypic characteristic of smooth muscle cells.

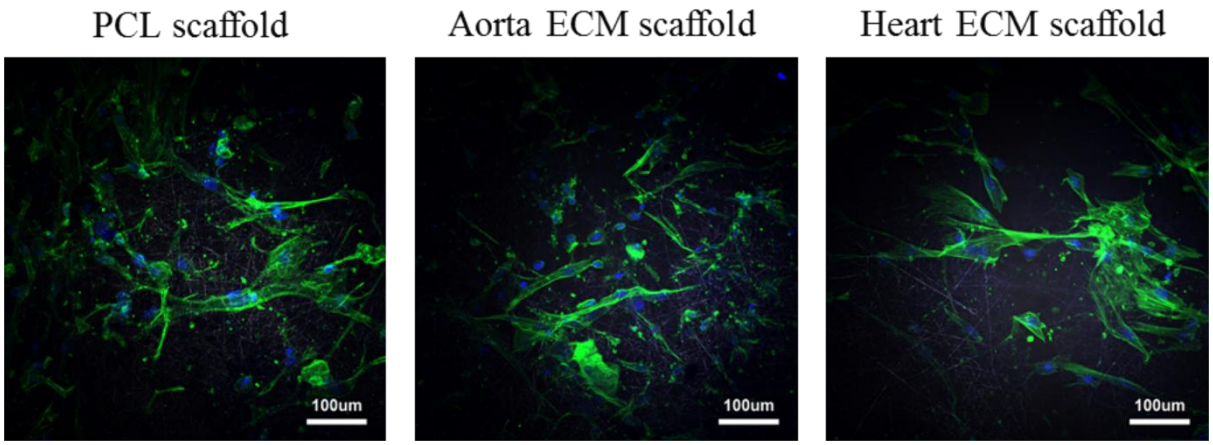

Figure 45: Representative nuclei (blue) and f-actin (green) stained HUVSMCs seeded on all three scaffolds (PCL, aorta ECM and heart ECM) after 10 days of culture.

4B.3.9 Gene Analysis

RT-qPCR analysis of cell seeded scaffolds showed some interesting trends, as seen in Figure 46. Two genes were analysed: myocardin and Interleukin 1 Alpha (IL1-α). Interestingly, myocardin showed no real difference between the three scaffolds at each time point, however, in all cases, the expression of myocardin increased as culture time increased. Myocardin is the key phenotypic gene in smooth muscle cells and is heavily involved in their contractile functionality [378–381].

IL1-α is upregulated during smooth muscle cell proliferation [431]. Interestingly, IL1-α expression increased over time, which falls in line with the cell viability and DNA quantification results, suggesting that the cells were proliferating as culture time increased. No real differences were noted between all three scaffold groups.

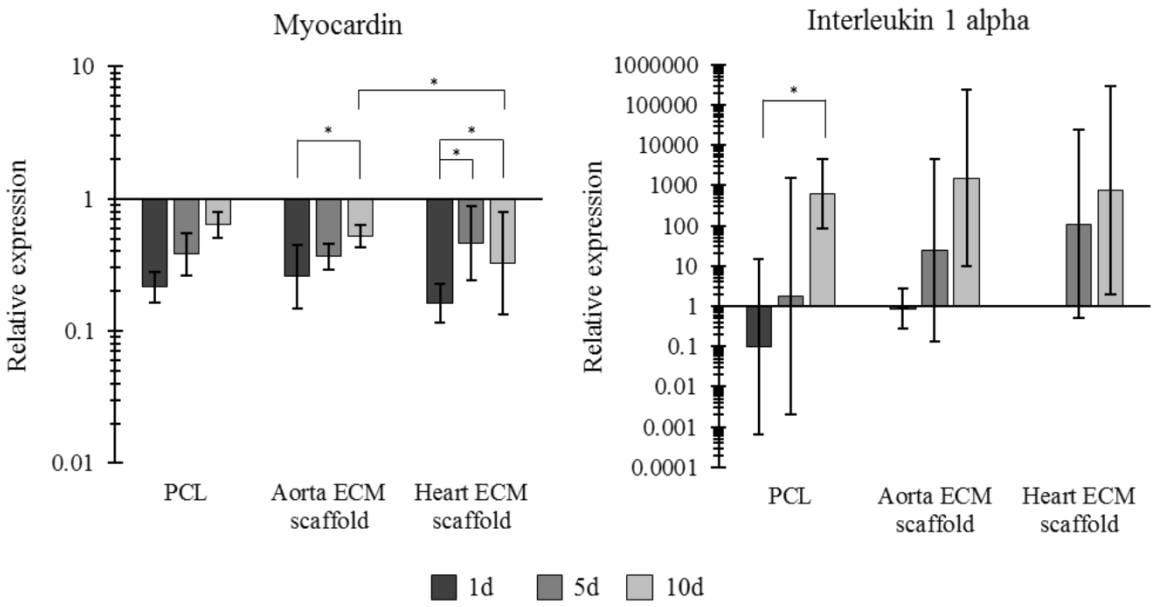

*Figure 46: RT-qPCR results showing Interleukin 1 alpha and myocardin gene expression from HUVSMCs cultured on the three scaffolds (PCL, aorta ECM and heart ECM). N=5, error bars = SD. *p < 0.05.*

4B.4 Discussion

Electrospun polymer scaffolds have been extensively utilised in tissue engineering, with PCL being widely used due to its FDA approval and its versatility with different solvents and scaffold manufacturing techniques [198,209,382]. Three different scaffolds with similar fibre diameters (diameters ranged from 0.69 µm to 0.77 µm) were electrospun, ensuring that all differences noted in the results can be attributed to the scaffold composition and not to the scaffold's morphology. H&E staining and DNA quantification (Figure 39) confirmed that the native tissues had been successfully decellularized to the acceptable standards [257]. Furthermore, FTIR spectra showed that the decellularized ECMs had been successfully incorporated into the electrospun PCL scaffolds. Peaks were noted at the Amide I and Amide II bond wavelengths (1654 and 1541 cm^{-1}) in the two ECMs alone and in the two PCL:ECM scaffolds. These peaks are characteristic peaks ECM proteins and their presence in the two PCL:ECM scaffolds shows that the ECM has been successfully incorporated into the PCL scaffold [432]. Furthermore, a peak was noted at 1720 cm^{-1} in the PCL only scaffold and the two PCL:ECM scaffolds. This peak is associated with the carboxyl group in the PCL [331].

Cell viability and DNA quantification results followed a very similar pattern, which is expected when cell number is directly proportional to cell viability. Both sets of results showed a significant increase in the two ECM scaffolds after 10 days of culture compared to the PCL only scaffold. Likewise, they both showed lower viability and DNA content after 1 day of culture for the ECM scaffolds compared to the PCL, however, large increases were noted after 5 days, whereas the PCL only scaffold showed no increase. These results suggest that either the aorta or heart ECM scaffold make a more suitable scaffold for the culture of SMCs if cell proliferation is the desired result. While over proliferation of SMCs is often associated with tumour formation and atherosclerosis, an initial proliferative response is desirable to promote new tissue formation [433,434].

Mechanical characterisation showed some interesting results. Firstly, the two ECM scaffolds both had stiffnesses approximately half of the PCL only scaffold for all five strain bands. Furthermore, the two ECM scaffolds both had a lower failure strain and a lower ultimate tensile strength than the PCL only scaffold. These results show that the inclusion of ECM did alter the mechanical properties of the scaffold and the way in which the ECM is incorporated into the fibre needs further study to fully assess exactly why the mechanical properties differ between the three scaffolds.

DAPI (nuclei) and phalloidin (f-actin) staining showed that all three scaffolds were able to maintain an SMC phenotype. The cells had an elongated morphology, stretching across several fibres which is a key marker for healthy vascular smooth muscle cells [435]. Furthermore, as seen in Figure 44, after 10 days of culture the cells on the aorta ECM scaffold reorganized themselves into bundles of cells. This is common phenotypic phenomena noted with VSMCs when culture *in vitro*, especially when cultured on 2D surfaces such as tissue culture plastic [389,436].

RT-qPCR results showing the gene expression of two key genes revealed some interesting trends. Firstly, myocardin gene expression was seen to upregulate on all three scaffolds as the culture time was increased. Myocardin is a gene associated with the contractile functionality of SMCs and its upregulation is a marker of a maturing SMC [378–381]. This would suggest that the SMCs matured on all three scaffolds and that the incorporation of ECM had no real impact on this. This result is somewhat expected as proliferating SMCs are gaining maturity. Likewise, the expression of IL1-α was seen to

be very low after 1 day of culture but increased on all three scaffolds as culture time was increased. IL1-α is upregulated in SMCs during cell proliferation, therefore, it would be expected that the two ECM scaffolds saw an upregulation of IL1-α as cell viability and DNA content both confirm that the cells were proliferating [431,437]. However, the upregulation noted on the PCL only scaffold is not expected as both cell viability and DNA content suggest that the cells were not proliferating. This phenomena could be attributed to a high rate of cell death on the PCL only scaffold meaning that while the cells are proliferating, the total number of cells on the scaffold may not be increasing.

4B.5 Conclusions

In conclusion, three unique scaffolds were fabricated with very similar morphologies. Vascular ECMs were successfully incorporated into the electrospun PCL scaffolds and their incorporation was confirmed using FTIR, which showed peaks at wavelengths associated with ECM proteins. VSMCs were successfully seeded onto the scaffolds and cultured for a 10 day period. Cell viability and DNA content results showed that the two ECM scaffolds were more suited for the seeded VSMCs with a final aim of cell proliferation. Furthermore, gene expression analysis showed no real difference between the three scaffolds, suggesting that either of the ECM scaffolds is best suited for accommodating VSMCs due to their superior cell proliferative capabilities.

Part C: Mechanical and Biological Characterisation of Aorta ECM scaffolds

4C.1 Introduction

Combining ECM with polymers to manufacture electrospun bioscaffolds has previously been utilised to harness the repeatable mechanical properties of the polymer with the biochemical and mechanical properties of the ECM [198,199,360,438]. Electrospinning polymers produces a network of fibres that can be heavily tailored depending on the properties desired [217]. They can be designed to have isotropic or anisotropic mechanical properties, along with 3 dimensional architectural properties that favour cell survival and growth [177]. It is possible through electrospinning to include bioactive cues into a repeatable polymer structure and alter its mechanical and physical properties [198,199,323,438]. This has huge implications in tissue engineering where mimicking the physical and biological properties of the native ECM are major research focusses, especially when the final aim is generation of new functional tissue.

Previous studies have shown that incorporating ECM into electrospun polymer scaffolds alters both its mechanical properties and also affects seeded cells. The present study found that the aorta ECM scaffold was best suited to the seeding of HUVECs. Therefore, the present study proposed electrospinning a combination of aortic ECM with PCL at two different ECM concentrations and biomechanically evaluating the resulting fibrous scaffolds.

4C.2 Materials and Methods

4C.2.1 Decellularization

Aorta and heart samples were collected from a 2 year old female cow and decellularized using a previously described method. More details can be found in Section 2.2.

4C.2.2 Electrospinning

Powdered ECM was dissolved at either 0.25% w/v or 1% w/v into HFIP. PCL was then added to the solutions at 8% w/v and dissolved on a roller overnight. PCL only scaffolds were used as controls. Solutions were electrospun using an EC-DIG electrospinning system. Samples were electrospun onto

an aluminium foil covered mandrel using the following criteria: 0.4 mm needle, 0.8 mL/h, 12 cm, +14 kV, -4 kV, 250 RPM and 8 cm distance between mandrel and needle tip. Scaffolds used with cells were sterilized for 10mins using 70% v/v ethanol. These electrospinning solutions lead to final fibre PCL:ECM ratios of 100:0 (PCL only), 96.875:3.125 (0.25% ECM) and 87.5:12.5 (1% ECM). More information can be found in Section 2.1.

4C.2.3 Scanning Electron Microscopy and Fibre Properties

Scaffolds were visualised using a scanning electron microscope. Prior to imaging all scaffolds were sputter coated with an Emscope SC500A splutter coating using gold-palladium at a ratio of 60:40. Cell seeded scaffolds were visualized after 6 days using a previously described osmium based method [346].

Scanning electron images were analysed using ImageJ software (NIH). Briefly, SEM images of the scaffolds were used with fibre diameter being deduced using the DiameterJ plugin and fibre orientation using the OrientationJ plugin [314]. A total of 58 fibres were used to measure fibre diameter and fibre orientation.

More details can be found in Section 2.5 and 2.9.

4C.2.4 Histology

Native and decellularized samples of aorta were fixed in 10% formalin overnight. This was followed by a series of dehydration ranging from 50% to 100% ethanol. Samples were washed in xylene prior to embedding in paraffin wax and were then stored at 4ºC. Samples were trimmed to 5 μm thicknesses and mounted onto slides for Haematoxylin and Eosin (H and E) staining. Samples then cleared with xylene and mounted in DPX. More details can be found in Section 2.4.

4C.2.5 Mechanical Properties

Tensile properties were measured using an Instron 3367 testing machine (Instron) with a 50 N load cell. More details can be found in Section 2.7.

4C.2.6 Contact Angle Measurements

Contact angle was measured on dry scaffolds. A 5 µL droplet of water was placed onto the scaffold and images were captured using a DMK 41AU02 monochrome camera at a frequency of 5 Hz. Analysis of the scaffolds was done on ImageJ using the LBADSA plugin [309]. N=5. More details can be found in Section 2.8.

4C.2.7 Cell Culture and Scaffold Seeding

HUVECs were expanded using MCBD 131 medium supplemented with 5% v/v FBS + 1% v/v L-glutamine + 1% v/v penicillin/streptomycin + 1 mg/L hydrocortisone + 50 mg/L ascorbic acid + 2 µg/L fibroblast growth factor + 10 µg/L epidermal growth factor + 2 µg/L insulin-like growth factor + and 1 µg/L VEGF.

HUVECs were lifted for scaffold seeding at 80% confluence. Scaffolds (10 mm diameter) were punched out of the electrospun sheet, sterilized in 70% ethanol and then placed into 48-well plates and soaked in serum free MCDB 131 medium overnight. Wetting medium was removed and scaffolds were then seeded at a density of 350,000 cells/cm^2. Briefly, cells were drip seeded in 30 µL of medium onto the middle of the scaffold. After 30 mins a further 20 µL of medium was added to stop the cells from drying out. After a further 30 mins, medium in each well was topped up to 500 µL. More details can be found in Section 2.3 and 2.12.

4C.2.8 Cell Viability

The assay was performed at 3 days and 6 days as per manufacturer's instructions. Briefly, measurements were taken at ex: 525 nm and em: 580-640 nm. For each condition group, n=4. More details can be found in Section 2.13.

4C.2.9 DNA Quantification

Native and decellularized samples were tested for total DNA content using a Quant-iTTMPicoGreen® assay kit as per the manufacturers' instructions, n=4. More details can be found in Section 2.14.

4C.2.10 Fourier Transform Infrared Spectroscopy

FTIR was used to confirm the successful inclusion of ECM into the PCL fibres. FTIR spectra were recorded in the wave range of 400-4000 cm^{-1} at a resolution of 1 cm^{-1}. N=5. More details can be found in Section 2.11.

4C.2.11 Statistical Analysis

Data was expressed as mean ± 1 standard deviation. Statistical analysis was performed using one-way ANOVA with post-hoc Fisher test.

4C.3 Results

4C.3.1 Decellularization

Bovine aorta was successfully decellularized using a 0.5% w/v SDS perfusion protocol. Relative DNA was measured using a Quant-iT™PicoGreen assay kit and showed a 96.5% drop in DNA content after decellularization, as seen in Figure 47. Furthermore, H and E staining showed that the nuclear content of the aorta had been successfully removed from the tissue, as seen in Figure 47.

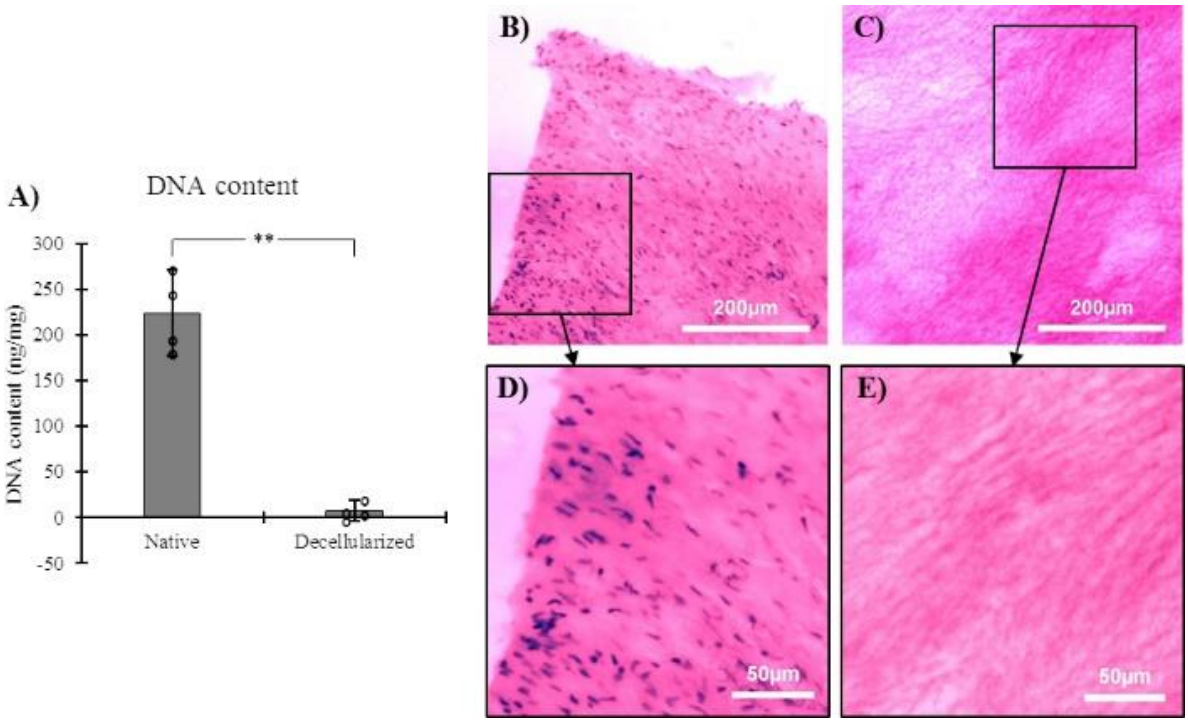

Figure 47: Bovine aorta was successfully decellularized using a 0.5% SDS protocol. (A) DNA content results showing a 96.5% decrease in DNA content. H and E staining of (B) and (D) native aortic tissue and (C) and (E) decellularized aortic tissue.

4C.3.2 Scaffold Properties

All three scaffolds were successfully electrospun using the same parameters, as seen in Figure 48. All three scaffolds were manufactured with very similar fibre morphologies. Fibre diameters ranging from 0.90 ± 0.19 µm to 0.97 ± 0.19 µm were noted across the three scaffolds, meaning that any differences noted between the three scaffolds can be attributed to the inclusion of ECM into the fibres and not due to differing fibre morphologies. Similarly, all three scaffolds had very similar fibre orientations with peaks noted at 45°.

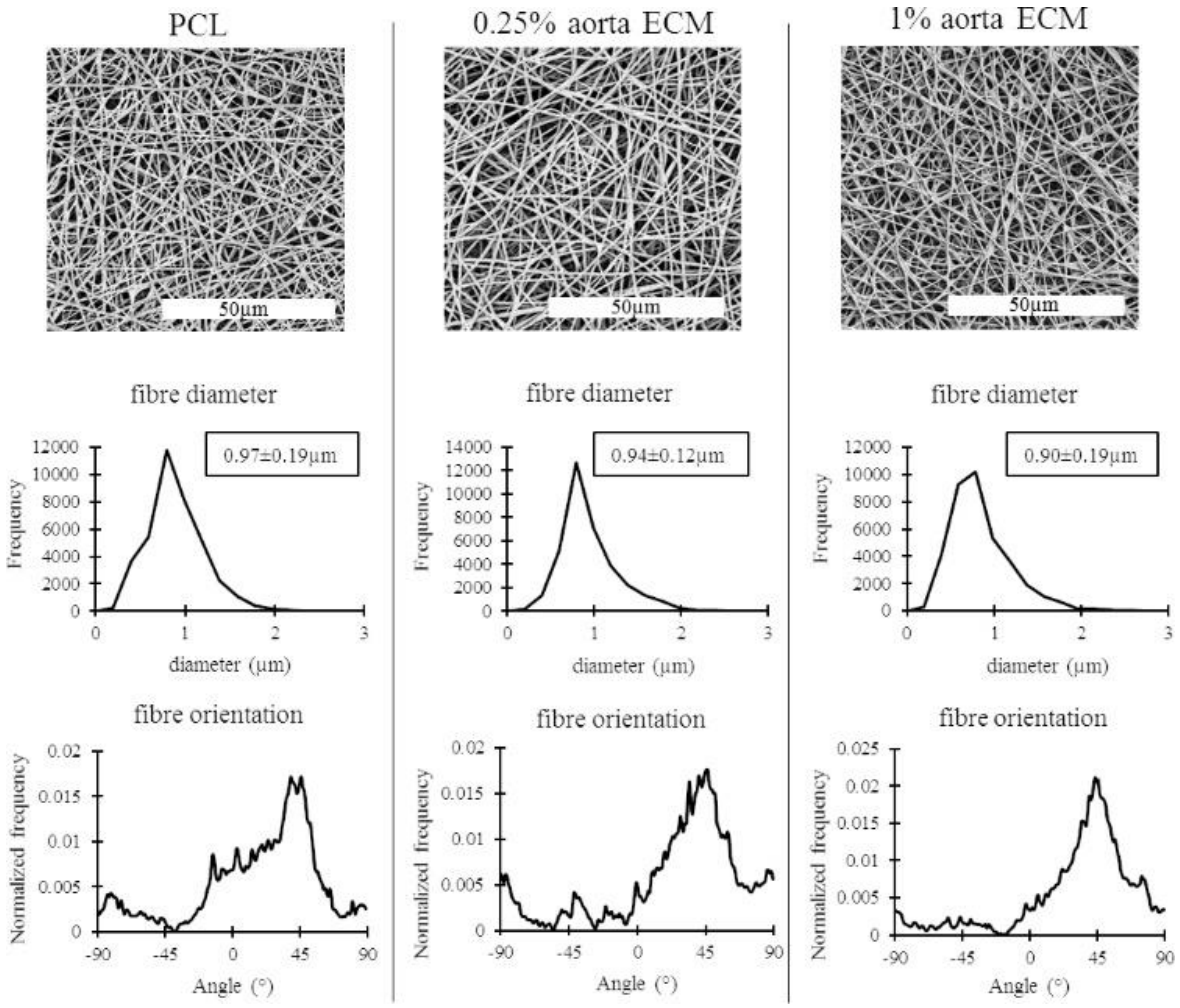

Figure 48: Assessment of scaffold morphology. SEM images of all three electrospun scaffolds (PCL, 0.25% aorta ECM and 1% aorta ECM) showing similar morphological properties, including fibre diameter and fibre orientation.

4C.3.3 Fourier Transform Infrared Spectroscopy

FTIR results showed that the aortic ECM was successfully incorporated into the electrospun fibres. Spectra were taken for the PCL fibres alone, the ECM alone and both ECM/PCL scaffolds. Characteristic peaks from the PCL and ECM could be seen in both ECM/PCL scaffolds, with larger peaks noted in the 1% ECM scaffold compared to the 0.25% ECM scaffold, suggesting that more ECM had been incorporated into the scaffold, as expected. Peaks can be seen at wavelength bands of 1705-1715, 1650-1660 and 1535-1545 cm^{-1} (Figure 49), which can be attributed to the carboxyl group in the PCL, and the amide I and amide II groups in the ECM, respectively [331,432].

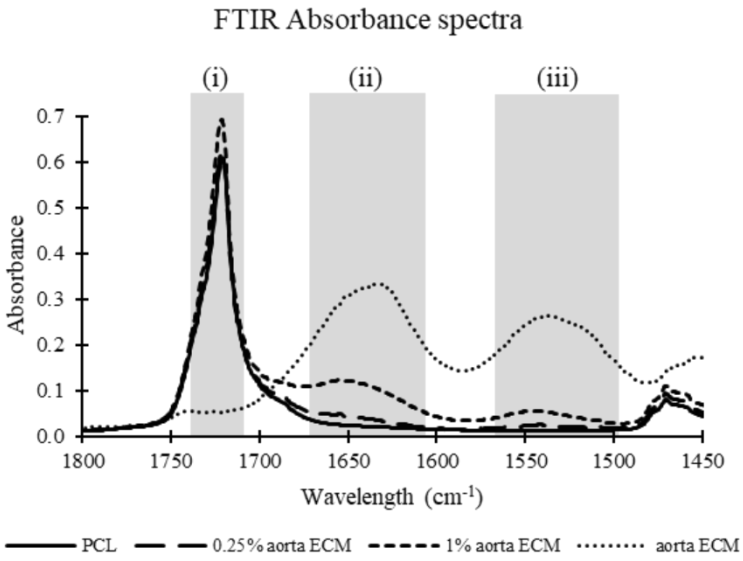

Figure 49: Representative FTIR spectra of the PCL scaffold; 0.25% aorta ECM scaffold; and 1% aorta ECM scaffold showing peaks at the i) carboxyl group, ii) amide I group and iii) amide II group.

4C.3.4 Mechanical Properties

Tensile testing was performed using an Instron tensile tester and showed significant differences in each scaffold's properties. All scaffolds were stretched until failure. The PCL scaffold showed the highest Young's modulus in the 0–5% strain range at 19.2 ± 1.7 MPa, decreasing to 16.1 ± 1.9 MPa for the 0.25% aorta ECM scaffold and then decreasing again to 13.5 ± 0.7 MPa for 1% aorta ECM scaffold. The Young's modulus dropped in each subsequent strain band with the trend of the higher ECM concentration showing lower Young's modulus reversing after 15% strain, as seen in the stress

strain curve in Figure 50. At approximately 20% strain the PCL only scaffold becomes very plastic, with the 1% aorta ECM scaffold remaining somewhat elastic and the 0.25% ECM scaffold being in between the two. This phenomena suggests that the incorporation of ECM is directly linked to the increase in scaffold elasticity into the higher strain range.

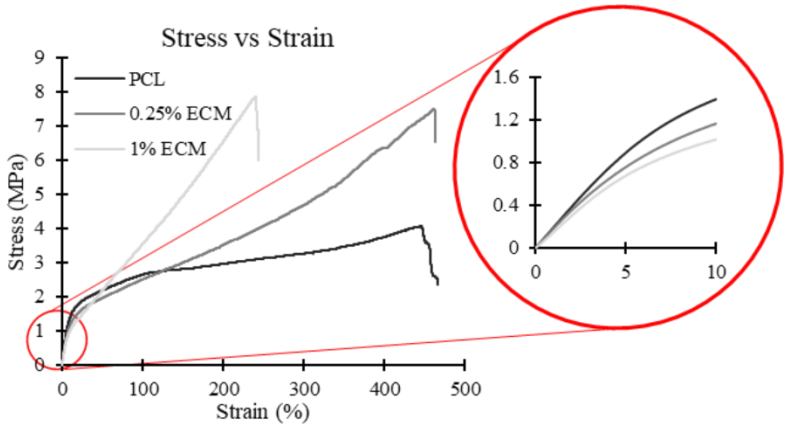

Figure 50: Representative stress vs strain curve for the three scaffolds (PCL, 0.25% aorta ECM and 1% aorta ECM).

It was also noted during tensile testing that the higher ECM concentrations lead to lower failure strains. The 1% aorta ECM and 0.25% aorta ECM scaffolds had failure strains 47% ($p > 0.001$) and 2.6% (no significance) lower than the PCL only scaffold, respectively (Table 20). Likewise, the ultimate tensile strength of the scaffolds increased by 84.3% ($p > 0.001$) and 77.9% ($p > 0.001$) for 1% aorta ECM and 0.25% aorta ECM compared to the PCL only scaffold, respectively (Table 20).

Values for compliance were calculated based on eq. (2). Compliance was seen to increase with ECM concentration: the 0.25% ECM and 1% ECM scaffolds had compliance values 19% ($p > 0.05$) and 42% ($p > 0.01$) larger than the PCL-only scaffold (Table 20).

Table 20: Mechanical properties and contact angles of all three scaffolds (PCL, 0.25% aorta ECM and 1% aorta ECM).

	PCL	0.25% ECM	1% ECM
Ultimate tensile strength (MPa)	4.26 ± 0.33[$]	7.58 ± 1.59	7.85 ± 1.03

Failure strain (%)	464 ± 40	452 ± 59	244 ± 29$
Compliance (mL/mmHg)	0.049 ± 0.004$	0.059 ± 0.006	0.070 ± 0.004
Contact angle after 0.2s (º)	114.4 ± 8.9	89.5 ± 37.7	75.4 ± 25.6
Contact angle after 5s (º)	98.7 ± 25.2&	68.8 ± 43.6	22.2 ± 10.5&

* Results with matching symbols (&) are significantly different to each other ($p<0.05$). Results with the $ symbol are significantly different to the two other scaffolds ($p<0.05$).

4C.3.5 Contact Angle Measurements

Contact angle measurements showed some interesting results on the effects of incorporating ECM into the electrospun scaffolds. It was noted that incorporating ECM increased the hydrophilicity of the scaffold, as seen in Table 20. Contact angle measurements after 0.2 s showed decreases in contact angles of 31.1% and 21.8% in the 1% aorta ECM and 0.25% aorta ECM scaffolds compared to the PCL only scaffold, respectively. The same trend was noted after 5 s which showed that incorporating ECM decreased the contact angle by 77.5% and 30.3% in the 1% aorta ECM scaffold and the 0.25% aorta ECM scaffold compared to the PCL only scaffold, respectively.

4C.3.6 Cell Viability

Cell viability showed no significant difference between the three scaffolds and showed no change in viability between 3 and 6 days of culture, as seen in Figure 51.

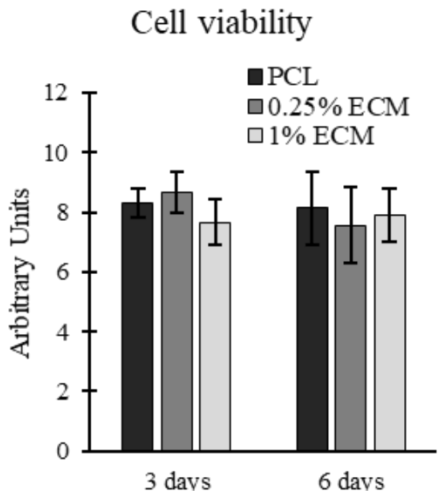

Figure 51: Cell viability of HUVECs seeded on the three scaffolds (PCL, 0.25% aorta ECM and 1% aorta ECM) after 3 and 6 days of culture. N=4, error bars = SD.

4C.3.7 Scanning Electron Microscopy

SEM images of HUVECs after 6 days of culture on all three scaffolds show confluencies ranging from 68 to 81% and appear to show cells with very similar morphologies, as seen in Figure 52. These results validate the cell viability results, suggesting that all three scaffolds were capable of accommodating a healthy monolayer of HUVECs.

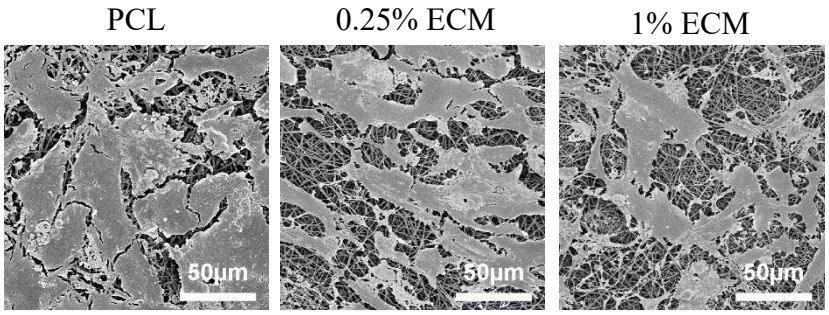

Figure 52: SEM images showing a healthy monolayer of HUVECs on all three scaffolds (PCL, 0.25% aorta ECM and 1% aorta ECM).

4C.4 Discussion

The present study used PCL, a commonly used polymer for tissue engineering application, especially in electrospinning [177,198]. Three similar scaffolds were electrospun using the same parameters, demonstrating the repeatable properties that electrospinning PCL possesses. Furthermore, the inclusion of ECM had very little effect on how the solution spun, with fibre diameter being similar for all three scaffolds (0.90, 0.94 and 0.97 µm). Having three very similar scaffold morphologies ensured that the only difference noted between scaffolds was the PCL:ECM ratio (100:0, ~ 97:3 and ~ 88:12). This meant results noted between the different scaffolds could be attributed to the PCL:ECM ratio.

The DNA quantification and H&E staining (Figure 47) confirmed that the native aortic tissue had been successfully decellularized. FTIR analysis was used to ensure that the decellularized ECM had been successfully incorporated into the electrospun fibres (Figure 49). These results showed peaks in the decellularized ECM and in the two PCL:ECM scaffolds at the Amide I and Amide II bonds which are two characteristic peaks of ECM proteins [326,432]. Interestingly, as ECM concentration increased,

the size of the peak at these two Amide bonds also increased, suggesting that increasing ECM concentration led to more ECM being incorporated into the PCL fibres. All three scaffolds showed peaks at the Carboxyl group which can be attributed to the PCL [409]. FTIR is a surface characterization method that has been shown to measure to depths of up to 5 μm [439] – the fibres in this study are all under 1μm thick, suggesting that a full characteristic profile of the fibre is being achieved through FTIR.

Tensile testing exposed some interesting results that demonstrate the effect of including ECM into the electrospun fibres. The 1% ECM scaffold had a lower stiffness than the PCL only scaffold. This can be explained by aortic arch ECM (the ECM used in this study) comprising of approximately 40% elastin and 20% collagen [20]. Elastin has been shown to have a half-life of around 74 years. As people age, the quantity of elastin in their aortas decreases, which leads to a very large increase in aortic stiffness – a 394% increase in stiffness was noted between the ages of 25 and 70 [16,440]. This suggests that a lower quantity of elastin in the scaffold would lead to a higher stiffness and lower compliance. Furthermore, including aortic ECM resulted in a drastic reduction in failure strain, as seen in Table 20. This can be explained by collagen having a failure strain of 13% and elastin between 100 and 150% [441], compared to the PCL only scaffold having a failure strain of 464% (our results). Hence, a fibre made up of a ~ 88:12 PCL to ECM ratio (1% ECM) would be expected to fail at a lower strain than the fibre with a 100:0 PCL to ECM ratio (PCL only).

Cellular testing and visualization showed that the HUVECs reacted similarly to all three scaffolds. Cell viability (Figure 5D) showed no significant differences between the three scaffolds over both timepoints suggesting that including ECM had no impact on their proliferation. Similarly, SEM images (Figure 5E) show that the HUVECs had similar morphologies on all three scaffolds. Further work looking into gene analysis is required to gain a full bioactivity profile for these scaffolds.

Studies have shown that altering the contact angle of a scaffold can have effects on cell adhesion [198,296]. Furthermore, the addition of ECM to an electrospun polymer scaffold has been shown to reduce water contact angle [198]. This result was noted in this study, with a 31.1% and 77.5% lower contact angle in the 1% ECM scaffold compared to the PCL only scaffold for the 0.2 s measurement and 5 s

measurement, respectively. After 0.2 s the PCL only scaffolds had a contact angle of 114.4° (hydrophobic [296]), compared to 75.4° for the 1% ECM scaffold. While a relatively hydrophilic contact angle of approximately 60° has been shown to lead to higher cell adhesion [296], this could also have problematic effects and lead to the binding of unwanted cells, proteins and growth factors found in the passing blood. It has been shown that blood-contacting devices and tissue engineering substrates require an appropriate balance of hydrophilic and hydrophobic entities to ensure local cells can adhere and grow, without causing unwanted binding of substances found in the blood [304]. Therefore, with the final goal for vascular tissue engineering strategies often being *in vivo* implantation, it is very important to consider the fact that the scaffold will be in contact with a variety of constituents that you may not want binding to the scaffold. Hence, in certain situations, higher hydrophobicity may be desirable to reduce the binding of unwanted substances. This applies for approaches such as bypass grafting where local cell attachment to the implant is unwanted. Therefore, being able to control the hydrophobicity of the scaffold/implant is desirable.

4C.5 Conclusions

In conclusion, aortic ECM was successfully combined at two different concentrations with PCL and electrospun to form random orientated nanofiber scaffolds. Increasing the ECM concentration reduced stiffness and increased compliance at lower strains, and increased the elasticity of the nanofibers beyond its yield strength. Furthermore, increasing the ECM concentration reduced the failure strain and increased the ultimate tensile strength of the scaffold, whilst reducing the water droplet contact angle. These results have shown that including decellularized ECMs into a scaffold is a viable method for altering the mechanical properties of the scaffold, whilst maintaining cellular performance.

Chapter 5: Scaffold Biofunctionalization using Cell Secretome

Introduction

There are a range of different strategies used in the treatment of vascular disease, including the use of PCL based scaffolds in tissue engineering, with work looking at incorporating ECMs/proteins and altering surfaces to increase the biofunctional potential of the scaffold [198,199,320,322]. Likewise, work has looked at how polymer scaffolds can have their surfaces activated to increase their binding potential for proteins. *Guler, et al.* looked at how plasma coating combined with 1-ethyl-3-(dimethyl-aminopropyl) carbodiimide hydrochloride (EDC)/N-hydroxyl succinimide (NHS) treatment could increase the quantity of albumin protein binding to the surface of the scaffold [331]. This work opens up the potential for binding cell secreted proteins onto the surfaces of these scaffolds.

Feeder layer systems have long been used in cell culture to help with the growth and proliferation of a desired cell line [442]. In short, they work by growing two different cell types next to each other: (i) a feeder cell line, and (ii) the target cell line. The feeder cell line is there to secrete growth factors and proteins into the medium to feed the target cell line and help with proliferation [442]. Furthermore, feeder layer systems often allow for serum free cell culture, which is desirable due to the scientific and ethical concerns surrounding the use of serums [111,443–445]. The principle of the feeder layer system is direct paracrinal cell interactions between the two different cell lines. However, the feeder cell line could be used separately to create conditioned medium that can then be used at a later date to help with the culture of a different cell line.

Herein, the present study proposes combining the theory behind feeder layer systems and scaffold surface activation methods to bind cell secretome to the surface of PCL scaffolds in an attempt to increase their biofunctionality and improve their potential as scaffolds for cell seeding. The cell secretome from two different cell types (HUVECs and HUVSMCs) were studied to see how they alter the performance of seeded cells.

Part A: Cell Secretome Study - Feasibility and Optimization

5A.1 Introduction

Various studies were underaken to assess the feasibility of binding secreted proteins onto a scaffolds surface and to optimize the protocol. Firstly, looking into how cells grew when cultured in medium containing cell secretome showed the potential benefits of using cell secretome conditioned medium. Carrying this knowledge forward, the aim was to try and bind proteins onto a PCL based scaffold to try and improve the scaffold's biological potential for seeded cells. The preliminary protein binding experiments used bovine serum albumin (BSA) dissolved in MES buffer as this is a fairly standard protein which can be accurately measured when using the BCA assay, allowing for the calculation of bound protein. The basis of these optimization studies are based off a study by *Guler, et al*. which showed how EDC/NHS chemistry could be used to improve a PCL scaffold's binding potential for BSA. Briefly, the EDC/NHS method works by the EDC activating the carboxyl groups on the polymer for reaction with the primary amines. This creates an unstable intermediate that can react with another amine. The NHS is then added to stabilize this intermediate by converting the unstable amine-reactive O-acylurea into a stable amine-reactive NHS ester.

5A.2 Culturing Endothelial Cells with Conditioned Medium

Firstly, an experiment was set up to see how seeded HUVECs responded to the different cell culture medium conditions. The aim of this was to see if cell secretome conditioned medium had an influence on cell growth. Briefly, three different mediums were collected: (1) a cell secretome conditioned serum free medium; (2) a serum free medium and (3) a serum containing medium. All three mediums used MCDB 131 as a base supplemented with 1% v/v L-glutamine; 1% v/v penicillin/streptomycin; 1 mg/L hydrocortisone; 50 mg/L ascorbic acid; 2 μg/L fibroblast growth factor ; 10 μg/L epidermal growth factor; 2 μg/L insulin-like growth factor; and 1 μg/L vascular endothelial growth factor. The following protocols were used to make each medium:

1) HUVECs were cultured in a T75 flask until 80% confluence using serum containing MCDB 131 with all the aforementioned supplements. The medium was then changed to 50% serum free medium, 50% serum containing medium for 24 h to help slowly bring the cells off of

serum. The medium was then changed to the base serum free medium mentioned above and cultured for 24 h allowing for the HUVECs to turnover and secrete various proteins and cytokines into the serum free medium. The medium was then lifted off and stored for subsequent cell feedings. This medium is referred to as conditioned serum free medium.

2) The aforementioned supplemented base medium with no serum added. This medium is referred to as non-conditioned serum free medium.
3) The aforementioned supplemented base medium with 5% FBS added. This medium is referred to as non-conditioned serum medium.

Once the mediums had been collected, HUVECs were seeded into 48-well plates and cultured with one of the three medium types for 40 h. Cell Titer Blue measurements were taken at 16 h and 40 h to see how the cells were growing under the three different medium types. While both serum free mediums showed significantly lower cell viability after 40 h of culture than the serum supplemented medium, the cell secretome conditioned serum free medium did show a significantly higher cell viability than non-conditioned serum free medium (Figure 53). This suggests that the cells are secreting proteins and cytokines into the medium that are beneficial for cell growth.

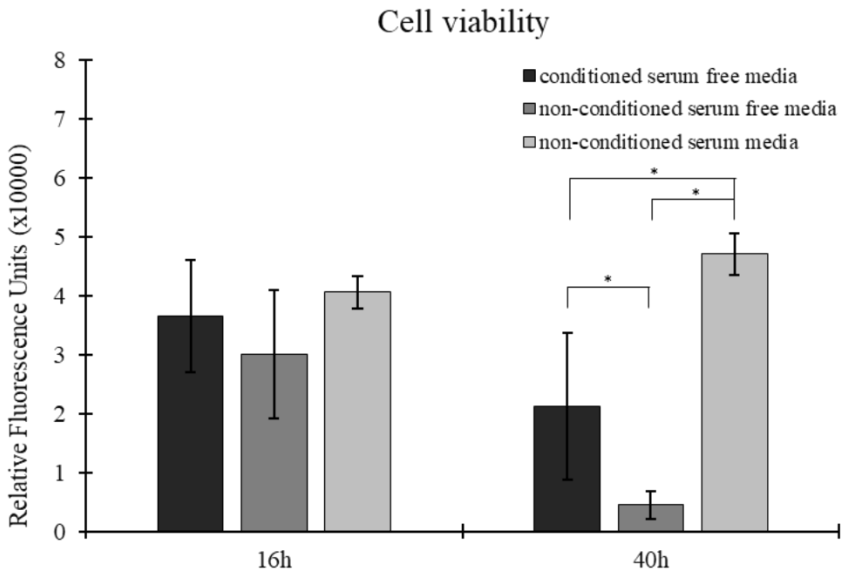

*Figure 53: Cell viability of HUVECs grown on tissue culture plastic with three different medias: conditioned serum free medium, serum free medium and serum containing medium. N=5, error bars = SD. *p < 0.05.*

5A.3 Scaffold Functionalization to Increase Protein Binding

The next step was to see how much protein could be bound/absorbed onto the surface of a scaffold. The previous experiment showed that cell secretome conditioned medium contained proteins that were beneficial for cell survival. This experiment was ran with a known concentration of BSA and an electrospun PCL scaffold. The aim of the experiment was to see which scaffold functionalization method lead to the most protein attachment.

Briefly, electrospun scaffolds were subjected to two different variables. Firstly, half of the scaffolds were oxygen plasma coated to improve hydrophilicity. Secondly, the scaffolds were subjected to five different concentrations of EDC and NHS in MES buffer [331]. Briefly, plasma coated scaffolds were subjected to 60 s of oxygen plasma at 10.2 W. The EDC and NHS concentrations were based off of literature [331]. Concentrations of 0/0, 0.5/0.5, 5/5, 50/50 and 200/200 mM of EDC/NHS in 0.5 M MES buffer (pH 5.7) were used to incubate the scaffolds and activate the surface as a means of aiding with protein binding. Scaffolds were incubated in this solution for 45 mins, washed thrice in PBS and then incubated in the protein solution for 4 h to allow for protein binding, whilst being agitate on a plate mixer.

A BCA protein assay was used to calculate the amount of protein bound to the scaffolds surface. The total protein content of the incubating BSA solution was calculated before and after incubation to deduce the total mass of protein binding to the PCL scaffold during the incubation period. In all instances, a higher amount of bound protein was detected on the plasma coated scaffolds compared to the non-plasma coated scaffolds, averaging approximately 25% more protein binding, as seen in Figure 54. With regards to EDC and NHS concentrations, the 5mM solution lead to increased protein binding, both with and without plasma treatment compared to the other concentrations of EDC and NHS. Therefore, moving forward, the 5mM EDC and NHS solution were used to activate the surface of PCL scaffolds.

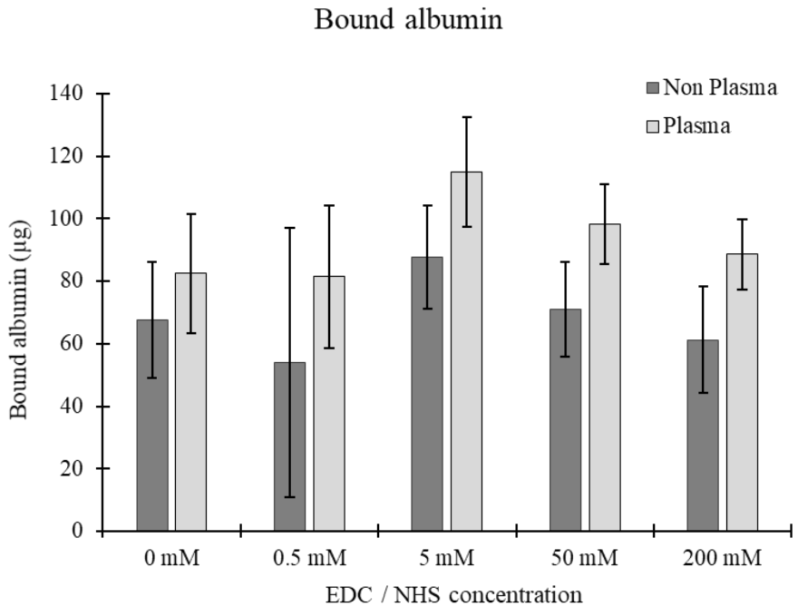

Figure 54: Total mass of bound bovine serum albumin when using four different concentrations of EDC/NHS treatment. N=5, error bars = SD.

5A.4 Addition of ECM to Improve Binding of Protein

The next experiment looked at whether further biofunctionalizing the scaffolds through the incorporation of native ECMs into the fibres would have effects on the quantity of bound protein. Native aortic bovine ECM was decellularized (Section 2.2) and electrospun (Section 2.1) with PCL creating an 88:12 PCL:ECM ratio electrospun fibre like the scaffold created in Chapter 4C. PCL only scaffolds were used as controls. The scaffolds underwent plasma treatment (Section 2.6) followed by 45 mins of incubation in a 5/5 mM NHS/EDC in MES buffer to activate the surface. The scaffolds were then incubated for 4 h in either non-conditioned serum free medium or conditioned serum free medium (serum free medium collected after culturing HUVECs for 24h), as seen in Figure 55.

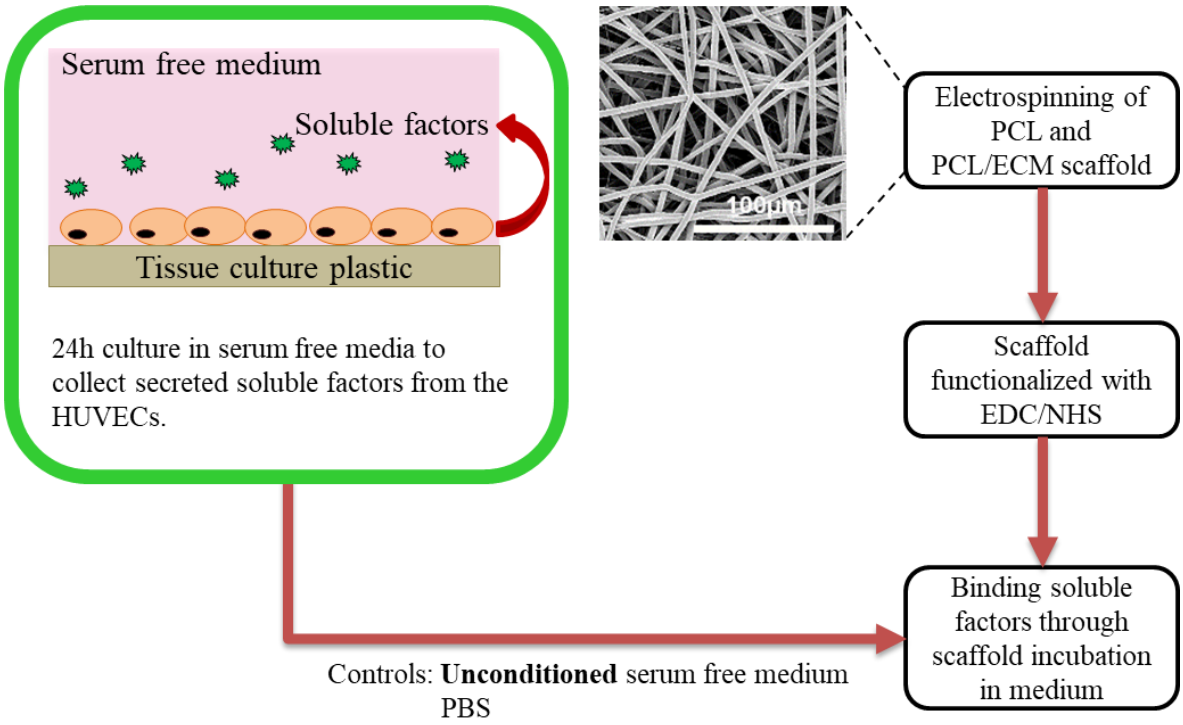

Figure 55: Schematic representation of the scaffold conditioning process. Scaffolds are electrospun and functionalized using EDC/NHS chemistry. The scaffolds are then incubated in conditioned medium.

A BCA assay was then used to deduce the amount of bound protein from the two mediums on either the PCL only scaffold or the ECM:PCL blended scaffold. Results showed that the PCL only scaffold lead to approximately 2.5 times more protein binding to the surface of the scaffold compared to the blended ECM:PCL scaffold, as seen in Figure 56. Therefore, going forward, the PCL only scaffold was used to increase the binding potential of the scaffold.

5A.5 Discussion and Conclusions

EDC and NHS treatments are commonly used to increase the quantity of free amide and carboxyl groups found on the surface of polymers. While the pH of the solution can be altered to increase the polymer's affinity for certain bond types, the exact formulation of the secretome conditioned medium was not known, therefore a standard protocol and pH level (pH of 5.7) for all protein types was used. A pH of 5.7 was chosen as pH levels lower than this lead to very short active half-life's, reducing the overall effectiveness of the procedure, and pH levels above this reduce the total activation of carboxyl groups [339]. Furthermore, pH's lower than 5.7 can also lead to protein denaturing.

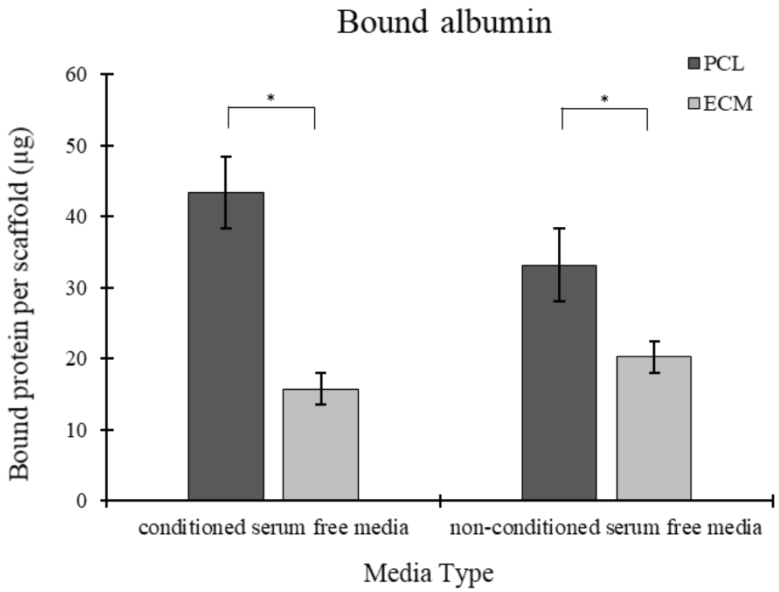

*Figure 56: Total mass of bound HUVEC secreted protein when using a PCL only scaffold and an ECM:PCL blended scaffold for two different media types. N=5, error bars = SD. *p < 0.05.*

Part B: Cell Secretome and Endothelial Cells

5B.1 Introduction

Electrospinning has been a widely used scaffold manufacturing technique used in vascular tissue engineering with endothelial cell lines [310,357,446]. Furthermore, the concept of grafting proteins, growth factors and peptides onto electrospun scaffold surfaces has also been used in tissue engineering [25,447]. While these methods have shown promise in the field of vascular tissue engineering, there are still shortfalls between the capabilities of lab-based materials and native tissues [129].

This study proposes utilising the principles of feeder layer systems in combination with known scaffold functionalization techniques. To improve the biofunctional properties of the scaffold, HUVEC secretome was collected in a serum free medium and bound to the surface of an electrospun scaffold. This technique allows for the cell's paracrinal secretomes to be engrafted onto the surface of the scaffold, which might help provide better original cell binding and gene expression in the early staged of implantation.

5B.2 Methods and Materials

5B.2.1 Electrospinning

PCL was dissolved at 20% w/v into a 5:1 mixture of Chlorofrom:Methanol. Briefly, the electrospun fibres were spun using the parameters in Table 21 and collected. Scaffolds with a 10 mm diameter were punched out. Extra-large fibre diameter scaffolds were used as they have previously shown better affinity for HUVECs. More details can be found in Section 2.1.

Table 21: Electrospinning parameters used for the HUVEC secretome scaffolds.

Needle bore (mm)	Flow rate (mL/h)	Total volume (mL)	Distance between needle tip and mandrel (cm)	Positive voltage (kV)	Negative Voltage (kV)	Mandrel rotational speed (RPM)
0.8	4	20	23	+18	-4	250

5B.2.2 Scanning Electron Microscopy

Scaffolds were imaged using a Hitachi TM4000 tabletop SEM as described in Section 2.5.

5B.2.3 Mechanical Analysis

Mechanical analysis was performed using an Instron 3367 testing rig with a 50 N load cell. Measurements were performed on 40mm x 5mm samples. Samples with a gauge length of 20 mm were stretched to failure at 10 mm/min. More details can be found in Section 2.7.

5B.2.4 Cell Growth

HUVECs were expanded using MCBD 131 medium supplemented with 5% v/v FBS; 1% v/v L-glutamine; 1% v/v penicillin/streptomycin; 1mg/L hydrocortisone; 50 mg/L ascorbic acid; 2 μg/L fibroblast growth factor; 10 μg/L epidermal growth factor; 2 μg/L insulin-like growth factor; and 1 μg/L vascular endothelial growth factor. HUVECs were lifted for scaffold seeding at 80% confluence. More details can be found in Section 2.3.

5B.2.5 Cell Secretome Collection

Briefly, HUVECs were cultured in a T75 flask to 70% confluence in cell MCDB 131 culture media containing FBS (as described in Section 5A.2.4). The media was then changed to 50:50 culture media containing FBS and culture media without any FBS for a further 24 h of culture. This was done to

slowly take the cells off of FBS before they were cultured serum free. The cells were then changed over to serum free media (10 mL) and cultured for 24 h, allowing sufficient time for the cells to release secretome (cytokines, proteins, etc.) into the serum free media. The media was then removed and used to soak the scaffolds.

5B.2.6 Scaffold Functionalization and Secretome Binding

Scaffolds underwent two steps of functionalization before being soaked in secretome filled media. Firstly, the scaffolds underwent 1min of oxygen plasma coating at 10.2 W to improve their surface energy and hydrophilicity. The scaffolds were then soaked in 5 mM of EDC and 5 mM of NHS in 0.5 M of MES buffer (pH 5.7) for 1h to create binding sites on the scaffold for binding proteins and cytokines in the secretome media. This was followed by three PBS washes. The scaffolds were then soaked in 250 µL of secretome filled media for 4 h, whilst being agitated to assist with the binding of factors. The scaffolds were then quickly dipped in PBS (1 s) to remove excess media before being seeded with cells. Scaffolds soaked in serum free media containing no secretome and PBS were used as controls.

5B.2.7 Protein Quantification

Protein quantification was used to measure the quantity of protein being bound/absorbed onto the scaffolds surface during the 4 h soaking phase. Briefly, a BCA protein assay was used with protein contents before and after soaking being measured and used to deduce the amount of protein bound to the scaffold. The assay was also used to measure the change in protein content of the media after the 24 h of culture to show how much protein was being added to the media during culture. More details can be found in Section 2.14.

5B.2.8 HUVEC Seeding and Culture

Once the scaffolds were functionalised and soaked in secretome they were ready for cell seeding. Briefly, 75,000 cells in 20 µL of serum free media per scaffold were drip seeded. After 1 h the media was topped up with 30 µL of media to ensure the cells did not dry out. After another hour the media

was topped up to a total volume of 500 µL. Timepoints of 12 h, 24 h and 48 h were used. More details can be found in Section 2.12.

5B.2.9 HUVEC cell Viability

The Cell Titer blue assay was performed as per manufacturer's instructions. The plate was measured at ex: 525 nm and em: 580-640 nm. More detail can be found in Section 2.13.

5B.2.10 Imaging of seeded HUVECs

Scaffolds were fixed in 10% formalin for 1 h and then washed thrice in PBS for cell imaging. Briefly, scaffolds were permeabilized in Triton-X solution before being stained in Phalloidin-iFluor™514 conjugate for 60 mins to visualize cell nuclei. Scaffolds were then washed thrice in PBS and then stained with 300 nM DAPI for 10 mins to visualise f-actin filaments followed by three PBS washes. Scaffolds were imaged using a Zeiss Axio Imager 2 microscope. More detail can be found in Section 2.17.

5B.2.11 Reverse Transcription Quantative Polymerase Chain Reaction (RT-qPCR)

RNA was extracted from the cell seeded scaffolds using a Tri-Reagent method and purified using Qiagen's RNeasy spin colum system. Real-time polymerase chain reaction was performed using a LightCycler® 480 Instrument II and Sensifast™ SYBR® High-ROX system. Forward and reverse sequences were designed and are displayed in Table 22. Relative quantification of RT-PCR results was carried out using the $2^{-\Delta\Delta ct}$ method [350]. Gene expression levels were expressed relative to GAPDH (housekeeping gene) and normalised to 70% confluent HUVECs on tissue culture plastic. More detail can be found in Section 2.18.

Table 22: Primer sequences used for RT-PCR for the HUVEC secretome conditioned scaffold study.

Gene	Primer	Sequence	Reference
Glyceraldehyde 3-phosphate dehydrogenase	GAPDH (forward)	GTCTCCTCTGACTTCAACAG	[31]
	GAPDH (reverse)	GTTGTCATACCAGGAAATGAG	
Matrix metalloproteinase-1	MMP1 (forward)	CGGTTTTTCAAAGGGAATAAGTACT	[31]
	MMP1 (reverse)	TCAGAAAGAGCAGCATCGATATG	
Matrix metalloproteinase-2	MMP2 (forward)	CGCTCAGATCCGTGGTGAG	[31]

	MMP2 (reverse)	TGTCACGTGGCGTCACAGT	
Intercellular Adhesion Molecule 1	ICAM1 (forward)	CCTTCCTCACCGTGTACTGG	
	ICAM1 (reverse)	AGCGTAGGGTAAGGTTCTTGC	[448]
Vascular endothelial growth factor	VEGF (forward)	AGACCAAAGAAAGATAGAGCAAGACAAG	
	VEGF (reverse)	GGCAGCGTGGTTTCTGTATCG	[31]
Platelet endothelial cell adhesion molecule	CD31 (forward)	ACTGGACAAGAAAGAGGCCATCCA	
	CD31 (reverse)	TCCTTCTGGATGGTGAAGTTGGCT	[361]

5B.2.12 Statistical Analysis

Data was expressed as mean ± 1 standard deviation. Statistical analysis was performed using one-way ANOVA with post-hoc Tukey test.

5B.3 Results

5B.3.1 Electrospinning

Scaffolds were successfully electrospun and showed uniform fibre sizes and a random orientation (Figure 57A). Fibre diameters were measured as being 5.95 ± 1.24 µm, which falls in line with the optimal fibre diameter for HUVECs deduced in Chapter 3.

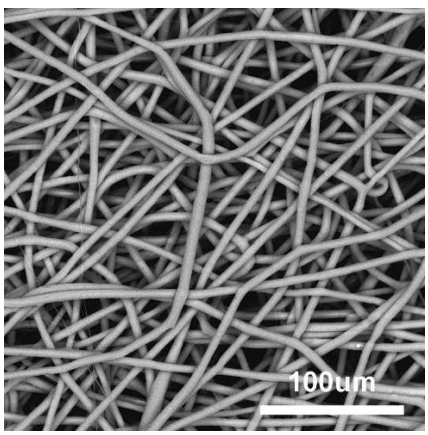

Figure 57: Representative SEM showing large fibred scaffold for seeding with HUVECs.

5B.3.2 Protein binding

The total mass of protein being bound onto the surface of the scaffolds was assessed using a Pierce™ BCA protein assay kit. The conditioned medium was found to have approximately 13% more protein

than the serum free medium. This suggests that the HUVECs being cultured caused a net increase in the quantity of protein in the medium. Therefore, it can be concluded that the cells are secreting proteins and cytokines into the medium. After 4 h of incubation the protein contents of both mediums dropped by over 150 ng/mL. This means that approximately 40 ng of protein bound on the secretome conditioned scaffolds and 37 ng of protein onto the serum free conditioned scaffolds, as seen in Table 23.

Table 23: Total mass of protein bound (HUVEC secretome) onto the scaffold's surface after 4h of incubation.

		Conditioned media	**Serum free media**
Protein content of media (µg/mL)	**Before protein binding**	782 ± 35	693 ± 29
	After protein binding	620 ± 40	542 ± 37
Protein bound/absorbed onto scaffold (µg)		40.6 ± 3.2	37.7 ± 3.0

5B.3.3 Cell Viability

Cell viability results showed that all three scaffolds were capable of maintaining cell viability when cultured using serum free medium, as seen in Figure 58. No significance was noted between the three groups at either of the time points. However, a significant increase was noted between 12 h and 48 h in the serum free medium functionalized scaffold.

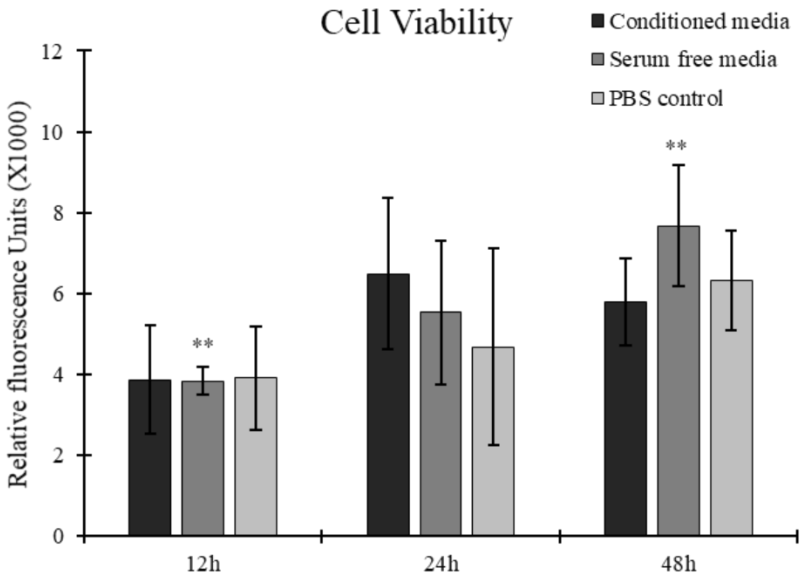

Figure 58: Cell viability of seeded HUVECs on all three scaffolds (PBS control, serum free media and conditioned media) after 12h, 24h and 48h of culture.

5B.3.4 Cell Imaging

DAPI and phalloidin fluorescence staining of the HUVECs on all three scaffolds at 12 h, 24 h and 48 h showed some interesting results, as seen in Figure 59. Interestingly, all three scaffolds are capable of maintaining the elongated phenotypic morphology of HUVECs up to 48 h of culture in a serum-free environment. In all three cases the HUVECs appear to be infiltrating the scaffold as expected when using the extra-large fibre morphology.

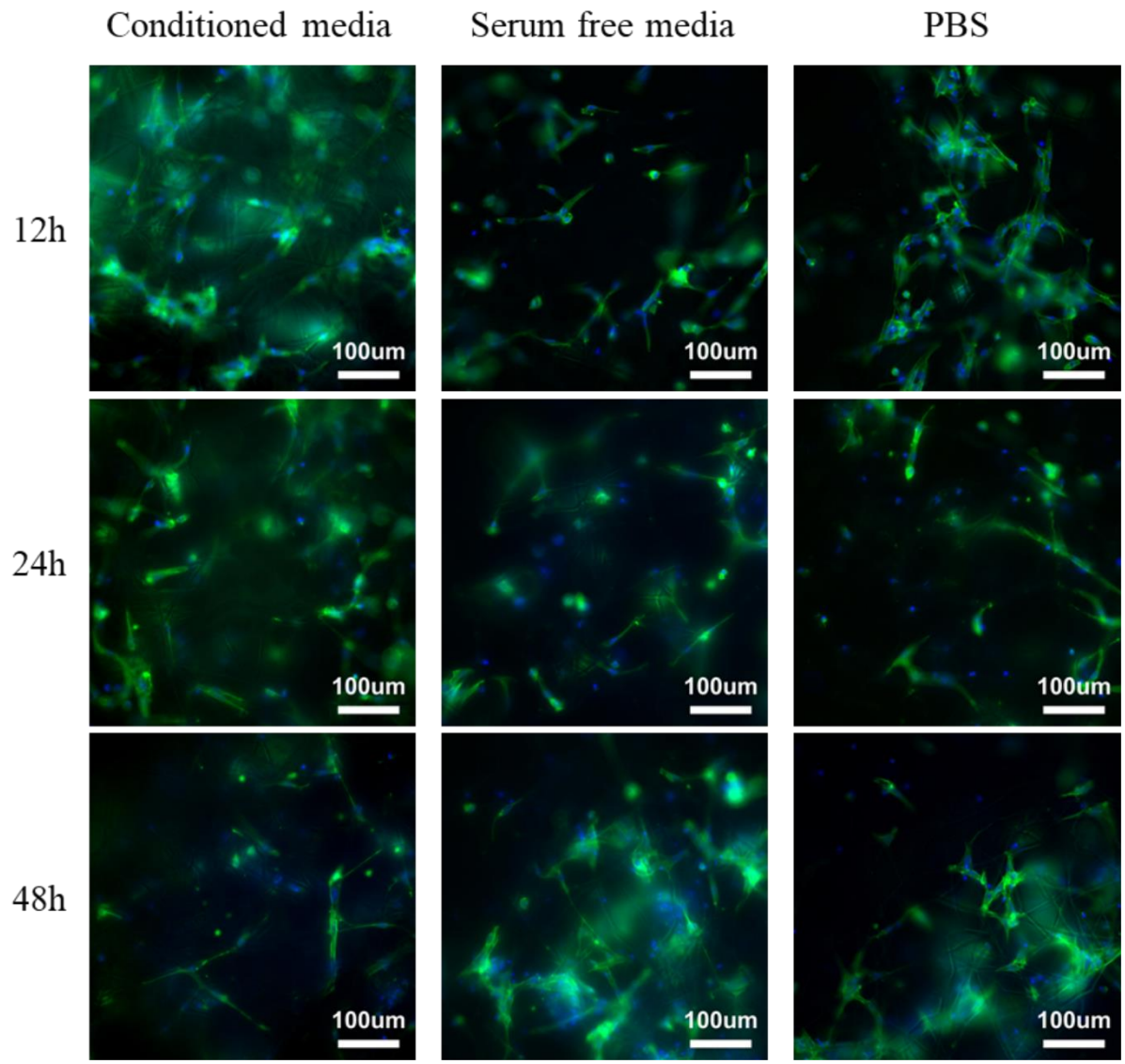

Figure 59: Representative DAPI (nuclei) and phallodin (f-actin) stained HUVECs on the three different scaffolds

5B.3.5 Reverse Transcription Quantative Polymerase Chain Reaction

RT-PCR results showed some interesting trends (Figure 60). Firstly, there was a general trend whereby the expressions of CD31, VEGF, ICAM1 and MMP2 were all slightly lower in the HUVECs seeded onto the scaffold that had been conditioned with cell secretome. While this was mostly not significant, there was some significance noted between some of the scaffolds. The expression of VEGF on the secretome conditioned scaffold after 48 h of culture was significantly lower than that on the control scaffold conditioned with PBS. Likewise, the expression of ICAM1 on the secretome

conditioned scaffolds was significantly lower after 48 h compared to the scaffolds conditioned with serum free media and the PBS conditioned control. Furthermore, after 48 h of culture the expression of MMP2 was also significantly lower on the secretome conditioned scaffold than on the serum free medium conditioned scaffold.

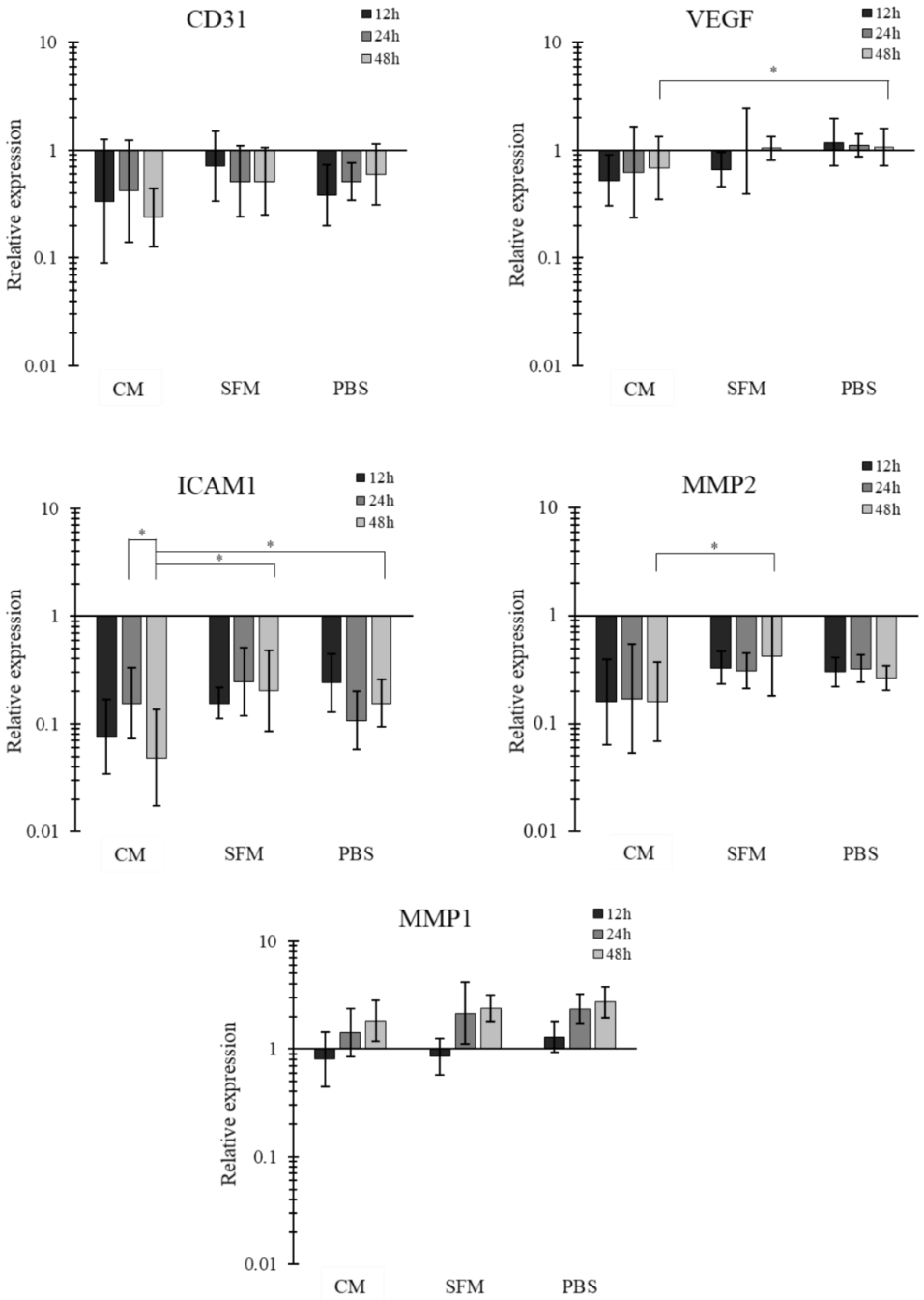

Figure 60: RT-PCR gene expression results for seeded HUVECs. Genes analysed: CD31, VEGF, ICAM1, MMP2 and MMP1 after 12h, 24h and 48h of culture. CM=secretome conditioned medium, SFM= serum free medium.

5B.4 Discussion

Firstly, a scaffold with extra-large fibres (diameter of 5.95 ± 1.24 μm) was successfully electrospun with uniform fibre sizes and a random alignment. The extra-large fibre was used due to the seeded HUVECs showing increased cell viability and upregulated gene expression compared to the smaller fibre sizes, as seen in Chapter 3.

Interestingly, the quantity of bound protein on the scaffolds soaked in secretome conditioned serum free medium and non-conditioned serum free medium were both fairly similar: 40.6 μg and 37.7 μg, respectively, which accounts for an increase of approximately 7.5% when soaked in the secretome media. Furthermore, the total mass of protein in the mediums was approximately 13% higher in the secretome conditioned media compared to the non-conditioned media before any soaking had taken place. This means that a higher proportion of the proteins in the non-conditioned medium were binding to the scaffold's surface compared to the proteins in the secretome conditioned medium. This may be due to the proteins being secreted by the HUVECs having a lower binding affinity with the functionalized PCL compared to the proteins already found in the serum free medium. Work by *Coad, et al.* found that different proteins (human serum albumin and streptavidin) with different chemical structures had different binding affinities to plasma coated polymers [449].

The exact formulation of the secretome conditioned medium is unknown, as a full proteomic study or the use of a Luminex assay would need to be carried out. However, work by *Fromer, et al.* found that HUVEC conditioned serum free medium contained an increased quantity of endolglin, fibroblast growth factor – 1 (FGF-1), FGF-2, and hepatocyte growth factor (HGF), compared to the non-conditioned medium containing serum [203]. Interestingly, the conditioned medium contained a reduced amount of VEGF compared to the serum containing non-conditioned medium, albeit the concentration was still very high [203]. Therefore, it would be expected that these proteins would all be found within the secretome conditioned medium in this study. However, this study was not able to confirm exactly which proteins had bound to the surface of the scaffold.

While this study does not look into exactly which proteins have bound to the surface of the scaffold, work by *Edlund, et al.* found that, when treated with EDC and NHS, VEGF was successfully grafted onto the surface of PCL [447]. Interestingly, VEGF was found to be one of the most prevalent proteins in HUVEC conditioned medium, therefore it would be expected that VEGF is binding to the surface of the scaffolds in this study [203].

The PCR results show some interesting trends between the three groups. There was a general trend whereby the expressions of CD31, VEGF, ICAM1 and MMP2 were all slightly lower in the HUVECs seeded onto the scaffold that had been conditioned with cell secretome conditioned medium. While these trends were mostly not significant, there was some significance noted between some of the scaffolds. As previously mentioned, the expression of VEGF on the secretome conditioned scaffold after 48h of culture was significantly lower than that on the control scaffold conditioned with PBS. Previous work by *Fromer, et al.* found that HUVECs secreted VEGF into their culture mediums, therefore elevating the total quantity of VEGF in the medium [203]. This may explain why VEGF expression was lower on the scaffolds soaked in the secretome conditioned medium, as the seeded HUVECs may not need to express as much VEGF into their surroundings due to the existing presence of VEGF already bound to the scaffold. Furthermore, VEGF expression on the two medium conditioned scaffolds increased over time, which may be caused by the VEGF present on the scaffold being turned over and used by the HUVECs, requiring them to increase the expression of VEGF to maintain HUVEC proliferation and migration [450].

Likewise, the expression of ICAM1 on the secretome conditioned scaffolds was significantly lower after 48 h compared to the scaffolds conditioned with serum free media and the PBS conditioned control. These interesting trends do suggest that the conditioning medium may have played an impact on the gene expression of the seeded HUVECs.

MMP2 is involved in the breakdown and remodelling of ECM [451]. Its downregulation in the scaffolds soaked in secretome conditioned medium could suggest homeostasis amongst the cells. Furthermore, MMP upregulations are often associated with degenerative diseases such as osteoarthritis and vascular disease, therefore are not necessarily desirable [451,452].

Interestingly, both the cell viability results and the DAPI/phalloidin staining show that all three scaffolds are capable of maintaining healthy HUVECs over a 48 h serum-free culture period. The staining shows elongated HUVECs, which is phenotypic characteristic associated with healthy HUVECs [453]. Furthermore, cell viability results showed no significant increase in viability over the 48h culture period for all three scaffolds.

This study has shown that the expression of certain genes can be controlled through the binding of cell secretomes onto the surface of the scaffold. Whilst the expression changes noted were small, a general trend can be seen suggesting that the bound proteins are having an effect on the seeded HUVECs. Going forward, a full proteomic study of the cell secretome medium and of the conditioned scaffolds would give more insight into why these trends are being seen. However, being able to control gene expression whilst also maintaining cell survival over the first 48h of attachment (when cultured serum-free) does have benefits for tissue engineering where initial cell infiltration and binding are required for the success of the implant.

5B.5 Conclusions

In this study, cell secretome conditioned medium was created by culturing HUVECs with serum-free medium for 24 h. It contained an elevated quantity of protein compared to the serum-free medium suggesting that the HUVECs were secreting proteins into the medium. Furthermore, approximately 37-40 μg of protein was successfully bound to the PCL scaffold. Cell viability showed that all three scaffolds were capable of maintaining cell growth when cultured in a serum-free environment over a 48 h period. Additionally, the binding of proteins (both from the cell secretome conditioned medium and the serum-free medium) to the scaffolds had effects on the gene expression noted from the seeded HUVECs. Most notably, several genes were downregulated on the secretome conditioned medium. These results show the potential benefits to binding cell secretome to the surface of the scaffold.

Part C: Cell Secretome and Smooth Muscle Cells

5C.1 Introduction

Electrospinning is a widely used scaffold manufacturing technique used in all facets of tissue engineering [177,311,347]. Furthermore, the technique has been widely used with smooth muscle cell lines [446,454,455]. In addition to this, engrafting proteins, growth factors and peptides onto electrospun scaffold surfaces has also shown promise in tissue engineering as a means of altering the scaffold's surface properties [25,447]. However, there is still a shortfall between the capabilities of lab-based materials and native tissues [129].

Herein, this study proposes collecting HUVSMC secretome in a serum free medium and binding the proteins to the surface of an electrospun scaffold to improve the biofunctional properties of the scaffold. This method allows for the cell's secreted proteins to be engrafted onto the surface of the scaffold, which might help provide better cell binding and gene expression in the early staged of implantation.

5C.2 Methods and Materials

5C.2.1 Electrospinning

PCL was dissolved at 8% w/v into HFIP. Briefly, the electrospun fibres were spun using the parameters in Table 24 and collected. Scaffolds with a 10 mm diameter were punched out. A small fibre diameter scaffolds were used as they have previously shown better affinity for HUVSMCs. More details can be found in Section 2.1.

Table 24: Electrospinning parameters used for the HUVSMC secretome conditioned scaffolds.

Needle bore (mm)	Flow rate (mL/h)	Total volume (mL)	Distance between needle tip and mandrel (cm)	Positive voltage (kV)	Negative Voltage (kV)	Mandrel rotational speed (RPM)
0.4	1	8	12	+14	-4	250

5C.2.2 Scanning Electron Microscopy

Scaffolds were imaged using an SEM with a 15 kV accelerating voltage and a 10 mm working distance. More details can be found in Section 2.5.

5C.2.3 Mechanical Analysis

Mechanical analysis was performed using an Instron testing rig. Samples with 40 x 5 mm dimensions were cut out for measurements. A gauge length of 20 mm was used and samples were stretched to failure at 10 mm/min. More details can be found in Section 2.7.

5C.2.4 Cell Growth

HUVSMCs were expanded to passage 4 in a 5% CO_2/37°C atmosphere. HUVSMCs were expanded using smooth muscle cell growth medium and then cultured using DMEM supplemented with 10% v/v FBS; 1% v/v penicillin/streptomycin; 1% v/v non-essential amino acids and 1% insulin transferrin selenium (ITS). HUVSMCs were lifted for scaffold seeding at 80% confluence. More details can be found in Section 2.3.

5C.2.5 Cell Secretome Collection

Briefly, HUVSMCs were cultured in a T75 flask to 70% confluence in supplemented DMEM. The media was then changed to 50:50 culture media containing FBS and culture media without any FBS for a further 24 h of culture. This was done to wean the cells off of FBS before they were cultured serum free. The cells were then changed over to serum free media (10 mL) and cultured for 24 h, allowing sufficient time for the cells to release secretome (cytokines, proteins, etc.) into the serum free media. The media was then removed and used to soak the scaffolds. The serum free medium used is the same as mentioned in 5C.2.4 but without serum.

5C.2.6 Scaffold Functionalization and Secretome Binding

Scaffolds underwent two different steps of functionalization before being soaked in secretome filled media. Firstly, scaffolds were oxygen plasma coated for 1min at 10.2 W to improve their surface energy and hydrophilicity. The scaffolds were then bathed in 5 mM of EDC and 5 mM of NHS in 0.5 M of MES buffer (pH 5.7) for 45 mins to create binding sites on the scaffold for the proteins in the secretome media. The scaffolds were then soaked in 250 µL of secretome filled media for 4h, whilst being agitated to assist with the binding of factors. The scaffolds were then seeded with cells. Soaking in serum free media containing no secretome and PBS were used as controls.

5C.2.7 Protein Quantification

Protein quantification was used to measure the quantity of protein being bound/absorbed onto the scaffolds surface during the 4 h soaking phase. Briefly, a BCA protein assay was used. Protein contents before and after soaking were measured and used to deduce the amount of protein bound to the scaffold. The assay was also used to measure the change in protein content of the media after the 24 h of culture to show how much protein was being added to the media during culture. More details can be found in Section 2.14

5C.2.8 Cell Seeding and Culture

Once the scaffolds were functionalised and soaked in secretome they were ready for cell seeding. Briefly, 25,000 cells in 20 µL of serum free media per scaffold were drip seeded. After 1 h the media was topped up with 30 µL of media to ensure the cells did not dry out. After another hour the media was topped up to a total volume of 500 µL. Timepoints of 12 h, 24 h and 48 h were used. More details can be found in Section 2.12.

5C.2.9 Cell Viability

The assay was performed as per manufacturer's instructions. Measurements were taken at at ex: 525 nm and em: 580-640 nm. More details can be found in Section 2.13.

5C.2.10 Cell Imaging

Scaffolds were fixed in 10% formalin then permeabilized in Triton-X solution before being stained in Phalloidin-iFluor™514 conjugate for 60 mins and DAPI for 10mins. Scaffolds were imaged using a Zeiss Axio Imager 2 microscope. More details can be found in Section 2.17.

5C.2.11 Reverse Transcription Quantative Polymerase Chain Reaction (RT-qPCR)

RNA was extracted from the cell seeded scaffolds using a Tri-Reagent method and purified using Qiagen's RNeasy spin colum system. Real-time polymerase chain reaction was performed using a LightCycler® 480 Instrument II and Sensifast™ SYBR® High-ROX system. Forward and reverse sequences were either designed or taken from literature and are displayed in Table 25. Relative quantification of RT-PCR results was carried out using the $2^{-\Delta\Delta ct}$ method [350]. Gene expression levels

were expressed relative to GAPDH (housekeeping gene) and normalised to 70% confluent HUVSMCs on tissue culture plastic. More details can be found in Section 2.18.

Table 25: Primer sequences used for RT-PCR gene expression analysis on seeded HUVSMCs.

Gene	Primer	Sequence	Reference
Glyceraldehyde 3-phosphate dehydrogenase	GAPDH (forward)	GTCTCCTCTGACTTCAACAG	[31]
	GAPDH (reverse)	GTTGTCATACCAGGAAATGAG	
Smooth muscle actin alpha 1	A-actin1 (forward)	CCGACCGAATGCAGAAGGA	[377]
	A-actin1 (reverse)	ACAGAGTATTTGCGCTCCGAA	
Myocardin	Myocardin (forward)	GGGTCTGAGCATTCCTTGCT	Self-designed
	Myocardin (reverse)	CTGGACGTTTCAGTGGTGGT	
Mesenchyme homeobox 2	MEOX-2 (forward)	AAAAGCGACAGCTCAGACTC	[289]
	MEOX-2 (reverse)	TTGCTGTCCACCCTTTACCC	
Interleukin 1 alpha	IL1-α (forward)	GCGTTTGAGTCAGCAAAGAAG	Self-designed
	IL1-α (reverse)	GCCGTGAGTTTCCCAGAAGA	

5C.2.12 Statistical Analysis

Data was expressed as mean ± 1 standard deviation. Statistical analysis was performed using one-way ANOVA with post-hoc Tukey test.

5C.3 Results

5C.3.1 Electrospinning

Scaffolds with a small fibre diameter were successfully electrospun showing uniform fibre diameter and a random alignment as seen in Figure 61. Fibre diameters were measured as being 1.42 ± 0.24 µm, which falls in line with the optimal fibre diameter for HUVSMCs deduced in Chapter 3.

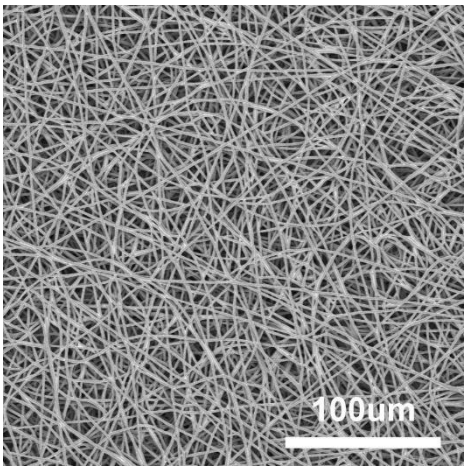

Figure 61: SEM image of the small diameter fibre electrospun scaffolds used for the binding of HUVSMC secretome.

5C.3.2 Protein Binding

The BCA protein assay was used to deduce the quantity of protein bound to the scaffolds, as seen in Table 26. Briefly, there was a 2.23% increase in protein content in the medium after 24 h of culture on a confluent monolayer of HUVSMCs. Interestingly, more protein from the serum free media bound to the scaffold than the conditioned media: 57.2 µg and 28.5 µg, respectively. These results suggest that the protein constituents of the media are altered during the 24 h of culture on the monolayer of HUVSMCs.

Table 26: Total quantity of bound protein onto each scaffold after 4h of incubation.

		Conditioned media	**Serum free media**
Protein content of media (µg/mL)	**Before protein binding**	1238 ± 23	1211 ± 55
	After protein binding	1124 ± 40	983 ± 37
Protein bound/absorbed onto scaffold (µg)		28.5 ± 1.1	57.2 ± 4.0

5C.3.3 Cell Viability

Cell viability showed some interesting trends, as seen in Figure 62. Firstly, there were no differences noted with cell viability between the scaffolds soaked with secretome conditioned medium and the scaffolds soaked in serum free medium. However, the PBS soaked scaffold with no protein binding showed the highest cell viability at all timepoints with approximately 75% more viability than the two other scaffolds after 12 h and 24 h of culture, and 125% more viability after 48 h of culture. However, this difference was not significant. Furthermore, viability was maintained between 12 h and 24 h for all three scaffolds, with viability falling after the 24 h timepoint.

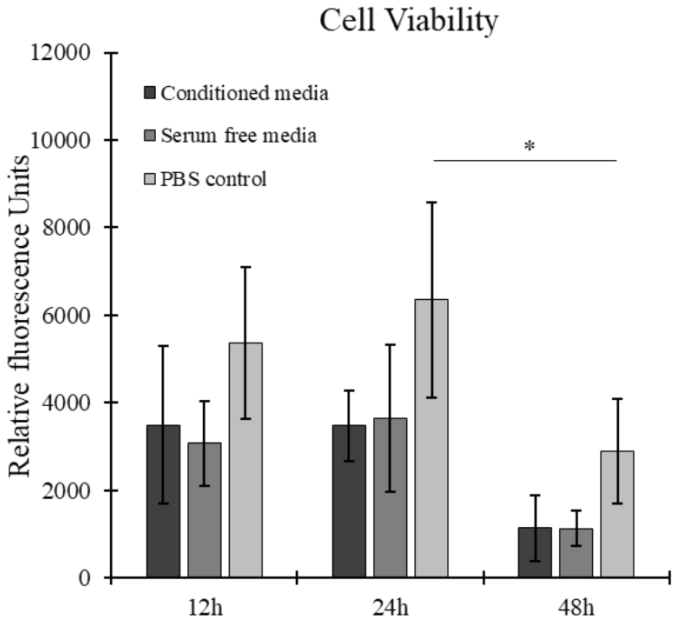

*Figure 62: Cell viability of seeded HUVSMCs on all three scaffolds (PBS control, serum free media and conditioned media) after 12, 24 and 48 h of culture. N=4. *p < 0.05.*

5C.3.4 Cell Imaging

DAPI (nuclei) and phalloidin (f-actin) fluorescence staining of the HUVSMCs on all three scaffolds at 12 h, 24 h and 48 h showed some interesting results, as seen in Figure 63. Firstly, all three scaffolds were capable of maintaining healthy HUVSMCs up to the 24 h mark whilst cultured serum free. The cells adopted an elongated phenotypic morphology. Interestingly, at the 48 h mark, the scaffolds conditioned with secretome containing medium and serum-free medium both appeared to have mostly rounded cells, which is a sign of apoptosis [362]. On the other hand, the control scaffold conditioned with PBS appeared to mostly maintain the elongated phenotypic morphology expected of HUVSMCs.

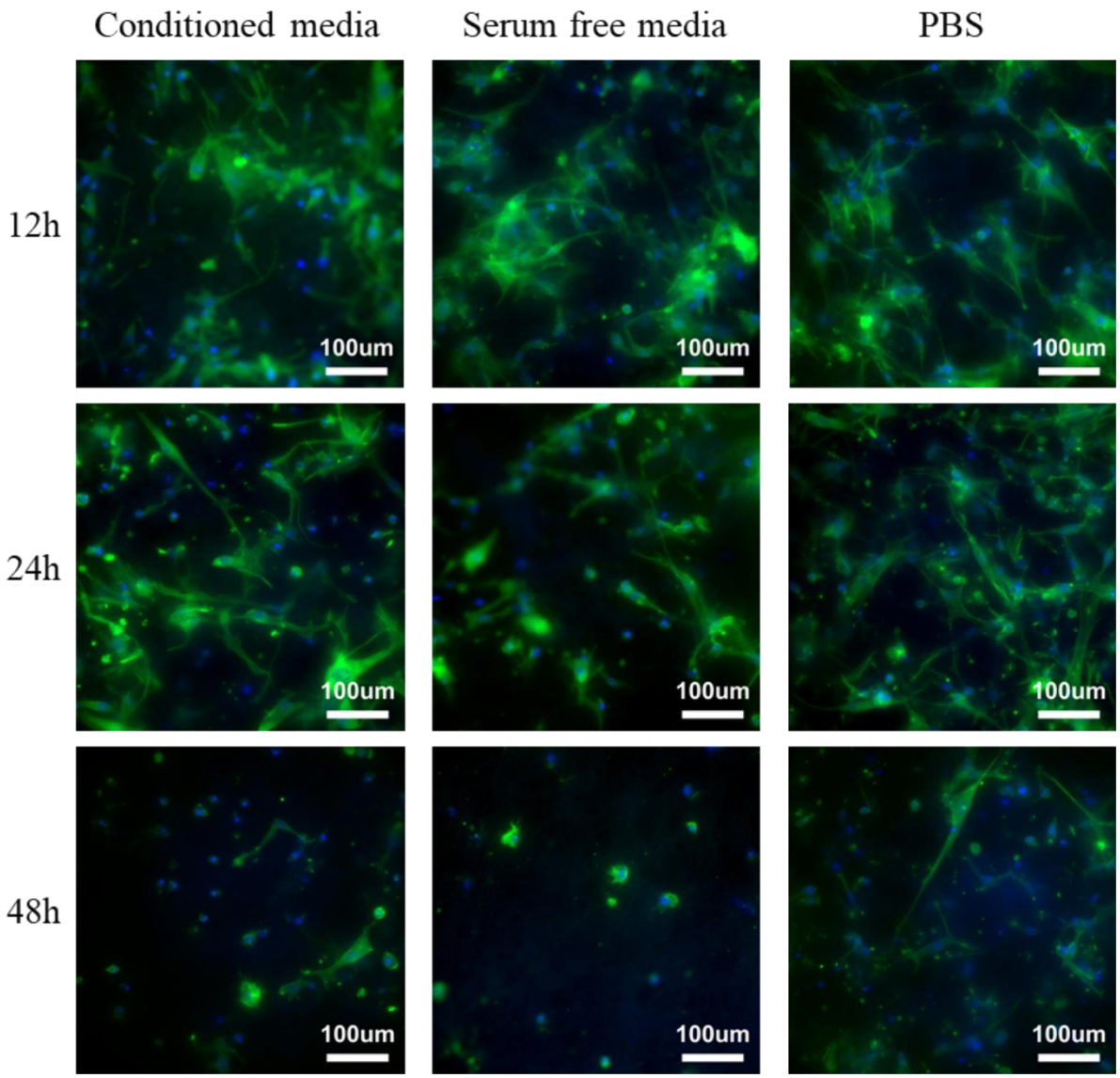

Figure 63: Representative DAPI (nuclei) and phalloidin (f-actin) stained HUVSMCs on the three scaffolds (PBS control serum free media and conditioned media) after 12, 24 and 48 h.

5C.3.5 Reverse Transcription Quantative Polymerase Chain Reaction

RT-PCR results showed some interesting trends between the three scaffolds, as seen in Figure 64. Firstly, all three scaffolds had very similar expression of smooth muscle alpha actin 1, with a downregulation noted over time. Likewise, the expression of Interleukin 1 alpha dropped over time for the secretome conditioned media scaffold and the PBS conditioned scaffold. On the other hand, the expression of interleukin 1 alpha did rise between 24 h and 48 h of culture on the serum-free conditioned scaffold, albeit without any significance. MEOX2 expression was seen to increase on all

three scaffolds between 12 h and 48 h of culture. Furthermore, Myocardin expression dropped between 12 h and 48 h of culture for the secretome conditioned scaffold and the PBS conditioned scaffold. On the other hand, my0cardin expression increased on the serum-free conditioned scaffold between 12 h and 48 h of culture. Significance was noted between the expressions of myocardin on the secretome conditioned scaffold and the serum-free conditioned scaffold after 48 h of culture, with the latter showing higher expression.

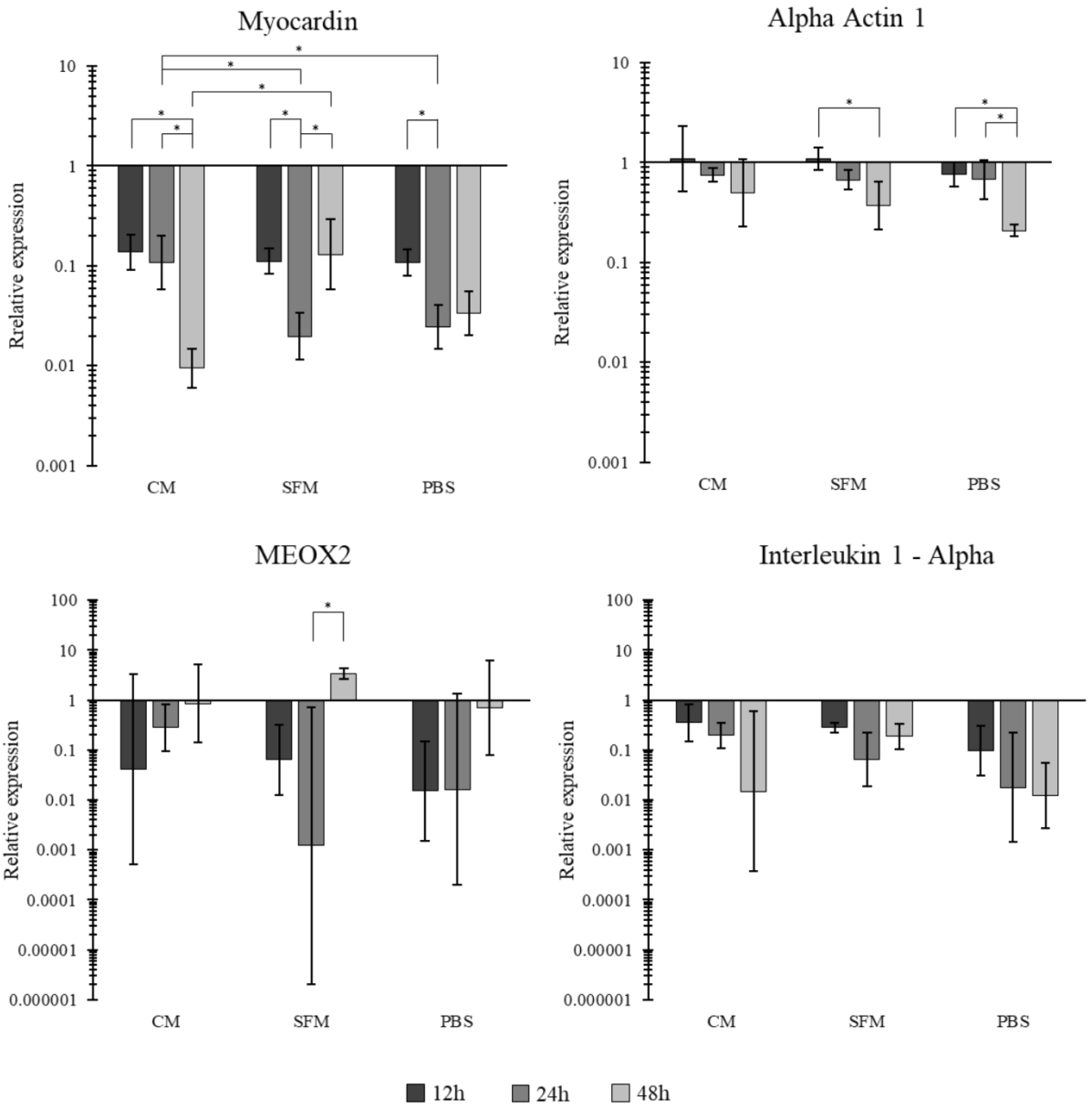

Figure 64: Gene expression results for four HUVSMC related genes: Myocardin, Alpha Actin 1, MEOX2 and Interleukin 1 alpha (IL1-α), on HUVSMC seeded on all three scaffold conditions. CM = condition media, SFM = serum free media. N=5, error bars = SD.

5C.4 Discussion

A scaffold was successfully electrospun with a small fibre diameter (1.42 ± 0.24 µm) showing uniform fibre size and a random fibre alignment. The small fibre diameter was chosen as this scaffold showed higher cell viability when seeded with HUVSMCs compared to the scaffolds with larger fibre diameters, as seen in Chapter 3B.

The BCA protein quantification assay revealed some interesting results regarding the quantity of bound protein from each of the two media types. Firstly, there was a net increase in the protein content in the secretome media compared to its serum-free counterpart. This suggests that the HUVSMCs are releasing some proteins into the media, however, the exact quantity cannot be concluded as the cells will be using up the protein already present in the media, whilst releasing other proteins. Furthermore, the BCA protein quantification assay showed that a lot more protein in the serum free media bound to the scaffolds than the secretome containing media. Work by *Coad, et al.* found that different proteins (Human serum albumin and Streptavidin) with structures and molecular weights (66.5 kDa vs 53 kDa) had different binding affinities to plasma coated polymers [449]. Furthermore, work by *Dupont, et al.* showed that the proteins secreted by human arterial smooth muscle cells had a range of different atomic mass contents ranging from 95 kDa to 20 kDa [456]. Therefore, these results suggest that the protein profile of the secretome media is different to that of the serum-free media, which indicates that there has been a high turnover of proteins within the media. A full proteomic analysis of the constituents of the secretome media is required to get a full image of the make-up of the HUVSMC secretome profile.

Cell viability analysis showed some interesting results regarding to how the HUVSMCs bound and proliferated on the scaffolds. At all three timepoints, the PBS conditioned scaffold had higher cell viability than the two media conditioned scaffolds (approximately 75% higher after 12 h and 24 h, and 150% higher after 48 h). These results suggest that the seeded HUVSMCs had difficulty attaching to the scaffolds that had been conditioned with the two protein containing mediums. However, the DAPI and phalloidin stained scaffolds show that all three scaffolds were able to accommodate a healthy layer of HUVSMCs, displaying phenotypic characteristics after 12 h and 24 h [389,436]. The CellTiter-

Blue® Cell Viability Assay is an assay that measures the metoabolic capacity of cells, therefore, it doesn't necessarily correlate with the total number of cells bound to the scaffold. This means that the lower cell viability noted in the two media conditioned scaffolds may be caused by the bound proteins reducing the metabolic capacity of the cells, as opposed to a lower quantity of cell binding. The DAPI and phalloidin stained scaffolds after 48 h of culture showed that the PBS conditioned scaffold was able to maintain HUVSMCs with a healthy phenotypic morphology [389,436]. In contrast, the HUVSMCs seeded onto the serum-free media conditioned scaffolds and to some extent, the HUVSMCs seeded on the secretome conditioned scaffolds both showed cell rounding, which is a sign of apoptosis [362].

Myocardin is a key phenotypic gene in SMCs and is involved in their contractile functionality [378,379]. The secretome conditioned scaffold and the PBS conditioned scaffold both showed downregulations over the 48h of culture. As SMCs proliferate and mature, an upregulation of this gene would be expected. Likewise, the expression of smooth muscle alpha actin 1 also dropped over time for all three scaffolds. Alpha actin 1, much like myocardin, is a key phenotypic gene associated with SMC maturity and contractility [377]. In addition, cell viability results suggest that the cells are not proliferating, which falls in line with the results found with myocardin expression and smooth muscle alpha actin 1 expression. Furthermore, the expression of IL1-α and MEOX2 also supports the theory that the cells are not proliferating. IL1-α is upregulated in SMCs during cell proliferation, therefore, its downregulation suggests that the cells are losing their proliferative potential on all three scaffolds [431,437]. Furthermore, the upregulation of MEOX2 has been shown to supress SMC proliferation and migration [289]. All three scaffolds showed an upregulation of MEOX2 between 12h and 48h of culture, which falls in line with IL1-α downregulation.

While the DAPI (nuclei) and phalloidin (f-actin) results show that the scaffolds were capable of maintaining a healthy layer of SMCs, the gene expression results and the cell viability results suggest that the cells which are bound to the scaffold after 48 h are losing their proliferative capabilities and the contractile functionality. However, this study does show that the proteins from both serum free media and cell secretome conditioned media can both be bound to a scaffolds surface. Furthermore, the binding of proteins did have an effect on cell viability and the phenotypic characteristics of the

seeded cells. These results suggest that binding cell secretome does have promise in tissue engineering applications where altering gene expression can be desirable.

5C.5 Conclusions

In this study, cell secretome conditioned medium was created by culturing HUVSMCs with serum-free medium for 24 h. The conditioned medium had a slightly elevated quantity of protein compared to the serum-free medium suggesting that the HUVSMCs were secreting proteins into the medium. Furthermore, an increased proportion of the proteins found in the serum-free media were bound to the scaffolds compared to the proteins in the secretome conditioned media (57.2 μg and 28.5 μg). This suggests that the proteins found in the secretome conditioned media have different structural makeups and different affinities for plasma coated and EDC/NHS functionalized polymer scaffolds. Cell viability was increased on the PBS conditioned scaffold compared to the two media conditioned scaffolds, suggesting that the bound protein is either affecting cell binding or it is affecting the metabolic capacity of the cells. Furthermore, gene expression results suggests that the scaffolds lead to reduced HUVSMC contractile functionality and proliferative capabilities. These results suggest that the binding of cell secretome to polymer scaffolds can alter the performance of seeded cells and does hold promise for tissue engineering applications where an altered gene expression is required.

Chapter 6: Environmental Stimuli and Endothelial Cells

Introduction

There are a variety of different environmental stimuli found *in vivo* that are often not replicated in *ex vivo* experiments. Examples of these environmental stimuli include various mechanical forces, such as pressure, shear stress and strain; biochemical stimuli from neighbouring cells types; and varying oxygen levels [457–466]. These environmental factors play a crucial role in maintaining healthy functional cells and their replication *in vitro* allows for more accurate modelling of the native environment [457,463].

Cells found in the arteries (endothelial cells and smooth muscle cells) undergo cyclic pressures due to the force of blood being forced around the body by the heart [8]. Depending on how far along the vasculature, the pressures seen by the cells can range from 120 mmHg in the aortic arch down to close to 0 mmHg in the capillaries [8]. During each heart beat the pressure felt by the local cells will increase and decrease cyclically at the same frequency as the heart is beating [8].

By mimicking the pressures seen by the native cells, a more physiologically accurate secretome profile can be generated *in vitro.* Binding the proteins generated under these physiological conditions to a scaffold will provide the seeded cells with the biochemical cues that are seen by the native cells when in their native environment.

Likewise, looking at how the aorta ECM/PCL scaffolds perform under hypoxic conditions will give a better image of how these scaffolds might perform in an *in vivo* environment. Endothelial cells have a differing cell response when undergoing hypoxic stress [467]. Hypoxia has been shown to stimulate endothelial cells to express various vasoactive substances and matrix regulating proteins [467]. Furthermore, hypoxia is heavily linked with inflammatory diseases and other vascular disease related to ageing [468]. Therefore, experimenting under hypoxic conditions creates a more accurate image of how these scaffolds might perform *in vivo* and allows us to test scaffolds in a disease state.

In this Chapter, two different ways of incorporating native environmental stimuli into these studies were looked at. Firstly, this present study proposes stimulating cells in a hydrostatic pressure bioreactor in order to alter their secretome profiles for subsequent binding onto scaffolds (Section

6A). Hypoxia combined with aorta ECM/PCL scaffolds were then assessed to see how they altered the performance of seeded cells (Section 6B).

Part A: Hydrostatic Pressure Cell Secretome and Endothelial Cells

6A.1 Introduction

Hydrostatic pressure bioreactors have been widely utilised in tissue engineering applications as a means of creating a more physiologically relevant environment for the cells [469]. They have been used on both 'soft' tissues such as the heart and vessels and 'hard' tissues such as bone and cartilage [470–473].

There are a range of different hydrostatic pressure bioreactors that have been developed for *in vitro* experimentation, which fall under two general methods. Firstly, several studies have used a simple bioreactor design which relies on the scaffold being sealed into a medium filled flexible bag/tube and placed into a water filled biochamber [474–476]. This water filled biochamber can then be compressed to very high pressures (+ 50 MPa). These designs are mostly used for cartilage and bone tissue engineering due to the high pressure which can be administered. Secondly, several studies have looked at bioreactors where the scaffold is immersed in culture medium that is in direct contact with the pressurized air [477–479]. This incubator air is passed through a compressor and enters the bioreactor and directly transmits this higher pressure to the medium, which in turn transmits it to the scaffold. This method allows for a low pressure to be applied to the cells and is usually used with softer tissues, such as vessels.

As mentioned in Chapter 5, feeder layer systems have been utilised in cell culture to help with the growth of certain cell lines [442]. The principle of the feeder cell system is to allow for direct paracrinal cell communication between the two cell lines. However, this can be done indirectly through the collection of the paracrinal cell secretomes in a serum free medium. The proteins from this medium will then be bound to a scaffold.

The aim of this study is to see how culturing cells under hydrostatic pressure alters their secretome profile compared to culturing at atmospheric pressure. By binding these proteins to a scaffold, the aim is to create a biofunctionalized scaffold containing the paracrinal secretomes released by the HUVECs when cultured under hypoxic conditions.

6A.2 Bioreactor Development

The bioreactor system was developed with the aim of compressing the cells with physiologically relevant pressures in the range found in the aorta and arteries. With this in mind, a bioreactor was developed where the surrounding air was compressed, transmitting the pressure directly to the media which in turn compresses the cells. In order to culture as many cells as possible, the aim was to design a bioreactor that could either accommodate well plates or tissue culture flasks. The design is simple and works by extracting air from an incubator and compressing it, as seen in Figure 65. The air is then brought to the desired pressure using a set of two control valves before going through an air filter to sterilize the air. The air is then fed into an air-tight box that can be placed into an incubator. This air-tight box is large enough to accommodate three tissue culture flasks. The box is held under constant pressure with a very low flow rate of new compressed incubator air fed into it, ensuring the cells receive the required oxygen from the air.

A pressure of 50 mmHg was used as this has been shown to have a similar effect on the level of gene expression as higher pressures (up to 150 mmHg). However, 50 mmHg does provide a lower proliferative index (the rate of proliferation was lower) compared to the higher pressures [458]. With this in mind, the main focus of this study is to generate a cellular secretome profile that differs from the secretome profile generated under atmospheric pressure. For this reason, 50 mmHg was used.

The system was set up with an air filter before the compressed air entered the bioreactor. The air filter used was an in-line HEPA filtration unit (Whatman®) designed to retain 99.97% of all particles ≥ 0.3 μm in air. This filter is specifically designed to prevent contamination in incubators, therefore was well suited for the removal of contaminants going into the bioreactor. The air being compressed was taken directly from the incubator (37°C and 5% CO_2). The compressor (ORAZIO®) used was a low decibel oil-free compressor. A low decibel compressor was used as to avoid noise pollution in the laboratory and oil-free was used as to reduce the potential for contaminants in the compressed air.

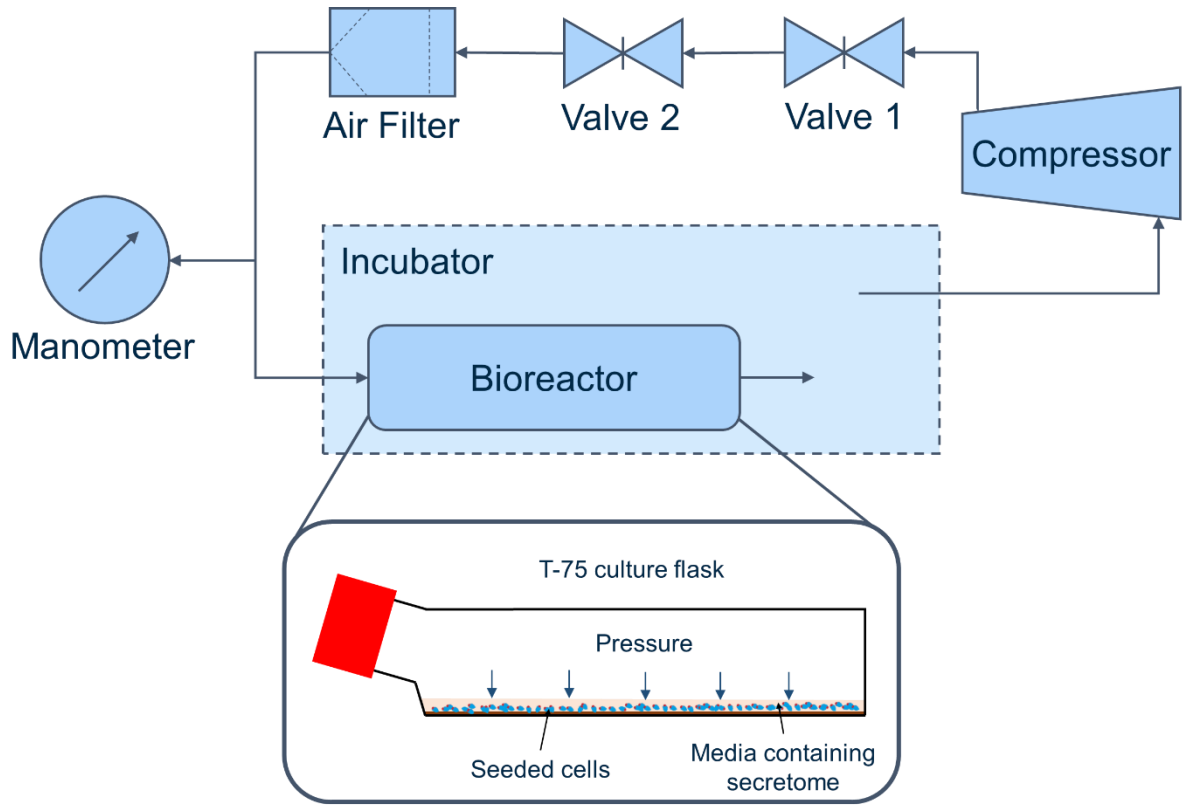

Figure 65: Schematic of bioreactor set up. Air is removed from an incubator (37°C and 5%CO_2) and compressed in an oil free air compressor. The compressed air is then fed through two valves to bring it down to 50 mmHg and through a filter (≥ 0.3 µm) before being brought back into the bioreactor.

6A.3 Methods and Materials

6A.3.1 Electrospinning

PCL was dissolved at 20% w/v into a 5:1 mixture of Chlorofrom:Methanol. Briefly, the electrospun fibres were spun and collected. Scaffolds with a 10mm diameter were punched out. Extra-large fibre diameter scaffolds were used as they have previously shown better affinity for HUVECs (Chapter 3A). Electrospinning parameters can be seen in Table 27. More details can be found in Section 2.1.

Table 27: Electrospinning parameters used to electrospin a large diameter fibre scaffold.

Needle bore (mm)	Flow rate (mL/h)	Total volume (mL)	Distance between needle tip and mandrel (cm)	Positive voltage (kV)	Negative Voltage (kV)	Mandrel rotational speed (RPM)
0.8	4	16	23	+14	-4	250

6A.3.2 Scanning Electron Microscopy

Scaffolds were imaged using a Hitachi TM4000 tabletop SEM as described in section 2.5.

6A.3.3 Mechanical Analysis

Mechanical analysis was performed using an Instron 3367 testing rig with a 50 N load cell. Samples if 40 mm x 5 mm were cut out. Measurements were performed to failure at 10 mm/min with a gauge length of 20 mm. More details can be found in Section 2.7.

6A.3.4 Cell Growth

HUVECs were expanded to passage 7 in using MCBD 131 medium supplemented with 5% v/v FBS; 1% v/v L-glutamine; 1% v/v penicillin/streptomycin; 1 mg/L hydrocortisone; 50 mg/L ascorbic acid; 2 μg/L fibroblast growth factor; 10 μg/L epidermal growth factor; 2 μg/L insulin-like growth factor; and 1 μg/L vascular endothelial growth factor. HUVECs were lifted for scaffold seeding at 80% confluence. More details can be found in Section 2.3.

6A.3.5 Cell Secretome Collection

Briefly, HUVECs were cultured in a T75 flask to 70% confluence in cell MCDB 131 culture media containing FBS (as described in Section 6A.3.4). The media was then changed to 50:50 culture media containing FBS and culture media without any FBS for a further 24 h of culture. The cells were then changed over to serum free media (10 mL) and cultured for 24 h in the hydrostatic pressure bioreactor at 50 mmHg. The media was then removed and used to soak the scaffolds. Alongside this, secretome media was also being collected from cells cultured at atmospheric pressure in an incubator to use as a control. The four conditions used in this study are: Hydrostatic pressure conditioned media (HP CM); atmospheric pressure conditioned media (AP CM); serum-free media (SF M); and PBS.

6A.3.6 Scaffold Functionalization and Secretome Binding

Scaffolds underwent 1min of plasma coating at 10.2 W to increase their surface energy and hydrophilicity. The scaffolds were then bathed in 5 mM of EDC and 5mM of NHS in 0.5M of MES buffer (pH 5.7) for 45 mins to create binding sites on the scaffold for the proteins in the secretome media. The scaffolds were then soaked in 250 μL of hydrostatic pressure secretome filled media for 4 h, whilst being agitated to assist with the binding of factors. The scaffolds were then seeded with

cells. Soaking in atmospheric pressure obtained secretome filled media, serum free media containing no secretome and PBS were used as controls. More detail can be found in Sections 2.6 and 2.15.

6A.3.7 Protein Quantification

Protein quantification was used to measure the quantity of protein being bound/absorbed onto the scaffolds surface during the 4 h soaking phase. Briefly, a BCA protein assay was used. Protein contents before and after soaking were measured and used to deduce the amount of protein bound to the scaffold. More detail can be found in Section 2.14.

6A.3.8 Cell Seeding and Culture

Once the scaffolds were functionalised and soaked in secretome they were ready for cell seeding. Briefly, 75,000 cells per scaffold were drip seeded in 20 µL of serum free media. After 1 h the media was topped up with 30 µL of media to ensure the cells did not dry out. After another hour the media was topped up to a total volume of 500 µL. Timepoints of 12 h, 24 h and 48 h were used. Scaffolds were cultured at atmospheric pressure in 37°C and 5% CO_2. More detail can be found in Section 2.3 and 2.12.

6A.3.9 Cell Viability

The assay was performed as per manufacturer's instructions at timepoints of 12 h, 24 h and 48 h. More detail can be found in Section 2.13.

6A.3.10 Cell Imaging

Briefly, scaffolds were permeabilized in Triton-X solution before being stained in Phalloidin-iFluor™514 conjugate and 300 nM DAPI. Scaffolds were imaged using a Zeiss Axio Imager 2 microscope. More detail can be found in Section 2.17.

6A.3.11 Reverse Transcription Quantative Polymerase Chain Reaction (RT-qPCR)

The method used for PCR is described in section 2.18. Forward and reverse sequences were designed and are displayed in Table 22. Relative quantification of RT-PCR results was carried out using the $2^{-\Delta\Delta ct}$ method [350]. Gene expression levels were expressed relative to GAPDH (housekeeping gene) and normalised to 70% confluent HUVECs on tissue culture plastic.

Table 28: Primer sequences used for RT-PCR on seeded HUVECs.

Gene	Primer	Sequence	Reference
Glyceraldehyde 3-phosphate dehydrogenase	GAPDH (forward)	GTCTCCTCTGACTTCAACAG	[31]
	GAPDH (reverse)	GTTGTCATACCAGGAAATGAG	
Matrix metalloproteinase-1	MMP1 (forward)	CGGTTTTTCAAAGGGAATAAGTACT	[31]
	MMP1 (reverse)	TCAGAAAGAGCAGCATCGATATG	
Matrix metalloproteinase-2	MMP2 (forward)	CGCTCAGATCCGTGGTGAG	[31]
	MMP2 (reverse)	TGTCACGTGGCGTCACAGT	
Vascular endothelial growth factor	VEGF (forward)	AGACCAAAGAAAGATAGAGCAAGACAAG	[31]
	VEGF (reverse)	GGCAGCGTGGTTTCTGTATCG	
Platelet endothelial cell adhesion molecule	CD31 (forward)	ACTGGACAAGAAAGAGGCCATCCA	[361]
	CD31 (reverse)	TCCTTCTGGATGGTGAAGTTGGCT	

6A.3.12 Statistical Analysis

Data was expressed as mean ± 1 standard deviation. Statistical analysis was performed using one-way ANOVA with post-hoc Tukey test.

6A.4 Results

6A.4.1 Electrospinning

Scaffolds were successfully electrospun and showed a large fibre morphology with uniform fibre sizes and a random alignment (Figure 66Figure 57). Scaffolds had fibre diameters of 5.63 ± 0.65 μm, which are similar to the optimal fibre diameter for HUVECs deduced in Chapter 3.

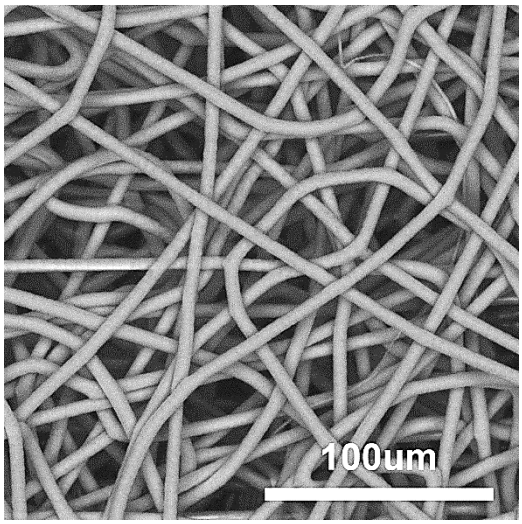

Figure 66: Representative SEM image showing the extra-large fibre diameter scaffold for seeding with HUVECs in the hydrostatic pressure secretome study.

6A.4.2 Protein Binding

The total mass of protein being bound onto the surface of the scaffolds was assessed using a Pierce™ BCA protein assay kit and can be seen in Figure 67. Interestingly, both secretome containing mediums had approximately the same amount of protein binding: 51.8ng and 47.2g, for the 50mmHg pressure secretome and the atmospheric pressure secretome, respectively.

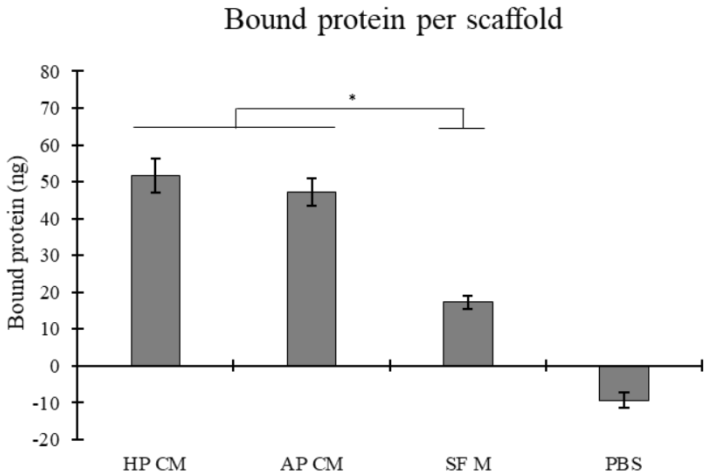

*Figure 67: Total mass of protein bound (cell secretome) to each scaffold. Hydrostatic pressure conditioned media (HP CM); atmospheric pressure conditioned media (AP CM); serum-free media (SF M); and PBS. N=6, error bars = SD. *p < 0.05.*

6A.4.3 Cell Viability

Cell viability results revealed some interesting trends between the four different scaffolds, as seen inFigure 68. Firstly, after 12 h of culture, cell viability was very similar across the four different scaffolds, suggesting that the binding of the different proteins did not have much of an effect on cell adhesion or cell viability. However, after 24 h and 48 h of culture, the two scaffolds that were functionalized with the secretome media (50 mmHg hydrostatic pressure and atmospheric pressure) showed higher cell viability than the serum-media scaffold and PBS conditioned scaffold.

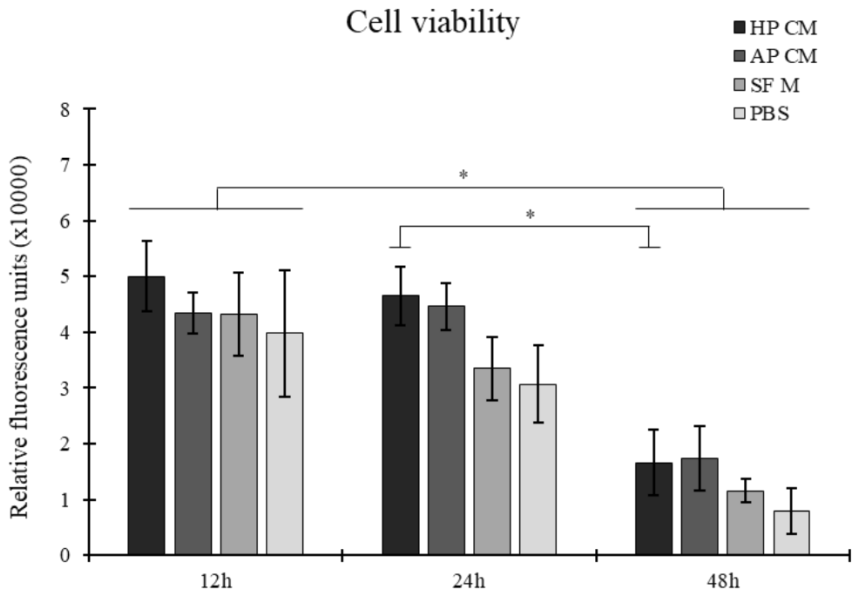

*Figure 68: Cell viability of seeded HUVECs on all four scaffolds after 12 h, 24 h and 48 h of culture. N=4, error bar = SD. *p < 0.05. Hydrostatic pressure conditioned media (HP CM); atmospheric pressure conditioned media (AP CM); serum-free media (SF M); and PBS.*

6A.4.4 Cell Imaging

DAPI (nuclei) and phalloidin (f-actin) fluorescence staining of the HUVECs on all four scaffolds at 12 h, 24 h and 48 h showed some interesting results, as seen inFigure 69. Interestingly, all four scaffolds were capable of maintaining the elongated phenotypic morphology of HUVECs up to 48h of culture in a serum-free environment.

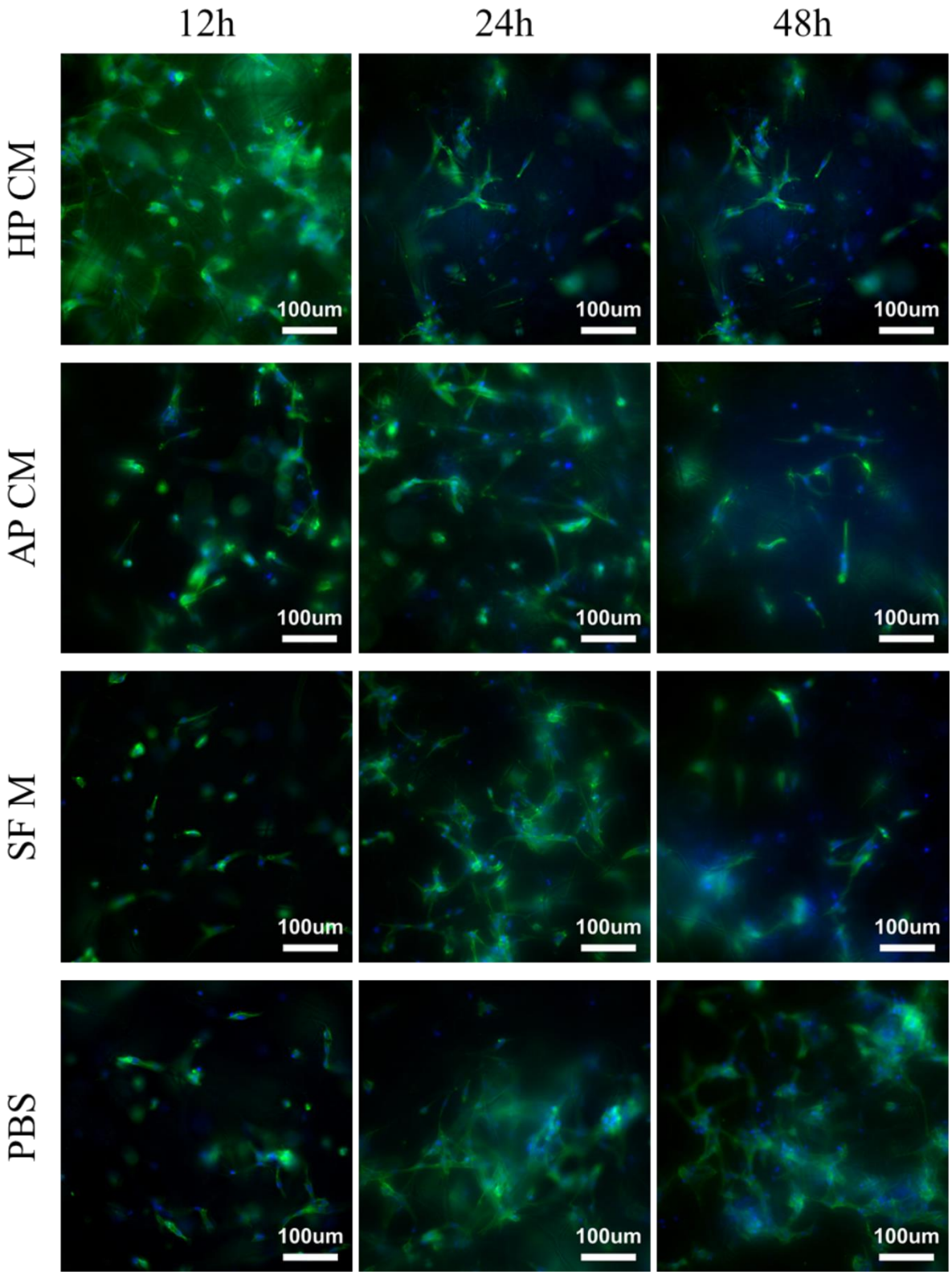

Figure 69: Representative DAPI (nuclei) and phalloidin (f-actin) stained HUVECs seeded on the four different scaffolds. Hydrostatic pressure conditioned media (HP CM); atmospheric pressure conditioned media (AP CM); serum-free media (SF M); and PBS.

6A.4.5 Reverse Transcription Quantative Polymerase Chain Reaction

RT-PCR results showed some interesting trends (Figure 70). Firstly, there was a general trend across all four scaffolds where the expression of CD31 increased over time. This suggests that the expression of CD31 is mostly mediated by cell maturity and not by the different proteins bound to the scaffold. Likewise, the expression of MMP1 increased with time for all four scaffold conditions. However, the expressions were higher on the three media conditioned scaffolds compared to the PBS conditioned scaffold. Similarly, MMP2 expression was slightly higher on the two scaffolds conditioned with secretome medium than the serum free medium and PBS conditioned scaffold. Interestingly, VEGF expression was very similar on all three scaffolds conditioned in medium, with all three higher than the expression on the PBS conditioned scaffold.

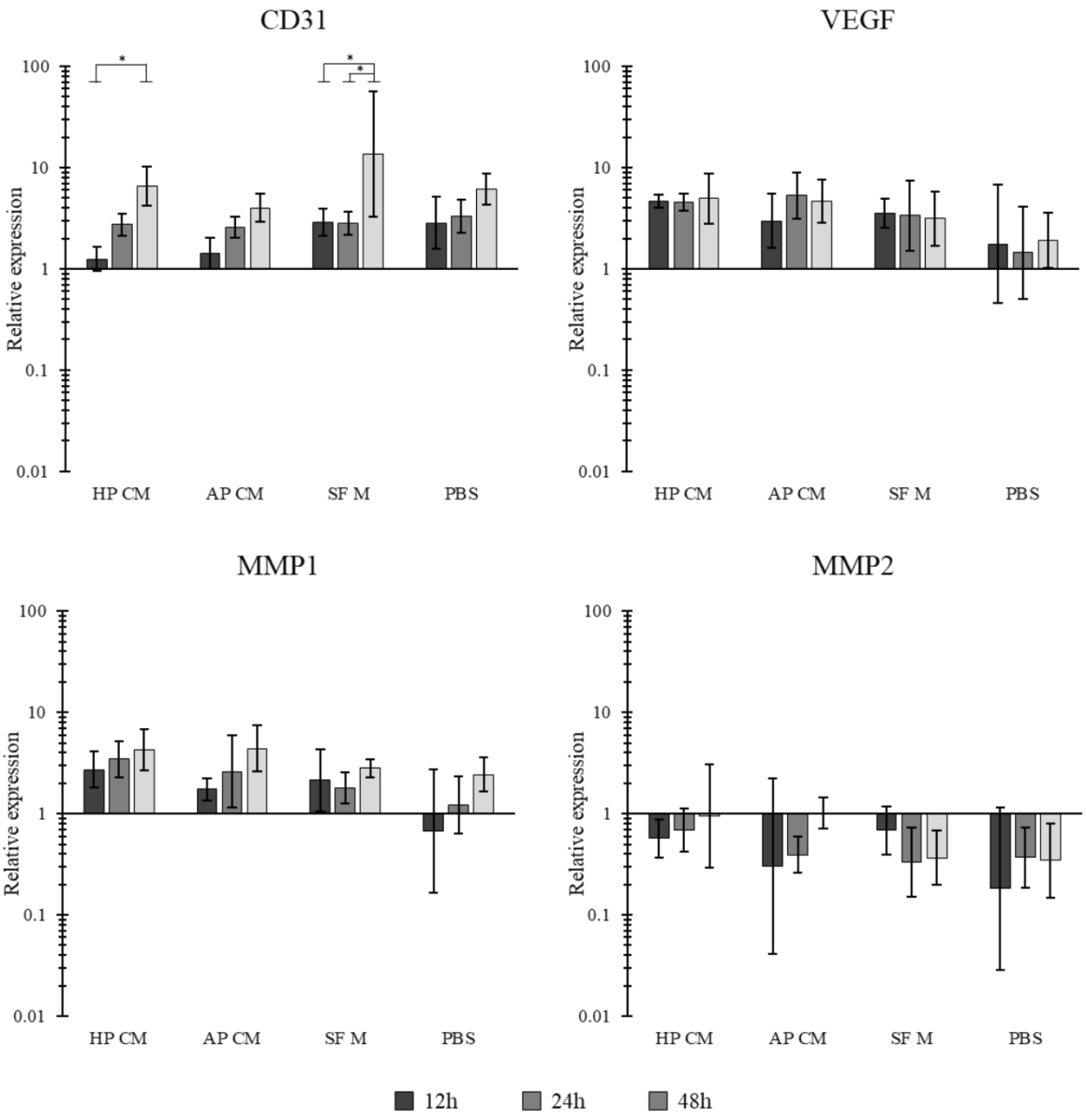

*Figure 70: Gene expression results on the seeded HUVECs of CD31, VEGF, MMP2 and MMP1 after 12 h, 24 h and 48 h of culture. HP CM = Hydrostatic pressure secretome conditioned medium, AP CM = Atmospheric pressure secretome conditioned medium, SF M= serum free medium. N=5, error bars = SD. *p < 0.05.*

6A.5 Discussion

Hydrostatic pressure has been shown to upregulate and downregulate a variety of different genes in ECs [458,480]. For example, work has shown that ECs downregulate the expression of vascular endothelial-cadherin when exposed to pressures of between 50-150 mmHg, resulting in increased proliferation and cell lengthening [458]. Likewise, work has shown that exposure to physiological pressures for as little as 4 h increases HUVEC proliferation through the activation of the α_v integrin

[480]. Therefore, it can be assumed that culturing HUVECs under 50 mmHg of hydrostatic pressure for 24 h would lead to alterations in their secretome profiles. Interestingly, work by P*rystopiuk, et al.* found that endothelial cells undergo a two-phase response to hydrostatic pressure: an initial response after 1 h and a further response to chronic application of pressure after 24 h [481]. They found that the majority of the chronic response is due to the increase in actin density and a loss of endothelial barrier cell function [481].

Interestingly, the expression of CD31 increased over time for all four scaffolds, suggesting that its expression was not affected by the binding of hydrostatic pressure HUVEC secretome. CD31 is an angiogenic gene involved in the creation of new vasculature, therefore its upregulation is desirable in the early stages of tissue formation [482]. VEGF, another angiogenic gene involved in cell migration and proliferation showed very little difference between the three media conditioned scaffolds across all three timepoints [450]. However, these three scaffolds did appear to promote a slight upregulation of VEGF compared to the PBS conditioned scaffold, albeit with no significance. While an upregulation of angiogenic genes such as CD31 and VEGF may be desirable in the short run, their overexpression has been associated with tumour formation in various tissue types [55,370].

Like CD31, MMP1 expression also increased over time for all four scaffolds. While this suggests that the expression of MMP1 is mostly mediated by cell maturity, the three media conditioned scaffolds did show slightly increased expression compared to the PBS conditioned scaffold. The same applies for MMP2 expression, where a relative downregulation was noted in the PBS conditioned scaffold compared to three media conditioned scaffolds. MMP1 and MMP2 are two genes associated with matrix remodelling and their relative upregulation in the media conditioned scaffolds suggests that the bound proteins might be stimulating collagen deposition [451].

Furthermore, interesting results were seen in the quantity of protein binding. The study found that more of the proteins found in the two conditioned medias bound to the scaffold compared to the serum-free media. As previously mentioned in Chapter 5, work by *Coad, et al.* found that different proteins with different structural makeups (66.5 kDa vs 53 kDa) had different binding affinities to

plasma coated polymers [449]. Therefore, the differences in the quantity of binding protein may be a results of the secreted proteins having different structures.

Cell viability showed some interesting trends between the four different scaffolds. At 24 h and 48 h, the cells seeded onto the two scaffolds that had been conditioned with secretome media (AP CM and HP CM) had a higher cell viability than that of the scaffolds conditioned with serum-free media and PBS. Furthermore, this trend was not noted after 12 h of culture, suggesting that the binding of proteins from the cell secretome had the effect of increasing cell viability but not cell attachment. Cell viability dropped for all four scaffolds over time due to the cells being cultured serum-free.

These results suggest that the binding of the proteins from the two secretome conditioned mediums did increase cell viability compared to the serum free media conditioned scaffold and the PBS conditioned scaffold. However, when looking at gene expression, the two secretome conditioned scaffolds and the serum free conditioned scaffold had very similar effects on gene expression, with the PBS conditioned scaffold showing differences for certain genes. This may suggest that the proteins found in the serum-free medium before undergoing secretome conditioning may be the ones that are having an effect on gene expression.

6A.6 Conclusions

In conclusion, proteins from three different types of serum-free culture media were bound to a scaffold; two of which had been conditioned with HUVEC secretome at two different pressures (50mmHg and atmospheric pressure). The proteins from these two conditioned mediums and a serum-free unconditioned media were bound to electrospun scaffolds and then seeded with HUVECs. These present results show that the binding of proteins from the two HUVEC conditioned mediums lead to higher cell viability after 48 h of culture compared to the serum-free media conditioned scaffold and the PBS conditioned scaffold. Furthermore, gene expression analysis suggested that the binding of proteins from all three mediums used lead to alteration in the expression of certain genes, such as VEGF, MMP1 and MMP2 compared to the PBS control. These results show the potential of binding

the secretome from mechanically stimulated HUVECs to an electrospun scaffold to enhance its biological potential for seeded cells.

Part B: Hypoxia and endothelial cells

6B.1 Introduction

Hypoxia in the vasculature is one of the leading causes of vascular diseases, such as pulmonary artery disease and atherosclerosis [483,484]. Therefore, it is of crucial importance that these hypoxic conditions are studied in *in vitro* experiments in order to more accurately mimic the diseased environment. Hypoxia's effect on ECs have been widely studied *in vitro*, with a range of results showing a cascade of biological responses [485]. For example, work by *Busse, et al.* found that ECs are responsible for the vasodilatory response of arteries to hypoxia [486]. Furthermore, work by *Faller,* found that prolonged exposure to hypoxia lead ECs to produce factors that induce SMC proliferation and remodelling [467].

Furthermore, while PCL only scaffolds seeded with ECs have previously been studied in hypoxic conditions [487], the incorporation of ECM and its effects on the performance of seeded ECs when cultured under hypoxic conditions have not been reported. Previous findings from Chapter 4 found that the incorporation of aorta ECM into the scaffold increased HUVEC cell viability. Therefore, this study aims to look at how PCL only and PCL/ECM scaffolds perform as platforms for seeded HUVECs in both normoxic and hypoxic culture conditions.

6B.2 Methods and Materials

6B.2.1 Decellularization

Bovine aorta ECM was perfusion decellularized using 0.5% w/s SDS, as described in section 2.2.

6B.2.2 Electrospinning

Decellularized ECM was milled into a powder and dissolved in HFIP at 0.25% w/v along with 8% w/v PCL. This created a scaffold with a 3:97 ratio of ECM:PCL. The PCL only scaffold was created using an 8% w/v solution of PCL in HFIP. Electrospinning parameters are shown in Table 29. More detail can be found in Section 2.1.

Table 29: Electrospinning parameters used to create the small diameter fibres (PCL and PCL/ECM blend) for the hypoxia study.

Needle bore (mm)	Flow rate (mL/h)	Total volume (mL)	Distance between needle tip and mandrel (cm)	Positive voltage (kV)	Negative Voltage (kV)	Mandrel rotational speed (RPM)
0.4	0.8	8	12	+14	-4	250

6B.2.3 Scanning Electron Microscopy

Scaffolds were imaged using a Hitachi TM4000 tabletop SEM as described in section 2.5.

6B.2.4 Cell Seeding and Culture

HUVECs were cultures using MCBD 131 medium supplemented with 5% v/v FBS; 1% v/v L-glutamine; 1% v/v penicillin/streptomycin; 1 mg/L hydrocortisone; 50 mg/L ascorbic acid; 2 μg/L fibroblast growth factor; 10 μg/L epidermal growth factor; 2 μg/L insulin-like growth factor; and 1 μg/L vascular endothelial growth factor. HUVECs (P7) were lifted at 80% confluence for scaffold seeding. Scaffolds were drip seeded at 50,000 cells/scaffold, as described in section 2.12. All scaffolds were cultured in Normoxia (16% O_2 / 5% CO_2) for 2 h to assist with cell binding. Scaffolds in the Normoxia group were left in the normoxic incubator. Scaffolds in the Hypoxia group were transferred over to an incubator set at 2% O_2 / 5% CO_2. The timepoints started after this 2 h period of normoxic incubation. See section 2.12 for more detail on cell culture.

6B.2.5 Cell Viability

The CellTiter-Blue® assay was performed as per manufacturer's instructions at timepoints of 12 h, 24 h and 48 h, as described in section 2.13.

6B.2.6 DNA Quantification

DNA quantification was performed as per manufacturer's protocol using a Quant-IT™ Picogreen® dsDNA assay. The assay was used to calculate the amount of protein bound to each scaffold. See section 2.16 for more details.

6B.2.7 Cell Imaging

Briefly, scaffolds were permeabilized in Triton-X solution before being stained in Phalloidin-iFluor™514 conjugate and 300 nM DAPI. Scaffolds were imaged using a Zeiss Axio Imager 2 microscope. See section 2.17 for more detail.

Cell seeded scaffolds visualized using SEM were fixed in 4% glutaraldehyde overnight before undergoing osmium tetroxide staining. Scaffolds were imaged using a Hitachi TM4000 tabletop SEM. See section 2.17 for more detail.

6B.2.8 Reverse Transcription Quantative Polymerase Chain Reaction

The method used for PCR is described in section 2.18. Forward and reverse sequences were designed and are displayed in Table 22. Relative quantification of RT-PCR results was carried out using the $2^{-\Delta\Delta ct}$ method [350]. Gene expression levels were expressed relative to GAPDH (housekeeping gene) and normalised to 70% confluent HUVECs on tissue culture plastic. More detail can be found in Section 2.18.

Table 30: Primer sequences used for RT-PCR on seeded HUVECs in the hypoxia study.

Gene	**Primer**	**Sequence**	**Reference**
Glyceraldehyde 3-phosphate dehydrogenase	GAPDH (forward) GAPDH (reverse)	GTCTCCTCTGACTTCAACAG GTTGTCATACCAGGAAATGAG	[31]
Basic Fibroblast Growth Factor	FGF2 (forward) FGF2 (reverse)	CACCTATAATTGGTCAAAGTGGTTG AAACGAGGGAGAAAGGATGGA	Self-designed
Hypoxia-inducible factor 1-alpha	HIF1-α (forward) HIF1-α (reverse)	ACTTGGCAACCTTGGATTGG GTGCAGTGCAATACCTTCCA	Self-designed
Nitric Oxide Synthase 3	eNOS (forward) eNOS (reverse)	AGATGTTCCAGGCTACAATCCGCT TGTATGCCAGCACAGCTACAGTGA	[361]

6B.2.9 Statistical Analysis

Data was expressed as mean ± 1 standard deviation. Statistical analysis was performed using one-way ANOVA with post-hoc Tukey test.

6B.3 Results

6B.3.1 Electrospinning

SEM images of the electrospun scaffolds showed that each scaffold had uniform fibre diameter and a random alignment, as seen in Figure 71. The PCL scaffold had a fibre diameter of 2.19 ± 0.25 µm and the aorta ECM scaffold had a fibre diameter of 1.67 ± 0.42 µm.

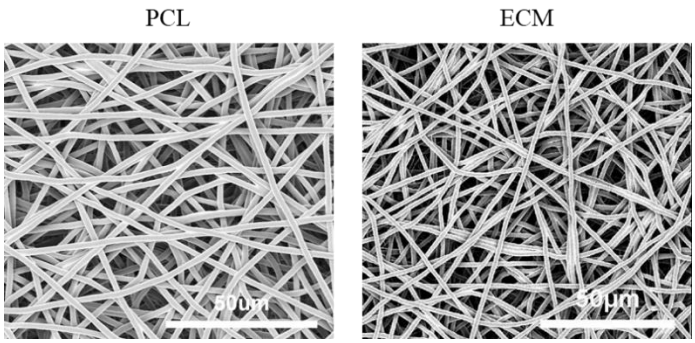

Figure 71: Representative SEM images of the two electrospun scaffolds. The PCL scaffold is composed of 100% PCL. The ECM scaffolds is 97% PCL and 3% ECM. Both scaffolds have a small diameter morphology.

6B.3.2 Cell Viability

Cell viability results showed some interesting results, as seen in Figure 72. There was no real difference between the HUVECs cultured on the PCL scaffold and the ECM scaffold in a hypoxic environment, however, under normoxic conditions the HUVECs on the PCL scaffold showed significantly higher viability than those on the ECM scaffold at 12 h and 48 h of culture.

Furthermore, significance was also noted between the HUVECs culture on the ECM scaffolds under hypoxic and normoxic conditions after 12 h of culture, with the hypoxic culture showing higher viability. Likewise, the HUVECs cultured on the PCL scaffold had significantly higher viability after 24 h of culture when cultured in hypoxic conditions compared to normoxic conditions.

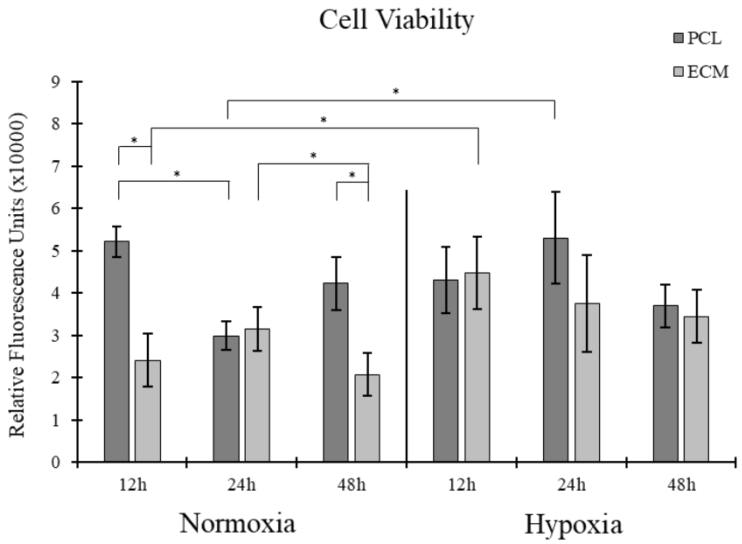

Figure 72: Cell viability results for HUVECs seeded on the two different scaffolds cultured under both normoxic conditions and hypoxic conditions. N=4, error bars = SD.

6B.3.3 DNA Quantification

DNA quantification results followed the exact same trends as the cell viability results, as seen in Figure 73. The PCL scaffold showed significantly higher quantities of DNA after 12 h and 48 h of culture in normoxic conditions compared to the ECM scaffold. Furthermore, significance was also seen between the ECM scaffolds after 12 h of culture and the PCL scaffolds after 24 h of culture, with the hypoxic culture conditions showing higher DNA content in both cases.

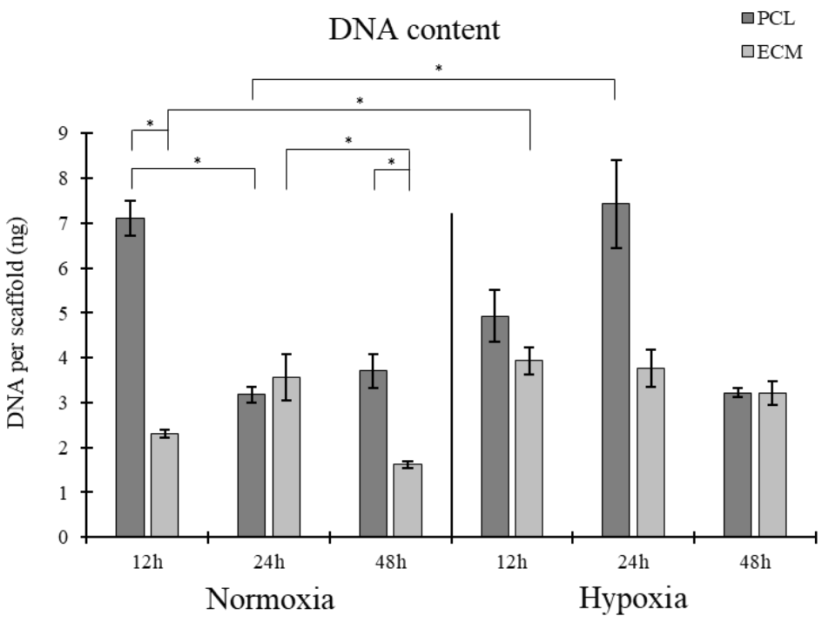

Figure 73: DNA content of the seeded HUVECs on each scaffold cultured under both normoxic and hypoxic conditions. N=4, error bars = SD.

6B.3.4 Cell Imaging

Representative DAPI and phalloidin stained cells on both scaffolds under normoxic and hypoxic conditions can be seen in Figure 74. Both scaffolds under both culture conditions showed good cell spreading after 12 h of culture. Interestingly, the HUVECs on the ECM scaffold cultured in normoxic conditions after 48h showed more elongation, which is a key phenotypic marker of healthy HUVECs [453].

The representative SEM images of HUVECs seeded onto the two scaffolds and cultured for 48 h under both normoxic and hypoxic conditions showed some interesting results, as seen in Figure 75. In both normoxic culture and hypoxic culture the ECM scaffold showed increased cell coverage compared to the PCL scaffold. The ECM scaffold had approximately 80% and 70% confluence when cultured in normoxic and hypoxic conditions, respectively. The PCL scaffolds had approximately 10% and 20% confluence in normoxic and hypoxic conditions, respectively.

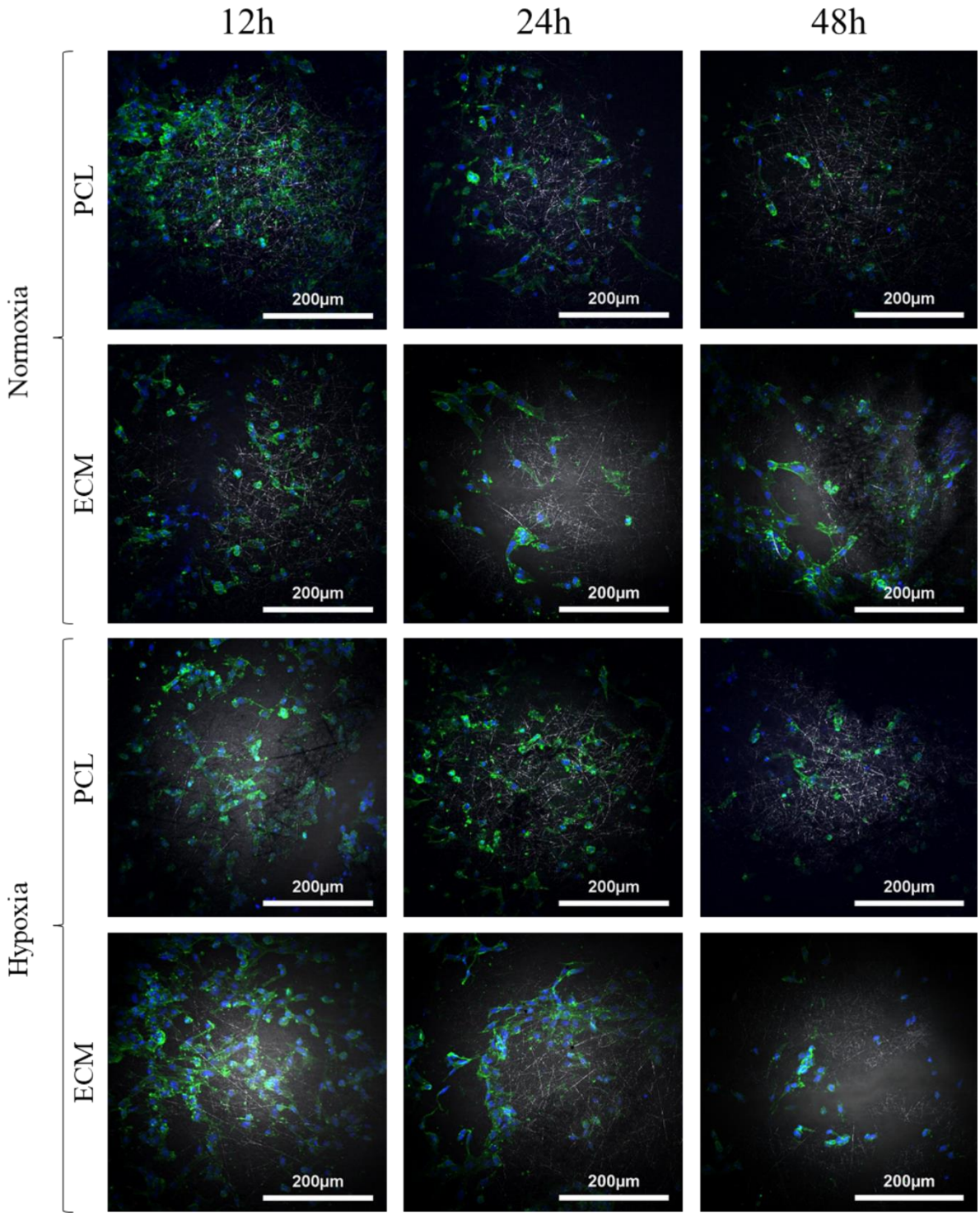

Figure 74: Representative DAPI (blue, nuclei) and phalloidin (green, f-actin) stained HUVECs on both scaffolds cultured under normoxic and hypoxic conditions at 12h, 24h and 48h of culture.

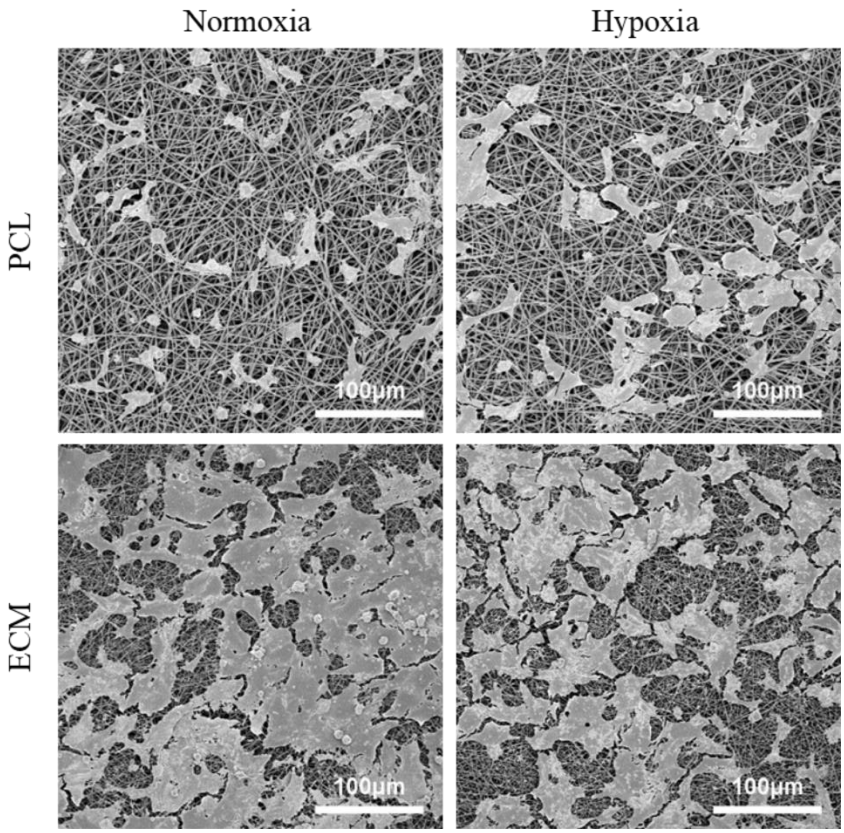

Figure 75: Representative SEM images of osmium stained HUVECs on both scaffolds (PCL and ECM/PCL blend) under normoxic and hypoxic conditions after 48h of culture.

6B.3.5 Reverse Transcription Quantative Polymerase Chain Reaction

RT PCR analysis showed some interesting trends in how the scaffold composition and the culturing conditions affected the seeded HUVECs, as seen in Figure 76. Firstly, there was a general trend whereby FGF2 expression was lower in the cells cultured in a hypoxic environment. FGF2 is a key gene for EC angiogenesis [58]. The expression of eNOS showed very little difference between the two scaffolds and the two culture conditions. It is a central regulator of EC function and plays an important role in the maintenance of endothelial homeostasis [488]. Likewise, the expression of HIF1a showed no real trend across the two different scaffolds and two culturing conditions. HIF1a is a gene involved in apoptosis in hypoxic conditions [489].

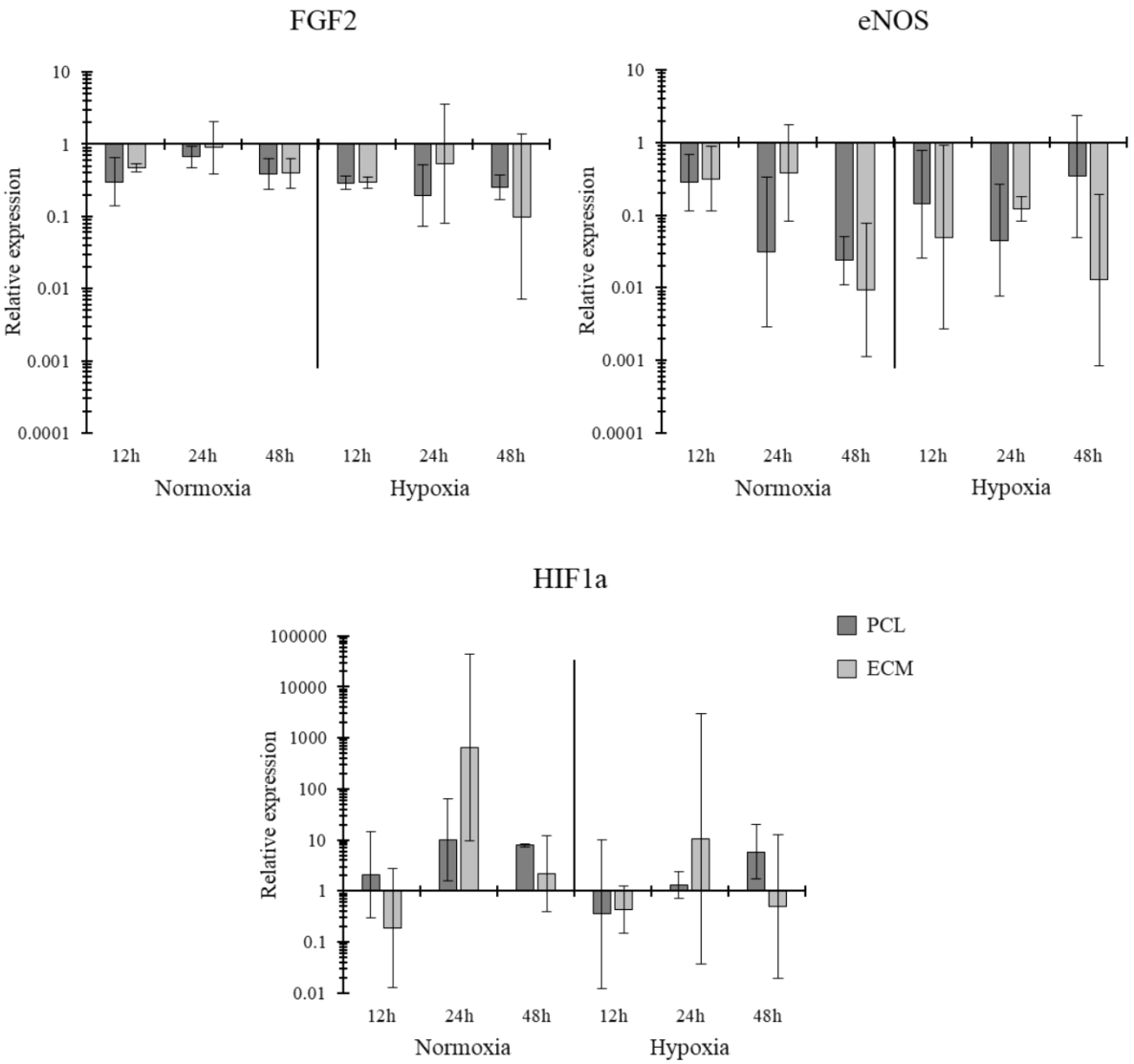

Figure 76: Gene expression results of the seeded HUVECs for three genes: FGF2, eNOS and HIF1a. Data normalized to 80% confluent HUVECs on tissue culture plastic. N=4, error bars = SD.

6B.4 Discussion

Polymers and decellularized ECMs both have their advantages when used as materials in scaffolds [246,363]. By combining the two materials, the aim is to harness the beneficial properties of both to create a reproducible scaffold that contains the bioactive factors of the ECM. Likewise, running experiments in hypoxic conditions allows for a more accurate image of how the scaffolds will perform in an *in vivo* environment, where oxygen levels are often reduced, resulting in the onset of various diseases [490].

Cell viability results showed no real difference between the scaffolds cultured under hypoxic and normoxic conditions. Interestingly, under hypoxic culture, the two scaffolds showed no real difference in cell viability across all three timepoints, suggesting that the ECM scaffolds would be able to sustain cell survival in an *in vivo* environment where hypoxic conditions are present. Work by *Jundzill, et al.* has shown that conventional PCL only scaffolds do improve vascularization when implanted into a *in vivo* hypoxic environment [491]. Therefore, being able to create a biofunctionalized scaffold that contains native ECM components and showing that it performs in a similar way to PCL only scaffolds in an *in vitro* environment is beneficial for vascular tissue engineering applications. As show in Chapter 4, incorporating ECM into scaffolds had the effect of altering their mechanical properties to more closely resemble that of native tissues. Therefore, having a platform that allows for changes in the mechanical properties of the scaffold, but does not alter cellular performance is desirable for a range of tissue engineering applications where local mechanical properties can vary. For example, studies have shown different stiffness values for the saphenous vein, ranging from 2.25 MPa to 23.7 MPa [301,302].

Furthermore, the SEM images of osmium stained HUVECs on the two scaffolds under both culture conditions show that the ECM scaffold was able to maintain higher confluency of cells than the PCL only scaffold. These results differ slightly from the cell viability results which suggest no differences between the cells. However, cell viability is a metabolic activity assay which does not necessarily correlate to the total number of HUVECs on the scaffold. Therefore, cell viability alone cannot be used to conclude the number of cells on the scaffold.

Interestingly, eNOS (a central regulator of EC function and endothelial homeostasis) has been shown to downregulate in ECs under hypoxic conditions due to the presence of miR-200b [488,492]. The present study's results show very little differences between the scaffolds cultured in normoxia or hypoxia. However, the study by *Janaszak-Jasiecka, et al.* found that the majority of this downregulation of the eNOS gene happened in the first 12 h of culture with no more downregulation noted after 16 h of culture [492]. Therefore, the timepoints used in this study may not give an overall image of how the cells

are responding in the first 12 h of culture, where the majority of eNOS downregulation has been noted.

FGF2 is responsible for neovascularization and angiogenesis [58]. Its upregulation is heavily linked with tumour formation [58]. The present study's results show no significance. Likewise, HIF1-alpha is a gene responsible for apoptosis in ECs when they are subject to hypoxic conditions [489]. The present study's results found very little difference between the two different culture environments. This may suggest that these electrospun scaffolds possess shielding properties against the upregulation of FGF2 and HIF1-alpha. This may suggest that these scaffolds both slow down angiogenesis and apoptosis in a hypoxic environment.

6B.5 Conclusions

In conclusion, this study showed that PCL/ECM scaffolds and PCL scaffolds were both capable of maintaining cell viability when cultured in a hypoxic environment. The incorporation of ECM into the fibres had no real effect on the level of gene expression for FGF2, eNOS and HIF1-α when cultured in both hypoxic and normoxic conditions. However, as previously shown, the incorporation of ECM alters the mechanical properties of the scaffold. Therefore, being able to create different platforms with different mechanical properties without altering gene expression in a hypoxic environment has benefits for vascular tissue engineering where hypoxia is prevalent and is often the main cause for the onset of vascular disease.

Chapter 7: Discussion and Conclusions

7.1 Discussion

7.1.1 Discussion of Results

The aim of this thesis was to investigate the effect of altering the composition and morphology of electrospun scaffolds on the function of two different vascular cell sources: HUVECs and HUVSMCs. Firstly, the effect of changing electrospun fibre diameter was investigated. Following on from this, the effect of incorporating two different sources of decellularized ECMs into the electrospun PCL fibres was studied [493,494]. Finally, the effect of binding cell secretome to an electrospun scaffold and how this alters cellular behaviour was investigated. The thesis then looks at two ways of altering culture environment in combination with the electrospun scaffolds.

Currently vascular disease accounts for upwards of 30% of all deaths across Europe [110]. One of the major contributors are diseases such as atherosclerosis and hyperplasia which result in the gradual narrowing of vessels, subsequently leading to blockages, which will eventually lead to further complications and death [90,108]. These blockages are often treated with bypass grafts, a relatively simple procedure that deviates blood flow around a blockage through a new passage. While bypass grafting is a fairly standard procedure, there are still many limitations associated with the use of synthetic grafts. Most notably, a large reduction in patency after only a few years when dealing with small diameter vessels [129]. Therefore, it is imperative that further study is carried out looking at how the bypass graft material and structure can be enhanced to improve mechanical properties and cell survival.

Electrospinning is a scaffold manufacturing technique that creates a network of homogenous fibres that resemble to collagenous network found in many different ECMs [495]. Electrospun scaffolds have been widely used in cardiovascular tissue engineering, with applications ranging from bypass grafts and stents to heart valves [176,179,214,398,400]. The polymer chosen in this thesis was PCL due to its biocompatibility, FDA approval and ease of use in the electrospinning process [218,496,497]. One advantage of using PCL is its controllable degradation rate and non-toxic degradation by-products [364,413]. Depending on the starting molecular weight of the PCL, it can take up to 2 years to degrade to a point where it loses its mechanical strength, allowing plenty of time for the engrafted

cells to deposit their own ECM [364,497]. Furthermore, PCL has also shown good electrospinning potential when used in conjunction with decellularized ECM and proteins, improving the bioactive properties of the scaffold [198,199,386]. Additionally, studies have shown that proteins and peptides can be grafted onto PCL, opening up the potential of binding cell secretome to these electrospun scaffolds [25]. Other polymers have also been widely used in the realm of vascular tissue engineering, such as poly (D,L-lactide-co-glycolide) and polylactic acid [352,355,498].

Scaffold morphology and topography have both shown to have drastic effects on cellular performance for a variety of different cell types [177,194,499]. This has also been shown in cardiovascular tissue engineering, with work looking at endothelial cells, smooth muscle cells and cardiomyocytes [355,357,500]. Previous studies have shown that altering the morphology and topography of polymer scaffolds had effects on both the spreading and proliferation of endothelial cells [357]. Additionally, previous work has also shown that fibre alignment had a big impact on the expression of α-smooth muscle actin in vascular smooth muscle cells; a key marker of smooth muscle cell maturity [454]. The work conducted in this thesis found some interesting results when scaffold morphology was altered (Chapter 3). Increasing the fibre diameter had the effect of increasing the infiltration depth of the both HUVECs and HUVSMCs. This finding was somewhat expected as the pore width increased linearly with the fibre diameter, creating bigger voids for the cells to penetrate into the scaffold. Studies have shown that increasing the size of pores does increase the ease at which cells can penetrate the scaffold [385,501]. Interestingly, for both the HUVECs and HUVSMCs, the jump between a surface monolayer cell culture and a 3D cell culture happened between the large (3.37 µm and 3.91 µm, respectively) and extra-large (4.83 µm and 5.91 µm, respectively) fibre diameters. 3D cell cultures of endothelial cells have shown favourable results with respect to the expression of key proteins [34,366]. This phenomenon can be attributed to 3D cell cultures more closely mimicking the native ECM and may explain why this study found increases in the gene expression of CD31; a key angiogenic gene, when fibre diameter was increased, allowing for the infiltration of cells. However, with the HUVSMCs, the small fibre diameter (0.77 µm) lead to higher cell viability along with the formation of a cell monolayer, which in turn showed the 'hill and valley' morphology that is commonly seen with SMCs *in vitro*

[389,390]. These results show that the smallest fibre diameter is well suited to the culture of HUVSMCs, however, this may not be optimal for long-term 3D cell cultures *in vivo*, where cell infiltration is required, as VSMCs are found interwoven around the ECM in thick layers of 40 to 60 cells [372].

The next set of studies (Chapter 4) looked at how the incorporation of two different bovine ECM sources into the PCL scaffold altered their mechanical properties and biological properties as platforms for cell seeding. Work has previously shown that the incorporation of ECM into electrospun fibres has benefits for meniscal and cartilage tissue engineering applications [198,199]. They found that ECM could easily be dissolved into a polymer/HFIP solution at high concentrations of up to 8% w/v. In these studies, ECM was dissolved into a PCL/HFIP solution at concentrations of 0.25% w/v and 1% w/v, resulting in a homogenous solution that electrospun uniform and consistent fibres. Both studies looking at aorta ECM and heart ECM, which showed that the incorporation of ECM did have an effect on the seeded HUVECs and HUVSMCs. Furthermore, the incorporation of ECM had clear effects on the mechanical properties of the scaffold. In summary these results indicate that incorporating ECM can be used to modify mechanical and biological responses in scaffold.

Interestingly, all of the scaffolds used in this thesis, with increasing fibre diameters and different quantities of ECM in them were found to have stiffnesses that fell in a similar realm to those noted in the literature for native vessels. The stiffnesses of the scaffolds ranged between 1.42 MPa and 22.58 MPa depending on the particular strain bracket being looked at. Values found in literature include longitudinal stiffnesses of 23.7 MPa and circumferential stiffnesses of 4.2 MPa and 2.25 MPa for the saphenous vein [301,302]. While there are a range of stiffnesses found for native vessels, the scaffolds designed in these study all fall within these values, suggesting that they would be capable of enduring the local environment seen by the native vessels. Moreover, the range of values noted in these studies shows the flexibility that electrospinning PCL scaffold possesses.

Next, the secretomes of two cell types (HUVECs and HUVSMCs) were collected in serum-free medium and then bound to the surface of scaffolds (Chapter 5). Interestingly, a higher quantity of the proteins in the HUVEC condition media bound onto the scaffold compared to the HUVSMC conditioned media. This may indicate that the proteins released from the two cell types have different

structures, as work by *Coad, et al.* found that different proteins had different affinities for plasma treated polymers [449]. Furthermore, the binding of HUVEC secretome lead to a slight decrease in the expression of several key genes for the seeded HUVECs, whereas the binding of HUVSMC secretome lead to very little change in the gene expression of seeded HUVSMCs.

Finally, the effect of two different environmental factors were studied to assess the performance of electrospun scaffolds in more physiologically relevant scenarios: hydrostatic pressure and hypoxia (Chapter 6). Firstly, a secretome conditioned HUVEC media was generated under hydrostatic pressures and was bound onto the surface of PCL scaffolds. These results showed that the binding of proteins from this hydrostatic pressure conditioned media and a similar atmospheric pressure conditioned media increased cell viability compared to the scaffolds conditioned with serum-free media and PBS. Additionally, some trends were noted in gene expression between the PBS conditioned scaffold and the three other scaffolds, suggesting that the main proteins involved in altering the gene expression may be found in the serum-free media before any conditioning takes place. Furthermore, the effect of hypoxia on PCL and ECM/PCL scaffolds was assessed. Results showed that the ECM scaffold lead to a higher cell confluency than the PCL scaffold when cultured in hypoxia and normoxia. These studies show the potential of these scaffolds when used in physiologically relevant environments and the importance of preconditioning scaffolds.

Overall, this thesis has shown that altering both morphology and composition of electrospun scaffolds influences the mechanical properties of the scaffold and the performance of seeded vascular cells.

7.1.2 Methods Review

The two cell lines used in this thesis: HUVECs and HUVSMCs, have both been widely used in *in vitro* experiments to study all aspects of vascular disease including vascular function and hypoxia [25,31,460,502–505]. These cell lines allow us to assess the functionality of different experimental conditions without the requirement of expensive, time consuming studies using animal models. Furthermore, two vascular cell lines from the same source (human umbilical vein) were used in these studies to keep consistency between the separate experiments.

While electrospinning has been widely used in tissue engineering applications and allows for a range of different scaffold morphologies to be created [177,220], the methods used in this thesis do possess some drawbacks. Results showed some variability between the fibre diameters achieved across studies. Temperature and humidity have been shown to drastically effect the outcome of electrospinning [506]. A study by *De Vrieze, et al.* found that the average diameter of electrospun fibres can change by up to 100% by changing ambient air temperature from 10°C to 20°. Likewise, they found that increasing relative humidity to above 60% lead to no fibre formation [506]. Therefore, creating an environment where temperature and humidity can both be controlled will improve the repeatability of these studies and ensure that fibre sizes stay uniform.

Decellularization of natively sourced tissues has been on the increase in tissue engineering, where wasted tissue can be used for its biochemical properties [198,199,256]. This study used heart and aorta ECMs from bovine sources. The samples were sourced from a local abattoir and would have been wasted otherwise. Using bovine heart and aorta ECM does have its benefits for tissue engineering due to the relatively similar structural characteristics found in them compared to their human counterparts [19,20]. Additionally, bovine ECMs have been used in FDA approved medical devices [257]. However, the use of a human source of ECM would have created a more physiologically accurate electrospun scaffold for *in vitro* experimentation.

The decellularization method used in this thesis relies on the perfusion of 0.5% SDS through the tissue. While SDS is a widely used detergent for the removal of cellular content [271,507], it does have its shortfalls. Overexposure to SDS and using SDS at too high a concentration have both been shown to damage the ECM [261]. Work by *He, et al.* showed that increasing the SDS concentration to above 0.25% w/v had detrimental effects on the retention of VEGF and bFGF in decellularized kidney ECM. They also showed that increasing exposure time from 4 h to 8 h significantly reduced sulfated glycosaminoglycan content in the ECM [261]. While these results don't directly translate across to the vascular tissue sources used in this thesis, it is worth considering how the decellularization protocol used in this thesis (0.5% w/v SDS and 36 h of decellularization) is altering the ECM's composition. Other decellularization methods have been successfully utilised in tissue engineering, including the

use of other detergents such as Triton X-100 and CHAPS; the use of enzymes such as trypsin and deoxyribonucleic; and mechanical methods such a high pressure and freeze-thaw cycles [263]. The use of other detergents and freeze-thaw cycles can be less detrimental to the structure of the ECM, but may result in less decellularization [508,509]. Enzymes, like the use of SDS have also been shown to have effects on the structural function of the decellularized tissue [510].

While HFIP is a widely used solvent for electrospinning purposes due to its high stability and uniform fibre creation, it does have its drawbacks when used with ECMs and proteins [256,310,311]. Studies have shown that collagen (one of the major components of the ECMs used) can have approximately 45% of its triple helical structure denatured into gelatin in the presence of HFIP [276]. While these FTIR results confirm that ECM protein is still present in the tissue after decellularization, the Amide I and Amide II bonds are characteristic of both collagen and gelatin, therefore no conclusion can be made on structural makeup of the ECM after electrospinning. The quantity of collagen found in the ECM before and after contact with the HFIP could be measured using an alkaline hydrolysis/hydroxyproline assay, which is sensitive to levels well below native collagen levels [511]. Nonetheless, collagen has been widely used with HFIP for the manufacturing of electrospun scaffolds, with results showing a positive influence on seeded cells [256,375].

One method used to assess the efficacy of decellularization was DNA quantification with a Quant-iT PicoGreen dsDNA assay [340]. Furthermore, the Quant-iT PicoGreen dsDNA assay was also used to measure the DNA content found on the seeded scaffolds. This assay uses fluorescence and is 1000 times more sensitive than conventional absorbance methods, capable of measuring down to 250 pg/mL. There are alternative methods widely used to measure the DNA content such as the use of flow cytometry or a Nanodropper [512,513]. This assay used in conjunction with cell viability can give a good overarching image of the number of cells. However, due to the porous nature of these scaffolds, many of the detached dead cells may still be entrapped within the structure of the scaffold and would increase the DNA contents of the scaffold.

Cell viability was measured using a CellTiter-Blue® assay, which relies on oxidation-reduction to indicate the mitochondrial activity of the cells. Mitochondrial activity is directly linked to the

metabolic viability of cells and not the total number of cells, therefore cell numbers cannot always be concluded from the CellTiter-Blue® assay. Studies have shown that these types of oxidation-reduction assays can give false-positives and that substrates found within the media can interfere with the viability measurements [514,515]. Furthermore, the accuracy of results with these assays could be affected by the porous nature of these scaffolds. If the active agent remains entrapped within the porous scaffold, it would not be accounted for when analysing the fluorescence of the sample [516]. In order to reduce the likelihood of this occurring, the plates were mixed before measurements were taken.

Sterilization in this thesis was achieved using 70% v/v ethanol, which is sufficient for *in vitro* studies, but is not a clinically translatable method of terminal sterilization. Studies have shown that some methods of terminal sterilization do have detrimental effects on the structure, mechanical integrity and cell hosting abilities of decellularized ECM [257,324]. The majority of currently marketed biological devices that use decellularized ECMs are terminally sterilized using either gamma irradiation, ethylene oxide or electron beam processing, which shows that decellularized ECMs can be efficiently sterilized before being translated to the clinic [517]. Furthermore, peracetic acid as a terminal sterilization method has been shown to have no effect on the structure or mechanical strength of ECM, whilst also maintaining its ability to host cells [324]. Therefore, translating this work to a clinical setting where an approved terminal sterilization method is required would rely on one of the aforementioned sterilization methods.

Plasma coating was used in Chapter 6 as a means of increasing the hydrophilicity of the scaffold and the quantity of available hydroxyl groups for the binding of proteins. While this is a regularly used method to coat polymer scaffolds [296,297,449], the application of plasma onto the scaffold needs to be even across the whole scaffold and over all the scaffolds being coated. Plasma coating significantly increased the amount of protein that could bind to the scaffold's surface, therefore it was imperative that all the scaffolds were equally coated. This was achieved by limiting the number of scaffolds being coated at one time, ensuring there was no overlap between adjacent scaffolds.

EDC and NHS treatment was used to further functionalize the surface of the scaffold. This is a widely used technique that has shown to help with the binding of proteins and peptides [331,336]. It is imperative

that EDC and NHS is completely removed from the surface of the scaffold before the binding of protein and subsequent cell seeding. Remnant EDC and NHS can lead to the formation of unwanted by-products that can negatively impact the seeded cells [518]. This can happen when the concentration of EDC and NHS are too high. Likewise, using a concentration that is too low will lead to incomplete activation of the polymer surface, reducing the quantity of bound protein. Furthermore, the activation yield achieved by the EDC/NHS functionalization was not assessed in this study. This can be achieved using the Beer-Lambert law which looks at the ratio of FTIR peaks at two wavelengths (1772 cm^{-1} and 2615 cm^{-1}) [331]. However, *Guler, et al.* found that the EDC/NHS concentrations with the highest activation yield were also the concentrations that lead to the most protein binding. Therefore, subsequent studies went forward with the 0.5 mM NHS and 0.5 mM EDC concentrations which led to the most BSA binding in the feasibility studies. Two further methods which have also been used in literature to assess the presence of amine bonds are the Ninhydrin test and Chloranil test [447]. The Chloranil test can also be used quantitatively to measure the amount of amine bonds being closed off by binding protein [447].

RT-PCR was used to analyse the gene expression profiles of the seeded cells. While this method gives an indication of how the cells are reacting to their substrates, gene expression is not directly correlated to protein synthesis due to the complicated post-translational mechanisms involved [519]. The primers used in this thesis were either taken from literature, where they had been shown to work effectively under similar experimental conditions to the equipment used in this thesis, or they were designed online. Primers were designed to cross exon-exon junctions, which reduces the possibility of genomic DNA amplification. Furthermore, optical density was used to measure the purity of the RNA post purification to ensure there was no contamination from the phenol and PCL [520]. Further work is required to assess cell function and protein production including the use of enzyme linked immunoabsorbant assay (ELISA) and mass spectrometry [521,522].

Tensile testing was used as the predominant method of mechanical analysis for these scaffolds as means of deducing how the mechanical characteristics of the scaffolds influences cells. Stiffness values (Young's modulus) were deduced from the stress vs strain data. In order to ensure minimal

error was introduced during the handling process, a C-shaped card mount was created to stabilise the sample before testing. This ensured the sample was the correct gauge length each time. Any slack in the sample would result in a larger gauge length which would affect the results. Error can also be introduced through the use of different strain rates. Studies have shown that changing the strain rate can have drastic effects on the measured stiffness, ultimate tensile strength and yield stress of polymers [523,524]. Therefore, the strain rate was kept consistent between studies. Further error can be introduced through the incorrect measurement of sample width and thickness, as these measurements are required to deduce the cross-sectional area. This was reduced by taking several measurements across each sample.

Scaffold seeding was a potential source of error between the different scaffolds. Care was taken when seeding to ensure the cells were always in suspension and hadn't sunk to the bottom of the cell/media suspension. Scaffolds were seeded across groups and timepoints to ensure that any time-dependant error (such as sinking cells) was spread across the groups and not isolated to a particular group.

The imaging of cells was performed using staining and fluorescent imaging. DAPI (nuclei) and phalloidin (f-actin) were used to stain for the cell nucleus and actin filaments within the cell cytoplasm. They are widely used to visualize the structure and morphology of the cell [525]. However, this is a qualitative technique that only allows for cell visualization. Immunohistochemical (IHC) staining allows for certain desired antibodies to be bound to their respective antigens. When used alongside appropriate negative and positive controls they can be indicative of antigen presence and can be used qualitatively [526].

7.1.3 Future Work

Only four different fibre diameters were studied in each of the sections of Chapter 3. Moving forward, it would be beneficial to look at a wider range of fibre diameters in order to analyse the full spectrum of fibre diameters and their effect on the seeded cells. In both studies, the depth of cell infiltration drastically increased between the large and extra-large fibre diameters, therefore looking at diameters in between these two scaffolds would allow us to see at exactly what fibre diameter infiltration starts

to happen. Additionally, trying to match the fibre diameters between the two studies (HUVECs and HUVSMCs) would allow us to compare the results of the two studies.

The rate of PCL and ECM degradation need to be considered. Implants need to be able to maintain structural integrity until adequate tissue regeneration has taken place. The rate at which the PCL is absorbed and metabolised needs to be carefully considered to ensure the proper support is given to the regenerating tissue. Work by *Sun, et al.* found that there was a linear correlation between the loss of molecular weight of PCL and time elapsed *in vivo* [497]. Further work by *Lam, et al* found that the mechanical strength of PCL was maintained until about 15,000 Mw [364]. These results show that the molecular weight of the PCL can be easily tailored to match the regeneration rate of the native tissue once it is known. Animal studies should be run to get an idea of the approximate regeneration rate of the diseased tissues when in contact with these scaffolds. This would allow us to alter the molecular weight of the PCL used. Furthermore, the degradation of the scaffold's ECM components into the media needs to be studied, as the effect of incorporating ECM into PCL on the overall mechanical properties is not known. Work by *Marrese, et al.* found that the gelatin component of PCL/gelatin electrospun scaffolds left the fibres and dissipated into the media [527]. They used AFM to measure the surface roughness of the scaffold and found it increased as the gelatin left the fibres [527]. This method could be used in future studies to look at how much of the ECM is leaving the fibres. Likewise, a BCA protein assay could also be used to measure any increases in media protein content. Alternatively, the PCL/ECM fibres could be cross-linked to maintain protein content in the fibres, however, this can reduce scaffold porosity and studies looking at polymer/collagen electrospun scaffolds found that this does not completely remove the problem of protein dissolution [415,527].

When manufacturing a scaffold with bioactive components it is essential to investigate toxicity. The work presented in Chapter 4, 5 and 6 all looks at incorporating or binding protein sources to a scaffold. ECM components from bovine sources have already been successfully used in medical implants, suggesting that the ECMs used in this study are non-toxic and safe to use [257]. However, animal to animal variability and different ECM sources within the body are compositionally different.

Therefore, *in vivo* evaluation and clinical studies are required to evaluate the safety and biocompatibility of the ECM and protein bound scaffolds used in this thesis.

Proteomic analysis of the ECM components within the scaffold and of the cell secretome bound to the scaffolds is required to fully understand the results within this thesis. Mass spectrometry-based proteomics is a widely used technique for large-scale protein characterization [528]. Unfortunately, due to the complex nature of proteomes and the intricate techniques required, analysing these in the ECM and cell secretome was not deemed as an effective use of resources. However, moving forward with a clearer image of how these scaffolds perform, the clear next step would be performing proteomics on both the scaffolds and secretome.

As previously mentioned, the surface activation yield and binding efficiency of the plasma coated and EDC/NHS treated scaffolds were not assessed for protein binding. This can be achieved using the Beer-Lambert law which uses FTIR peaks at two wavelengths (1772 cm^{-1} and 2615 cm^{-1}) [331]. This would allow us to assertively conclude which EDC/NHS concentrations had the greatest activation yield. However, the present studies found that the quantity of protein binding onto the scaffold's surface was not sufficient to be picked up in FTIR analysis. Alternative methods such as the Ninhydrin test and Chloranil test can be used to qualitatively test for binding efficiency as they rely on a colour change in the presence of open bonds [447]. The Chloranil test has also been used quantitatively, whereby the more colour change means more open bonds [447]. The use of these two tests moving forward would allow for measurement of the binding efficiency of each EDC/NHS treatment.

A shelf-life study looking at how long-term storage affects the proteins bound to the scaffolds (from Chapter 5) is required for the end goal of product commercialization. With translatability from lab to implant in mind, it is imperative that the shelf-life of these scaffolds is examined. The conditions under which proteins are stored can have massive effects on the shelf-life of the protein, with 4°C storage typically resulting in a 1 month shelf-life and proteins stored at -80°C typically lasting years [529]. Furthermore, if the bonds between the protein and PCL scaffold degrade over time, then the

quantity of bound protein will also drop. This step is imperative for assessing the translatability of these scaffolds.

This study looked at HUVEC and HUVSMC cultures separately. Future work should look at co-culturing these two cell lines together on the different scaffolds. These two cell types are found together in the vasculature and undergo paracrine interaction resulting in a variety of different endothelial functions [530]. Likewise, the co-culture of ECs and SMCs has been widely done *in vitro* with results showing that they self-regulate each other through the release of various different proteins and cytokines [504,531,532]. These studies showed that each cell type reacted differently to the individual scaffolds. For example, the extra-large fibre diameter increased angiogenic gene expression in the HUVECs, but the smallest fibre diameter increased cell viability and cell spreading in the HUVSMCs. Therefore, it would be interesting to see how combining these two fibres in a co-culture system would enhance cell function. Similarly, it would also be interesting to see how the binding of HUVEC secretome would alter the performance of seeded HUVSMCs, and vice versa with the HUVSMC secretome and seeded HUVECs. As mentioned above, these two cells release a variety of cytokines that alter each other's functions, therefore, it would be expected that binding these factors to a scaffold would alter cell functionality.

On the topic of binding cell secretome to a scaffold, looking at how other mechanical stimuli such as strain and shear stress affect the secretome profile released from these two cell types would lead to some interesting results. Studies have shown that strain and shear stress both alter cell function and protein expression from endothelial cells and smooth muscle cells [533]. Work by *Patrick Jr, et al.* found that HUVECs under shear stress increased the expression of ICAM, VCAM and bFGF, which are all angiogenic genes that stimulate the formation of new vasculature [533]. Likewise, mechanical strain has been shown to increase the expression of PDGF-B and PDGF-β in vascular SMCs [534]. These two genes contribute to cell proliferation in SMCs.

7.2 Conclusions

The aims outlined for this thesis were:

1) Manufacture electrospun scaffolds with differing morphologies and assess their impact on HUVECs and HUVSMCs.
2) Incorporate decellularized vascular ECMs into polymer scaffolds and assess their impact on HUVECs and HUVSMCs.
3) Bind cell secretome to polymer scaffolds to further biofunctionalize them and assess their impact on HUVECs and HUVSMCs.
4) Use physiologically relevant environmental conditions to alter cell secretome and cell functionality.

This thesis has successfully contributed to each of these aims. The studies presented in this thesis represent investigations of novel electrospun scaffolds as platforms for vascular tissue engineering. Each aim has been addressed in individual Chapters.

In Chapter 3, a range of different scaffold morphologies were investigated. Scaffolds were electrospun with increasing fibre diameters and were assessed as platforms for the growth of HUVECs and HUVSMCs. The scaffolds produced all had different fibre diameters and were random in their alignment. Results showed that altering the fibre diameter lead to increases in cell infiltration, cell viability and gene expression.

Chapter 4 looked at incorporating decellularized ECMs into the electrospun fibres, in order to increase the bioactive potential of the scaffolds. Bovine aorta and heart ECM sources were successfully decellularized and incorporated into the electrospun PCL fibres. The addition of ECM altered the mechanical properties of the scaffold and biological responses of the seeded cells. The incorporation of ECM into the scaffold increased cell viability for both cells used. Furthermore, no real trends in gene expression were noted. Therefore, incorporating ECM allowed for the mechanical properties of the scaffold to be altered whilst maintaining cell viability and without altering the gene expression.

Chapter 5 looked at how binding cell secretome to the surface of the scaffold altered their bioactive potential as platforms for cell seeding. Cell secretome conditioned media was collected for both cell types and was successfully bound onto the surface of the PCL scaffolds. Binding the proteins from the

HUVEC secretome conditioned media to the scaffold had the effect of slightly reducing the expression of several key phenotypic and angiogenic genes. Additionally, the binding of proteins from the HUVSMC secretome media and the serum-free media to the scaffold had the effect of reducing cell viability compared to the PBS conditioned scaffold. This Chapter represents the first time the secretome from two vascular cell types has been bound to the surface of a scaffold with subsequent cellular performance analysed.

Chapter 6 then looked at how environmental factors could be used to alter cellular performance on PCL and PCL/ECM scaffolds and to look at how these factors could alter the HUVEC secretome profile. The incorporation of ECM into the scaffolds did not alter their performance in a hypoxic environment. Moreover, hydrostatic pressure induced cell secretome and atmospheric pressure induced secretome could both be bound to scaffolds and maintained cell viability.

Overall, this thesis has used a combination of novel techniques to manufacture a range of scaffolds that mimic some of the native arterial properties, both in terms of morphology, biological composition and mechanical properties. The results from this thesis highlight the potential that these scaffolds have in the field of vascular tissue engineering and sets a strong foundation for future research.

References

1. Martini, F. H., Nath, J. L. & Bartholemew, E. F. The Heart. in *Fundamentals of Anatomy & Physiology* (ed. Berriman, L.) 684–722 (Pearsons, 2015).

2. Vogiatzidis, K. *et al.* Physiology of pericardial fluid production and drainage. *Front. Physiol.* **6**, 1–6 (2015).

3. Sacks, M. S. & Yoganathan, A. P. Heart valve function: A biomechanical perspective. *Philos. Trans. R. Soc. B Biol. Sci.* **362**, 1369–1391 (2007).

4. Saha, A. & Roy, S. Papillary muscles of right ventricle—morphological variations and its clinical relevance. *Cardiovasc. Pathol.* **34**, 22–27 (2018).

5. Maron, B. J. & Hutchins, G. M. The development of the semilunar valves in the human heart. *Am. J. Pathol.* **74**, 331–340 (1974).

6. London, G. M. & Pannier, B. Arterial functions: How to interpret the complex physiology. *Nephrol. Dial. Transplant.* **25**, 3815–3823 (2010).

7. Dora, K. A. *et al.* Isolated human pulmonary artery structure and function pre -and post-cardiopulmonary bypass surgery. *J. Am. Heart Assoc.* **5**, 1–9 (2016).

8. Martini, F. H., Nath, J. L. & Bartholemew, E. F. Blood Vessels and Circulations. in *Fundamentals of Anatomy & Physiology* (ed. Berriman, L.) 723–780 (Pearsons, 2015).

9. Franklin, K. J. Zection of tbe lbtitorp of fIebictne . *Proc. R. Soc. Med.* 1–33 (1927).

10. Rucker, R. B. & Tinker, D. S. Structure and metabolism of arterial elastin. *Rev Exp Pathol* **17**, 1–47 (1977).

11. Nissen, R., Cardinale, G. J. & Udenfriendt, S. Increased turnover of arterial collagen in hypertensive rats (hydroxyproline). *Med. Sci.* **75**, 451–453 (1978).

12. Gosline, J. *et al.* Elastic proteins: Biological roles and mechanical properties. *Philos. Trans. R. Soc. B Biol. Sci.* **357**, 121–132 (2002).

13. Eyre, D. Cross-Linking in Collagen and Elastin. *Annu. Rev. Biochem.* **53**, 717–748 (1984).

14. Luchsinger, B. P. C., Snell, R. E., Patel, D. J., Ph, D. & Fry, D. L. Instantaneous Pressure Distribution Along the Human Aorta. *Circ. Res.* **15**, 503–510 (1964).

15. Sage, H. Structure-function relationships in the evolution of elastin. *J. Invest. Dermatol.* **79**, 146–153 (1982).

16. Astrand, H. *et al.* In vivo estimation of the contribution of elastin and collagen to the mechanical properties in the human abdominal aorta: effect of age and sex. *J. Appl. Physiol.* **110**, 176–187 (2011).

17. Keeley, F. W., Bellingham, C. M. & Woodhouse, K. A. Elastin as a self-organizing biomaterial: Use of recombinantly expressed human elastin polypeptides as a model for investigations of structure and self-assembly of elastin. *Philos. Trans. R. Soc. B Biol. Sci.* **357**, 185–189 (2002).

18. Shadwick, R. E. Elastic energy storage in tendons: Mechanical differences related to function and age. *J. Appl. Physiol.* **68**, 1033–1040 (1990).

19. Bartoš, F. & Ledvina, M. Collagen, elastin and desmosines in three layers of bovine aortas of different ages. *Exp. Gerontol.* **14**, 21–26 (1979).

20. Grant, R. A. Content and districbution of aortic collagen, elastin and carbohydrate in different species. *J. Atheroscler. Res.* **7**, 463–472 (1966).

21. Park, H.-J. *et al.* Human umbilical vein endothelial cells and human dermal microvascular endothelial cells offer new insights into the relationship between lipid metabolism and angiogenesis. *Stem Cell Rev.* **6**, 1–10 (2006).

22. Jaffe, E. A., Nachman, R. L., Becker, C. G. & Minick, C. R. Culture of Human Endothelial Cells Derived from Umbilical Veins. *J. Clin. Invest.* **52**, 2745–2756 (1973).

23. Jiménez, N., Krouwer, V. J. D. & Post, J. A. A new, rapid and reproducible method to obtain high quality endothelium in vitro. *Cytotechnology* **65**, 1–14 (2013).

24. Weymann, A. *et al.* Bioartificial heart: A human-sized porcine model - The way ahead. *PLoS One* **9**, 1–8 (2014).

25. Dettin, M. *et al.* Facile and selective covalent grafting of an RGD-peptide to electrospun scaffolds improves HUVEC adhesion. *J. Pept. Sci.* **21**, 786–795 (2015).

26. Imaizumi, T. *et al.* Expression of vascular endothelial growth factor in human umbilical vein endothelial cells stimulated with interleukin-1alpha--an autocrine regulation of angiogenesis and inflammatory reactions. *Thromb. Haemost.* **83**, 949–955 (2000).

27. Muñoz-Chápuli, R., Quesada, A. R. & Medina, M. Á. Angiogenesis and signal transduction in endothelial cells. *Cell. Mol. Life Sci.* **61**, 2224–2243 (2004).

28. Liao, H. *et al.* Effects of long-term serial cell passaging on cell spreading, migration, and cell-surface ultrastructures of cultured vascular endothelial cells. *Cytotechnology* **66**, 229–238 (2014).

29. Donnini, D., Perrella, G., Stel, G., Ambesi-Impiombato, F. S. & Curcio, F. A new model of human aortic endothelial cells in vitro. *Biochimie* **82**, 1107–1114 (2000).

30. Kevil, C. G. *et al.* Intercellular Adhesion Molecule-1 (ICAM-1) Regulates Endothelial Cell Motility through a Nitric Oxide-dependent Pathway. *J. Biol. Chem.* **279**, 19230–19238 (2004).

31. Callanan, A., Davis, N. F., McGloughlin, T. M. & Walsh, M. T. Development of a rotational cell-seeding system for tubularized extracellular matrix (ECM) scaffolds in vascular surgery. *J. Biomed. Mater. Res. - Part B Appl. Biomater.* **102**, 781–788 (2014).

32. Han, J., Gerstenhaber, J. A., Lazarovici, P. & Lelkes, P. I. Tissue factor activity and ECM-related gene expression in human aortic endothelial cells grown on electrospun biohybrid scaffolds. *Biomacromolecules* **14**, 1338–1348 (2013).

33. Raedecke, C. E. *et al.* Coronary artery endothelial cells and microparticles increase expression of VCAM-1 in myocardial infarction. *Thromb. Haemost.* **113**, 605–616 (2015).

34. Gualtero, D. F., Lafaurie, G. I. & Fontanilla, M. R. Differential responses of endothelial cells on three-dimensional scaffolds to lipopolysaccharides from periodontopathogens. *Mol. Oral Microbiol.* (2019). doi:10.1111/omi.12263

35. Bhattacharyya, A., Lin, S., Sandig, M. & Mequanint, K. Regulation of Vascular Smooth Muscle Cell Phenotype in Three-dimensional Coculture System by Jagged-selective Notch3 signalling. *Tissue Eng. Part A* **20**, 1175–1187 (2014).

36. Singelyn, J. M. *et al.* Biomaterials Naturally derived myocardial matrix as an injectable scaffold for cardiac tissue engineering. *Biomaterials* **30**, 5409–5416 (2009).

37. Bacakova, L. *et al.* The Role of Vascular Smooth Muscle Cells in the Physiology and Pathophysiology of Blood Vessels. *Muscle Cell Tissue - Curr. Status Res. F.* (2018). doi:10.5772/intechopen.77115

38. Gabbiani, G. *et al.* Vascular smooth muscle cells differ from other smooth muscle cells: Predominance of vimentin filaments and a specific a-type actin. *Proc Natl Acad Sci USA* **78**, 298–302 (1981).

39. Katsumoto, T., Mitsushima, A. & Kurimura, T. The role of the vimentin intermediate filaments in rat 3Y1 cells elucidated by immunoelectron microscopy and computer-graphic reconstruction. *Biol. Cell* **68**, 139–146 (1990).

40. Paulin, D. & Li, Z. Desmin: A major intermediate filament protein essential for the structural integrity and function of muscle. *Exp. Cell Res.* **301**, 1–7 (2004).

41. Schwartz, S. M., Campbell, G. R. & Campbell, J. H. Replication of smooth muscle cells in vascular disease. *Circ. Res.* **58**, 427–444 (1986).

42. Gard, D. L., Bell, P. B. & Lazarides, E. Coexistence of desmin and the fibroblastic intermediate filament subunit in muscle and nonmuscle cells: identification and comparative peptide analysis. *Proc. Natl. Acad. Sci.* **76**, 3894–3898 (1979).

43. Fatigati, V. & Murphy, R. A. Actin and Tropomyosin Variants in Smooth Muscles. *J. Biol. Chem.* **259**, 14383–14388 (1984).

44. Rodriguez, L. V. *et al.* Clonogenic multipotent stem cells in human adipose tissue differentiate into functional smooth muscle cells. *Proc. Natl. Acad. Sci.* **103**, 12167–12172 (2006).

45. Woodcock, E. A. & Matkovich, S. J. Cardiomyocytes structure, function and associated pathologies. *Int. J. Biochem. Cell Biol.* **37**, 1746–1751 (2005).

46. Dorn, G. W. & Force, T. Protein kinase cascades in the regulation of cardiac hypertrophy. *J. Clin. Invest.* **115**, 527–537 (2005).

47. Kai, D., Prabhakaran, M. P., Jin, G. & Ramakrishna, S. Guided orientation of cardiomyocytes on electrospun aligned nanofibers for cardiac tissue engineering. *J. Biomed. Mater. Res. - Part B Appl. Biomater.* **98 B**, 379–386 (2011).

48. Smith, A. S. T., Macadangdang, J., Leung, W., Laflamme, M. A. & Kim, D.-O. Human iPSC-derived cardiomyocytes and tissue engineering strategies for disease modeling and drug screening. *Physiol. Behav.* **176**, 139–148 (2017).

49. Nguyen, A. H. *et al.* Cardiac tissue engineering: State-of-the-art methods and outlook. *J. Biol. Eng.* **13**, 1–21 (2019).

50. Husse, B. & Franz, W. M. Generation of cardiac pacemaker cells by programming and differentiation. *Biochim. Biophys. Acta - Mol. Cell Res.* **1863**, 1948–1952 (2016).

51. Li, R. A. Gene-and cell-based bio-artificial pacemaker: What basic and translational lessons have we learned. *Gene Ther.* **19**, 588–595 (2012).

52. Ou, D. B., Lang, H. J., Chen, R., Liu, X. T. & Zheng, Q. S. Using embryonic stem cells to form a biological pacemaker via tissue engineering technology. *BioEssays* **31**, 246–252 (2009).

53. Ferrara, N., Gerber, H. P. & LeCouter, J. The biology of VEGF and its receptors. *Nat. Med.* **9**, 669–676 (2003).

54. Senger, D. R. *et al.* Tumor cells secrete a vascular permeability factor that promotes accumulation of ascites fluid. *Science (80-.).* **219**, 983–985 (1983).

55. Harmey, J. H. & Bouchier-Hayes, D. Vascular endothelial growth factor (VEGF), a survival factor for tumour cells: Implications for anti-angiogenic therapy. *BioEssays* **24**, 280–283 (2002).

56. Gorski, D. H. *et al.* Blockade of the vascular endothelial growth factor stress response increases the antitumor effects of ionizing radiation. *Cancer Res.* **59**, 3374–3378 (1999).

57. Chintalgattu, V., Nair, D. M. & Katwa, L. C. Cardiac myofibroblasts: A novel source of vascular endothelial growth factor (VEGF) and its receptors Flt-1 and KDR. *J. Mol. Cell. Cardiol.* **35**, 277–286 (2003).

58. Murakami, M. & Simons, M. Fibroblast growth factor regulation of neovascularization Masahiro. *Curr Opin Hematol* **15**, 215–220 (2008).

59. Unger, E. F. *et al.* Basic fibroblast growth factor enhances myocardial collateral flow in a canine model. *Am. J. Physiol. - Hear. Circ. Physiol.* **266**, (1994).

60. Seghezzi, G. *et al.* Fibroblast growth factor-2 (FGF-2) induces vascular endothelial growth factor (VEGF) expression in the endothelial cells of forming capillaries: An autocrine mechanism contributing to angiogenesis. *J. Cell Biol.* **141**, 1659–1673 (1998).

61. Huang, X. *et al.* Ectopic activity of fibroblast growth factor receptor 1 in hepatocytes accelerates hepatocarcinogenesis by driving proliferation and vascular endothelial growth factor-induced angiogenesis. *Cancer Res.* **66**, 1481–1490 (2006).

62. Claffey, K. P. *et al.* Fibroblast growth factor 2 activation of stromal vascular endothelial growth factor expression and angiogenesis. *Lab. Investig.* **81**, 61–75 (2001).

63. Onimaru, M. *et al.* Fibroblast growth factor-2 gene transfer can stimulate hepatocyte growth factor expression irrespective of hypoxia-mediated downregulation in ischemic limbs. *Circ. Res.* **91**, 923–930 (2002).

64. Theocharis, A. D., Skandalis, S. S., Gialeli, C. & Karamanos, N. K. Extracellular matrix structure. *Adv. Drug Deliv. Rev.* **97**, 4–27 (2016).

65. Abedin, M. & King, N. Diverse evolutionary paths to cell adhesion. *Trends Cell Biol.* **20**, 734–742 (2010).

66. Carey, D. J. Matrix proteins. *Annu Rev Physiol* **53**, 161–177 (1991).

67. Gasser, T. C. Aorta. in *Biomechanics of Living Organs: Hyperelastic Constitutive Laws for Finite Element Modeling* 169–191 (2017). doi:10.1016/B978-0-12-804009-6.00008-0

68. Vlachopoulos, C., O'Rourke, M. F. & Nichols, W. W. *McDonald's blood flow in arteries : theoretical, experimental and clinical principles*. (CRC Press, 2011).

69. Ghanaeian, A. & Soheilifard, R. Mechanical elasticity of proline-rich and hydroxyproline-rich collagen-like triple-helices studied using steered molecular dynamics. *J. Mech. Behav. Biomed. Mater.* **86**, 105–112 (2018).

70. Lowry, O. H., Gilligan, D. R. & Katersky, E. M. The determination of Collagen and Elastin in Tissues, with results obtained in various normal tissues from different species. *J. Biol. Chem.*

139, 795–805 (1941).

71. Weber, K. T. *et al.* Collagen remodeling of the pressure-overloaded, hypertrophied nonhuman primate myocardium. *Circ. Res.* **62**, 757–765 (1988).

72. *Collagen - Structure and Mechanics*. (Springer, 2008).

73. Pauling, L. & Corey, R. B. The structure of fiborous proteins of the collagen - gelatin group. *Proc. Natl. Acad. Sci. U. S. A.* **37**, 272–281 (1951).

74. Scott, J. E. Elasticity in extracellular matrix 'shape modules' of tendon, cartilage, etc. A sliding proteoglycan-filament model. *J. Physiol.* **553**, 335–343 (2003).

75. O'Connell, M. K. *et al.* The Three-Dimensional Micro- and Nanostructure of the Aortic Medial Lamellar Unit Measured Using 3D Confocal & Electron Microscopy Imaging. *Matrix Biol* **27**, 171–181 (2008).

76. Wenger, M. P. E., Bozec, L., Horton, M. A. & Mesquidaz, P. Mechanical properties of collagen fibrils. *Biophys. J.* **93**, 1255–1263 (2007).

77. Langewouters, G. J., Wesseling, K. H. & Goedhard, W. J. A. The static elastic properties of 45 human thoracic and 20 abdominal aortas in vitro and the parameters of a new model. *J. Biomech.* **17**, 425–435 (1984).

78. Mithieux, B. S. M. & Weiss, A. S. Elastin is a key extracellular matrix protein that is critical to the elasticity I . Elastic Fiber The extracellular matrix imparts structural integrity on the tissues and. *Adv. Protein Chem.* **70**, 437–461 (2006).

79. Ramirez, F. Pathophysiology of the microfibril/elastic fiber system: Introduction. *Matrix Biol.* **19**, 455–456 (2000).

80. Kagan, H. M. & Sullivan, K. A. Lysyl Oxidase: Preparation and Role in Elastin Biosynthesis. *Methods Enzymol.* **82**, 637–650 (1982).

81. Cleary, E. G. The microfibrillar component of the elastic fibers. in *Connective Tissue Disease. Molecular Pathology of the Extracellular Matrix* (eds. Uitto, J. & Perejda, A. J.) 55–81 (Dekker, 1987).

82. Sakai, L. Y., Keene, D. R. & Engvall, E. Fibrillin, a new 350-kD glycoprotein, is a component ofextracellular microfibrils. *J. Cell Biol.* **103**, 2499–2509 (1986).

83. Zhang, H. *et al.* Structure and expression of fibrillin-2, a novel microfibrillar component preferentially located in elastic matrices. *J. Cell Biol.* **124**, 855–863 (1994).

84. Aaron, B. B. & Gosline, J. M. Elastin as a random-network elastomer: A mechanical and optical analysis of single elastin fibers. *Biopolymers* **20**, 1247–1260 (1981).

85. Fung, Y. C. *Biomechanics. Mechanical properties of living tissues*. (Springer-Verlag, 1993).

86. Wu, K. K. & Thiagarajan, P. Role of Endothelium in Thrombosis and Hemostasis. *Annu. Rev. Med.* **47**, 315–331 (2002).

87. Davis, B. T. *et al.* Targeted disruption of LDLR causes hypercholesterolemia and atherosclerosis in Yucatan miniature pigs. *PLoS One* **9**, 1–11 (2014).

88. Insull, W. The Pathology of Atherosclerosis: Plaque Development and Plaque Responses to Medical Treatment. *Am. J. Med.* **122**, S3–S14 (2009).

89. Derdeyn, C. P. & Chimowitz, M. I. Angioplasty and Stenting for Atherosclerotic Intracranial

Stenosis: Rationale for a Randomized Clinical Trial. *Neurimaging Clin N Am* **17**, 1–7 (2007).

90. Sabik, J. F. Understanding Saphenous Vein Graft Patency. *Circulation* **124**, 273–275 (2011).

91. Diodato, M. & Chedrawy, E. G. Coronary Artery Bypass Graft Surgery: The Past, Present, and Future of Myocardial Revascularisation. *Surg. Res. Pract.* **2014**, 1–6 (2014).

92. Slovut, D. P. & Olin, J. W. Fibromuscular Dysplasia RAS. *N. Engl. J. Med.* **350**, 1862–1871 (2004).

93. Schwartz, R. S. Pathophysiology of restenosis: Interaction of thrombosis, hyperplasia, and/or remodeling. *Am. J. Cardiol.* **81**, 14E-17E (1998).

94. Stanley, J. C., Gewertz, B. L., Bove, E. L., Sottiurai, V. & Fry, W. J. Arterial Fibrodysplasia. *Arch Surg* **110**, 561–566 (1975).

95. Archondakis, E., Pero, G., Valvassori, L., Boccardi, E. & Scialfa, G. Angiographic follow-up of traumatic carotid cavernous fistulas treated with endovascular stent graft placement. *Am. J. Neuroradiol.* **28**, 342–347 (2007).

96. Plouin, P.-F. *et al.* High Prevalence of Multiple Arterial Bed Lesions in Patients With Fibromuscular Dysplasia. *Hypertension* **70**, 652–658 (2017).

97. Furie, B. & Furie, B. C. Mechanisms of Thrombus Formation. *N. Engl. J. Med.* **359**, 938–949 (2008).

98. Ouriel, K., Green, R. M., Greenberg, R. K. & Clair, D. G. The anatomy of deep venous thrombosis of the lower extremity. *J. Vasc. Surg.* **31**, 895–900 (2000).

99. Tapson, V. F. Acute pulmonary embolism. *N. Engl. J. Med.* **358**, 1037–1052 (2008).

100. Mellor, A. & Soni, N. Fat Embolism. *Anaesthesia* **56**, 145–154 (2001).

101. Mirski, M. A., Lele, A. V, Fitzsimmons, L. & Toung, T. J. K. Diagnosis and treatment of air embolism. *Anesthesiology* **106**, 164–177 (2007).

102. Naito, N., Abe, M., Fukasawa, M. & Takeshi, A. Pulmonary embolism by a foreign body that migrated in the inferior vena cava during lumbar spine surgery. *BMJ Case Rep.* **2014**, 1–2 (2014).

103. Gossage, J. A., Ali, T., Chambers, J. & Burnand, K. G. Peripheral arterial embolism: Prevalence, outcome, and the role of echocardiography in management. *Vasc. Endovascular Surg.* **40**, 280–286 (2006).

104. Carson, J. L. *et al.* The clinical course of pulmonary embolism. *N. Engl. J. Med.* **326**, 1240–1245 (1992).

105. Yoo H H B, Queluz T H A T & El Dib R. Anticoagulant treatment for subsegmental pulmonary embolism (Review). *Cochrane Database Syst. Rev.* **1**, CD010222 (2016).

106. Kuo, W. T. *et al.* Pulmonary embolism response to fragmentation, embolectomy, and catheter thrombolysis (PERFECT): Initial results from a prospective multicenter registry. *Chest* **148**, 667–673 (2015).

107. Becker, D. M., Philbrick, J. T. & Selby, B. Inferior Vena Cava Filters. *arch Intern Med* **152**, 1985–1994 (2012).

108. Hansson, G. K. Inflammation, Atherosclerosis, and Coronary Artery Disease. *N. Engl. J. Med.* **352**, 1685–1695 (2005).

109. Townsend, N., Williams, J., Bhatnagar, P., Wickramasinghe, K. & Rayner, M. *Cardiovascular Disease Statistics 2014*. (2014).

110. Wilkins, E. *et al.* European Cardiovascular Disease Statistics - 2017 edition. *Eur. Hear. Network, Brussels* (2017). doi:978-2-9537898-1-2

111. Desai, M., Seifalian, A. M. & Hamilton, G. Role of prosthetic conduits in coronary artery bypass grafting. *Eur. J. Cardio-thoracic Surg.* **40**, 394–398 (2011).

112. Simard, T. *et al.* The Evolution of Coronary Stents: A Brief Review. *Can. J. Cardiol.* **30**, 35–45 (2014).

113. Thygesen, K., Alpert, J. S. & White, H. D. Universal Definition of Myocardial Infarction Kristian. *J. Am. Coll. Cardiol.* **50**, (2007).

114. Jaffe, A. S. *et al.* It's time for a change to a troponin standard. *Circulation* **102**, 1216–1220 (2000).

115. Criqui, M. H. & Aboyans, V. Epidemiology of Peripheral Artery Disease. *Circ. Res.* **116**, 1509–1526 (2015).

116. Uccioli, L. *et al.* Critical limb ischemia: Current challenges and future prospects. *Vasc. Health Risk Manag.* **14**, 63–74 (2018).

117. Matchar, D. B., McCrory, D. C., Barnett, H. J. M. & Feussner, J. R. Guidelines for medical treatment for stroke prevention. *Ann. Intern. Med.* **121**, 41–53 (1994).

118. Ntaios, G. & Hart, R. G. Embolic Stroke. *Circulation* **136**, 2403–2405 (2017).

119. Andersen, K. K., Olsen, T. S., Dehlendorff, C. & Kammersgaard, L. P. Hemorrhagic and ischemic strokes compared: Stroke severity, mortality, and risk factors. *Stroke* **40**, 2068–2072 (2009).

120. Evans, G. H. C., Stansby, G. & Hamilton, G. Suggested standard for reporting on arterial aneurysms. *J. Vasc. Res.* **15**, 456 (1992).

121. Sakalihasan, N., Limet, R. & Defawe, O. D. Abdominal aortic aneurysm. *Lancet* **365**, 1577–1589 (2005).

122. Staarmann, B., Smith, M. & Prestigiacomo, C. J. Shear stress and aneurysms: a review. *Neurosurg. Focus* **47**, E2 (2019).

123. Thompson, M. M. Controlling the expansion of abdominal aortic aneurysms. *Br. J. Surg.* **90**, 897–898 (2003).

124. Wilmink, T. B. M., Quick, C. R. G., Hubbard, C. S. & Day, N. E. The influence of screening on the incidence of ruptured abdominal aortic aneurysms. *J. Vasc. Surg.* **30**, 203–208 (1999).

125. Braunwald, E. Biomarkers in heart failure. *N. Engl. J. Med.* **358**, 2148–2159 (2008).

126. Mosterd, A. & Hoes, A. W. Clinical epidemiology of heart failure. *heart* **93**, 1137–1146 (2007).

127. Jondeau, G. & Milleron, O. Beta-Blockers in Acute Heart Failure: Do They Cause Harm? *JACC Hear. Fail.* **3**, 654–656 (2015).

128. Cohn, J. N. *et al.* A comparison of enalapril with hydralazine-isosorbide dinitrate in the treatment of chronic congestive heart failure. *N. Engl. J. Med.* **325**, 303–310 (1991).

129. Pashneh-Tala, S., MacNeil, S. & Claeyssens, F. The Tissue-Engineered Vascular Graft—Past, Present, and Future. *Tissue Eng. Part B Rev.* **22**, 68–100 (2016).

130. Brewster, D. G. Current controversies in the management of aortoiliac occlusive disease. *J. Vasc. Surg.* **25**, 365–379 (1997).

131. Chlupác, J., Filová, E. & Bačáková, L. Blood vessel replacement: 50 years of development and tissue engineering paradigms in vascular surgery. *Physiol. Res.* **58**, 119–140 (2009).

132. Hortmann, H. C., de Oliveira, H. G., de Oliveira, S. C., Rabello, R. R. & Rocha, E. A. V. Comparison of patency between radial artery and saphenous vein in a coronary artery bypass grafting post operative with return of the symptoms. *Brazilian J. Cardiovasc. Surg.* **25**, 218–223 (2010).

133. Devine, C., Hons, B. & McCollum, C. Heparin-bonded dacron or polytetrafluoroethylene for femoropopliteal bypass grafting: A multicenter trial. *J. Vasc. Surg.* **33**, 533–539 (2001).

134. Hayward, P. A. R. *et al.* Comparable patencies of the radial artery and right internal thoracic artery or saphenous vein beyond 5 years: Results from the Radial Artery Patency and Clinical Outcomes trial. *J. Thorac. Cardiovasc. Surg.* **139**, 60–67 (2010).

135. Ballotta, E., Renon, L., Toffano, M. & Da Giau, G. Prospective randomized study on bilateral above-knee femoropopliteal revascularization: Polytetrafluoroethylene graft versus reversed saphenous vein. *J. Vasc. Surg.* **38**, 1051–1055 (2003).

136. Green, R. M. *et al.* Prosthetic above-knee femoropopliteal bypass grafting: Five-year results of a randomized trial. *J. Vasc. Surg.* **31**, 417–425 (2000).

137. Taylor, L. M., Edwards, J. M., Brant, B., Phinney, E. S. & Porter, J. M. Autogenous reversed vein bypass for lower extremity ischemia in patients with absent or inadequate greater saphenous vein. *Am. J. Surg.* **153**, 505–510 (1987).

138. Chew, D. K. W. *et al.* Bypass in the absence of ipsilateral greater saphenous vein: Safety and superiority of the contralateral greater saphenous vein. *J. Vasc. Surg.* **35**, 1085–1092 (2002).

139. Karaman, O., Şen, M. & Demirci, E. A. Electrospun scaffolds for vascular tissue engineering. in *Electrospun Materials for Tissue Engineering and Biomedical Applications: Research, Design and Commercialization* 261–287 (2017). doi:10.1016/B978-0-08-101022-8.00006-5

140. Barner, H. B. CORONARY BYPASS: AUTOGRAFT, ALLOGRAFT OR HETEROGRAFT. *Am. J. od Cardiol.* **38**, 666–667 (1976).

141. Wald, D. S. *et al.* Ran-domized trial of preventive angioplasty in myocardialinfarction. *N. Engl. J. Med.* **369**, 1115–1123 (2013).

142. Bonati, L. H., Lyrer, P., Ederle, J., Featherstone, R. & Brown, M. M. Percutaneous transluminal angioplasty and stenting for carotid artery stenosis. *Cochrane Database Syst. Rev.* 1–94 (2012). doi:10.1002/14651858.CD000515.pub3

143. Smith, C., Smith, L. & Hasso, N. Fibromuscular Artery Treated by Balloon. *Radiology* **155**, 645–648 (1985).

144. Gruntzig, A. R., Senning, A. & Siegenthaler, W. E. Nonoperative Dilation of Coronary-artery Stenosis. *N. Engl. J. Med.* **301**, 61–68 (1979).

145. Fischman, D. L. *et al.* A Randomized Comparison of Coronary-Stent Placement and Balloon Angioplasty in the Treatment of Coronary Artery Disease. *N. Engl. J. Med.* **331**, 496–501

(1994).

146. Moses, J. W. *et al.* Sirolimus-Eluting Stents versus Standard Stents in Patients with Stenosis in a Native Coronary Artery. *N. Engl. J. Med.* **349**, 1315–1323 (2003).

147. Stone, G. W. *et al.* A Polymer-Based, Paclitaxel-Eluting Stent in Patients with Coronary Artery Disease. *N. Engl. J. Med.* **350**, 221–231 (2004).

148. Buccheri, D., Piraino, D., Andolina, G. & Cortese, B. Understanding and managing in-stent restenosis: A review of clinical data, from pathogenesis to treatment. *J. Thorac. Dis.* **8**, E1150–E1162 (2016).

149. Komiyama, H. *et al.* Neoatherosclerosis: Coronary stents seal atherosclerotic lesions but result in making a new problem of atherosclerosis. *World J. Cardiol.* **7**, 776 (2015).

150. Nakazawa, G. *et al.* The Pathology of Neoatherosclerosis in Human Coronary Implants: Bare Metal and Drug-Eluting Stents. *J Am Coll Cardiol* **57**, 1–21 (2011).

151. Garg, S., Bourantas, C. & Serruys, P. W. New concepts in the design of drug-eluting coronary stents. *Nat. Rev. Cardiol.* **10**, 248–260 (2013).

152. Dézsi, C. A. & Szentes, V. The Real Role of β-Blockers in Daily Cardiovascular Therapy. *Am. J. Cardiovasc. Drugs* **17**, 361–373 (2017).

153. Freemantle, N. *et al.* β Blockade after Myocardial Infarction : Systematic Review and Meta Regression Analysis Linked references are available on JSTOR for this article : Papers P Blockade after myocardial infarction : systematic review and meta regression analysis. **318**, 1730–1737 (2016).

154. Ong, H. T. B Blockers in Hypertension and Cardiovascular Disease. *Br. Med. J.* **334**, 946–949 (2007).

155. Shah, S. U., Anjum, S. & Littler, W. A. Use of diuretics in cardiovascular diseases: (1) Heart failure. *Postgrad. Med. J.* **80**, 201–205 (2004).

156. Shah, S. U., Anjum, S. & Littler, W. A. Use of diuretics in cardiovascular disease: (2) Hypertension. *Postgrad. Med. J.* **80**, 271–276 (2004).

157. Fireman, M., DiMartini, A. F., Armstrong, S. C. & Cozza, K. L. Immunosuppressants. *Psychosomatics* **45**, 354–360 (2004).

158. Miller, L. W. Cardiovascular toxicities of immunosuppressive agents. *Am. J. Transplant.* **2**, 807–818 (2002).

159. Tepperman, E. *et al.* Vascular effects of immunosuppression Elissa. *Can J Surg* **53**, 57–63 (2010).

160. Habib, A. & Finn, A. V. Antiproliferative Drugs for Restenosis Prevention. *Interv. Cardiol. Clin.* **5**, 321–329 (2016).

161. Hollenberg, S. M. Vasodilators in acute heart failure. *Heart Fail. Rev.* **12**, 143–147 (2007).

162. Koch-Weser, J. Vasodilator Drugs in the Treatment of Hypertension. *arch Intern Med* **133**, 1017–1027 (1974).

163. Young, P. P. & Schafer, R. Cell-based therapies for cardiac disease: a cellular therapist's perspective. *Transfusion* **55**, 1–19 (2015).

164. Müller, P., Lemcke, H. & David, R. Stem Cell Therapy in Heart Diseases-Cell Types,

Mechanisms and Improvement Strategies. *Cell. Physiol. Biochem.* **48**, 2607–2655 (2018).

165. Bagno, L., Hatzistergos, K. E., Balkan, W. & Hare, J. M. Mesenchymal Stem Cell-Based Therapy for Cardiovascular Disease: Progress and Challenges. *Mol. Ther.* **26**, 1610–1623 (2018).

166. Florea, V. *et al.* Dose comparison study of allogeneic mesenchymal stem cells in patients with ischemic cardiomyopathy (The TRIDENT study). *Circ. Res.* **121**, 1279–1290 (2017).

167. Van Der Spoel, T. I. G. *et al.* Human relevance of pre-clinical studies in stem cell therapy: Systematic review and meta-analysis of large animal models of ischaemic heart disease. *Cardiovasc. Res.* **91**, 649–658 (2011).

168. Zsebo, K. *et al.* Long-term effects of AAV1/SERCA2a gene transfer in patients with severe heart failure: Analysis of recurrent cardiovascular events and mortality. *Circ. Res.* **114**, 101–108 (2014).

169. King, K. R. *et al.* IRF3 and type i interferons fuel a fatal response to myocardial infarction. *Nat. Med.* **23**, 1481–1487 (2017).

170. Fuchs, S. *et al.* Transendocardial delivery of autologous bone marrow enhances collateral perfusion and regional function in pigs with chronic experimental myocardial ischemia. *J. Am. Coll. Cardiol.* **37**, 1726–1732 (2001).

171. Bartolucci, J. *et al.* Safety and efficacy of the intravenous infusion of umbilical cord mesenchymal stem cells in patients with heart failure: A phase 1/2 randomized controlled trial (RIMECARD trial [Randomized clinical trial of intravenous infusion umbilical cord mesenchymal . *Circ. Res.* **121**, 1192–1204 (2017).

172. Patel, A. N. *et al.* Ixmyelocel-T for patients with ischaemic heart failure: a prospective randomised double-blind trial. *Lancet* **387**, 2412–2421 (2016).

173. Camci-Unal, G., Annabi, N., Dokmeci, M. R., Liao, R. & Khademhosseini, A. Hydrogels for cardiac tissue engineering. *NPG Asia Mater.* **6**, e99 (2014).

174. Yanamandala, M. *et al.* Overcoming the Roadblocks to Cardiac Cell Therapy Using Tissue Engineering. *J Am Coll Cardiol* **70**, 766–775 (2017).

175. J.V., S. & S., G. Vascular tissue engineering: Biodegradable scaffold platforms to promote angiogenesis. *Stem Cell Res. Ther.* **4**, 1–8 (2013).

176. Singh, C., Wong, C. & Wang, X. Medical Textiles as Vascular Implants and Their Success to Mimic Natural Arteries. *J. Funct. Biomater.* **6**, 500–525 (2015).

177. Burton, T. P., Corcoran, A. & Callanan, A. The effect of electrospun polycaprolactone scaffold morphology on human kidney epithelial cells. *Biomed. Mater.* **13**, 015006 (2017).

178. Sun, B. *et al.* Electrospun anisotropic architectures and porous structures for tissue engineering. *J. Mater. Chem. B* **3**, 5389–5410 (2015).

179. Hasan, A. *et al.* Electrospun scaffolds for tissue engineering of vascular grafts. *Acta Biomater.* **10**, 11–25 (2014).

180. Wu, J. & Hong, Y. Enhancing cell infiltration of electrospun fibrous scaffolds in tissue regeneration. *Bioact. Mater.* **1**, 56–64 (2016).

181. Lim, K. S., Martens, P. & Poole-Warren, L. Biosynthetic Hydrogels for Cell Encapsulation. in *Functional Hydrogels as Biomaterials* (eds. Li, J., Osada, Y. & Cooper-White, J.) **12**, 1–29

(Springer-Verlag, 2018).

182. Silva, A. K. A., Richard, C., Bessodes, M., Scherman, D. & Merten, O. W. Growth factor delivery approaches in hydrogels. *Biomacromolecules* **10**, 9–18 (2009).

183. Kaiser, N. J., Kant, R. J., Minor, A. J. & Coulombe, K. L. K. Optimizing Blended Collagen-Fibrin Hydrogels for Cardiac Tissue Engineering with Human iPSC-derived Cardiomyocytes. *ACS Biomater. Sci. Eng.* **5**, 887–899 (2019).

184. Dunphy, S., Reid, J. A., Burton, T. P. & Callanan, A. Mechanical characterisation of directionally frozen polycaprolactone scaffolds using 1,4-dioxane and glacial acetic acid for articular cartilage tissue engineering. *Biomed. Phys. Eng. Express* **4**, 057004 (2018).

185. Cohen, S. & Gurion, B. Utilization of Directional Freezing for the Construction of Tissue. 3–6 (2003).

186. Munir, N., Larsen, R. S. & Callanan, A. Fabrication of 3D cryo-printed scaffolds using low-temperature deposition manufacturing for cartilage tissue engineering. *Bioprinting* **10**, 1–8 (2018).

187. Cho, Y. S., Kim, B. S., You, H. K. & Cho, Y. S. A novel technique for scaffold fabrication: SLUP (salt leaching using powder). *Curr. Appl. Phys.* **14**, 371–377 (2014).

188. Yao, D. *et al.* Salt-leached silk scaffolds with tunable mechanical properties. *Biomacromolecules* **13**, 3723–3729 (2012).

189. Ashammakhi, N. *et al.* Bioinks and bioprinting technologies to make heterogeneous and biomimetic tissue constructs. *Mater. Today Bio* **1**, 100008 (2019).

190. Faramarzi, N. *et al.* Patient-Specific Bioinks for 3D Bioprinting of Tissue Engineering Scaffolds. *Adv. Healthc. Mater.* **7**, 1–9 (2018).

191. Gopinathan, J. & Noh, I. Recent trends in bioinks for 3D printing. *Biomater. Res.* **22**, 1–15 (2018).

192. Costantini, M. & Barbetta, A. *Gas foaming technologies for 3D scaffold engineering*. *Functional 3D Tissue Engineering Scaffolds: Materials, Technologies, and Applications* (Elsevier Ltd, 2017). doi:10.1016/B978-0-08-100979-6.00006-9

193. Skoog, S. A., Goering, P. L. & Narayan, R. J. Stereolithography in tissue engineering. *J. Mater. Sci. Mater. Med.* **25**, 845–856 (2014).

194. Yeong, W. Y. *et al.* Porous polycaprolactone scaffold for cardiac tissue engineering fabricated by selective laser sintering. *Acta Biomater.* **6**, 2028–2034 (2010).

195. Vaidyanathan, R. *et al.* Extrusion freeforming of functional ceramic prototypes. *Jom* **52**, 34–37 (2000).

196. Abdelaal, O. A. & Darwish, S. M. Fabrication of tissue engineering scaffolds using rapid prototyping techniques. *J. World Acad. Sci. Eng. Technol.* **59**, 577–585 (2011).

197. Murphy, S. V. & Atala, A. 3D bioprinting of tissues and organs. *Nat. Biotechnol.* **32**, 773–785 (2014).

198. Gao, S. *et al.* Fabrication and characterization of electrospun nanofibers composed of decellularized meniscus extracellular matrix and polycaprolactone for meniscus tissue engineering. *J. Mater. Chem. B* **5**, 2273–2285 (2017).

199. Garrigues, N. W., Little, D., Sanches-Adams, J., Ruch, D. S. & Guilak, F. Electrospun Cartilage-Derived Matrix Scaffolds for Cartilage Tissue Engineering. *J. Biomed. Mater. Res. - Part A* **102**, 3998–4008 (2014).

200. Gilbert, T. W., Sellaro, T. L. & Badylak, S. F. Decellularization of tissues and organs. *Biomaterials* **27**, 3675–3683 (2006).

201. Chakrapani, V. Y., Gnanamani, A., Giridev, V. R., Madhusoothanan, M. & Sekaran, G. Electrospinning of Type I Collagen and PCL Nanofibers Using Acetic Acid. *J. Appl. Polym. Sci.* **125**, 3221–3227 (2012).

202. Law, J. X., Liau, L. L., Saim, A., Yang, Y. & Idrus, R. Electrospun Collagen Nanofibers and Their Applications in Skin Tissue Engineering. *Tissue Eng. Regen. Med.* **14**, 699–718 (2017).

203. Fromer, M. W. *et al.* The endothelial cell secretome as a novel treatment to prime adipose-derived stem cells for improved wound healing in diabetes. *J. Vasc. Surg.* **68**, 234–244 (2018).

204. Hathout, Y. Approaches to the study of the cell secretome. *Expert Rev. Proteomics* **4**, 239–248 (2007).

205. Zhao, J. *et al.* Bioreactors for tissue engineering: An update. *Biochem. Eng. J.* **109**, 268–281 (2016).

206. Oragui, E., Nannaparaju, M. & Khan, W. S. The Role of Bioreactors in Tissue Engineering for Musculoskeletal Applications. *Open Orthop. J.* **5**, 267–270 (2011).

207. Park, J.-S. Electrospinning and its applications. *GAdvances Nat. Sci. Nanosci. Nanotechnol.* **32**, 91–95 (2006).

208. Hale Karakaş. Electrospinning of nanofibers and their applications. *Funtex* (2012).

209. Han, D. G. *et al.* Optimization of electrospun poly(caprolactone) fiber diameter for vascular scaffolds to maximize smooth muscle cell infiltration and phenotype modulation. *Polymers (Basel).* **11**, (2019).

210. Sundaramurthi, D., Krishnan, U. M. & Sethuraman, S. Electrospun nanofibers as scaffolds for skin tissue engineering. *Polym. Rev.* **54**, 348–376 (2014).

211. Huang, F., Wei, Q., Cai, Y. & Wu, N. Surface structures and contact angles of electrospun poly(vinylidene fluoride) nanofiber membranes. *Int. J. Polym. Anal. Charact.* **13**, 292–301 (2008).

212. El-hadi, A. M. & Al-Jabri, F. Y. Influence of electrospinning parameters on fiber diameter and mechanical properties of poly(3-Hydroxybutyrate) (PHB) and polyanilines (PANI) blends. *Polymers (Basel).* **8**, (2016).

213. Zhu, G., Zhao, L. Y., Zhu, L. T., Deng, X. Y. & Chen, W. L. Effect of Experimental Parameters on Nanofiber Diameter from Electrospinning with Wire Electrodes. *IOP Conf. Ser. Mater. Sci. Eng.* **230**, (2017).

214. Wang, Z. *et al.* The effect of thick fibers and large pores of electrospun poly(ε-caprolactone) vascular grafts on macrophage polarization and arterial regeneration. *Biomaterials* **35**, 5700–5710 (2014).

215. Ayres, C. *et al.* Modulation of anisotropy in electrospun tissue-engineering scaffolds: Analysis of fiber alignment by the fast Fourier transform. *Biomaterials* **27**, 5524–5534 (2006).

216. Pham, Q. P., Sharma, U. & Mikos, A. G. Electrospun poly (ε-caprolactone) microfiber and

multilayer nanofiber/microfiber scaffolds: Characterization of scaffolds and measurement of cellular infiltration. *Biomacromolecules* **7**, 2796–2805 (2006).

217. Agarwal, S., Wendorff, J. H. & Greiner, A. Use of electrospinning technique for biomedical applications. *Polymer (Guildf).* **49**, 5603–5621 (2008).

218. Ghobeira, R. *et al.* Wide-ranging diameter scale of random and highly aligned PCL fibers electrospun using controlled working parameters. *Polymer (Guildf).* **157**, 19–31 (2018).

219. Simbara, M. M. O., Santos, A. R., Andrade, A. J. P. & Malmonge, S. M. Comparative study of aligned and nonaligned poly(ε-caprolactone) fibrous scaffolds prepared by solution blow spinning. *J. Biomed. Mater. Res. - Part B Appl. Biomater.* 1462–1470 (2018). doi:10.1002/jbm.b.34238

220. Ahmed, F. E., Lalia, B. S. & Hashaikeh, R. A review on electrospinning for membrane fabrication: Challenges and applications. *Desalination* **356**, 15–30 (2015).

221. Haider, A., Haider, S. & Kang, I. K. A comprehensive review summarizing the effect of electrospinning parameters and potential applications of nanofibers in biomedical and biotechnology. *Arab. J. Chem.* **11**, 1165–1188 (2018).

222. Ji, W. *et al.* Bioactive electrospun scaffolds delivering growth factors and genes for tissue engineering applications. *Pharm. Res.* **28**, 1259–1272 (2011).

223. Jayasinghe, S. N. Cell electrospinning: A novel tool for functionalising fibres, scaffolds and membranes with living cells and other advanced materials for regenerative biology and medicine. *Analyst* **138**, 2215–2223 (2013).

224. Preciado, J. A., Cohen, S., Skandakumaran, P. & Rubinsky, B. Utilization of directional freezing for the construction of tissue engineering scaffolds. in *American Society of Mechanical Engineers, Heat Transfer Division, (Publication) HTD* **374**, 439–442 (2003).

225. Reed, S. *et al.* Macro- and micro-designed chitosan-alginate scaffold architecture by three-dimensional printing and directional freezing. *Biofabrication* **8**, (2016).

226. Arav, A. & Natan, D. Directional freezing of reproductive cells and organs. *Reprod. Domest. Anim.* **47**, 193–196 (2012).

227. Munir, N. & Callanan, A. Novel phase separated polycaprolactone/collagen scaffolds for cartilage tissue engineering. *Biomed. Mater.* **13**, 051001 (2018).

228. Hou, Q., Grijpma, D. W. & Feijen, J. Porous polymeric structures for tissue engineering prepared by a coagulation, compression moulding and salt leaching technique. *Biomaterials* **24**, 1937–1947 (2003).

229. Loh, Q. L. & Choong, C. Three-Dimensional Scaffolds for Tissue Engineering Applications: Role of Porosity and Pore Size. *Tissue Eng. Part B Rev.* **19**, 485–502 (2013).

230. Nam, Y. S., Yoon, J. J. & Park, T. G. A novel fabrication method of macroporous biodegradable polymer scaffolds using gas foaming salt as a porogen additive. *J. Biomed. Mater. Res.* **53**, 1–7 (2000).

231. Poursamar, S. A. *et al.* Potential application of gelatin scaffolds prepared through in situ gas foaming in skin tissue engineering. *Int. J. Polym. Mater. Polym. Biomater.* **65**, 315–322 (2016).

232. El-Sherbiny, I. M. & Yacoub, M. H. Hydrogel scaffolds for tissue engineering: Progress and

challenges. *Glob. Cardiol. Sci. Pract.* **38**, 316–342 (2013).

233. Garg, T., Singh, O., Arora, S. & Murthy, R. S. R. Scaffold: A novel carrier for cell and drug delivery. *Crit. Rev. Ther. Drug Carrier Syst.* **29**, 1–63 (2012).

234. Bryant, S. J. & Anseth, K. S. Controlling the spatial distribution of ECM components in degradable PEG hydrogels for tissue engineering cartilage. *J. Biomed. Mater. Res. - Part A* **64A**, 70–79 (2002).

235. Saldin, L. T., Cramer, M. C., Velankar, S. S., White, L. J. & Badylak, S. F. Extracellular matrix hydrogels from decellularized tissues: Structure and function. *Acta Biomater.* **49**, 1–15 (2017).

236. Claudio-Rizo, J. A., Delgado, J., Quintero-Ortega, I. A., Mata-Mata, J. L. & Mendoza-Novelo, B. Decellularized ECM-Derived Hydrogels: Modification and Properties. *Intech* 3–22 (2016). doi:http://dx.doi.org/10.5772/57353

237. Su, J., Satchell, S. C., Shah, R. N. & Wertheim, J. A. Kidney decellularized extracellular matrix hydrogels: Rheological characterization and human glomerular endothelial cell response to encapsulation. *J. Biomed. Mater. Res. - Part A* **106**, 2448–2462 (2018).

238. Chua, C. K., Leong, K. F. & An, J. Introduction to rapid prototyping of biomaterials. in *Rapid Prototyping of Biomaterials: Principles and Applications* 1–15 (Elsevier Ltd., 2020). doi:10.1533/9780857097217.1

239. Liew, A. W. L. & Zhang, Y. In vitro pre-vascularization strategies for tissue engineered constructs–Bioprinting and others. *Int. J. Bioprinting* **3**, 3–17 (2017).

240. Bibb, R., Nottrodt, N. & Gillner, A. Artificial vascularized scaffolds for 3D-tissue regeneration - a report of the ArtiVasc 3D Project. *Int. J. Bioprinting* **2**, 93–102 (2016).

241. Ji, S. & Guvendiren, M. Recent Advances in Bioink Design for 3D Bioprinting of Tissues and Organs. *Front. Bioeng. Biotechnol.* **5**, 1–8 (2017).

242. Berg, J. *et al.* Optimization of cell-laden bioinks for 3D bioprinting and efficient infection with influenza A virus. *Sci. Rep.* **8**, 1–13 (2018).

243. Nguyen, D. *et al.* Cartilage Tissue Engineering by the 3D Bioprinting of iPS Cells in a Nanocellulose/Alginate Bioink. *Sci. Rep.* **7**, 1–10 (2017).

244. Pati, F. *et al.* Printing three-dimensional tissue analogues with decellularized extracellular matrix bioink. *Nat. Commun.* **5**, 1–11 (2014).

245. Kačarević, Ž. P. *et al.* An introduction to 3D bioprinting: Possibilities, challenges and future aspects. *Materials (Basel).* **11**, (2018).

246. Tapias, L. . & Ott, H. . Decellularized Scaffolds as a Platform for Bioengineered Organs. *Curr. Opin. Organ Transplant.* **19**, 145–152 (2014).

247. Sheridan, W. S., Duffy, G. P. & Murphy, B. P. Optimum parameters for freeze-drying decellularized arterial scaffolds. *Tissue Eng. - Part C Methods* **19**, 981–990 (2013).

248. Negishi, J. *et al.* Porcine radial artery decellularization by high hydrostatic pressure. *J. Tissue Eng. Regen. Med.* **9**, E144–E151 (2015).

249. Syazwani, N., Azhim, A., Morimoto, Y., Furukawa, K. S. & Ushida, T. Decellularization of aorta tissue using sonication treatment as potential scaffold for vascular tissue engineering. *J. Med. Biol. Eng.* **35**, 258–269 (2015).

250. Vafaee, T. *et al.* Decellularization of human donor aortic and pulmonary valved conduits using low concentration sodium dodecyl sulfate. *J. Tissue Eng. Regen. Med.* **12**, e841–e853 (2018).

251. Mazza, G. *et al.* Rapid production of human liver scaffolds for functional tissue engineering by high shear stress oscillation-decellularization. *Sci. Rep.* **7**, 1–14 (2017).

252. Gulati, A. K. Evaluation of acellular and cellular nerve grafts in repair of rat peripheral nerve. *J. Neurosurg.* **68**, 117–123 (1988).

253. Flynn, L. E. The use of decellularized adipose tissue to provide an inductive microenvironment for the adipogenic differentiation of human adipose-derived stem cells. *Biomaterials* **31**, 4715–4724 (2010).

254. Lin, P., Chan, W. C. W., Badylak, S. F. & Bhatia, S. N. Assessing Porcine Liver-Derived Biomatrix for Hepatic Tissue Engineering PAUL. *Tissue Eng.* **10**, 1046–1055 (2004).

255. Funamoto, S. *et al.* The use of high-hydrostatic pressure treatment to decellularize blood vessels. *Biomaterials* **31**, 3590–3595 (2010).

256. Grant, R., Hallett, J., Forbes, S., Hay, D. & Callanan, A. Blended electrospinning with human liver extracellular matrix for engineering new hepatic microenvironments. *Sci. Rep.* **9**, 1–12 (2019).

257. Crapo, P. M., Gilbert, T. W. & Badylak, S. F. An overview of tissue and whole organ decellularization processes. *Biomater* **32**, 3233–3243 (2012).

258. Giusti, S., Bogetti, M. E., Bonafina, A. & Fiszer De Plazas, S. An improved method to obtain a soluble nuclear fraction from embryonic brain tissue. *Neurochem. Res.* **34**, 2022–2029 (2009).

259. Perea-Gil, I. *et al.* In vitro comparative study of two decellularization protocols in search of an optimal myocardial scaffold for recellularization. *Am. J. Transl. Res.* **7**, 558–573 (2015).

260. Du, L., Wu, X., Pang, K. & Yang, Y. Histological evaluation and biomechanical characterisation of an acellular porcine cornea scaffold. *Br. J. Ophthalmol.* **95**, 410–414 (2011).

261. He, M., Callanan, A., Lagaras, K., Steele, J. A. M. & Stevens, M. M. Optimization of SDS exposure on preservation of ECM characteristics in whole organ decellularization of rat kidneys. *J. Biomed. Mater. Res. - Part B Appl. Biomater.* **105**, 1352–1360 (2017).

262. Reing, J. E. *et al.* The Effects of Processing Methods upon Mechanical and Biologic Properties of Porcine Dermal Extracellular Matrix Scaffolds. *Biomaterials* **31**, 1–17 (2010).

263. Gilpin, A. & Yang, Y. Decellularization Strategies for Regenerative Medicine: From Processing Techniques to Applications. *Biomed Res. Int.* **2017**, (2017).

264. Young, R. C. & Goloman, G. Allo- and xeno-reassembly of human and rat myometrium from cells and scaffolds. *Tissue Eng. - Part A* **19**, 2112–2119 (2013).

265. Elder, B. D., Vigneswaran, K., Athanasiou, K. A. & Kim, D. H. Biomechanical, Biochemical, and Histological Characterization of Canine Lumbar Facet Joint Cartilage. *Neurosurgery* **66**, 722–727 (2010).

266. Ijima, H., Nakamura, S., Bual, R., Shirakigawa, N. & Tanoue, S. Physical Properties of the Extracellular Matrix of Decellularized Porcine Liver. *Gels* **4**, 39 (2018).

267. Giraldo-Gomez, D. M. *et al.* Trypsin as enhancement in cyclical tracheal decellularization: Morphological and biophysical characterization. *Mater. Sci. Eng. C* **59**, 930–937 (2016).

268. Hodde, J. *et al.* Effects of sterilization on an extracellular matrix scaffold: Part I. Composition and matrix architecture. *J. Mater. Sci. Mater. Med.* **18**, 537–543 (2007).

269. Murphy, C. M., O'Brien, F. J., Little, D. G. & Schindeler, A. Cell-scaffold interactions in the bone tissue engineering triad. *Eur. Cells Mater.* **26**, 120–132 (2013).

270. Freytes, D. O., Badylak, S. F., Webster, T. J., Geddes, L. A. & Rundell, A. E. Biaxial strength of multilaminated extracellular matrix scaffolds. *Biomaterials* **25**, 2353–2361 (2004).

271. Simsa, R. *et al.* Systematic in vitro comparison of decellularization protocols for blood vessels. *PLoS One* **13**, 1–19 (2018).

272. Syed, O., Walters, N. J., Day, R. M., Kim, H. W. & Knowles, J. C. Evaluation of decellularization protocols for production of tubular small intestine submucosa scaffolds for use in oesophageal tissue engineering. *Acta Biomater.* **10**, 5043–5054 (2014).

273. Prasertsung, I., Kanokpanont, S., Bunaprasert, T., Thanakit, V. & Damrongsakkul, S. Development of acellular dermis from porcine skin using periodic pressurized technique. *J. Biomed. Mater. Res. - Part B Appl. Biomater.* **85**, 210–219 (2008).

274. Cole, M. B. Alteration of cartilage matrix morphology with histological processing. *J. Microsc.* **133**, 129–140 (1984).

275. Rahman, S., Griffin, M., Naik, A., Szarko, M. & Butler, P. E. M. Optimising the decellularization of human elastic cartilage with trypsin for future use in ear reconstruction. *Sci. Rep.* **8**, 1–11 (2018).

276. Yang, L. *et al.* Mechanical properties of single electrospun collagen type I fibers. *Biomaterials* **29**, 955–962 (2008).

277. Friedrich, E. E. *et al.* Residual sodium dodecyl sulfate in decellularized muscle matrices leads to fibroblast activation in vitro and foreign body response in vivo. *J. Tissue Eng. Regen. Med.* **12**, e1704–e1715 (2018).

278. Beck, E. C. *et al.* Chondroinductive Hydrogel Pastes Composed of Naturally Derived Devitalized Cartilage. *Ann. Biomed. Eng.* **44**, 1863–1880 (2016).

279. Kornmuller, A., Brown, C. F. C., Yu, C. & Flynn, L. E. Fabrication of extracellular matrix-derived foams and microcarriers as tissue-specific cell culture and delivery platforms. *J. Vis. Exp.* **2017**, 1–11 (2017).

280. Fu, Y. *et al.* Decellularization of porcine skeletal muscle extracellular matrix for the formulation of a matrix hydrogel: A preliminary study. *J. Cell. Mol. Med.* **20**, 740–749 (2016).

281. Ribeiro, M. P., Relvas, R., Chiquita, S. & Correia, I. J. Isolation of human umbilical arterial smooth muscle cells (HUASMC). *J. Vis. Exp.* 2–3 (2010). doi:10.3791/1940

282. Wan, X. *et al.* Electrospun PCL/keratin/AuNPs mats with the catalytic generation of nitric oxide for potential of vascular tissue engineering. *J. Biomed. Mater. Res. - Part A* **106**, 3239–3247 (2018).

283. Song, L. J. *et al.* Construction of cavernosum smooth muscle using umbilical artery smooth muscle cells seeded on acellular corporal collagen matrices. *Int. J. Androl.* **32**, 514–523 (2009).

284. Hoerstrup, S. P. *et al.* Living, autologous pulmonary artery conduits tissue engineered from human umbilical cord cells. *Ann. Thorac. Surg.* **74**, 46–52 (2002).

285. Khan, S., Tijare, M., Jain, M. & Desai, A. Artifacts in Histopathology: A Potential Cause of Misinterpretation. *Res. Rev. J. ofDental Sci.* **2014**, 23–31 (2014).

286. Fischer, A. H., Jacobson, K. A., Rose, J. & Zeller, R. Cutting sections of paraffin-embedded tissues. *Cold Spring Harb. Protoc.* **3**, 4987–4990 (2008).

287. Titford, M. The long history of hematoxylin. *Biotech. Histochem.* **80**, 73–78 (2005).

288. Rosai, J. Why microscopy will remain a cornerstone of surgical pathology. *Lab. Investig.* **87**, 403–408 (2007).

289. Zheng, H. *et al.* Gax regulates human vascular smooth muscle cell phenotypic modulation and vascular remodeling. *Am. J. Transl. Res.* **8**, 2912–2925 (2016).

290. Chan, J. K. C. The wonderful colors of the hematoxylin-eosin stain in diagnostic surgical pathology. *Int. J. Surg. Pathol.* **22**, 12–32 (2014).

291. Cardiff, R. D., Miller, C. H. & Munn, R. J. Manual hematoxylin and eosin staining of mouse tissue sections. *Cold Spring Harb. Protoc.* **2014**, 655–658 (2014).

292. Lattouf, R. *et al.* Picrosirius Red Staining: A Useful Tool to Appraise Collagen Networks in Normal and Pathological Tissues. *J. Histochem. Cytochem.* **62**, 751–758 (2014).

293. Velidandla, S. *et al.* Histochemical analysis of polarizing colors of collagen using Picrosirius Red staining in oral submucous fibrosis. *J Int Oral Heal.* **6**, 33–38 (2014).

294. Junqueira, L. C. U., Bignolas, G. & Brentani, R. R. Picrosirius stain- ing plus polarization microscopy, a specific method for col- lagen detection in tissue sections. *Histochem. J.* **11**, 4476–455 (1979).

295. Brody, S. *et al.* Characterizing nanoscale topography of the aortic heart valve basement membrane for tissue engineering heart valve scaffold design. *Tissue Eng.* **12**, 413–421 (2006).

296. Dowling, D. P., Miller, I. S., Ardhaoui, M. & Gallagher, W. M. Effect of surface wettability and topography on the adhesion of osteosarcoma cells on plasma-modified polystyrene. *J. Biomater. Appl.* **26**, 327–347 (2011).

297. Ivanova, A. A. *et al.* Effect of low-temperature plasma treatment of electrospun polycaprolactone fibrous scaffolds on calcium carbonate mineralisation. *RSC Adv.* **8**, 39106–39114 (2018).

298. Ghobeira, R. *et al.* Effects of different sterilization methods on the physico-chemical and bioresponsive properties of plasma-treated polycaprolactone films. *Biomed. Mater.* **12**, (2017).

299. Behnisch, J., Holländer, A. & Zimmermann, H. Factors influencing the hydrophobic recovery of oxygen-plasma-treated polyethylene. *Surf. Coatings Technol.* **59**, 356–358 (1993).

300. Abbott, W. M., Megerman, J., Hasson, J. E., L'Italien, G. & Warnock, D. F. Effect of compliance mismatch on vascular graft patency. *J. Vasc. Surg.* **5**, 376–382 (1987).

301. Stekelenburg, M., Rutten, M. C. M., Snoeckx, L. H. E. H. & Baaijens, F. P. T. Dynamic Straining Combined with Fibrin Gel Cell Seeding Improves Strength of Tissue-Engineered Small-Diameter Vascular Grafts. *Tissue Eng. Part A* **15**, 1081–1089 (2009).

302. Soletti, L. *et al.* A Bi-Layered Elastomeric Scaffold for Tissue Engineering of Small-Diameter Vascular Grafts. *Acta Biomater.* **6**, 110–122 (2010).

303. Maldonado-Codina, C. & Efron, N. Dynamic wettability of pHEMA-based hydrogel contact

lenses. *Ophthalmic Physiol. Opt.* **26**, 408–418 (2006).

304. Menzies, K. L. & Jones, L. The impact of contact angle on the biocompatibility of biomaterials. *Optom. Vis. Sci.* **87**, 387–399 (2010).

305. Bracco, G. & Holst, B. Contact Angle and Wetting Properties. in *Surface Science Techniques* (eds. Yuan, Y. & Lee, T. .) **51**, (2013).

306. Pethica, B. A. The physical chemistry of cell adhesion. *Exp. Cell Res.* **8**, 123–140 (1961).

307. Maldonado-Codina, C. & Morgan, P. B. In vitro water wettability of silicone hydrogel contact lenses determined using the sessile drop and captive bubble techniques. *J. Biomed. Mater. Res. Part A* 496–502 (2006). doi:10.1002/jbm.a

308. Samoilova, N. A. *et al.* Polyelectrolyte thromboresistant affinity coatings for modification of devices contacting blood. *J. Biomed. Mater. Res. Part A* 589–598 (2006). doi:10.1002/jbm.a

309. Stalder, A. F. *et al.* Low-bond axisymmetric drop shape analysis for surface tension and contact angle measurements of sessile drops. *Colloids Surfaces A Physicochem. Eng. Asp.* **364**, 72–81 (2010).

310. Keun Kwon, I., Kidoaki, S. & Matsuda, T. Electrospun nano- to microfiber fabrics made of biodegradable copolyesters: Structural characteristics, mechanical properties and cell adhesion potential. *Biomaterials* **26**, 3929–3939 (2005).

311. Bashur, C. A., Dahlgren, L. A. & Goldstein, A. S. Effect of fiber diameter and orientation on fibroblast morphology and proliferation on electrospun poly(d,l-lactic-co-glycolic acid) meshes. *Biomaterials* **27**, 5681–5688 (2006).

312. Delaine-Smith, R. M., Green, N. H., Matcher, S. J., MacNeil, S. & Reilly, G. C. Monitoring fibrous scaffold guidance of three-dimensional collagen organisation using minimally-invasive second harmonic generation. *PLoS One* **9**, (2014).

313. Liu, C. *et al.* The effect of the fibre orientation of electrospun scaffolds on the matrix production of rabbit annulus fibrosus-derived stem cells. *Bone Res.* **3**, (2015).

314. Hotaling, N. A., Bharti, K., Kriel, H. & Simon, C. G. DiameterJ: A validated open source nanofiber diameter measurement tool. *Biomaterials* **61**, 327–338 (2015).

315. Xiao, X. *et al.* The promotion of angiogenesis induced by three-dimensional porous beta-tricalcium phosphate scaffold with different interconnection sizes via activation of PI3K/Akt pathways. *Sci. Rep.* **5**, 1–11 (2015).

316. Karageorgiou, V. & Kaplan, D. Porosity of 3D biomaterial scaffolds and osteogenesis. *Biomaterials* **26**, 5474–5491 (2005).

317. Soliman, S. *et al.* Controlling the porosity of fibrous scaffolds by modulating the fiber diameter and packing density. *J. Biomed. Mater. Res. - Part A* **96 A**, 566–574 (2011).

318. Choi, S.-W., Zhang, Y. & Xia, Y. Three-dimensional Scaffolds for Tissue Engineering: The Importance of Uniformity in Pore Size and Structure. *Langmuir* **49**, 1841–1850 (2009).

319. Griffiths, P. R. & de Haseth, J. A. *Fourier Transform Infrared Spectroscopy*. (John Wiley and Sons, 2007).

320. Carvalho, M. S. *et al.* Co-culture cell-derived extracellular matrix loaded electrospun microfibrous scaffolds for bone tissue engineering. *Mater. Sci. Eng. C* **99**, 479–490 (2019).

321. Aslani, S., Kabiri, M., Kehtari, M. & Hanaee-Ahvaz, H. Vascular tissue engineering: Fabrication and characterization of acetylsalicylic acid-loaded electrospun scaffolds coated with amniotic membrane lysate. *J. Cell. Physiol.* **234**, 16080–16096 (2019).

322. Hartman, O. *et al.* Biofunctionalization of electrospun PCL-based scaffolds with perlecan domain IV peptide to create a 3-D pharmacokinetic cancer model. *Biomaterials* **31**, 5700–5718 (2011).

323. Schoen, B. *et al.* Electrospun Extracellular Matrix: Paving the Way to Tailor-Made Natural Scaffolds for Cardiac Tissue Regeneration. *Adv. Funct. Mater.* **27**, 1–9 (2017).

324. Matuska, A. M., Mcfetridge, P. S. & Family, J. C. P. The effect of terminal sterilization on structural and biophysical properties of a decellularized collagen-based scaffold; implications for stem cell adhesion. *J Biomed Mater Res B Appl Biomater* **103**, 1–22 (2016).

325. Baker, M. J. *et al.* Using Fourier transform IR spectroscopy to analyze biological materials. *Nat. Protoc.* **9**, 1771-1791. (2014).

326. Camacho, N. P., West, P., Torzilli, P. A. & Mendelsohn, R. FTIR Microscopic Imaging of Collagen and Proteoglycan in Bovine Cartilage. *Biopolymers* **62**, 1–8 (2001).

327. Impens, S., Chen, Y., Mullens, S., Luyten, F. & Schrooten, J. Controlled cell-seeding methodologies: A first step toward clinically relevant bone tissue engineering strategies. *Tissue Eng. - Part C Methods* **16**, 1575–1583 (2010).

328. Promega. Technical Bulletin: CellTiter-Blue Cell Viability Assay. 1–16 (2016).

329. Scientific, T. PierceTM BCA Protein Assay Kit. (2013). doi:10.1016/j.ijproman.2010.02.012

330. Walker, J. M. The bicinchoninic acid (BCA) assay for protein quantitation. *Methods Mol. Biol.* 11–16 (2009). doi:10.1385/1-59259-169-8:11

331. Guler, Z. & Sarac, A. S. Electrochemical impedance and spectroscopy study of the EDC/NHS activation of the carboxyl groups on poly(ε-caprolactone)/poly(m-anthranilic acid) nanofibers. *Express Polym. Lett.* **10**, 96–110 (2016).

332. Yu, T. T. & Shoichet, M. S. Guided cell adhesion and outgrowth in peptide-modified channels for neural tissue engineering. *Biomaterials* **26**, 1507–1514 (2005).

333. Shalumon, K. T. *et al.* Fabrication of chitosan/poly(caprolactone) nanofibrous scaffold for bone and skin tissue engineering. *Int. J. Biol. Macromol.* **48**, 571–576 (2011).

334. Dai, N. T., Williamson, M. R., Khammo, N., Adams, E. F. & Coombes, A. G. A. Composite cell support membranes based on collagen and polycaprolactone for tissue engineering of skin. *Biomaterials* **25**, 4263–4271 (2004).

335. Fischer, M. J. E. Amine Coupling Through EDC/NHS: A Practical Approach. in *Surface Plasmon Resonance: Methods and Protocols* (eds. Mol, N. J. & Fischer, M. J. E.) 55–73 (Humana Press, 2010). doi:10.1007/978-1-60761-670-2_3

336. Bartczak, D. & Kanaras, A. G. Preparation of peptide-functionalized gold nanoparticles using one pot EDC/Sulfo-NHS coupling. *Langmuir* **27**, 10119–10123 (2011).

337. Hua, J. *et al.* Preparation and properties of EDC/NHS mediated crosslinking poly (gamma-glutamic acid)/epsilon-polylysine hydrogels. *Mater. Sci. Eng. C* **61**, 879–892 (2016).

338. Wang, C., Yan, Q., Liu, H. B., Zhou, X. H. & Xiao, S. J. Different EDC/NHS activation mechanisms between PAA and PMAA brushes and the following amidation reactions.

Langmuir **27**, 12058–12068 (2011).

339. Nakajima, N. & Ikada, Y. Mechanism of Amide Formation by Carbodiimide for Bioconjugation in Aqueous Media. *Bioconjug. Chem.* **6**, 123–130 (1995).

340. Devices, M. *Quant-iT PicoGreen dsDNA assay with SpectraMax Microplate Readers*. (2015).

341. BioSystems, T. Quant-iT Pico Green dsDNA kit. *Turn. Biosyst.* 1–4

342. Kilgore, J. A., Dolman, N. J. & Davidson, M. W. A review of reagents for fluorescence microscopy of cellular compartments and structures, Part III: Reagents for actin, tubulin, cellular membranes, and whole cell and cytoplasm. *Curr. Protoc. Cytom.* 1–17 (2014). doi:10.1002/0471142956.cy1232s67

343. Kapuscinski, J. DAPI: A DMA-Specific fluorescent probe. *Biotech. Histochem.* **70**, 220–233 (1995).

344. Mouras, R., Bagnaninchi, P., Downes, A. & Elfick, A. Multimodal, label-free nonlinear optical imaging for applications in biology and biomedical science. *J. Raman Spectrosc.* **44**, 1373–1378 (2013).

345. Hopwood, D. Theoretical and practical aspects of glutaraldehyde fixation. *Histochem. J.* **4**, 267–303 (1972).

346. Thiery, G., Bernier, J. & Bergeron, M. A simple technique for staining of cell membranes with imidazole and osmium tetroxide. *J. Histochem. Cytochem.* **43**, 1079–1084 (1995).

347. Sizeland, K. H. *et al.* Nanostructure of electrospun collagen: Do electrospun collagen fibers form native structures? *Materialia* **3**, 90–96 (2018).

348. Pouliot, R. A. *et al.* Development and characterization of a naturally derived lung extracellular matrix hydrogel. *J. Biomed. Mater. Res. - Part A* **104**, 1922–1935 (2016).

349. Grant, R., Hay, D. & Callanan, A. From scaffold to structure: The synthetic production of cell derived extracellular matrix for liver tissue engineering. *Biomed. Phys. Eng. Express* **4**, (2018).

350. Livak, K. J. & Schmittgen, T. D. Analysis of relative gene expression data using real-time quantitative PCR and the 2-ΔΔCT method. *Methods* **25**, 402–408 (2001).

351. Rao, X., Huang, X., Zhou, Z. & Lin, X. An improvement of the 2ˆ(-delta delta CT) method for quantitative real-time polymerase chain reaction data analysis. *Biostat. Bioinforma. Biomath.* **3**, 71–85 (2013).

352. Lee, S. J., Yoo, J. J., Lim, G. J., Atala, A. & Stitzel, J. In vitro evaluation of electrospun nanofiber scaffolds for vascular graft application. *J. Biomed. Mater. Res. - Part A* **83A**, 999–1008 (2007).

353. Balint, R., Cassidy, N. J. & Cartmell, S. H. Electrical Stimulation: A Novel Tool for Tissue Engineering. *Tissue Eng. Part B Rev.* **19**, 48–57 (2013).

354. Burton, T. P. & Callanan, A. A Non-woven Path: Electrospun Polylactic Acid Scaffolds for Kidney Tissue Engineering. *J. Tissue Eng. Regen. Med.* **15**, 301–310 (2018).

355. McGlohorn, J. B., Holder, W. D., Grimes, L. W., Thomas, C. B. & Burg, K. J. L. Evaluation of Smooth Muscle Cell Response Using Two Types of Porous Polylactide Scaffolds with Differing Pore Topography. *Tissue Eng.* **10**, 505–514 (2004).

356. Noriega, S. E., Hasanova, G. I., Schneider, M. J., Larsen, G. F. & Subramanian, A. Effect of

fiber diameter on the spreading, proliferation and differentiation of chondrocytes on electrospun chitosan matrices. *Cells Tissues Organs* **195**, 207–221 (2012).

357. Taskin, M. B., Xia, D., Besenbacher, F., Dong, M. & Chen, M. Nanotopography featured polycaprolactone/polyethyleneoxide microfibers modulate endothelial cell response. *Nanoscale* **9**, 9218–9229 (2017).

358. Azimi, B., Nourpanah, P., Rabiee, M. & Arbab, S. Poly (lactide -co- glycolide) Fiber : An Overview. *J. Eng. Fiber. Fabr.* **9**, 74–90 (2014).

359. Albelda, S. M., Muller, W. A., Buck, C. A. & Newman, P. J. Molecular and Cellular Properties of PECAM-1(endoCAM/CD31): A Novel Vascular Cell-Cell Adhesion Molecule. *J. Cell Biol.* **114**, 1059–1068 (1991).

360. Grant, R., Hay, D. C. & Callanan, A. A Drug-Induced Hybrid Electrospun Poly-Capro-Lactone: Cell-Derived Extracellular Matrix Scaffold for Liver Tissue Engineering. *Tissue Eng. Part A* **23**, 650–662 (2017).

361. Fischer, L. J. *et al.* Endothelial Differentiation of Adipose-Derived Stem Cells: Effects of Endothelial Cell Growth Supplement and Shear Force. *J. Surg. Res.* **152**, 157–166 (2009).

362. Suzanne, M. & Steller, H. Shaping organisms with apoptosis. *Cell Death Differ.* **20**, 669–675 (2013).

363. Dhandayuthapani, B., Yoshida, Y., Maekawa, T. & Kumar, D. S. Polymeric scaffolds in tissue engineering application: A review. *Int. J. Polym. Sci.* **2011**, (2011).

364. Lam, C. X. F., Savalani, M. M., Teoh, S. & Hutmacher, D. W. Dynamics of in vitro polymer degradation of polycaprolactone-based scaffolds : accelerated versus simulated physiological conditions. *Biomed. Mater.* **3**, 034108 (2008).

365. Denchai, A., Tartarini, D. & Mele, E. Cellular Response to Surface Morphology: Electrospinning and Computational Modeling. *Front. Bioeng. Biotechnol.* **6**, 1–11 (2018).

366. Edmondson, R., Broglie, J. J., Adcock, A. F. & Yang, L. Three-Dimensional Cell Culture Systems and Their Applications in Drug Discovery and Cell-Based Biosensors. *Assay Drug Dev. Technol.* **12**, 207–218 (2014).

367. Zhang, Q., Gerlach, J. C., Schmelzer, E. & Nettleship, I. Effect of Calcium-Infiltrated Hydroxyapatite Scaffolds on the Hematopoietic Fate of Human Umbilical Vein Endothelial Cells. *J. Vasc. Res.* **54**, 376–385 (2017).

368. Deroanne, C. F. *et al.* Cdc42 downregulates MMP-1 expression by inhibiting the ERK1/2 pathway. *J. Cell Sci.* **118**, 1173–1183 (2005).

369. Raffetto, J. D. & Khalil, R. A. Matrix metalloproteinases and their inhibitors in vascular remodeling and vascular disease. *Biochem. Pharmacol.* **75**, 346–359 (2008).

370. Sapino, A. *et al.* Expression of CD31 by cells of extensive ductal in situ and invasive carcinomas of the breast. *J. Pathol.* **194**, 254–261 (2001).

371. Stefansson, I. M. *et al.* Increased angiogenesis is associated with a 32-gene expression signature and 6p21 amplification in aggressive endometrial cancer. *Oncotarget* **6**, (2015).

372. Bank, A. J. *et al.* Contribution of collagen, elastin, and smooth muscle to in vivo human brachial artery wall stress and elastic modulus. *Circulation* **94**, 3263–3270 (1996).

373. Owens, G. K., Kumar, M. S. & Wamhoff, B. R. Molecular regulation of vascular smooth

muscle cell differentiation in development and disease. *Physiol. Rev.* **84**, 767–801 (2004).

374. Murphy, C. M., Haugh, M. G. & O'Brien, F. J. The effect of mean pore size on cell attachment, proliferation and migration in collagen-glycosaminoglycan scaffolds for bone tissue engineering. *Biomaterials* **31**, 461–466 (2010).

375. Fu, W. *et al.* Electrospun gelatin / PCL and collagen / PLCL scaffolds for vascular tissue engineering. *Int. J. Nanomedicine* **9**, 2335–2344 (2014).

376. Bridge, J. C. *et al.* Electrospun gelatin-based scaffolds as a novel 3D platform to study the function of contractile smooth muscle cells in vitro. *Biomed. Phys. Eng. Express* **4**, (2018).

377. Goldberg, M. T., Han, Y. P., Yan, C., Shaw, M. C. & Garner, W. L. TNF-α suppresses α-smooth muscle actin expression in human dermal fibroblasts: An implication for abnormal wound healing. *J. Invest. Dermatol.* **127**, 2645–2655 (2007).

378. Parmacek, M. S. Myocardin Dominant Driver of the Smooth Muscle Cell Contractile Phenotype. *Arter. Thromb Vasc Biol* **28**, 1416–1417 (2008).

379. Huang, J. *et al.* Myocardin regulates expression of contractile genes in smooth muscle cells and is required for closure of the ductus arteriosus in mice. *J. Clin. Invest.* **118**, 515–525 (2008).

380. Long, X., Bell, R. D., Gerthoffer, W. T., Zlokovic, B. V & Miano, J. M. Myocardin is Sufficient for a Smooth Muscle-Like Contractile Phenotype. *Arter. Thromb Vasc Biol* **28**, 1505–1510 (2008).

381. Wang, Z., Wang, D. Z., Pipes, G. C. T. & Olson, E. N. Myocardin is a master regulator of smooth muscle gene expression. *Proc. Natl. Acad. Sci. U. S. A.* **100**, 7129–7134 (2003).

382. Woodruff, M. A. & Hutmacher, D. W. The return of a forgotten polymer – Polycaprolactone in the 21st century Maria. *Prog. Polym. Sci.* (2010).

383. Han, J., Wu, Q., Xia, Y., Wagner, M. B. & Xu, C. Cell alignment induced by anisotropic electrospun fibrous scaffolds alone has limited effect on cardiomyocyte maturation Jingjia. *Stem Cell Res.* **16**, 740–750 (2016).

384. Kołbuk, D., Sajkiewicz, P., Maniura-Weber, K. & Fortunato, G. Structure and morphology of electrospun polycaprolactone/gelatine nanofibres. *Eur. Polym. J.* **49**, 2052–2061 (2013).

385. Whited, B. M., Whitney, J. R., Hofmann, M. C., Xu, Y. & Rylander, M. N. Pre-osteoblast infiltration and differentiation in highly porous apatite-coated PLLA electrospun scaffolds. *Biomaterials* **32**, 2294–2304 (2011).

386. Phipps, M. C., Clem, W. C., Grunda, J. M., Clines, G. A. & Bellis, S. L. Increasing the pore sizes of bone-mimetic electrospun scaffolds comprised of polycaprolactone, collagen I and hydroxyapatite to enhance cell infiltration. *Biomaterials* **33**, 524–534 (2012).

387. Noda, S. *et al.* Effect of cell culture density on dental pulp-derived mesenchymal stem cells with reference to osteogenic differentiation. *Sci. Rep.* **9**, 1–5 (2019).

388. Sukho, P. *et al.* Effect of Cell Seeding Density and Inflammatory Cytokines on Adipose Tissue-Derived Stem Cells: an in Vitro Study. *Stem Cell Rev. Reports* **13**, 267–277 (2017).

389. Powell, R. J., Cronenwett, J. L., Fillinger, M. F., Wagner, R. J. & Sampson, L. N. Endothelial cell modulation of smooth muscle cell morphology and organizational growth pattern. *Ann. Vasc. Surg.* **10**, 4–10 (1996).

390. Endlich, N., Endlich, K., Taesch, N. & Helwig, J. J. Culture of vascular smooth muscle cells from small arteries of the rat kidney. *Kidney Int.* **57**, 2468–2475 (2000).

391. Heron, M. Deaths: Leading Causes for 2015. *Natl. Vital Stat. Rep.* **66**, 1–76 (2017).

392. Blanche, C. *et al.* Heart transplantation in patients seventy years of age and older: a comparative analysis of outcome. *J. Thorac. Cardiovasc. Surg.* **121**, 532–541 (2001).

393. Ravi, S. & Chaikof, E. Biomaterials for vascular tissue engineering. *Regen. Med.* **5**, 1–21 (2010).

394. Jiang, B., Akgun, B., Lam, R. C., Ameer, G. A. & Wertheim, J. A. A polymer-extracellular matrix composite with improved thromboresistance and recellularization properties. *Acta Biomater.* **18**, 50–58 (2015).

395. Hutmacher, D. W. Scaffolds in tissue engineering bone and cartilage. *Biomaterials* **21**, 2529–2543 (2000).

396. Wu, S., Liu, Y. L., Cui, B., Qu, X. H. & Chen, G. Q. Study on decellularized porcine aortic valve/poly (3-hydroxybutyrate-co-3- hydroxyhexanoate) hybrid heart valve in sheep model. *Artif. Organs* **31**, 689–697 (2007).

397. Hong, H. *et al.* Fabrication of biomatrix/polymer hybrid scaffold for heart valve tissue engineering in vitro. *ASAIO J.* **54**, 627–632 (2008).

398. Masoumi, N. *et al.* Tri-layered elastomeric scaffolds for engineering heart valve leaflets. *Biomaterials* **35**, 7774–7785 (2014).

399. Lu, T. Y. *et al.* Repopulation of decellularized mouse heart with human induced pluripotent stem cell-derived cardiovascular progenitor cells. *Nat. Commun.* **4**, 1–11 (2013).

400. Abdal-hay, A., Bartnikowski, M., Hamlet, S. & Ivanovski, S. Electrospun biphasic tubular scaffold with enhanced mechanical properties for vascular tissue engineering. *Mater. Sci. Eng. C* **82**, 10–18 (2018).

401. Sanchez, P. . *et al.* Acellular human heart matrix: A critical step toward whole heart grafts. *Biomaterials* **61**, 279–289 (2015).

402. Kasimir, M.-T. *et al.* Decellularization does not eliminate thrombogenicity and inflammatory stimulation in tissue-engineered porcine heart valves. *J. Heart Valve Dis.* **15**, 278–86; discussion 286 (2006).

403. Kang, Y., Kim, S., Khademhosseini, A. & Yang, Y. Creation of bony microenvironment with CaP and cell-derived ECM to enhance human bone-marrow MSC behavior and delivery of BMP-2. *Biomaterials* **32**, 6119–6130 (2011).

404. Bhowmick, S. *et al.* Biomimetic electrospun scaffolds from main extracellular matrix components for skin tissue engineering application – The role of chondroitin sulfate and sulfated hyaluronan. *Mater. Sci. Eng. C* **79**, 15–22 (2017).

405. Kilic, A., Emani, S., Sai-Sudhakar, C. B., Higgins, R. S. D. & Whitson, B. A. Donor selection in heart transplantation. *J. Thorac. Dis.* **6**, 1097–1104 (2014).

406. Munir, N., McDonald, A. & Callanan, A. A combinatorial approach: Cryo-printing and electrospinning hybrid scaffolds for cartilage tissue engineering. *Bioprinting* e00056 (2019). doi:10.1016/j.bprint.2019.e00056

407. Carroll, G. T., McGloughlin, T. M., O'Keeffe, L. M., Callanan, A. & Walsh, M. T. Realistic

temporal variations of shear stress modulate MMP-2 and MCP-1 expression in arteriovenous vascular access. *Cell. Mol. Bioeng.* **2**, 591–605 (2009).

408. Davis, L. M. *et al.* On the potential of hydrated storage for naturally derived ECMs and associated effects on mechanical and cellular performance. *J. Biomed. Mater. Res. - Part B Appl. Biomater.* **102**, 89–97 (2014).

409. Elzein, T., Nasser-Eddine, M., Delaite, C., Bistac, S. & Dumas, P. FTIR study of polycaprolactone chain organization at interfaces. *J. Colloid Interface Sci.* **273**, 381–387 (2004).

410. Huber, F. *et al.* Emergent complexity of the cytoskeleton: From single filaments to tissue. *Adv. Phys.* **62**, 1–112 (2013).

411. Saha, K., Pollock, J. F., Schaffer, D. V & Healy, K. E. Designing synthetic materials to control stem cell phenotype Krishanu. *Curr. Opin. Chem. Biol.* **11**, 381–387 (2007).

412. O'Brien, F. J. Biomaterials & scaffolds for tissue engineering. *Mater. Today* **14**, 88–95 (2011).

413. Sukanya, V. S. & Mohanan, P. V. Degradation of Poly (e-aprolactone) and bio-interactions with mouse bone marrow mesenchymal stem cells. *Colloids Surfaces B Biointerfaces* **163**, 107–118 (2018).

414. Zhang, Y., Ouyang, H., Chwee, T. L., Ramakrishna, S. & Huang, Z. M. Electrospinning of gelatin fibers and gelatin/PCL composite fibrous scaffolds. *J. Biomed. Mater. Res. - Part B Appl. Biomater.* **72**, 156–165 (2005).

415. Heydarkhan-Hagvall, S. *et al.* Three-dimensional electrospun ECM-based hybrid scaffolds for cardiovascular tissue engineering. *Biomaterials* **29**, 2907–2914 (2008).

416. Hwang, J. *et al.* Molecular assessment of collagen denaturation in decellularized tissues using a collagen hybridizing peptide. *Acta Biomater.* **53**, 268–278 (2017).

417. Ross, E. A., Williams, M. J. & Batich, C. D. Embryonic Stem Cells Proliferate and Differentiate when Seeded into Kidney Scaffolds. *J. Am. Soc. Nephroology* **20**, 2338–2347 (2009).

418. Nakayama, K. H., Batchelder, C. A., Lee, C. I. & Tarantal, A. F. Decellularized Rhesus Monkey Kidney as a Three-Dimensional Scaffold for Renal Tissue Engineering. *Tissue Eng. Part A* **16**, 2207–2216 (2010).

419. Ott, H. C. *et al.* Perfusion-decellularized matrix: Using nature's platform to engineer a bioartificial heart. *Nat. Med.* **14**, 213–221 (2008).

420. Ott, H. C. *et al.* Regeneration and orthotopic transplantation of a bioartificial lung. *Nat. Med.* **16**, 927–933 (2010).

421. Oberwallner, B. *et al.* Preparation of cardiac extracellular matrix scaffolds by decellularization of human myocardium. *J. Biomed. Mater. Res. - Part A* **102**, 3263–3272 (2014).

422. Cheheltani, R. *et al.* Fourier transform infrared spectroscopy to quantify collagen and elastin in an in vitro model of extracellular matrix degradation in aorta. *Analyst* **139**, 3039–3047 (2014).

423. Jahnavi, S., Kumary, T. V, Bhuvaneshwar, G. S., Natarajan, T. S. & Verma, R. S. Engineering of a polymer layered bio-hybrid heart valve scaffold. *Mater. Sci. Eng. C* **51**, 263–273 (2015).

424. Sheibani, N. & Frazier, W. a. Down-regulation of platelet endothelial cell adhesion molecule-1 results in thrombospondin-1 expression and concerted regulation of endothelial cell phenotype.

Mol. Biol. Cell **9**, 701–13 (1998).

425. Baldwin, H. S. *et al.* Platelet Endothelial-Cell Adhesion Molecule-1 (Pecam-1 Cd31) - Alternatively Spliced, Functionally Distinct Isoforms Expressed During Mammalian Cardiovascular Development. *Development* **120**, 2539–2553 (1994).

426. Wang, Z. *et al.* A preliminary study of pamidronic acid downregulation of angiogenic factors IGF-1/ PECAM-1 expression in circulating level in bone metastatic breast cancer patients. *Onco. Targets. Ther.* **9**, 3147–3152 (2016).

427. Nayak, N. R. & Brenner, R. M. Vascular Proliferation and Vascular Endothelial Growth Factor Expression in the Rhesus Macaque Endometrium. *J. Clin. Endocrinol. Metab.* **87**, 1845–1855 (2002).

428. Batra, J. *et al.* Matrix metalloproteinase-10 (MMP-10) interaction with tissue inhibitors of metalloproteinases TIMP-1 and TIMP-2: Binding studies and crystal structure. *J. Biol. Chem.* **287**, 15935–15946 (2012).

429. Wiseman, B. S. *et al.* Site-specific inductive and inhibitory activities of MMP-2 and MMP-3 orchestrate mammary gland branching morphogenesis. *J. Cell Biol.* **162**, 1123–1133 (2003).

430. Garidel, P. & Schott, H. Fourier-Transform Midinfrared Spectroscopy for Analysis and Screening of Liquid Protein Formulations. *BioProcess Tech.* **1**, 48–55 (2006).

431. Porreca, E. *et al.* Effect of interleukin-1 receptor antagonist on vascular smooth muscle cell proliferation. *Atherosclerosis* **99**, 71–78 (1993).

432. Belbachir, K., Noreen, R., Gouspillou, G. & Petibois, C. Collagen types analysis and differentiation by FTIR spectroscopy. *Anal. Bioanal. Chem.* **395**, 829–837 (2009).

433. Jeremy, J. Y., Rowe, D., Emsley, A. M. & Newby, A. C. Nitric oxide and the proliferation of vascular smooth muscle cells. *Cardiovasc. Res.* **43**, 580–594 (1999).

434. Takeuchi, H., Hashimoto, N., Kitai, R., Kubota, T. & Kikuta, K. I. Proliferation of vascular smooth muscle cells in glioblastoma multiforme: Laboratory investigation. *J. Neurosurg.* **113**, 218–224 (2010).

435. Chang, S. *et al.* Phenotypic modulation of primary vascular smooth muscle cells by short-term culture on micropatterned substrate. *PLoS One* **9**, (2014).

436. Endlich, N., Endlich, K., Taesch, N. & Helwig, J. J. Culture of vascular smooth muscle cells from small arteries of the rat kidney. *Kidney Int.* **57**, 2468–2475 (2000).

437. Beasley, D., McGuiggin, M. E. & Dinarello, C. A. Human vascular smooth muscle cells produce an intracellular form of interleukin-1 receptor antagonist. *Am. J. Physiol. - Cell Physiol.* **269**, (1995).

438. Kim, T. H., Jung, Y. & Kim, S. H. Nanofibrous Electrospun Heart Decellularized Extracellular Matrix-Based Hybrid Scaffold as Wound Dressing for Reducing Scarring in Wound Healing. *Tissue Eng. Part A* ten.tea.2017.0318 (2018). doi:10.1089/ten.tea.2017.0318

439. Kazarian, S. G. & Chan, K. L. A. ATR-FTIR spectroscopic imaging: recent advances and applications to biological systems. *Analyst* **138**, 1940 (2013).

440. Shapiro, S. D., Endicott, S. K., Province, M. A., Pierce, J. A. & Campbell, E. J. Marked longevity of human lung parenchymal elastic fibers deduced from prevalence of D-aspartate and nuclear weapons-related radiocarbon. *J. Clin. Invest.* **87**, 1828–1834 (1991).

441. Muiznieks, L. D. & Keeley, F. W. Molecular assembly and mechanical properties of the extracellular matrix: A fibrous protein perspective. *Biochim. Biophys. Acta - Mol. Basis Dis.* **1832**, 866–875 (2013).

442. Llames, S., García-Pérez, E., Meana, Á., Larcher, F. & Del Río, M. Feeder Layer Cell Actions and Applications. *Tissue Eng. - Part B Rev.* **21**, 345–353 (2015).

443. Amit, M., Shariki, C., Margulets, V. & Itskovitz-Eldor, J. Feeder Layer- and Serum-Free Culture of Human Embryonic Stem Cells1. *Biol. Reprod.* **70**, 837–845 (2004).

444. Fang, C. Y., Wu, C. C., Fang, C. L., Chen, W. Y. & Chen, C. L. Long-term growth comparison studies of FBS and FBS alternatives in six head and neck cell lines. *PLoS One* **12**, 1–27 (2017).

445. Brunner, D. *et al.* Serum-free Cell Culture: The Serum-free Media Interactive Online Database. *ALTEX* **1**, 53/62 (2010).

446. Liu, H., Li, X., Zhou, G., Fan, H. & Fan, Y. Electrospun sulfated silk fibroin nanofibrous scaffolds for vascular tissue engineering. *Biomaterials* **32**, 3784–3793 (2011).

447. Edlund, U., Sauter, T. & Albertsson, A. C. Covalent VEGF protein immobilization on resorbable polymeric surfaces. *Polym. Adv. Technol.* **22**, 2368–2373 (2011).

448. Lu, C. Y. *et al.* Andrographolide inhibits TNFα-induced ICAM-1 expression via suppression of NADPH oxidase activation and induction of HO-1 and GCLM expression through the PI3K/Akt/Nrf2 and PI3K/Akt/AP-1 pathways in human endothelial cells. *Biochem. Pharmacol.* **91**, 40–50 (2014).

449. Coad, B. R. *et al.* Functionality of proteins bound to plasma polymer surfaces. *ACS Appl. Mater. Interfaces* **4**, 2455–2463 (2012).

450. Favot, L., Keravis, T., Holl, V., Le Bec, A. & Lugnier, C. VEGF-induced HUVEC migration and proliferation are decreased by PDE2 and PDE4 inhibitors. *Thromb. Haemost.* **90**, 334–343 (2003).

451. Vincenti, M. P. The Matrix Metalloproteinase (MMP) and Tissue Inhibitor of Metalloproteinase (TIMP) Genes. *Matrix Met. Protoc.* **151**, 79–120 (2000).

452. Hobeika, M. J., Thompson, R. W., Muhs, B. E., Brooks, P. C. & Gagne, P. J. Matrix metalloproteinases in peripheral vascular disease. *J. Vasc. Surg.* **45**, 849–857 (2007).

453. Kopp, P. M. *et al.* Studies on the morphology and spreading of human endothelial cells define key inter- and intramolecular interactions for talin1. *Eur. J. Cell Biol.* **89**, 661–673 (2010).

454. Ng, F. L. *et al.* A facile method for fabricating a three-dimensional aligned fibrous scaffold for vascular application. *RSC Adv.* **9**, 13054–13064 (2019).

455. Nivison-Smith, L. & Weiss, A. S. Alignment of human vascular smooth muscle cells on parallel electrospun synthetic elastin fibers. *J. Biomed. Mater. Res. - Part A* **100 A**, 155–161 (2012).

456. Dupont, A. *et al.* The proteome and secretome of human arterial smooth muscle cells. *Proteomics* **5**, 585–596 (2005).

457. Shaikh, F. M. *et al.* New pulsatile hydrostatic pressure bioreactor for vascular tissue-engineered constructs. *Artif. Organs* **34**, 153–158 (2010).

458. Ohashi, T., Sugaya, Y., Sakamoto, N. & Sato, M. Hydrostatic pressure influences morphology

and expression of VE-cadherin of vascular endothelial cells. *J. Biomech.* **40**, 2399–2405 (2007).

459. Müller-Marschhausen, K., Waschke, J. & Drenckhahn, D. Physiological hydrostatic pressure protects endothelial monolayer integrity. *Am. J. Physiol. - Cell Physiol.* **294**, 324–332 (2008).

460. Baldea, I. *et al.* Effects of different hypoxia degrees on endothelial cell cultures—Time course study. *Mech. Ageing Dev.* **172**, 45–50 (2018).

461. Chan, C. K. & Vanhoutte, P. M. Hypoxia, vascular smooth muscles and endothelium. *Acta Pharm. Sin. B* **3**, 1–7 (2013).

462. Lu, D. & Kassab, G. S. Role of shear stress and stretch in vascular mechanobiology. *J. R. Soc. Interface* **8**, 1379–1385 (2011).

463. Paszkowiak, J. J. & Dardik, A. Arterial wall shear stress: Observations from the bench to the bedside. *Vasc. Endovascular Surg.* **37**, 47–57 (2003).

464. Kakisis, J. D., Liapis, C. D. & Sumpio, B. E. Effects of cyclic strain on vascular cells. *Endothel. J. Endothel. Cell Res.* **11**, 17–28 (2004).

465. Wilson, E., Mai, Q., Sudhir, K., Weiss, R. H. & Ives, H. E. Mechanical strain induces growth of vascular smooth muscle cells via autocrine action of PDGF. *J. Cell Biol.* **123**, 741–747 (1993).

466. Naomi Handly, L., Pilko, A. & Wollman, R. Paracrine communication maximizes cellular response fidelity in wound signaling. *Elife* **4**, 1–18 (2015).

467. Faller, D. V. Endothelial cell responses to hypoxic stress. *Clin. Exp. Pharmacol. Physiol.* **26**, 74–84 (1999).

468. Wu, J., Lei, Z. & Yu, J. Hypoxia induces autophagy in human vascular endothelial cells in a hypoxia-inducible factor 1-dependent manner. *Mol. Med. Rep.* **11**, 2677–2682 (2014).

469. Kennamer, A. *et al.* Bioreactor conditioning of valve scaffolds seeded internally with adult stem cells. *Tissue Eng. Regen. Med.* **13**, 507–515 (2016).

470. Toyoda, T. *et al.* Hydrostatic Pressure Modulates Proteoglycan Metabolism in Chondrocytes Seeded in Agarose. *Arthritis Rheum.* **48**, 2865–2872 (2003).

471. Schroder, C. *et al.* A Closed Loop Perfusion Bioreactor for Dynamic Hydrostatic Pressure Loading and Cartilage Tissue Engineering. *J. Mech. Med. Biol.* **16**, 1–16 (2016).

472. Fassina, L., Magenes, G., Gimmelli, R. & Naro, F. Modulation of the cardiomyocyte contraction inside a hydrostatic pressure bioreactor: In vitro verification of the frank-starling law. *Biomed Res. Int.* **2015**, (2015).

473. Piola, M. *et al.* Full Mimicking of Coronary Hemodynamics for Ex-Vivo Stimulation of Human Saphenous Veins. *Ann. Biomed. Eng.* **45**, 884–897 (2017).

474. Meyer, E. G., Buckley, C. T., Steward, A. J. & Kelly, D. J. The effect of cyclic hydrostatic pressure on the functional development of cartilaginous tissues engineered using bone marrow derived mesenchymal stem cells. *J. Mech. Behav. Biomed. Mater.* **4**, 1257–1265 (2011).

475. Elder, S. H. *et al.* Chondrocyte Response to Cyclic Hydrostatic Pressure in Alginate Versus Pellet Culture. *J. Orthop. Res.* **24**, 740–747 (2006).

476. Nakamura, S. *et al.* Hydrostatic Pressure Induces Apoptosis of Chondrocytes Cultured in

Alginate Beads. *J. Orthop. Res.* **24**, 733–739 (2006).

477. Dumont, K. *et al.* Design of a new pulsatile bioreactor for tissue engineered aortic heart valve formation. *Artif. Organs* **26**, 710–714 (2002).

478. Sodia, R. *et al.* New pulsatile bioreactor for fabrication of tissue-engineered patches. *J. Biomed. Mater. Res.* **58**, 401–405 (2001).

479. Schulte, J. *et al.* A Novel Seeding and Conditioning Bioreactor for Vascular Tissue Engineering. *Processes* **2**, 526–547 (2014).

480. Schwartz, E. A., Bizios, R., Medow, M. S. & Gerritsen, M. E. Exposure of Human Vascular Endothelial Cells to Sustained Hydrostatic Pressure Stimulates Proliferation Involvement of the ␣ V Integrins. (1999).

481. Prystopiuk, V. *et al.* A two-phase response of endothelial cells to hydrostatic pressure. *J. Cell Sci.* **131**, jcs206920 (2018).

482. DeLisser, H. M. *et al.* Involvement of endothelial PECAM-1/CD31 in angiogenesis. *Am. J. Pathol.* **151**, 671–677 (1997).

483. Voelkel, N. F., Mizuno, S. & Bogaard, H. J. The role of hypoxia in pulmonary vascular diseases: A perspective. *Am. J. Physiol. - Lung Cell. Mol. Physiol.* **304**, (2013).

484. Versari, D., Daghini, E., Virdis, A., Ghiadoni, L. & Taddei, S. Endothelial dysfunction as a target for prevention of cardiovascular disease. *Diabetes Care* **32 Suppl 2**, (2009).

485. Michiels, C., Arnould, T. & Remacle, J. Endothelial cell responses to hypoxia: initiation of a cascade of cellular interactions. *Biochim. Biophys. Acta* **1497**, 1–10 (2000).

486. Busse, R., Pohl, U., Kellner, C. & Klemm, U. Endothelial cells are involved in the vasodilatory response to hypoxia. *Pflügers Arch. Eur. J. Physiol.* **397**, 78–80 (1983).

487. Bertlein, S. *et al.* Development of Endothelial Cell Networks in 3D Tissues by Combination of Melt Electrospinning Writing with Cell-Accumulation Technology. *Small* **14**, 1–7 (2018).

488. Heiss, C., Rodriguez-Mateos, A. & Kelm, M. Central Role of eNOS in the Maintenance of Endothelial Homeostasis. *Antioxidants Redox Signal.* **22**, 1230–1242 (2015).

489. Greijer, A. E. & Van Der Wall, E. The role of hypoxia inducible factor 1 (HIF-1) in hypoxia induced apoptosis. *J. Clin. Pathol.* **57**, 1009–1014 (2004).

490. Wu, D. & Yotnda, P. Induction and testing of hypoxia in cell culture. *J. Vis. Exp.* 4–7 (2011). doi:10.3791/2899

491. Jundziłł, A. *et al.* Vascularization potential of electrospun poly(L-lactide-co-caprolactone) scaffold: The impact for tissue engineering. *Med. Sci. Monit.* **23**, 1540–1551 (2017).

492. Janaszak-Jasiecka, A. *et al.* eNOS expression and NO release during hypoxia is inhibited by miR-200b in human endothelial cells. *Angiogenesis* **21**, 711–724 (2018).

493. Reid, J. A. & Callanan, A. The Influence of Aorta Extracellular Matrix in Electrospun Polycaprolactone Scaffolds. *J. Appl. Polym. Sci.* **136**, 48181 (2019).

494. Reid, J. A. & Callanan, A. Hybrid cardiovascular sourced extracellular matrix scaffolds as possible platforms for vascular tissue engineering. *J. Biomed. Mater. Res. Part B - Appl. Biomater.* 1–15 (2019).

495. Li, M. *et al.* Electrospun protein fibers as matrices for tissue engineering. *Biomaterials* **26**, 5999–6008 (2005).

496. Malikmammadov, E., Tanir, T. E., Kiziltay, A., Hasirci, V. & Hasirci, N. PCL and PCL-based materials in biomedical applications. *J. Biomater. Sci. Polym. Ed.* **29**, 863–893 (2018).

497. Sun, H., Mei, L., Song, C., Cui, X. & Wang, P. The in vivo degradation , absorption and excretion of PCL-based implant. *Biomaterials* **27**, 1735–1740 (2006).

498. Feng, Y. *et al.* Electrospun Poly(lactide-co-glycolide-co-3(S)-methylmorpholine- 2,5-dione) nanofibrous scaffolds for tissue engineering. *Polymers (Basel).* **8**, 1–14 (2016).

499. Fleischer, S., Miller, J., Hurowitz, H., Shapira, A. & Dvir, T. Effect of fiber diameter on the assembly of functional 3D cardiac patches. *Nanotechnology* **26**, (2015).

500. Safaeijavan, R., Soleimani, M., Divsalar, A., Eidi, A. & Ardeshirylajimi, A. Comparison of random and aligned PCL nanofibrous electrospun scaffolds on cardiomyocyte differentiation of human adipose-derived stem cells. *Iran. J. Basic Med. Sci.* **17**, 903–911 (2014).

501. Vaquette, C. & Cooper-White, J. J. Increasing electrospun scaffold pore size with tailored collectors for improved cell penetration. *Acta Biomater.* **7**, 2544–2557 (2011).

502. Callanan, A., Davis, N. F., McGloughlin, T. M. & Walsh, M. T. The effects of stent interaction on porcine urinary bladder matrix employed as stent-graft materials. *J. Biomech.* **47**, 1885–1893 (2014).

503. Zanetta, L. *et al.* Expression of von Willebrand factor, an endothelial cell marker, is up-regulated by angiogenesis factors: A potential method for objective assessment of tumor angiogenesis. *Int. J. Cancer* **85**, 281–288 (2000).

504. Wu, P. K. & Ringeisen, B. R. Development of human umbilical vein endothelial cell (HUVEC) and human umbilical vein smooth muscle cell (HUVSMC) branch/stem structures on hydrogel layers via biological laser printing (BioLP). *Biofabrication* **2**, (2010).

505. Elsayed, Y., Lekakou, C., Labeed, F. & Tomlins, P. Smooth muscle tissue engineering in crosslinked electrospun gelatin scaffolds. *J. Biomed. Mater. Res. - Part A* **104**, 313–321 (2016).

506. De Vrieze, S. *et al.* The effect of temperature and humidity on electrospinning. *J. Mater. Sci.* **44**, 1357–1362 (2009).

507. Sullivan, D. C. *et al.* Decellularization methods of porcine kidneys for whole organ engineering using a high-throughput system. *Biomaterials* **33**, 7756–7764 (2012).

508. Lu, H., Hoshiba, T., Kawazoe, N. & Chen, G. Comparison of decellularization techniques for preparation of extracellular matrix scaffolds derived from three-dimensional cell culture. *J. Biomed. Mater. Res. - Part A* **100 A**, 2507–2516 (2012).

509. Fernández-Pérez, J. & Ahearne, M. The impact of decellularization methods on extracellular matrix derived hydrogels. *Sci. Rep.* **9**, 1–12 (2019).

510. Zhou, J. *et al.* Impact of heart valve decellularization on 3-D ultrastructure, immunogenicity and thrombogenicity. *Biomaterials* **31**, 2549–2554 (2010).

511. Da Silva, C. M. L., Spinelli, E. & Rodrigues, S. V. Fast and sensitive collagen quantification by alkaline hydrolysis/hydroxyproline assay. *Food Chem.* **173**, 619–623 (2015).

512. Darzynkiewicz, Z., Huang, X. & Zhao, H. Analysis of Cellular DNA Content by Flow

Cytometry. *Curr. Protoc. Cytom.* **82**, 7.5.1-7.5.20 (2017).

513. Desjardins, P. & Conklin, D. NanoDrop microvolume quantitation of nucleic acids. *J. Vis. Exp.* 1–4 (2010). doi:10.3791/2565

514. Quent, V. M. C., Loessner, D., Friis, T., Reichert, J. C. & Hutmacher, D. W. Discrepancies between metabolic activity and DNA content as tool to assess cell proliferation in cancer research. *J. Cell. Mol. Med.* **14**, 1003–1013 (2010).

515. Shenoy, N. *et al.* Drugs with anti-oxidant properties can interfere with cell viability measurements by assays that rely on the reducing property of viable cells. *Lab. Investig.* **97**, 494–497 (2017).

516. Divieto, C. & Sassi, M. P. A first approach to evaluate the cell dose in highly porous scaffolds by using a nondestructive metabolic method. *Futur. Sci. OA* **1**, (2015).

517. Freytes, D. O. & Badylak, S. F. Sterilization of Biologic Scaffold Materials. in *Encyclopedia of Medical Devices and Instrumentation* (ed. Webster, J. G.) 273–282 (Wiley & Sons, Inc, 2006). doi:10.1002/0471732877.emd241

518. Palazon, F. *et al.* Carbodiimide/NHS derivatization of COOH-terminated SAMs: Activation or byproduct formation? *Langmuir* **30**, 4545–4550 (2014).

519. Vogel, C. & Marcotte, E. M. Insights into regulation of pr1. Vogel, C. & Marcotte, E. M. Insights into regulation of protein abundance from proteomics and transcriptomis analyses. Nat. Rev. Genet. 13, 227–232 (2013).otein abundance from proteomics and transcriptomis analyses. *Nat. Rev. Genet.* **13**, 227–232 (2013).

520. Haque, K. A. *et al.* Performance of high-throughput DNA quantification methods. *BMC Biotechnol.* **3**, 1–10 (2003).

521. Kolker, E., Higdon, R. & Hogan, J. M. Protein identification and expression analysis using mass spectrometry. *Trends Microbiol.* **14**, 229–235 (2006).

522. Mendoza, L. G. *et al.* High-throughput microarray-based enzyme-linked immunosorbent assay (ELISA). *Biotechniques* **27**, 778–788 (1999).

523. Siviour, C. R. & Jordan, J. L. High Strain Rate Mechanics of Polymers: A Review. *J. Dyn. Behav. Mater.* **2**, 15–32 (2016).

524. Richeton, J., Ahzi, S., Vecchio, K. S., Jiang, F. C. & Adharapurapu, R. R. Influence of temperature and strain rate on the mechanical behavior of three amorphous polymers: Characterization and modeling of the compressive yield stress. *Int. J. Solids Struct.* **43**, 2318–2335 (2006).

525. Frickmann, H., Schröpfer, E. & Dobler, G. Actin assessment in addition to specific immuno-fluorescence staining to demonstrate rickettsial growth in cell culture. *Eur. J. Microbiol. Immunol.* **3**, 198–203 (2013).

526. de Matos, L. L., Trufelli, D. C., de Matos, M. G. L. & Pinhal, M. A. da S. Immunohistochemistry as an important tool in biomarkers detection and clinical practice. *Biomark. Insights* **2010**, 9–20 (2010).

527. Marrese, M., Cirillo, V., Guarino, V. & Ambrosio, L. Short-Term Degradation of Bi-Component Electrospun Fibers: Qualitative and Quantitative Evaluations via AFM Analysis. *J. Funct. Biomater.* **9**, 27 (2018).

528. Aebersold, R. & Mann, M. Mass spectrometry-based proteomics: Abstract: Nature. *Nature* **422**, 198–207 (2003).

529. Scientific, T. *Protein stability and storage*. *Thermo Scientific* doi:10.1016/S0891-5849(97)00429-2

530. Chang, S. F. *et al.* Different modes of endothelial-smooth muscle cell interaction elicit differential β-catenin phosphorylations and endothelial functions. *Proc. Natl. Acad. Sci. U. S. A.* **111**, 1855–1860 (2014).

531. Schiavi, M. P., Grando, M. D., Vercesi, J. A. & Bendhack, L. M. Endothelial cells (EC) regulate ROS generation in vascular smooth muscle cells (VSMC) from hypertensive rats. *Free Radic. Biol. Med.* **128**, S35–S36 (2018).

532. Ge, D. *et al.* Human vascular endothelial cells reduce sphingosylphosphorylcholine-induced smooth muscle cell contraction in co-culture system through integrin B4 and Fyn. *Acta Pharmacol. Sin.* **33**, 57–65 (2012).

533. Patrick Jr, C. W. & McIntire, L. V. Shear Stress and Cyclic Strain Modulation of Gene Expression in Vascular Endothelial Cells. *Blood Purif.* **13**, 112–124 (1995).

534. Ma, Y. H., Ling, S. & Ives, H. E. Mechanical strain increases PDGF-B and PDGF β receptor expression in vascular smooth muscle cells. *Biochem. Biophys. Res. Commun.* **265**, 606–610 (1999).

Appendix 1: The Influence of Aorta Extracellular Matrix in Electrospun Polycaprolactone Scaffolds

Journal of Applied Polymer Science

Influence of aorta extracellular matrix in electrospun polycaprolactone scaffolds

James A. Reid, Anthony Callanan
Institute for Bioengineering, School of Engineering, The University of Edinburgh, Edinburgh, United Kingdom
Correspondence to: A. Callanan (E-mail: anthony.callanan@ed.ac.uk)

ABSTRACT: Cardiovascular disease is the leading cause of mortality worldwide. Therefore, new research strategies for the treatment of cardiovascular disease are required. Previously, extracellular matrices (ECMs) have been used alongside polymers to generate hybrid bioscaffolds. Herein, we propose combining aortic ECMs with a polycaprolactone electrospun scaffold and biomechanically evaluating the scaffolds. We electrospun three scaffolds with varying ECM concentrations and found that increasing the ECM concentration leads to decreased stiffness at low strains, increased elasticity at high strain, reduction in failure strain, and an increase in yield strength. We also noted a decrease in water droplet contact angle with the increasing ECM concentration. Furthermore, we found that all three scaffolds were capable of maintaining human umbilical vein endothelial cell attachment and survival. These findings show the wide spectrum of mechanical properties that can be achieved through the addition of different concentrations of ECM into the fibers. © 2019 The Authors. *Journal of Applied Polymer Science* published by Wiley Periodicals, Inc. J. Appl. Polym. Sci. **2019**, *136*, 48181.

KEYWORDS: decellularization; electrospinning; extracellular matrix; polycaprolactone; tissue engineering; vascular

Received 14 November 2018; accepted 5 June 2019
DOI: 10.1002/app.48181

INTRODUCTION

Cardiovascular disease (CVD) is Europe's biggest killer, causing 3.9 million deaths in 2017, accounting for 45% of all deaths.[1] Furthermore, over 85 million people were living with CVD in Europe, leading to an estimated annual economic cost of €210 billion to the European Union alone.[1] Due to the high prevalence and huge socioeconomic burden caused by CVD, the demand for novel treatments is increasing.

There are currently a variety of strategies for the treatment of vascular disease (a subset of CVD focusing on the vessels), including extracellular matrix (ECM) mimicking structures, the use of native ECM components, and functionalized protein laden scaffolds.[2–5] Combining ECM with polymers to manufacture electrospun bioscaffolds has previously been utilized to harness the repeatable mechanical properties of the polymer with the biochemical and mechanical properties of the ECM.[5–8] Electrospinning polymers produces a network of fibers that can be heavily tailored depending on the properties desired.[9] They can be designed to have isotropic or anisotropic mechanical properties, along with three-dimensional architectural properties that favor cell survival and growth.[10] It is possible through electrospinning to include bioactive cues into a repeatable polymer structure and alter its mechanical and physical properties.[5–7,11] This has huge implications in tissue engineering where mimicking the physical and biological properties of the native ECM are major research focusses, especially when the final aim is generation of new functional tissue.

Previous studies have shown that including ECM or ECM proteins into an electrospun polymer scaffold alters its mechanical properties and positively affects seeded cells.[5–7,12] Therefore, in this study, we propose electrospinning a combination of aortic ECM with polycaprolactone (PCL) at two different ECM concentrations and biomechanically evaluating the resulting fibrous scaffolds along with a conventional PCL-only scaffold. Aortic ECM has been chosen as we are looking at a novel solution for the treatment of vascular disease, and therefore have decided to use a type of native ECM directly from a vascular source.

EXPERIMENTAL

ECM Production

Bovine aorta was harvested from a 2 year old female cow. Samples were frozen within 4 h of harvesting at −80 °C and stored until required. A 40 mm diameter sample from the aortic arch was cut out, and all connective tissue was removed after cleaning with ethanol and bathing in water for 30 min to remove blood. A 2 mm punch was used to punch out pieces of aorta for decellularization. The pieces were placed in a decellularizing device and perfusion decellularized with 0.5% w/v sodium dodecyl sulfate (SDS) in diH_2O for 36 h as previously described.[13] Aorta samples were then

perfused with 20 L of diH_2O at 170 mL/min to remove remnant SDS. Samples were frozen and lyophilized in a FreeZone 4.5 freeze-drier (Labconco). Dry ECM was then milled in a plenary ball mill PM 100 (Retsch). ECM powder was then collected and stored at 4 °C for use in electrospinning.

Electrospinning

Powdered ECM was dissolved at either 0.25% w/v or 1% w/v into hexafluoroisopropanol (HFIP) (Manchester Organics). PCL (Mn = 80,000, Sigma Aldrich) was then added to the solutions at 8% w/v and dissolved with agitation. PCL-only scaffolds were used as controls. Solutions were then placed into a 20 mL syringe and pumped using an EP-H11 syringe pump (Harvard Apparatus) into an EC-DIG electrospinning system (IME Technologies). The parameters used were based upon a previously described method: 0.4 mm needle, 0.8 mL/h, 12 cm, +14 kV, −4 kV, 250 RPM.[10] Electrospun fibers were collected onto aluminum foil on a rotating mandrel (diameter = 8 cm) and stored at 4 °C. Scaffolds used with cells were sterilized for 10 min using 70% v/v ethanol. A schematic representation of the decellularizing and electrospinning processes can be seen in Figure 1. These electrospinning solutions lead to final fiber PCL:ECM ratios of 100:0 (PCL only), 96.875:3.125 (0.25% ECM), and 87.5:12.5 (1% ECM).

Scanning Electron Microscopy

Scaffolds were visualized using a Hitachi S4700 fueled emission scanning electron microscope (SEM; Hitachi) with a 5 kV accelerating voltage and a 12 mm working distance. Prior to imaging, all scaffolds were sputter coated with an Emscope SC500A splutter coating using gold–palladium at a ratio of 60:40. Cell seeded scaffolds were visualized after 6 days using a previously described osmium-based method.[8]

Fiber Properties

Scanning electron images were analyzed using ImageJ software (NIH). Briefly, SEM images of the scaffolds were used with fiber diameter being deduced using the DiameterJ plugin and fiber orientation using the OrientationJ plugin.[14] A total of 58 fibers were used to measure fiber diameter and fiber orientation.

Hematoxylin and Eosin Staining

Native and decellularized samples of aorta were fixed in 10% formalin overnight. This was followed by a series of dehydration ranging from 50 to 100% ethanol. Samples were washed in xylene prior to embedding in paraffin wax and were then stored at 4 °C. Samples were trimmed to 5 μm thicknesses and mounted onto slides for hematoxylin and eosin (H&E) staining. Samples then cleared with xylene and mounted in DPX.

Mechanical Testing

Tensile properties were measured using an Instron 3367 testing machine (Instron) with a 50 N load cell. Briefly, 40 mm × 10 mm strips of scaffold were cut and were stretched with a starting gauge length of 20 mm. Scaffolds were stretched to failure at 10 mm/min. Scaffold width was measured using calipers and scaffold thickness measured using a DMK 41 AU02 monochrome 1280 × 960 camera. Incremental Young's modulus was calculated using the formula

$$E_{\text{incremental}} = \frac{\sigma}{\varepsilon} = \frac{FL_0}{A\Delta L} \quad (1)$$

where $E_{\text{incremental}}$ is Young's modulus between two strain bands, σ is stress, ε is strain, F is the applied force, A is the cross-sectional area, ΔL is change in length, and L_0 is the original length. Young's moduli for each scaffold were analyzed and expressed at regular incremental intervals, as previously described.[15–19] Compliance was calculated using following equation

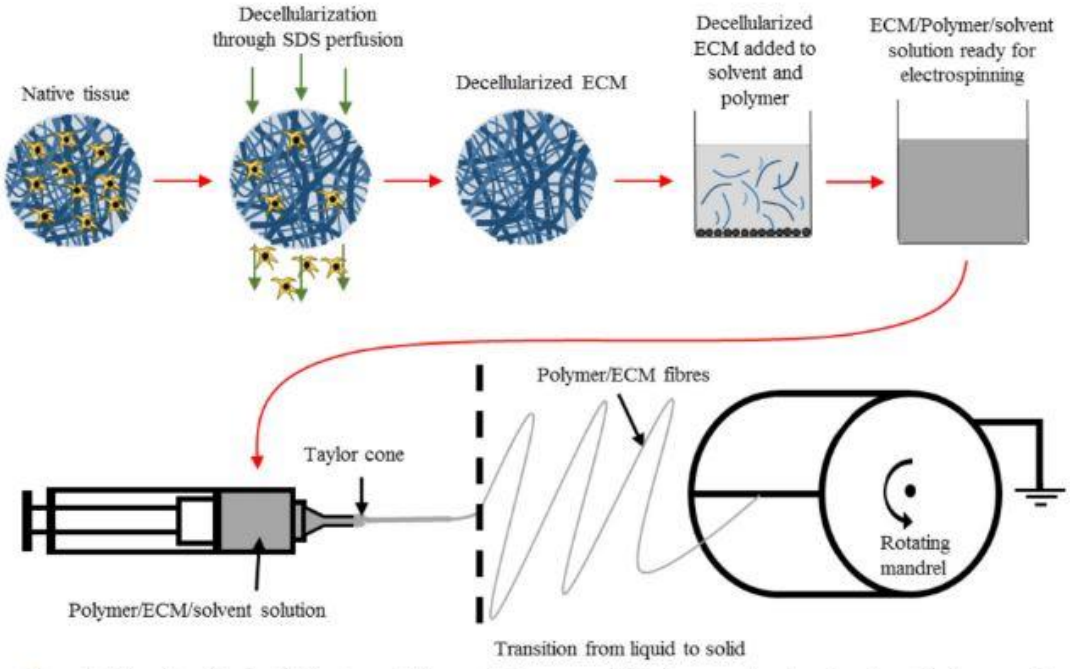

Figure 1. Schematic of the decellularization and electrospinning process. [Color figure can be viewed at wileyonlinelibrary.com]

$$C = \frac{\Delta V}{\Delta P} = \frac{V_1 - V_2}{P_1 - P_2} \quad (2)$$

where V_1 and V_2 are volumes at 0 and 5% strain and P_1 and P_2 are pressures at 0 and 5% strain. Values for ΔP and ΔV between 0 and 5% strain were deduced from thin-wall pressure vessel theory. Briefly, the equation for circumferential stress was reorganized to give us an equation that told us the representative pressure (P_n) at a given stress value σ_n (subscript n denoting that the value is at n% strain).

$$\sigma_n = \frac{P_n d_n}{2t} \quad (3)$$

$$P_n = \frac{\sigma_n \times 2t}{d_n} \quad (4)$$

where σ_n is stress, d_n is the diameter of the representative cylinder, and t is the thickness of the scaffold. Representative volume (V_n) was calculated by treating the strip of scaffold as a cylinder and the strain as a volume increase to this cylinder (subscript n denoting that the value is at n% strain)

$$V_n = \pi \times \left(\frac{d_n}{2}\right)^2 \times w \quad (5)$$

where d_n is the diameter of the representative cylinder and w is the width of the scaffold. For each condition group, $n = 5$.

Contact Angle Measurement

Contact angle was measured on dry scaffolds. A 5 µL droplet of water was placed onto the scaffold, and images were captured using a DMK 41 AU02 monochrome camera at a frequency of 5 Hz. Analysis of the scaffolds was done on ImageJ (NIH) using the LBADSA plugin, as seen in Figure 2.[20]

Cell Culture and Scaffold Seeding

Human umbilical vein endothelial cells (HUVECs) from an infant male Caucasian donor were obtained cryopreserved at passage 1 (Pro-moCell GmbH) and expanded to passage 7 in a 5% CO_2/37 °C atmosphere. HUVECs were expanded using MCBD 131 medium (Life Technologies) supplemented with 5% v/v fetal bovine serum (ThermoFisher Scientific), 1% v/v L-glutamine, 1% v/v penicillin/streptomycin (Life Technologies), 1 mg/L hydrocortisone, 50 mg/L ascorbic acid (Sigma), 2 µg/L fibroblast growth factor (PeproTech), 10 µg/L epidermal growth factor (PeproTech), 2 µg/L insulin-like growth factor (PeproTech), and 1 µg/L VEGF (PeproTech). HUVECs were lifted for scaffold seeding at 80% confluence. Scaffolds (10 mm diameter) were punched out of the electrospun sheet, sterilized in 70% ethanol, and then placed into 48-well plates and soaked in serum free MCDB 131 medium overnight. Wetting medium was removed and scaffolds were then seeded at a density of 350,000 cells/cm^2. Briefly, cells were drip seeded in 30 µL of medium onto the middle of the scaffold. After 30 min, a further 20 µL of medium was added to stop the cells from drying out. After a further 30 min, medium in each well was topped up to 500 µL.

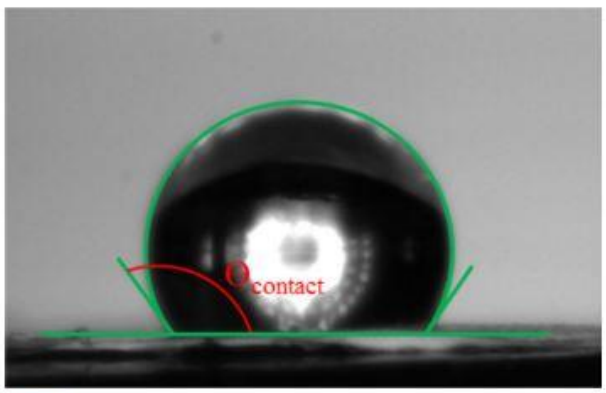

Figure 2. Contact angle measurement using the LBADSA plugin on ImageJ. [Color figure can be viewed at wileyonlinelibrary.com]

SEM of Cell Seeded Scaffolds. Cell seeded scaffolds were visualized using SEM after 6 days using a previously described osmium-based method.[8] Briefly, the cell seeded scaffolds were fixed overnight in 4% glutaraldehyde overnight before being incubated in 0.1% osmium for 30 min followed by dehydration in ethanol and hexamethyldisilazane. Scaffolds were then sputter coated and visualized as per Scanning Electron Microscopy section above. Scaffold confluency was estimated during the imaging process. The representative SEM images shown in Figure 4(e) were taken to best represent the confluency found across the whole scaffold. Confluency was measured using ImageJ (NIH) software. Briefly, SEM images were thresholded to differentiate between the scaffold and the cells. Total area coverage was then measured and converted into a percentage confluency.

CellTiter-Blue Cell Viability Assay

The assay was performed at 3 and 6 days as per manufacturer's instructions (Promega). Briefly, cell seeded scaffolds were removed and placed in new wells (48-well plate). Each well was topped up with 300 µL of media and 75 µL of CellTiter-Blue assay (4:1 ratio). The plate was lightly shaken for 1 min and then wrapped in tinfoil and incubated for 3.5 h. After incubation, 100 µL samples (×3) of the media/assay were taken from each scaffold and pipetted into a black well plate. The plate was measured in a Modulus II microplate reader at ex: 525 nm and em: 580–640 nm. For each condition group, $n = 4$.

DNA Quantification

Native and decellularized samples were frozen and lyophilized before being incubated in a papain digestion solution containing 2.5 U of papain, 5 m*M* cysteine HCL, and 5 m*M* *Ethylenediaminetetraacetic acid* (ETDA) in DNA-free water at 60 °C for 24 h (all reagents from Sigma-Aldrich, U.K.). Total DNA content was measured using a Quant-iTTMPicoGreen assay kit (ThermoFisher, U.K.) as per the manufacturers' instructions, $n = 4$.

Fourier Transform Infrared Spectroscopy

Fourier transform infrared spectroscopy (FTIR) was used to confirm the successful inclusion of ECM into the electrospun PCL fibers. FTIR spectra were recorded using a Nicolet iS10 spectrometer with a Smart iTX diamond attenuated total reflection detector (all from Thermo Fisher Scientific), in the wave range of 400–4000 per cm at a resolution of 1 per cm using OMNIC Spectra software (Thermo Fisher Scientific), $n = 5$.

Statistical Analysis

Data were expressed as mean ± 1 standard deviation. Statistical analysis was performed using one-way analysis of variance with *post hoc* Fisher test.

RESULTS

Decellularization

Bovine aorta was successfully decellularized using a 0.5% SDS perfusion treatment. Relative DNA content was measured using a Quant-iT PicoGreen assay kit (ThermoFisher) and dropped 96.5% as shown in Figure 3. Furthermore, H&E staining shows that the nuclear content of the aorta has been successfully removed [Figure 3(b, c)].

Scaffold Structure

All three scaffolds were successfully electrospun using the same parameters (Figure 4). This leads to three scaffolds with very similar architectures. No significant differences in average fiber diameter were noted across the three scaffolds, with diameters ranging from 0.90 ± 0.19 μm for the 1% aorta ECM scaffold to 0.97 ± 0.19 μm for the PCL-only scaffold (Figure 4). Similarly, the fiber orientations for all three scaffolds was very similar, with normalized frequency of fiber orientation peaking at an angle of 45° for all three scaffolds (Figure 4).

Fourier Transform Infrared Spectroscopy

The FTIR results showed that the aorta ECM was successfully incorporated into the electrospun fibers at both concentrations. Spectra were taken for the PCL fibers alone, both PCL/ECM concentrations fibers and the decellularized ECM. Characteristic peaks from the PCL and the ECM were found in both ECM/PCL scaffolds suggesting that the ECM had been incorporated into the PCL fibers. As expected, ECM peaks were more pronounced in the 1% ECM scaffolds than the 0.25% ECM scaffold which suggests that a higher quantity of ECM had been incorporated into the PCL fibers. Figure 5(a) shows peaks at 1705–1715, 1650–1660, and 1535–1545 per cm, which can be attributed to the carboxyl group in the PCL, the amide I group in the ECM, and the amide II group in the ECM, respectively.[21–23]

Mechanical Testing

Tensile Testing. Tensile testing was performed using an Instron tensile tester and showed significant differences in how each scaffold performed mechanically. All scaffolds were stretched until failure. The PCL scaffold had the highest Young's modulus in the 0–5% strain range (19.2 ± 1.7 MPa), followed by the 0.25% aorta ECM scaffold (16.1 ± 1.9 MPa) and then 1% aorta ECM scaffold (13.5 ± 0.7 MPa) [Figure 5(c)]. The Young's modulus for each scaffold dropped at each subsequent strain band, with the trend of lower stiffness for higher ECM concentration reversing in the 15–20% strain band. This phenomena can be seen in the stress versus strain curve [Figure 5(b)], where after approximately 20% strain, the PCL scaffold becomes very plastic (shallow gradient) and the 1% aorta ECM scaffold remains somewhat elastic (steeper gradient), with the 0.25% aorta ECM scaffold having a gradient between the two other scaffolds. This suggests that the incorporation of ECM is directly related to this increase in scaffold elasticity into the higher strain range.

It was also noted during tensile testing that the higher ECM concentrations lead to lower failure strains. The 1% aorta ECM and 0.25% aorta ECM scaffolds had failure strains 47% ($p > 0.001$)

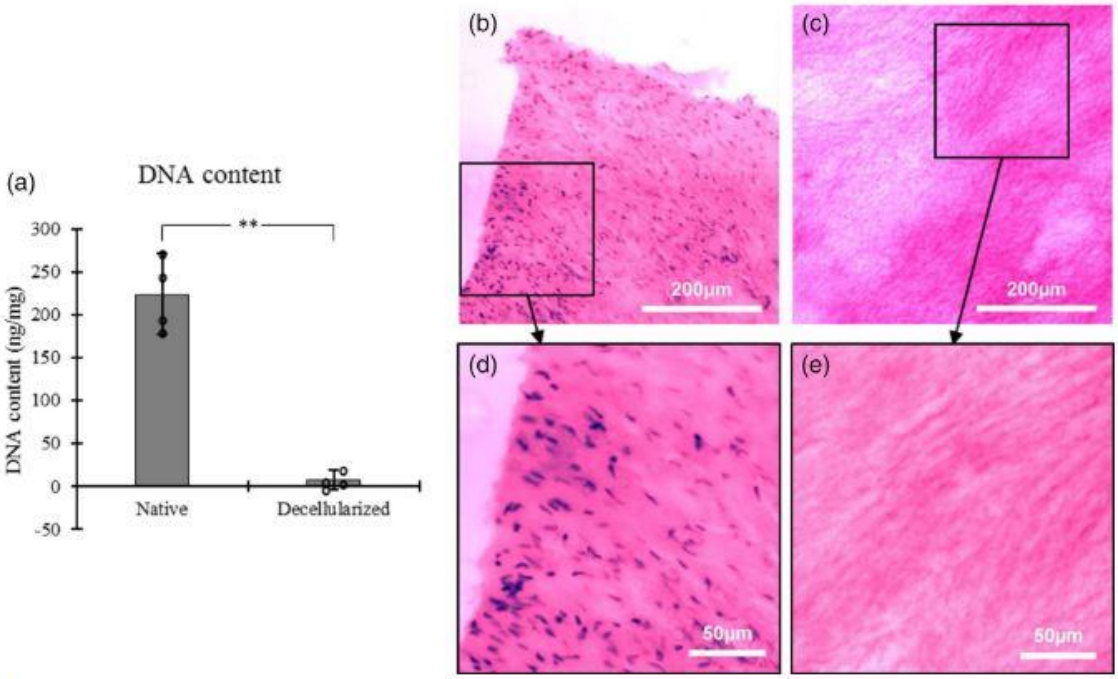

Figure 3. (a) DNA content of aorta before and after decellularization. (b, d) The aorta before decellularization. (c, e) The aorta after decellularization. [Color figure can be viewed at wileyonlinelibrary.com]

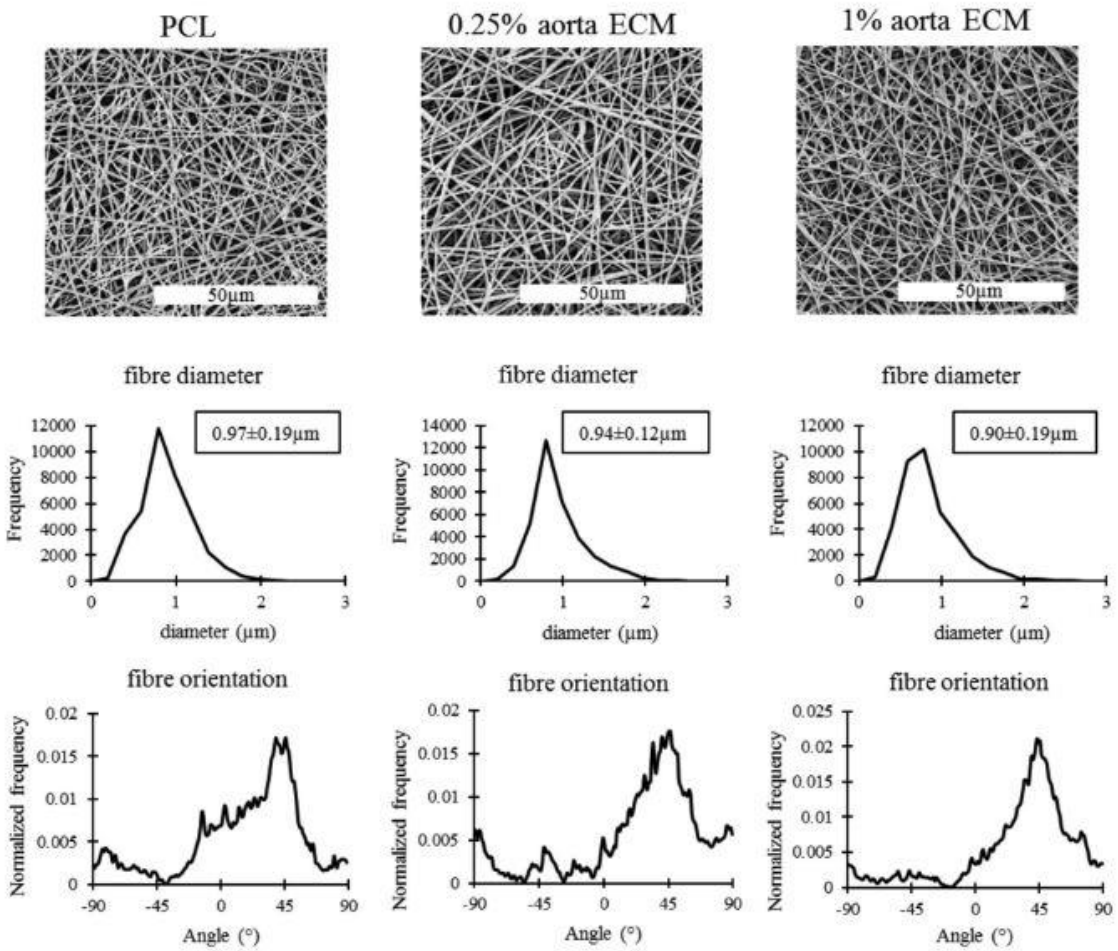

Figure 4. (a) SEM images of the three electrospun scaffolds. (b) Fiber diameter distribution of all three scaffolds. (c) Fiber orientation distribution of all three scaffolds.

and 2.6% (no significance [ns]) lower than the PCL-only scaffold, respectively. Likewise, the ultimate tensile strength of the scaffolds increased by 84.3% ($p > 0.001$) and 77.9% ($p > 0.001$) for 1% aorta ECM and 0.25% aorta ECM compared to the PCL-only scaffold, respectively.

Compliance Measurements. Values for compliance were calculated based on eq. (2). Compliance was seen to increase with ECM concentration—the 0.25% ECM and 1% ECM scaffolds had compliance values 19% ($p > 0.05$) and 42% ($p > 0.01$) larger than the PCL-only scaffold. Results shown in Table I.

Contact Angle Measurement

Contact angle measurements showed how incorporating aorta ECM into the scaffold drastically increased the hydrophilicity of the scaffold (Table I). After 0.2 s (first image after contact), the 1% aorta ECM and 0.25% aorta ECM scaffolds had contact angles 31.1% (ns) and 21.8% (ns) lower than the PCL-only scaffold. This drop in contact angle was even bigger after 5 s, where the 1% aorta ECM and 0.25% aorta ECM scaffolds had contact angles 77.5% ($p > 0.01$) and 30.3% (ns) lower than the PCL-only scaffold.

Cellular Testing/Visualization

Cell Viability. Cell viability results showed no significant differences between the three scaffolds and no change in viability between the two time points [Figure 5(d).

Scanning Electron Microscopy. SEM images show a functional HUVEC monolayer after 6 days of culture on all three scaffolds [Figure 5(e). Furthermore, the three scaffolds showed confluences ranging from 68 to 81%, and all three scaffolds appear to show HUVECs with very similar morphologies. These results validate the cell viability results, suggesting that all three scaffolds were capable of accommodating a healthy layer of HUVECs.

DISCUSSION

Electrospun polymer scaffolds have regularly been used in tissue engineering as platforms for vascular tissue regeneration.[24] Electrospinning generates fibrous scaffolds with a high degree of

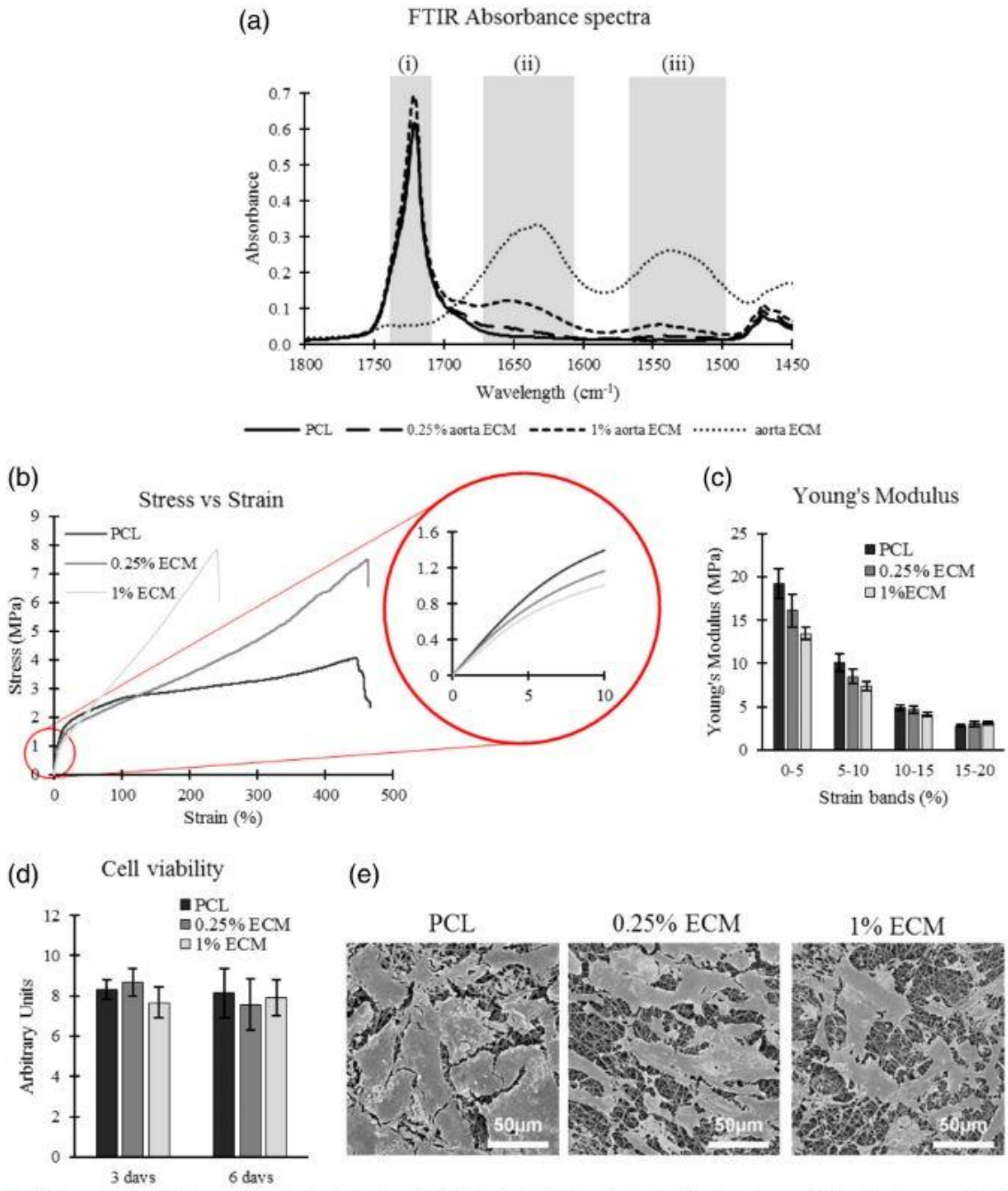

Figure 5. (a) Representative FTIR curves showing the inclusion of ECM into the PCL fibers. Peaks for (i) carbonyl group, (ii) amide I group, and (iii) amide II group are highlighted. (b) Representative stress versus strain for the three scaffolds. (c) Young's modulus of all three scaffolds at different strain bands, $n = 6$. (d) Cell viability of HUVECs on all three scaffolds after 3 and 6 days, $n = 4$. (e) Representative SEM images of HUVEC monolayer on all three scaffolds after 6 days. [Color figure can be viewed at wileyonlinelibrary.com]

architectural and mechanical repeatability.[17,24] In this study, we have used PCL, a commonly used polymer for electrospinning tissue engineering application.[5,10] We were able to spin three extremely similar scaffolds using the same parameters, which demonstrates the repeatable properties that electrospinning PCL possess. Furthermore, we noted that the inclusion of ECM had very little effect on how the solution spun, with fiber diameter being similar for all three scaffolds (0.90, 0.94, and 0.97 μm). By having three similar morphologies (fiber diameter and fiber orientation, as seen in Figure 3), we have ensured that the only

Table I. Mechanical Properties of Scaffolds

	PCL	0.25% ECM	1% ECM
Ultimate tensile strength (MPa)	4.26 ± 0.33	7.58 ± 1.59	7.85 ± 1.03
Failure strain (%)	464 ± 40	452 ± 59	244 ± 29
Compliance (mL/mmHg)	0.049 ± 0.004	0.059 ± 0.006	0.070 ± 0.004
Contact angle after 0.2 s (°)	114.4 ± 8.9	89.5 ± 37.7	75.4 ± 25.6
Contact angle after 5 s (°)	98.7 ± 25.2	68.8 ± 43.6	22.2 ± 10.5

difference between the three scaffolds is the PCL:ECM ratio within the fibers (100:0, ~97:3, and ~ 88:12), meaning that the PCL:ECM ratio of the scaffold can be one of the factors attributed to the differences in mechanical properties and cellular performance.

FTIR results [Figure 5(a) showed that the decellularized ECM had been successfully incorporated into the PCL scaffolds. Peaks at the amide I and amide II bonds (two characteristic bonds found in ECM proteins) can be seen in both PCL/ECM scaffolds, showing that the ECM had been incorporated into the scaffold.[22,23] Interestingly, as the ECM concentration increased, the peak at these two Amide bonds also increased, suggesting that increasing ECM concentration did lead to more ECM being incorporated into the PCL fibers. All three scaffolds showed peaks at the carboxyl group, which can be attributed to the PCL.[21] FTIR is a surface characterizing method that has been shown to measure to depths of 5 μm[25]—the fibers in this study are all under 1 μm thick, suggesting that a full characteristic profile of the fiber is being achieved through FTIR.

Tensile testing leads to some interesting results that demonstrate the effect of including ECM into the electrospun fibers. We noted that the 1% ECM scaffold had a lower stiffness than the PCL-only scaffold. This result can possibly be explained by aortic arch ECM (the ECM used in this study), comprising of approximately 40% elastin and 20% collagen.[26] Elastin has been shown to have a half-life of around 74 years. As people age, the quantity of elastin in their aortas decreases, which leads to a very large increase in aortic stiffness—a 394% increase in stiffness was noted between the ages of 25 and 70.[27,28] This suggests that a lower quantity of elastin in the scaffold would lead to a higher stiffness and lower compliance.

Furthermore, including aortic ECM resulted in a drastic reduction in failure strain, as seen in Table I. This can possibly be explained by collagen having a failure strain of 13% and elastin between 100 and 150%,[29] compared to the PCL-only scaffold having a failure strain of 464% (our results). Hence, a fiber made up of a ~88:12 PCL to ECM ratio (1% ECM) would be expected to fail at a lower strain than the fiber with a 100:0 PCL to ECM ratio (PCL only). Additionally, most cells feel and respond to the stiffness of their substrate/environment, therefore being able to tailor scaffold stiffness has benefits for tissue engineering.[30]

Water droplet contact angle is defined as the angle formed at the intersection of the liquid–solid interface—the lower this angle is, the more hydrophilic the solid is.[31] Studies have shown that altering the contact angle of a scaffold can have effects on cell adhesion.[5,32] Furthermore, the addition of ECM to an electrospun polymer scaffold has been shown to reduce water contact angle.[5] This result was noted in our study, with a 31.1 and 77.5% lower contact angle in the 1% ECM scaffold compared to the PCL-only scaffold for the 0.2 s measurement and 5 s measurement, respectively. After 0.2 s, the PCL-only scaffolds had a contact angle of 114.4° (hydrophobic[32]), compared to 75.4° for the 1% ECM scaffold.

Cellular testing and visualization showed that the HUVECs reacted similarly to all three scaffolds. Cell viability [Figure 5(d) showed no significant differences between the three scaffolds over both time points, suggesting that including ECM had no impact on their proliferation. Similarly, SEM images [Figure 5(e) show that the HUVECs had similar morphologies on all three scaffolds. Further work looking into gene analysis is required to gain a full bioactivity profile for these scaffolds.

Sterilization in this study was achieved using 70% ethanol, which is sufficient for preliminary *in vitro* studies but is not a clinically translatable method of terminal sterilization. Studies have shown that some methods of terminal sterilization do have detrimental effects on the structure, mechanical integrity, and cell hosting abilities of decellularized ECM.[33,34] The majority of currently marketed biological devices that use decellularized ECMs are terminally sterilized using gamma irradiation, ethylene oxide, or electron beam processing, which shows that decellularized ECMs can be efficiently sterilized before being translated to the clinic.[35] Furthermore, peracetic acid as a terminal sterilization method has been shown to have no effect on the structure or mechanical strength of ECM, while also maintaining its ability to host cells.[33] Therefore, translating this work to a clinical setting where an approved terminal sterilization method is required would rely on one of the aforementioned sterilization methods.

Although a relatively hydrophilic contact angle of approximately 60° has been shown to lead to higher cell adhesion,[32] this could also have problematic effects and leads to the binding of unwanted cells, proteins, and growth factors. It has been shown that blood-contacting devices and tissue engineering substrates require an appropriate balance of hydrophilic and hydrophobic entities.[36] Therefore, with the final goal for vascular tissue engineering strategies often being *in vivo* implantation, it is very important to consider the fact that the scaffold will be in contact with a variety of constituents that you may not want binding to the scaffold. Hence, in certain situations, higher hydrophobicity may be desirable to reduce the binding of unwanted substances. This applies for approaches such as bypass grafting where local cell attachment to the implant is unwanted. Therefore, being able to control the hydrophobicity of the scaffold/implant is desirable.

CONCLUSIONS

In this study, we successfully combine aortic ECM with PCL and electrospun randomly aligned nanofiber scaffolds. We noted that including ECM reduced stiffness and increased compliance at lower strains and increased the elasticity of the nanofibers beyond its yield strength. Furthermore, the inclusion of ECM reduced the failure strain and increased the ultimate tensile strength of the scaffold. Additionally, including ECM into the scaffold had the effect of reducing the water droplet contact angle. Future work should focus on quantifying the elastin and collagen in the ECM and/or scaffold to validate any theorem regarding these ECM proteins altering the mechanical and physical properties of the scaffold.

Our findings show that the mechanical properties of electrospun scaffolds can be changed through the addition of ECM. By altering the polymer to ECM ratio, a wide array of mechanical properties can be achieved, allowing for tissue-specific tailoring of scaffolds.

ACKNOWLEDGMENTS

The authors would like to thanks Alistair Elfick for use of lab facilities (Institute of Bioengineering, the University of Edinburgh) and Steve Mitchell for imaging assistance (BioSEM). This work was funded by an Engineering & Physical Sciences Research Council (ESPRC) doctoral training partnership studentship EP/N509644/1 and a UK Regenerative Medicine Platform II grant MR/L022974/1.

REFERENCES

1. Wilkins, E.; Wilson, L.; Wickramasinghe, K.; Bhatnagar, P.; Leal, J.; Luengo-Fernandez, R.; Burns, R.; Rayner, M.; Townsend, N. European Cardiovascular Disease Statistics; European Heart Network: Brussels, Belgium, **2017**.
2. Hartman, O.; Zhang, C.; Adams, E. L.; Farach-Carson, M. C.; Petrelli, N. J.; Chase, B. D.; Rabolt, J. F. *Biomaterials*. **2011**, *31*, 5700.
3. Han, J.; Gerstenhaber, J. A.; Lazarovici, P.; Lelkes, P. I. *Biomacromolecules*. **2013**, *14*, 1338.
4. Ott, H. C.; Matthiesen, T. S.; Goh, S. K.; Black, L. D.; Kren, S. M.; Netoff, T. I.; Taylor, D. A. *Nat. Med.* **2008**, *14*, 213.
5. Gao, S.; Guo, W.; Chen, M.; Yuan, Z.; Wang, M.; Zhang, Y.; Liu, S.; Xi, T.; Guo, Q. *J. Mater. Chem. B*. **2017**, *5*, 2273.
6. Garrigues, N. W.; Little, D.; Sanches-Adams, J.; Ruch, D. S.; Guilak, F. *J. Biomed. Mater. Res. Part A*. **2014**, *102*, 3998.
7. Kim, T. H.; Jung, Y.; Kim, S. H. *Tissue Eng. Part A*. **2018**, *24*, 830.
8. Grant, R.; Hay, D. C.; Callanan, A. *Tissue Eng. Part A*. **2017**, *23*, 650.
9. Agarwal, S.; Wendorff, J. H.; Greiner, A. *Polymer (Guildf)*. **2008**, *49*, 5603.
10. Burton, T. P.; Corcoran, A.; Callanan, A. *Biomed. Mater.* **2017**, *13*, 015006.
11. Schoen, B.; Avrahami, R.; Baruch, L.; Efraim, Y.; Goldfracht, I.; Elul, O.; Davidov, T.; Gepstein, L.; Zussman, E.; Machluf, M. *Adv. Funct. Mater.* **2017**, *27*, 1.
12. Chakrapani, V. Y.; Gnanamani, A.; Giridev, V. R.; Madhusoothanan, M.; Sekaran, G. *J. Appl. Polym. Sci.* **2012**, *125*, 3221.
13. Grant, R.; Hallett, J.; Forbes, S.; Hay, D.; Callanan, A. *Sci. Rep.* **2019**, *9*, 1.
14. Hotaling, N. A.; Bharti, K.; Kriel, H.; Simon, C. G., Jr. *Biomaterials*. **2015**, *61*, 327.
15. Munir, N.; Callanan, A. *Biomed. Mater.* **2018**, *13*, 051001.
16. Dunphy, S.; Reid, J. A.; Burton, T. P.; Callanan, A. *Biomed. Phys. Eng. Express*. **2018**, *4*, 057004.
17. Burton, T. P.; Callanan, A. *J. Tissue Eng. Regen. Med.* **2018**, *15*, 301.
18. Callanan, A.; Davis, N. F.; Walsh, M. T.; McGloughlin, T. M. *Med. Eng. Phys.* **2012**, *34*, 1368.
19. Callanan, A.; Davis, N. F.; McGloughlin, T. M.; Walsh, M. T. *J. Biomech.* **2014**, *47*, 1885.
20. Stalder, A. F.; Melchior, T.; Müller, M.; Sage, D.; Blu, T.; Unser, M. *Colloids Surf. A Physicochem. Eng. Asp.* **2010**, *364*, 72.
21. Elzein, T.; Nasser-Eddine, M.; Delaite, C.; Bistac, S.; Dumas, P. *J. Colloid Interface Sci.* **2004**, *273*, 381.
22. Camacho, N. P.; West, P.; Torzilli, P. A.; Mendelsohn, R. *Biopolymers*. **2001**, *62*, 1.
23. Garidel, P.; Schott, H. *BioProcess Tech.* **2006**, *1*, 48.
24. Karaman, O.; Şen, M.; Demirci, E. A. In Electrospun Materials for Tissue Engineering and Biomedical Applications: Research, Design and Commercialization; Woodhead Publishing: Sawston, Cambridge, **2017**. p. 261.
25. Kazarian, S. G.; Chan, K. L. A. *Analyst*. **2013**, *138*, 1940.
26. Grant, R. A. *J. Atheroscler. Res.* **1966**, *7*, 463.
27. Astrand, H.; Stalhand, J.; Karlsson, J.; Karlsson, M.; Sonesson, B.; Lanne, T. *J. Appl. Physiol.* **2011**, *110*, 176.
28. Shapiro, S. D.; Endicott, S. K.; Province, M. A.; Pierce, J. A.; Campbell, E. J. *J. Clin. Invest.* **1991**, *87*, 1828.
29. Muiznieks, L. D.; Keeley, F. W. *Biochim. Biophys. Acta.* **2013**, *1832*, 866.
30. Discher, D. E. *Science*. **2005**, *310*, 1139.
31. Bracco, G.; Holst, B. In Surface Science Techniques; Yuan, Y.; Lee, T., Eds.; Springer: Berlin, Germany, **2013**; p. 3.
32. Dowling, D. P.; Miller, I. S.; Ardhaoui, M.; Gallagher, W. M. *J. Biomater. Appl.* **2011**, *26*, 327.
33. Matuska, A. M.; Mcfetridge, P. S.; Family, J. C. P. *J. Biomed. Mater. Res. B Appl. Biomater.* **2016**, *103*, 1.
34. Crapo, P. M.; Gilbert, T. W.; Badylak, S. F. *Biomaterials*. **2012**, *32*, 3233.
35. Freytes, D. O.; Badylak, S. F. In Encyclopedia of Medical Devices and Instrumentation; Webster, J. G., Ed., Wiley & Sons, Inc: Hoboken, New Jersey, United States, **2006**; p. 273.
36. Menzies, K. L.; Jones, L. *Optom. Vis. Sci.* **2010**, *87*, 387.

Appendix 2: Hybrid Cardiovascular Sourced Extracellular Matrix Scaffolds as Possible Platforms for Vascular Tissue Engineering

Received: 15 January 2019 | Revised: 5 July 2019 | Accepted: 9 July 2019

DOI: 10.1002/jbm.b.34444

ORIGINAL RESEARCH REPORT

Hybrid cardiovascular sourced extracellular matrix scaffolds as possible platforms for vascular tissue engineering

James A. Reid | Anthony Callanan

Institute for Bioengineering, School of Engineering, The University of Edinburgh, Edinburgh, UK

Correspondence
Anthony Callanan, Institute for Bioengineering, School of Engineering, The University of Edinburgh, Edinburgh, UK.
Email: anthony.callanan@ed.ac.uk

Funding information
Engineering and Physical Sciences Research Council, Grant/Award Number: EP/N509644/1; Medical Research Council, Grant/Award Number: MR/L012766/1

Abstract

The aim when designing a scaffold is to provide a supportive microenvironment for the native cells, which is generally achieved by structurally and biochemically imitating the native tissue. Decellularized extracellular matrix (ECM) possesses the mechanical and biochemical cues designed to promote native cell survival. However, when decellularized and reprocessed, the ECM loses its cell supporting mechanical integrity and architecture. Herein, we propose dissolving the ECM into a polymer/solvent solution and electrospinning it into a fibrous sheet, thus harnessing the biochemical cues from the ECM and the mechanical integrity of the polymer. Bovine aorta and myocardium were selected as ECM sources. Decellularization was achieved using sodium dodecyl sulfate (SDS), and the ECM was combined with polycaprolactone and hexafluoro-2-propanol for electrospinning. The scaffolds were seeded with human umbilical vein endothelial cells (HUVECs). The study found that the inclusion of aorta ECM increased the scaffold's wettability and subsequently lead to increased HUVEC adherence and proliferation. Interestingly, the inclusion of myocardium ECM had no effect on wettability or cell viability. Furthermore, gene expression and mechanical changes were noted with the addition of ECM. The results from this study show the vast potential of electrospun ECM/polymer bioscaffolds and their use in tissue engineering.

KEYWORDS
electrospinning, endothelial cells, extracellular matrix, polycaprolactone, scaffold

1 | INTRODUCTION

In 2015, cardiovascular disease killed around 630,000 people in the United States, accounting for 23.4% of all deaths (Heron, 2017). Approximately 80% of those deaths fell in the category of over 65 year olds (Heron, 2017). One of the major reasons for the increase in people requiring sophisticated and complex cardiac interventions is the ever increasing average life expectancy across the world's population (Blanche et al., 2001). For example, it was found that between 1999 and 2010, in excess of 83% of over 60 year olds in the USA were found to have hypertension or prehypertension symptoms (Guo, He, Zhang, & Walton, 2012). Alongside this, over 7.6 million premature deaths were noted globally in 2001 due to cardiovascular disease, with this number rising (Lawes, Vander, & Rodgers, 2008; Makridakis & DiNicolantonio, 2014). With such a high prevalence in the elderly population and a

Abbreviations: ANOVA, analysis of variance; CD31/PECAM1, platelet endothelial cell adhesion molecule; DAPI, 4′,6-diamidino-2-phenylindole; ECM, extracellular matrix; EDTA, ethylenediaminetetraacetic acid; FBS, fetal bovine serum; FTIR, Fourier transform infrared spectroscopy; GAPDH, glyceraldehyde 3-phosphate dehydrogenase; HCL, hydrochloric acid; HFIP, hexafluoro-2-propanol; HUVEC, human umbilical vein endothelial cell; MMP1, matrix metalloproteinase-1; MMP2, matrix metalloproteinase-2; PBS, phosphate buffer saline; PCL, polycaprolactone; RT-qPCR, quantitative reverse transcription polymerase chain reaction; SDS, sodium dodecyl sulfate; SEM, scanning electron microscope; VEGF, vascular endothelial growth factor

rapidly increasing global ageing population, it is of no surprise that the demand for vascular treatments is increasing (United Nations, 2015).

There are currently a large variety of vascular tissue engineering strategies utilized in the treatment of arterial disease (Ravi & Chaikof, 2010). These include scaffold materials that mimic the native extracellular matrix (ECM), promote ECM production, reduce inflammation and thrombogenicity, and stimulate neovascularization and angiogenesis (Jiang, Akgun, Lam, Ameer, & Wertheim, 2015; Ravi & Chaikof, 2010). Materials used in vascular tissue engineering include decellularized extracellular matrices, biopolymers, bioabsorbable polymers, and collagen (Gilbert, Sellaro, & Badylak, 2006; Hong et al., 2008; Hutmacher, 2000; Jiang et al., 2015; Lu, Lin, Kim, et al., 2013; Masoumi et al., 2014; Reid & Callanan, 2019; Wu, Liu, Cui, Qu, & Chen, 2007). Electrospinning is a widely used technique that mimics the nanoscale and microscale structure of tissues and has been utilized in a large number of tissue engineering avenues for various organs (Burton & Callanan, 2018; Burton, Corcoran, & Callanan, 2017; Dettin et al., 2015; Gao et al., 2017; Garrigues, Little, Sanches-Adams, et al., 2014; Grant, Hay, & Callanan, 2017; Han, Gerstenhaber, Lazarovici, & Lelkes, 2013; Hong et al., 2008; Kumbar, Nukavarapu, James, Nair, & Laurencin, 2008; Masoumi et al., 2014; Sundaramurthi, Krishnan, & Sethuraman, 2014). Furthermore, while polymers can control architecture, they lack some of the unique biomolecular cues found in native tissue, which is why, in recent years, there has been an increase in demand for decellularized ECM (Kasimir et al., 2006; Sanchez, Fernandez-Santos, Costanza, et al., 2015; Tapias & Ott, 2014; Weymann, Patil, Sabashnikov, et al., 2014). The ECM is the pivotal factor in the intracellular microenvironment, thus it plays a major role in maintaining and regulating tissue function (Kang, Kim, Khademhosseini, & Yang, 2011). Therefore, incorporating components of the ECM into a scaffold to more closely mimic the native environment is an effective way to promote tissue regeneration (Bhowmick et al., 2017; Choi et al., 2010). While there have been huge advances in the treatment of cardiovascular disease, there is still a large demand to increase patency and surgical outcome.

Hybrid scaffolds that incorporate ECM with a polymer into a spun fiber have shown improved cellular performance when using meniscus and cartilage (Gao et al., 2017; Garrigues et al., 2014). Other methods of manufacturing scaffolds/constructs using vascular ECM and polymers have ranged from repopulating aortic valves to vascular grafts in the cardiovascular realm (Schoen, Avrahami, Baruch, et al., 2017). Interestingly, studies focusing on vascular ECM have shown improvements in native cell repopulation and mechanical properties when combining the ECM with a polymer (Hong et al., 2008; Jahnavi, Kumary, Bhuvaneshwar, Natarajan, & Verma, 2015; Jiang et al., 2015; Wu et al., 2007). Furthermore, electrospinning was successfully utilized to generate these hybrid structures that showed increased mechanical strength and improved cellular repopulation (Hong et al., 2008; Jahnavi et al., 2015; Wu et al., 2007). These previous studies combining vascular ECM and polymers to create hybrid scaffolds show promising results, with improvements in cellular performance noted in most cases.

Current treatments are not keeping up with the increased demand for surgery and transplantation (Blanche et al., 2001; Kilic, Emani, Sai-Sudhakar, Higgins, & Whitson, 2014). Herein, we propose incorporating the native vascular ECM into the electrospun polymer fibers via solubilization of the ECM. By combining heart and aorta ECM with polycaprolactone (PCL), the aim is to manufacture an improved platform for the attachment and growth of endothelial cells, with the aim of improving vascular regeneration.

2 | MATERIALS AND METHODS

2.1 | ECM production

Bovine heart and aorta were harvested from a 2-year-old female. Samples were frozen within 4 hr of harvesting at −80°C. Heart tissue was sliced up into 5-mm-thick slices using a meat slicer. The aorta was opened up and flattened out and subsequently had 40-mm-circular samples punched out. This was repeated for the heart slices. Slices were cleaned with ethanol and placed in water for 30 min to remove excess blood. Samples were then cut up into 2 mm × 2 mm square pieces to increase surface area for decellularization. Pieces were perfused with 0.5% w/v sodium dodecyl sulfate (SDS) in deionized water for 36 hr at 170 mL/min. Samples were then perfused with 10 L of deionised water at 170 mL/min. Decellularized samples were then frozen at −80°C before being lyophilized in a FreeZone® 4.5 freeze-drier (Labconco®). Dry ECM was then crushed up into ~0.5 mm pieces before being milled in a planetary ball mill PM 100 (Retsch). ECM powder was then collected in water, frozen at −80°C, and lyophilized leaving behind ECM powder. Powder was stored at 4°C.

2.2 | Histology

Native and decellularized samples of bovine heart and aorta were fixed in 10% formalin for 24 hr. Samples were then dehydrated in a series of ethanol washes starting at 50% concentration and ending at 100% concentration. Samples were washed in xylene before being embedded in paraffin wax and then stored at 4°C. All samples were then trimmed to 5 μm thicknesses and mounted onto glass slides for haematoxylin and eosin (H&E) staining and Picrosirius Red staining. Samples were cleared in xylene before staining and mounted in Distyrene Plasticizer Xylene (DPX) after staining.

2.2.1 | Haematoxylin and eosin staining

Samples were cleared of paraffin before undergoing rehydration in a series of ethanol and H_2O washes. Samples were stained in haematoxylin for 6 min and Eosin for 90 s, leading to a vivid pink color for the eosinophilic substances (cell cytoplasm and ECM proteins) and a dark blue/black for the nuclear substances (cell nucleus).

2.2.2 | Picrosirius red staining

Samples were cleared of paraffin before undergoing rehydration in a series of ethanol and H_2O washes. Samples were stained in 0.1% Sirius Red for 1 hr, leading to a vivid red color for the collagenous substances (ECM) and a dull yellow color for the cellular substances (cell cytoplasm and cell nucleus) (Velidandla, Gaikwad, Ealla, et al., 2014).

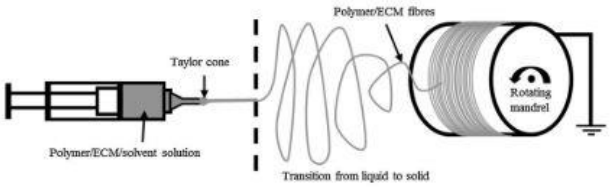

FIGURE 1 Electrospinning setup. The polymer/solvent solution is drawn across from the Taylor cone formed at the needle tip to the charged rotating mandrel. As the solution is drawn across, it transitions from a liquid into a solid fiber that attaches itself to the rotating mandrel

2.3 | Scaffold manufacture (electrospinning)

Powdered heart or aorta ECM was dissolved at 0.25% w/v in hexafluoroisopropanol (HFIP). PCL was then dissolved at 8% w/v into the HFIP/ECM solution overnight with agitation. The solutions were placed into a 20 mL syringe and pumped using a syringe pump EP-H11 (Harvard Apparatus) into the EC-DIG electrospinning system (IME Technologies). PCL/ECM scaffolds were electrospun using the following parameters: 0.4 mm needle bore, 0.8 mL/hr volume flow rate (6 mL in total), 12 cm mandrel: needle distance, +14 kV positive charge, −4 kV negative charge, and 250 revolutions per minute mandrel rotational speed. These parameters have been shown to create uniform randomly aligned small fibers of PCL (Burton et al., 2017). The mandrel was coated with aluminum foil for collection. Once collected, the electrospun sheet was left to dry for 24 hr in the hood before being stored at 4°C. Scaffolds were punched out using a 10 mm punch and left in ethanol for 30 min to sterilize and assist with removal from the aluminum foil. The 0.25% ECM scaffolds had final PCL:ECM ratios of 96.97:3.03 (approximated to 97:3 for simplicity). This ratio was deduced from the remnant PCL:ECM ratio left over once the solvent had left the solution, which was 8% w/v PCL:0.25% w/v ECM. The electrospinning process is shown in Figure 1.

2.4 | Scanning electron microscopy

Both unseeded and seeded scaffolds were visualized at day 0 and day 10 using a Hitachi S4700 fueled emission scanning electron microscope (SEM, Hitachi) with a 5 kV accelerating voltage and a working distance of 12 mm. Briefly, the day 10 seeded scaffolds (n = 2) were fixed in 4% v/v glutaraldehyde overnight, before being stored in phosphate buffer saline (PBS) at 4°C for 3 days. Scaffolds were then incubated in 0.1% v/v osmium for 30 min, followed by four rinses in DiH_2O. Samples were then dehydrated in ethanol using 30 s intervals of increasing ethanol concentration from 30 to 100% v/v to achieve critical point drying. Scaffolds were then placed in HDMS for 1 min. HDMS was then replaced and left to evaporate overnight in a fume cupboard. Prior to imaging, all scaffolds were sputter coated using an Emscope SC500A splutter coater using gold–palladium (60:40).

The process of glutaraldehyde fixation followed by Osmium tetroxide staining allows for clear viewing of the cellular membrane and ECM components on the scaffold. Glutaraldehyde fixation causes rapid crosslinking of the proteins within the cells (Hopwood, 1972). Osmium tetroxide is then used as a lipid stain by embedding a heavy metal directly into the cell membrane, thus creating a high electron scattering rate allowing for clear visualization of the cell membrane (Thiery, Bernier, & Bergeron, 1995).

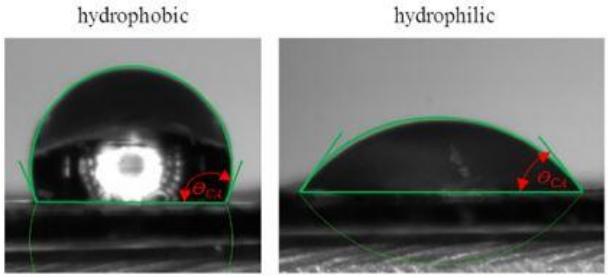

FIGURE 2 Representative images showing the LBADSA plugin on ImageJ measuring contact angle on a hydrophobic (>90° contact angle) and hydrophilic (<90° contact angle) sample (θ_{CA} = contact angle)

2.5 | Mechanical testing

An Instron 3,367 tensile testing machine (Instron, UK) with a 50 N load cell was used to test scaffolds in tension. Young's modulus of the scaffolds was assessed on unseeded scaffolds and on scaffolds after 10 days of culture. Briefly, 20 mm × 4 mm strips of scaffold were cut out for mechanical testing. These samples had a gauge length of 14 mm and were stretched at 10 mm/min until failure or 200% strain was achieved. The incremental Young's modulus was deduced by using the formula:

$$E = \frac{FL_0}{A\Delta L}$$

where E is Young's modulus, F is the applied force, A is the cross sectional area, ΔL is change in length, and L_0 is the original length. Data were analyzed using a previously described analysis method. Briefly, incremental Young's moduli are calculated to show how stiffness changes with increasing strain (Burton et al., 2017; Burton & Callanan, 2018; Callanan, Davis, McGloughlin, Walsh, 2014a; Callanan, Davis, Walsh, & McGloughlin, 2012; Munir, Larsen, & Callanan, 2018; Munir, McDonald, & Callanan, 2019; Santoro et al., 2018) (N = 5 independent replicates).

2.6 | Contact angle measurement

Samples were measured using dry scaffolds. Briefly, a single 5-μL droplet of water was placed on the scaffold, and images were captured at 5 Hz using a DMK 41AU02 monochrome 1,280 × 960 camera. Analysis was done using ImageJ software with a previously developed plugin: LBADSA (Stalder et al., 2010), as seen in Figure 2 (N = 5).

2.7 | Fourier transform infrared spectroscopy

Fourier transform infrared spectroscopy (FTIR) was used to confirm the successful inclusion of vascular ECMs into the electrospun PCL

fibers. Samples were cut into 6-mm-diameter scaffolds. All spectra were obtained using a Nicolet™ iS™10 spectrometer with a Smart™ iTX diamond attenuated total reflection detector (all from Thermo Fisher Scientific). Spectra were acquired between 4,000 and 400 cm^{-1} with a resolution of 1 cm^{-1} using OMNIC™ Spectra software (Thermo Fisher Scientific) (N = 5 independent replicates).

2.8 | Cell growth

Human umbilical vein endothelial cells (HUVECs) from an infant male Caucasian donor were obtained cryopreserved at passage 1 (PromoCell GmbH) and expanded to passage 7 in a 5% CO_2/37°C atmosphere. HUVECs were expanded using MCBD 131 medium (Life Technologies) supplemented with 5% v/v fetal bovine serum (FBS; ThermoFisher Scientific); 1% v/v L-glutamine; 1% v/v penicillin/streptomycin (Life Technologies); 1 mg/L hydrocortisone; 50 mg/L ascorbic acid (Sigma); 2 μg/L fibroblast growth factor (PeproTech); 10 μg/L epidermal growth factor (PeproTech); 2 μg/L insulin-like growth factor (PeproTech); and 1 μg/L vascular endothelial growth factor (PeproTech) (Callanan, Davis, McGloughlin, Walsh, 2014b; Carroll, McGloughlin, O'Keeffe, et al., 2009; Davis et al., 2014).

2.9 | Cell seeding and culture

Scaffolds were punched out using a 10 mm punch and left in 70% v/v ethanol for 30 min before being seeded. Scaffolds were plated into a 48 well plate and were then presoaked in serum free MCDB 131 medium (same cocktail as cell growth medium minus FBS) overnight to increase their hydrophilicity. Cells were seeded at 35,000 cells per scaffold. Briefly, a 35,000 cell suspension in 20 μL of medium was dropped onto the middle of the scaffold and left for 30 min, before an additional 30 μL of medium was added to ensure that the cells did not dry up. After another 30 min, 450 μL of medium was added, increasing the total volume of media to 500 μL. Seeded scaffolds were fed every 2 days using the same MCBD 131 medium cocktail as previously described.

Scaffolds for mechanical testing were cut out at 20 mm × 4 mm and seeded at the same seeding density as the 1-mm-diameter scaffolds.

2.10 | CellTiter-blue® cell viability assay

The assay was performed at 1, 5, and 10 days as the manufacturer's instructions (Promega). Briefly, scaffolds were moved into new media in a fresh 48-well plate to prevent reading the activity of cells bound to the tissue culture plastic. Measurements were made with a Modulus™ II microplate reader at Excitation 525 nm and Emission 580–640 nm (N = 4 independent replicates).

2.11 | DNA quantification

Cell seeded scaffolds cultured for 1, 5, and 10 days were frozen and lyophilized before being incubated in a papain digest solution of 2.5 U papain, 5 mM cysteine HCL, and 5 mM EDTA in DNA free water (all reagents from Sigma-Aldrich, UK) at 60°C for 24 hr and periodically mixed using a vortexer. Total DNA content of the samples was calculated using a Quant-iT™PicoGreen® assay kit (ThermoFisher, UK) as per the manufacturers' instructions. Fluorescence was read using a Modulus™ II microplate reader at Excitation 490 nm and Emission 510–570 nm (N = 4 independent replicates).

2.12 | Cell imaging

Scaffolds were washed thrice in PBS and fixed using 500 μL of 4% v/v formalin solution in PBS for 24 hr, then washed again three times in PBS. Permeabilization achieved by placing scaffolds in 0.2% v/v TritonX-100 solution in PBS for 5 min, followed by three PBS washes.

Scaffolds were stained with 0.1 mL of 0.1 μL 1000X Phalloidin-iFluor™514 conjugate (AAT Bioquest, Stratech) in 0.1 mL PBS with 1% v/v bovine serum albumin for 60 min. Scaffolds were washed thrice in PBS for 10 min. Scaffolds were then stained with 0.1 mL of 300 nM 4′,6-diamidino-2-phenylindole (DAPI) (Sigma-Aldrich, UK) in PBS for 10 min followed by three 10 min PBS washes.

All scaffolds were imaged using a Coherent Anti-Stokes Raman scattering microscope.

2.13 | Real-time RT-qPCR

RNA was extracted from the scaffolds using standard Tri-Reagent (Invitrogen, ThermoFisher) methods and purified using Qiagen's RNeasy spin column system. Real-time polymerase chain reaction was performed using a LightCycler® 480 Instrument II (Roche Life Science) and Sensifast™ SYBR® High-ROX system (Bioline). Forward and reverse sequences were designed with Sigma-Aldrich and are displayed in Table 1 (Callanan et al., 2014b; Fischer et al., 2009). Relative quantification of Reverse transcription polymerase chain reaction (RT-PCR) results was carried out using the $2^{-\Delta\Delta ct}$ method (Livak & Schmittgen, 2001). Gene expression levels were expressed relative to Glyceraldehyde 3-phosphate dehydrogenase (GAPDH) (housekeeping gene) and normalized to expression on the day 1 PCL control.

2.14 | Statistical analysis

Data were expressed as mean ± 1 SD, unless stated otherwise. Statistical analysis was performed using one-way analysis of variance (ANOVA) with post hoc Fisher test for DNA content, CellTiter-Blue®, and real-time qPCR, unless stated otherwise. One-way ANOVA with post hoc Fisher's test has been widely used in literature when comparing a large range of variable sizes (Bédouin, Gordin, Pellen-Mussi, et al., 2018; Nayak & Brenner, 2002; Vogels et al., 2017; Woods & Gratzer, 2005).

3 | RESULTS

3.1 | Decellularization and scaffold manufacture

Bovine heart and aorta ECM were successfully decellularized using 0.5% w/v SDS as seen in Figure 3a. H&E staining showed that the cells were

TABLE 1 The sequences for forward and reverse gene specific primers used in RT-PCR amplification

Gene	Primer	Sequence	Sequence length	Reference
Glyceraldehyde 3-phosphate dehydrogenase	GAPDH (forward)	GTCTCCTCTGACTTCAACAG	20	(Callanan et al. 2014b)
	GAPDH (reverse)	GTTGTCATACCAGGAAATGAG	21	
Matrix metalloproteinase-1	MMP1 (forward)	CGGTTTTTCAAAGGGAATAAGTACT	25	(Callanan et al. 2014b)
	MMP1 (reverse)	TCAGAAAGAGCAGCATCGATATG	23	
Matrix metalloproteinase-2	MMP2 (forward)	CGCTCAGATCCGTGGTGAG	19	(Callanan et al. 2014b)
	MMP2 (reverse)	TGTCACGTGGCGTCACAGT	19	
Vascular endothelial growth factor	VEGF (forward)	AGACCAAAGAAAGATAGAGCAAGACAAG	28	(Callanan et al. 2014b)
	VEGF (reverse)	GGCAGCGTGGTTTCTGTATCG	21	
Platelet endothelial cell adhesion molecule	CD31 (forward)	ACTGGACAAGAAAGAGGCCATCCA	24	(Fischer et al. 2009)
	CD31 (reverse)	TCCTTCTGGATGGTGAAGTTGGCT	24	

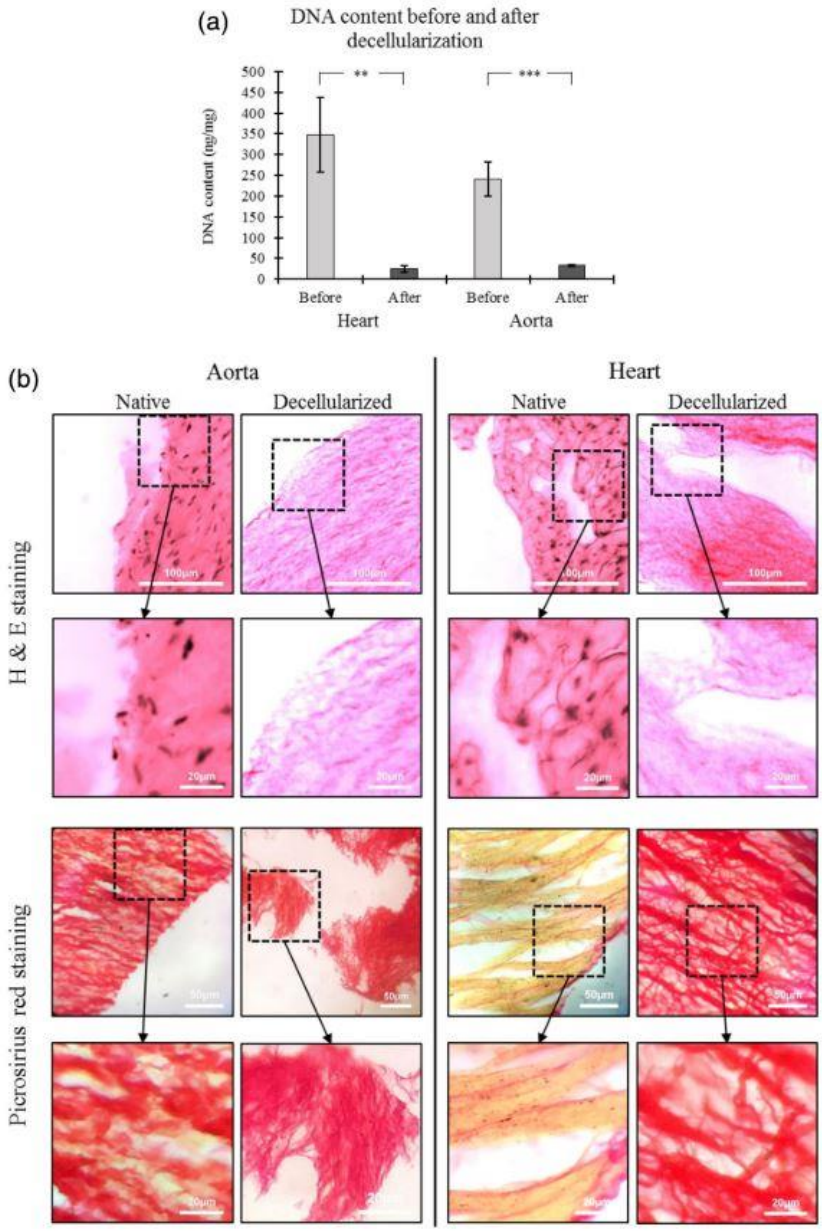

FIGURE 3 (a) DNA content of aorta and heart before and after decellularizing treatment. Data shown as mean ± 1 *SD*, student 2 sample *t*-test performed (**$p < .01$, ***$p < .001$, and $n = 4$). (b) H&E staining and Picrosirius red staining of the aorta and heart tissue before and after decellularization. H&E staining shows a vivid pink color for the eosinophilic substances (cell cytoplasm and ECM proteins) and a dark blue/black color for the nuclear substances (cell nucleus). Picrosirius red staining shows a vivid red color for the collagenous substances (ECM) and a dull yellow color for the cellular substances (cell cytoplasm and cell nucleus). ECM, extracellular matrix; H&E, haematoxylin and eosin

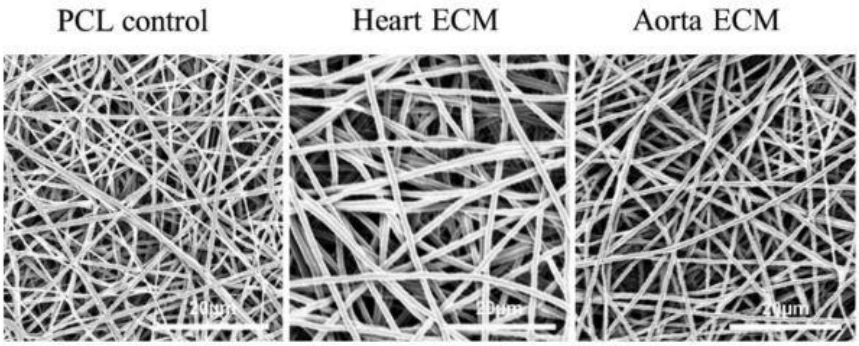

FIGURE 4 Scanning electron microscopy images of the three electrospun sheets. All three scaffolds appear to have a smooth fiber structure and show relatively uniform fiber diameter throughout (fiber diameters of 0.97 ± 0.19, 1.20 ± 0.09, and 0.94 ± 0.12 μm, respectively, for the PCL, heart ECM, and aorta ECM scaffolds). ECM, extracellular matrix; PCL, polycaprolactone

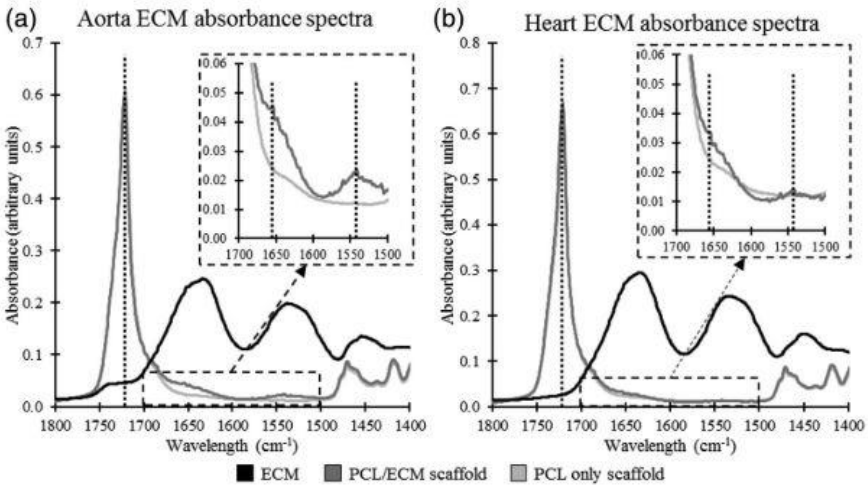

FIGURE 5 Representative FTIR absorbance spectra for (a) aorta ECM scaffolds and (b) heart ECM scaffolds. ECM, extracellular matrix; FTIR, Fourier transform infrared spectroscopy

successfully removed from both tissues (see Figure 3b). Furthermore, Picrosirius red staining showed that the collagenous composition of the ECM was maintained after decellularization (Figure 3b). Electrospun fibrous sheets (as seen in Figure 4) were successfully fabricated using the previously described parameters (Burton et al., 2017). The fibers within each scaffold are fairly uniform in size (fiber diameters of 0.97 ± 0.19, 1.20 ± 0.09, and 0.94 ± 0.12 μm, respectively, for the PCL, heart ECM, and aorta ECM scaffolds) and show a randomness in their orientation. Furthermore, the fibers appear to be smooth in structure.

3.2 | Fourier Transform Infrared Spectroscopy

The FTIR results showed that the bovine heart and aorta ECMs were incorporated into the electrospun PCL fibers. Spectra were taken for PCL fibers, ECM/PCL fibers, and ECM alone. Characteristic peaks from both the PCL and ECM were found in the ECM/PCL fibers demonstrating that the electrospinning process integrated the decellularized ECM into the PCL fiber. Figure 5 shows peaks in absorbance at 1720, 1654, and 1,541 cm^{-1} for both heart and aorta ECM (See Supplementary Figure S1 in the appendix for overlay graphs of all five samples for each group). These peaks can be attributed to the stretching of the carbonyl group in PCL, the amide I bond in the ECM, and the amide II bond in the ECM, respectively (Camacho, West, Torzilli, & Mendelsohn, 2001; Elzein, Nasser-Eddine, Delaite, Bistac, & Dumas, 2004; Garidel & Schott, 2006). These values are shown in Table 2. Furthermore, differences in absorbance values between PCL only scaffolds and the PCL/ECM scaffolds were quantified at each wavelength to show that the differences were observed due to the inclusion of ECM. Briefly, increases of 84.3 ± 8.0% ($p < .01$) and 109.2 ± 18.6% ($p < .01$) were seen at 1654 and 1,541 cm^{-1}, respectively, for the aorta ECM, with a decrease of 19.4 ± 15.5% ($p < .05$) at 1720 cm^{-1}. The heart ECM showed increases of 35.2 ± 6.7% ($p < .01$) and 26.8 ± 10.7% and a decrease of 10.5 ± 15.2% for the three wavelengths. These values are displayed in Table 3.

3.3 | Mechanical testing

Mechanical testing performed using an Instron tensile tester showed no statistically significant difference between cell seeded and unseeded scaffolds for each scaffold at all the strain bands. However, the general trend for the PCL scaffold and the heart ECM scaffold is a slightly higher Young's modulus in the seeded scaffolds then the unseeded scaffold, as seen in Table 4. However, as previously mentioned, this difference is not significant. The only statistical significance is in the aorta ECM scaffold for the 3–4% strain band, where the seeded scaffold was significantly lower than the unseeded scaffold ($p < .05$). The general trend noted is that the two ECM scaffolds had consistently higher Young's moduli at all strain brackets compared with the PCL control. This was significant at

the 0–1% strain band for both scaffolds where the heart ECM was 23.2% higher and aorta ECM 28.4% higher ($p < .05$); and the 1–2% strain band for aorta ECM which was 31.0% higher ($p < .05$). As expected, Young's modulus drops at each subsequent strain bracket for all the scaffold (with the exception of unseeded aorta ECM scaffold between the 0–1% and 1–2% strain brackets). Representative stress–strain graphs for each scaffold are displayed in Figure 6a.

TABLE 2 Absorbance values for each peak

Wavelength of peak (cm^{-1})	Absorbance values		
	PCL	Aorta ECM	Heart ECM
1,720	0.774 ± 0.110	0.624 ± 0.040	0.693 ± 0.039
1,654	0.025 ± 0.001	0.046 ± 0.004	0.034 ± 0.002
1,541	0.011 ± 0.001	0.023 ± 0.004	0.014 ± 0.001

Abbreviations: ECM, extracellular matrix; PCL, polycaprolactone.

3.4 | Contact angle

The addition of aorta ECM had the effect of increasing the hydrophilicity of the scaffold compared with the conventional PCL scaffold and heart ECM scaffold, as seen in Table 4. These results were significant when comparing the aorta ECM scaffold with the heart ECM scaffold—26.9% lower ($p < .05$), but not when comparing either with the PCL scaffold. Furthermore, the percentage drop in contact angle between 0.2 s postcontact and 5 s postcontact was higher for the aorta ECM scaffold than the two others.

3.5 | Cell viability and DNA quanitification

Cell viability was assessed using a CellTitre-Blue® fluorescence assay. Results (Figure 6b) showed that after 10 days, the aorta ECM scaffold and the heart ECM scaffold both showed a significant increase in cell

TABLE 3 Wavelength of peaks noted in FTIR spectra

Wavelength of peak (cm^{-1})	Assignment	Caused by	Change in absorbance between PCL fiber and ECM/PCL fiber	
			Aorta ECM	Heart ECM
1,720	Carbonyl group stretching	PCL	− 19.4 ± 15.5%	− 10.5 ± 15.2%
1,654	Amide I bond	ECM (collagen and elastin)	+ 84.3 ± 8.0%	+ 35.2 ± 6.7%
1,541	Amide II bond	ECM (collagen and elastin)	+ 109.2 ± 18.6%	+ 26.8 ± 10.7%

Abbreviations: ECM, extracellular matrix; PCL, polycaprolactone.

TABLE 4 Mechanical properties of the three scaffolds

	Scaffold type					
	PCL		Heart ECM		Aorta ECM	
	Unseeded	Seeded	Unseeded	Seeded	Unseeded	Seeded
Young's modulus at % strain (MPa)						
0–1	17.05 ± 1.81	19.48 ± 2.14	21.00 ± 1.87	22.58 ± 2.13	21.90 ± 2.93	21.60 ± 1.91
1–2	16.80 ± 1.27	18.10 ± 2.21	20.87 ± 2.60	20.68 ± 2.37	22.00 ± 3.11	18.76 ± 1.95
2–3	15.03 ± 1.89	15.25 ± 2.47	16.27 ± 2.22	18.18 ± 1.62	18.04 ± 2.29	15.82 ± 1.12
3–4	13.93 ± 1.53	14.55 ± 3.00	15.96 ± 1.69	15.84 ± 1.60	17.34 ± 1.95	14.30 ± 0.85
4–5	12.45 ± 1.75	13.08 ± 2.80	12.64 ± 1.40	14.16 ± 1.18	14.90 ± 1.76	12.92 ± 0.64
0–5[a]	15.05 ± 1.54	16.09 ± 2.49	17.35 ± 1.83	18.29 ± 1.72	18.84 ± 2.28	16.68 ± 1.26
Contact angle after 0.2 s (degree)	114.4 ± 8.9		122.5 ± 3.5		89.6 ± 37.7	
Contact angle after 1 s (degree)	103.6 ± 19.6		118.8 ± 10.7		72.8 ± 43.9	
Contact angle after 5 s (degree)	98.7 ± 25.2		106.3 ± 27.2		68.8 ± 43.6	
Percentage drop in contact angle between 0.2 and 1 s	9.44%		3.02%		18.75%	
Percentage drop in contact angle between 0.2 and 5 s	13.72%		13.22%		23.21%	
Fiber diameter (μm)	0.97 ± 0.19		1.20 ± 0.09		0.94 ± 0.12	

Note: Values displayed ± 1 *SD*.
Abbreviations: ECM, extracellular matrix; PCL, polycaprolactone.
[a]Young's modulus across the entire strain range from 0 to 5% strain.

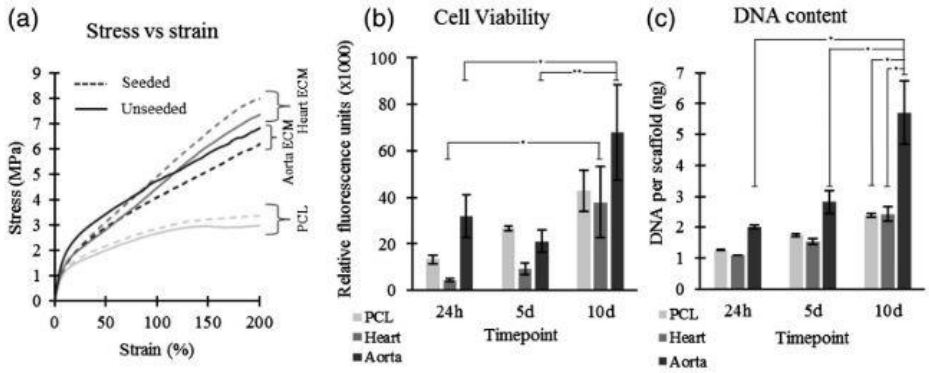

FIGURE 6 (a) Representative stress versus strain graphs of each scaffold—Unseeded and after 10 days of HUVEC culture. (b) Cell viability of scaffolds analyzed using CellTitre blue® fluorescence assay. A statistically significant increase in cell viability was seen in the heart ECM and aorta ECM scaffolds between day 1 and day 10. (c) DNA content of scaffolds assessed using a Picogreen assay. The aorta ECM showed the largest increase in DNA content between day 1 and day 10 and showed a significantly higher DNA content than the PCL scaffold and heart ECM scaffold at day 10. $n = 4$, error bars = 1 *SD*, one-way ANOVA with Fishers' post hoc performed (*$p < .05$ and **$p < .01$). ANOVA, analysis of variance; ECM, extracellular matrix; HUVEC, human umbilical vein endothelial cell

viability compared with viability after 1 day ($p < .05$). The aorta ECM scaffold also showed a significant increase compared with its viability after 5 days ($p < .01$). On the other hand, the PCL scaffold showed no significant increase in cell viability between all three time points, although an upward trend in cell viability is noted. After 10 days, the aorta ECM scaffold had a 40% higher cell viability than the heart ECM and the PCL scaffold. However, this increase was not found to be significant.

DNA quantification was performed using a Picogreen assay. The DNA content (Figure 6c) of the aorta ECM scaffolds at 10 days is significantly different from the aorta ECM scaffold at day 1 (a 275% increase). Alongside this, the day 10 aorta ECM scaffold was also significantly higher by approximately 240% than the heart ECM and PCL scaffolds ($p < .05$). The trend noted across the three time points is an increase in DNA content for all three scaffolds, but a larger increase in the aorta ECM scaffolds.

3.6 | Cell imaging

Representative SEM images taken using a Hitachi S4700 fuelled emission SEM (Hitachi) show the functional cell layers on scaffolds after 10 days of culture (Figure 7a). Interestingly, the aorta ECM scaffold appears to be 100% confluent with HUVECs, compared with approximately 30% for the PCL scaffold and 50% for the heart ECM scaffold. These results validate the cell viability and DNA quantification results, suggesting that the incorporation of aorta ECM into the scaffold improved HUVEC proliferation. Furthermore, all three scaffolds show similar HUVEC morphology.

Representative images taken using coherent antistoke Raman scattering further confirm that the incorporation of aorta ECM into the scaffold had a favorable effect on HUVECs (Figure 7b). After 1 day of growth, the cells on the aorta ECM scaffold already appear greater in number and have a higher quantity of visible actin filaments. The heart ECM scaffolds show very poor cell attachment after 1 day, which matches the cell viability and DNA quantification results. Furthermore, cell number appears to increase for all scaffolds between day 1 and day 10. Interestingly, the actin filaments appear more characterized after 10 days, which is a sign of maturing cells (Huber et al., 2013).

3.7 | Gene analysis

Multiple genes associated with vascular function were assayed for their expression, including cluster of differentiation (CD31), matrix metalloproteinase-1 (MMP1), matrix metalloproteinase-2 (MMP2), and vascular endothelial growth factor (VEGF) (Figure 8). Statistical significance was noted in CD31 expression changes, with downregulation observed for all three scaffolds between day 1 and day 5. Within the day 1 scaffolds, the heart ECM scaffold showed higher CD31 expression than the two other scaffolds. MMP1 expression showed downregulation over time for all three scaffolds, with the biggest reduction in expression seen for the aorta ECM scaffold. Significantly lower expressions were also noted for the aorta ECM scaffolds at 5 and 10 days when compared with the two other scaffolds. Conversely, MMP2 expression was seen to increase over time, with significant increases for the PCL and heart ECM scaffolds. Furthermore, the aorta ECM scaffold had a significantly higher expression at day 1 compared with the PCL and heart ECM scaffolds. VEGF showed no real trend over time, with the only exception being that aorta ECM scaffold had a significantly higher expression than the heart ECM scaffold at day 1.

4 | DISCUSSION

Polymer scaffolds have long been utilized in tissue engineering as a platform for tissue regeneration (Dhandayuthapani, Yoshida, Maekawa, & Kumar, 2011; O'Brien, 2011; Saha, Pollock, Schaffer, & Healy, 2007). Physical characteristics can be designed into the scaffold to support cellular activity and promote differentiation, proliferation, and deposition

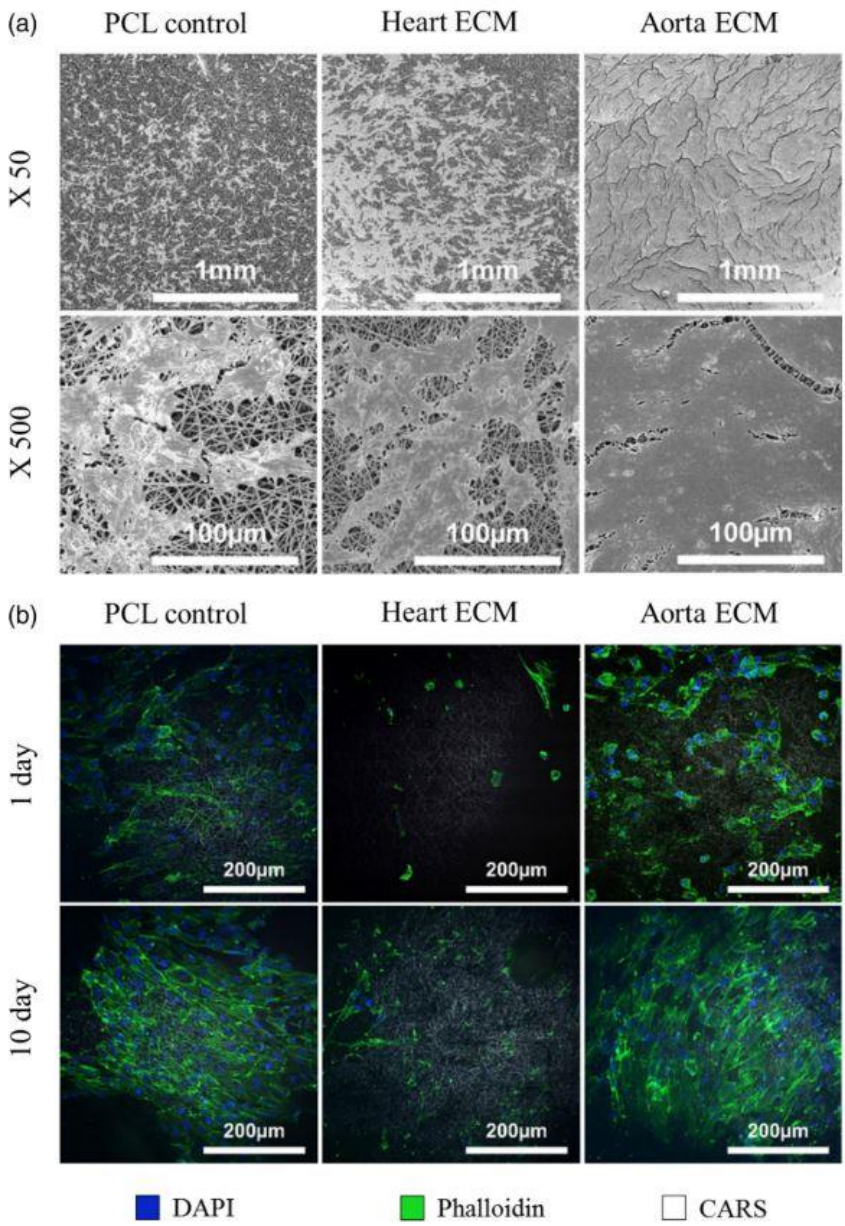

FIGURE 7 (a) Representative SEM images of scaffolds and a functional layer of HUVEC cells. The aorta ECM scaffold showed 100% confluence after 10 days of culture compared with approximately 30% for the PCL scaffold and 50% for the heart ECM scaffold. (b) Representative coherent antistoke Raman scattering (CARS) images of HUVECs on all three scaffolds at 1 day and 10 days. DAPI staining (blue) highlights the cells nucleus. Phalloidin staining (green) highlights the actin filaments which are predominantly found in the cell cytoplasm. PCL scaffold fibers (white). ECM, extracellular matrix; HUVEC, human umbilical vein endothelial cell; SEM, scanning electron microscope; PCL, polycaprolactone

of new functional ECM (O'Brien, 2011). In this study, we have used PCL as the polymer component as it is commonly used in tissue engineering due to its physical and chemical properties, especially in electrospinning where it has been used in a variety of tissue engineering applications (Burton et al., 2017; Dunphy, Reid, Burton, et al., 2018; Gao et al., 2017; Grant et al., 2017; Sundaramurthi et al., 2014). Alongside polymers, decellularized tissue has been used in tissue engineering due to its cell-supporting physical and chemical characteristics (Lu et al., 2013; Tapias & Ott, 2014). The aim when decellularizing is to maintain the physical and chemical characteristics of the remnant ECM (Gilbert et al., 2006). In this study, we used SDS (at a concentration of 0.5%), which is a commonly used ionic detergent for decellularizing tissues (Nakayama, Batchelder, Lee, & Tarantal, 2010; Oberwallner et al., 2014; Ott et al., 2008; Ott et al., 2010; Ross, Williams, & Batich, 2009) and successfully reduced DNA content approximately 8–14 fold across the two tissue types (Figure 3a). It is a very effective means of removing nuclear components and cytoplasmic proteins (Woods & Gratzer, 2005) and has been used with varying concentrations ranging from 0.1 to 4%, with results showing complete removal of cellular material while maintaining structural integrity and a network of laminin and collagen (Nakayama et al., 2010; Oberwallner et al., 2014; Ott et al., 2008; Ott et al., 2010; Ross et al., 2009). H&E staining confirmed the removal of the DNA content from the two tissue types after decellularization, and the Picrosirius red staining confirmed that the collagenous structure of the ECM was maintained during decellularization (Figure 3b). The FTIR results for the two ECMs showed peaks in the areas associated with structural

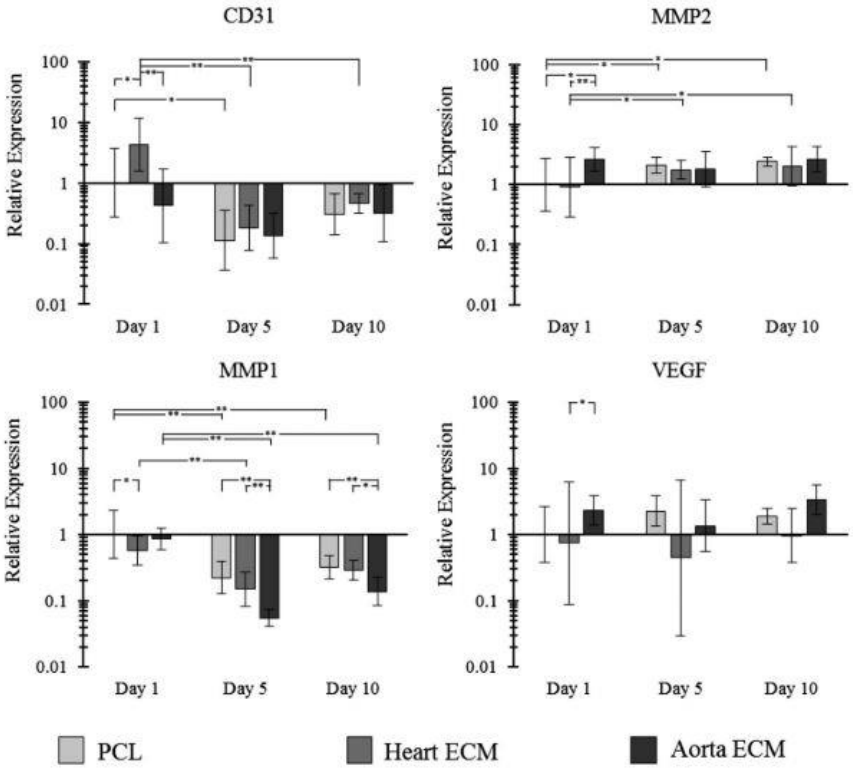

FIGURE 8 Real time qPCR data using the $2^{-\Delta\Delta Ct}$ method showing the expression of four genes (MMP1, MMP2, CD31, and VEGF) relative to GAPDH. All results are normalized to the PCL scaffold on day 1. $N = 5$, data shown as mean ± 1 *SD*, one-way ANOVA with Fishers' post hoc performed (*$p < .05$ and **$p < .01$). ANOVA, analysis of variance; CD31, cluster of differentiation; GAPDH, glyceraldehyde 3-phosphate dehydrogenase; MMP1, matrix metalloproteinase-1; MMP2, matrix metalloproteinase-2; PCL, polycaprolactone

proteins such as collagen and elastin, suggesting that the decellularizing process maintained the protein's integrity (Cheheltani, McGoverin, Rao, et al., 2014).

As previously described, polymers and ECM both have their advantages when used as scaffolds for tissue engineering (Dhandayuthapani et al., 2011; Tapias & Ott, 2014). In this study, we have combined the two in an attempt to harness the beneficial characteristics from each to create a bioscaffold more suited for vascular tissue engineering. Recently, work has focused on combining the two to take advantage of these characteristics, in a similar vein to this study (Gao et al., 2017; Hong et al., 2008; Jahnavi et al., 2015; Jiang et al., 2015; Wu et al., 2007). For example, coating vascular ECM with polymers has been implemented before, with the aim of improving biochemical and mechanical performance (Jahnavi et al., 2015; Wu et al., 2007). These studies both noted improved mechanical properties. However, the final structure of the scaffold is limited by the size and architecture of the ECM. By integrating the ECM directly into the polymer fibers, as we have done in this study using electrospinning, we are able to create a highly tailored and physically repeatable structure that both includes the biochemical cues found in native ECM, and has the mechanical strength of the electrospun polymer. Moreover, as found in this study and previous, there are mechanical and biochemical benefits to combining ECM with polymers (Jahnavi et al., 2015; Wu et al., 2007).

The inclusion of ECM into the PCL fibers was confirmed through the use of FTIR. The two PCL/ECM scaffolds shared absorbance peaks with the PCL only scaffold and the ECM alone. These peaks were noted at 1720, 1654, and 1,541 cm^{-1}, and have assignments with the carbonyl group in PCL, and the amide I and amide II groups found in ECM (Camacho et al., 2001; Elzein et al., 2004). The changes in absorbance found at these peaks due to the addition of the two ECMs were quantified, as shown in Tables 2 and 3, and were found to be in line with what we would expect from literature (Gao et al., 2017).

The technique proposed in this study solubilizes vascular ECMs into a PCL/HFIP solution; a method previously used with decellularized meniscus and cartilage ECM (Gao et al., 2017; Garrigues et al., 2014). Gao et al. used a range of PCL and meniscus ECM concentrations up to 8 and 6% w/v, respectively. While this ECM concentration is substantially higher than the ones used in this study, they found that the addition of ECM had a positive effect in reducing contact angle, a phenomena also noted with the inclusion of aorta ECM in this study. Similarly, Garrigues et al. dissolved decellularized cartilage ECM into a solution of PCL and HFIP at 8% w/v, showing that ECM could successfully be incorporated into an electrospun polymer fiber and provide a platform for cell growth (Garrigues et al., 2014). Gene expression changes were observed with the addition of cartilage ECM, in similar vein to this study. We have shown that the same procedure can be used with vascular tissues, with the incorporation of ECM altering mechanical and cellular performance.

The inclusion of ECM into the electrospun polymer fibers had the effect of increasing the scaffold's tensile Young's modulus, as noted in Table 4. Significant differences were seen at the 0–1% strain band for both scaffolds where the heart ECM was 23.2% higher and aorta ECM 28.4% higher, and the 1–2% strain band for aorta ECM which was 31.0% higher. This can be explained by these native vascular ECMs being made up of constituent proteins such as collagen, which has been found to have much higher stiffnesses at lower strains than

PCL alone (bulk properties), 1–21 GPa for collagen compared with 300–400 MPa for PCL (Eshraghi & Das, 2010; Wenger, Bozec, Horton, & Mesquida, 2007). Interestingly, this phenomenon has also been noted when electrospinning combinations of liver ECM, fibronectin, and collagen with polylactic acid (Grant, Hallett, Forbes, et al., 2019). They found that the scaffold's Young's modulus increased by between 13 and 66% depending on which protein was blended (Grant et al., 2019).

A trend of decreasing MMP1 expression for all three scaffolds was noted. MMP1 is an enzyme involved in the breakdown and remodeling of collagen (one of the major components of vascular ECMs) (Batra et al., 2012). Its downregulation suggests that the cells are not trying to breakdown the collagen within the ECM, suggesting that they are in a position of homeostatic equilibrium with their scaffold. A significant downregulation was noted across all three scaffolds between day 1 and day 5, with no real change between day 5 and day 10. Interestingly, the largest downregulation was noted in the aorta ECM scaffold. While this downregulation may suggest that there is a change in collagen content within the ECM scaffolds, similar trends were noted between the ECM scaffolds and the PCL only scaffold suggesting that scaffold architecture is likely the biggest driver in gene expression and that the ECM is having a limited effect on gene activity.

In contrast, a significant upregulation of MMP2 was noted in all three scaffolds after 5 and 10 days. Furthermore, after 1 day, a significantly higher expression was seen in the aorta ECM scaffold compared with the two other scaffolds. This enzyme is involved in the breakdown and remodeling of gelatin (another major component of vascular ECMs) (Wiseman et al., 2003). Its upregulation suggests the presence of gelatin in the ECM scaffolds. We noted an upregulation across both ECM scaffolds, as well as the PCL only scaffold after 10 days of culture, with no significant differences noted between the three scaffolds. This suggests that this upregulation is unlikely to be caused by the presence of gelatin in the ECM scaffolds and is probably a result of something other than the constituents of the two native ECMs, such as scaffold architecture, as previously mentioned.

On the other hand, no real trend in VEGF expression was noted. VEGF is a signal protein that stimulates the formation of new blood vessels (angiogenesis) in tissue regeneration (Ferrara, Gerber, & LeCouter, 2003). Its overexpression is also associated with tumor growth and intraocular neovascular disorders (Ferrara et al., 2003). During cellular proliferation, an upregulation of VEGF would be expected (Nayak & Brenner, 2002). It has been suggested that HUVECs "overexpress" VEGF in the first 24 hr, which may explain this down regulation over time compared with the day 1 scaffolds (Imaizumi et al., 2000).

A downward trend in CD31 expression was seen for all three scaffolds. CD31, also known as PECAM1 (platelet endothelial cell adhesion molecule 1) is a protein found on the surface of many cells and is involved in angiogenesis and integrin activation. Overexpression of CD31 can inhibit morphogenesis in cells (Sheibani & Frazier, 1998). Its downregulation suggests that: the HUVECs are struggling to adhere to each other (Baldwin, Shen, Yan, et al., 1994), which SEM and fluorescence microscopy images disprove, or the HUVECs are not attempting to create new vasculature (angiogenesis) (Wang et al., 2016). This is the most likely reason that can be attributed to the issue of poor cellular infiltration which is required in order to achieve full tissue regeneration. A lack of infiltration in this study resulted in a monolayer of cells growing on the surface of the scaffold. Studies have shown the contribution of porosity and pore interconnectivity on cell survival and HUVEC angiogenesis (Munir & Callanan, 2018; Xiao, Wang, Liu, et al., 2015). Despite this, the ECM scaffolds in this study are still viable platforms for cell attachment, and cellular infiltration can be improved by either increasing the mean pore diameter (Murphy, Haugh, & O'Brien, 2010; Phipps, Clem, Grunda, Clines, & Bellis, 2012; Wu & Hong, 2016), or by increasing the hydrophilicity of the scaffold through plasma treatment and the addition of functional groups (Burton et al., 2017; Dettin et al., 2015), two easily applicable techniques.

In this study, there was a noticeable trend in the data suggesting that the aorta ECM scaffold had enhanced adhesive properties compared with the two other scaffolds. DNA quantification and cell viability were both higher for the aorta ECM scaffold at 24 hr. The FTIR results showed a greater increase in absorbance at the amide I and amide II peaks when aorta ECM was added to the fiber compared with when heart ECM was added to the fiber. FTIR is a surface analysis method that has been shown to measure to depths ranging from 0.2 to 5 μm (Kazarian & Chan, 2013). The fibers in this study are approximately 1 μm thick suggesting that the shifts in absorbance may be due to the location of the ECM within the fiber. Higher absorbance in the aorta ECM scaffolds may be caused by the ECM mobilizing onto the surface of the fibers, where they would be more readily picked up by FTIR. Furthermore, the aorta ECM scaffold was found to have a lower contact angle than the two other scaffolds, which has been shown to result in higher cell adhesion and proliferation (Dowling, Miller, Ardhaoui, & Gallagher, 2011; Gao et al., 2017). The differences in contact angle may be due to the components of ECM at the fiber surface increasing the surface energy of the scaffold (Faucheux, Schweiss, Lützow, Werner, & Groth, 2004).

There are some limitations to this work. First, a thorough investigation of electrospinning in HFIP's denaturing effect on the ECM is required. Previous studies have shown that HFIP can have a denaturing effect on various proteins, including collagen (Agarwal, Wendorff, & Greiner, 2008; Herskovits, Gadegbeku, & Jaillet, 1970; Zeugolis et al., 2008), with one study suggesting that approximately 45% of the triple helical structure of collagen became denatured (and becoming gelatin) when dissolved in HFIP (Yang et al., 2008), which would suggest that the ECM used in this study could be denatured. They also found that pure collagen fibers were water soluble when they were not crosslinked, suggesting that crosslinking would increase the integrity of electrospun protein fibers (Yang et al., 2008). However, it has also been shown that crosslinking electrospun ECM protein scaffolds drastically alters their morphology, often leading to large reductions in porosity (Heydarkhan-Hagvall et al., 2008), which has been shown to negatively impact certain cells (Badylak & Gilbert, 2008; Lowery, Datta, & Rutledge, 2010). Furthermore, PCL/gelatin blended scaffolds have shown loss of protein when cultured in both PBS and cell culture medium (Marrese, Cirillo, Guarino, et al., 2018).

They found that surface roughness increased over a culture period of 9 days due to the gelatin dissolving from the scaffold and interestingly found that this was more pronounced in culture medium than in PBS (Marrese et al., 2018). Likewise, collagen/elastin/polymer (elastin and collagen being the two most prominent ECM proteins) blends with approximately 75% crosslinking have shown varying degrees of mechanical integrity when in culture conditions. Over the course of 8 weeks of culture, reductions in inner diameter ranging from 10% (PCL and PLLA) to 70% (PLCL) were seen depending on the polymer used. This reduction in mechanical integrity could potentially be explained by the dissolution of collagen and elastin from the scaffold fibers. In addition to this, the electric field which the ECM particles are subjected to may also have a denaturing effect. It has been shown that high voltages can alter the structure of proteins (Freedman, Haq, Edel, et al., 2013). Therefore, while both collagen denaturing and protein dissolution are possible during processing, the retained bioactivity from the ECM within the scaffold outweighs the losses seen (Badylak, Freytes, & Gilbert, 2009; Choudhury, Tun, Wang, & Naing, 2018).

SDS has been shown to induce protein denaturing and requires further study on its effects with vascular ECMs (Bhuyan, 2010). While this study did show the successful maintenance of collagen in both tissues after decellularization (Picrosirius Red staining in Figure 3b), other ECM proteins such as elastin were not looked at. However, studies have shown successful decellularization using SDS without damaging the components of the ECM (Garrigues et al., 2014; He & Callanan, 2013; Oberwallner et al., 2014; Sullivan et al., 2012). Furthermore, a thorough proteomic study of the ECM components and the cellular secretome would act as validation for the PCR results and would give a better understanding of which proteins lead to the improved adhesive properties (Chang, Dalgliesh, Lopez, et al., 2016; Hathout, 2007). Further analysis on how the ECM was incorporated into the electrospun fibers is required. Studies have shown contradictory results with some showing complete protein integration into the fibers (Gao et al., 2017; Garrigues et al., 2014), and others showing globular protein microparticles in the fibers (Chakrapani, Gnanamani, Giridev, Madhusoothanan, & Sekaran, 2012). However, the studies which incorporated ECM into electrospun fibers, along with this study, showed improvements in cellular and mechanical performance, suggesting that there is a large potential for these hybrid bioscaffolds in tissue engineering.

5 | CONCLUSION

In this study, we have shown that the integration of decellularized vascular ECM into an electrospun polymer fibers has promise for vascular tissue engineering applications. We successfully combined decellularized ECM from bovine myocardium and aorta into a PCL/HFIP solution and electrospun it into a network of fibers. Our results show that the inclusion of these ECMs had both effects on the performance of seeded HUVECs and on the mechanical characteristics of the scaffold. Cell viability was shown to increase with the inclusion of aorta ECM in the scaffold. Furthermore, Young's modulus was increased through the addition of both vascular ECMs, and hydrophilicity was increased with the addition of aorta ECM. The inclusion of aorta ECM resulted in a stiffer scaffold that had improved biomechanical properties for the attachment of cells—leading to the increased cell adherence noted in this study. The method we have described combines the controllable physical properties of the polymer (PCL) with the biochemical and mechanical properties of the ECM (aorta and myocardium wall) to create a tailored hybrid bioscaffold. We believe that the combination of a natural ECM and a synthetic polymer to generate a hybrid bioscaffold has many potential applications in vascular tissue engineering.

ACKNOWLEDGMENTS

The authors would like to thank Professor Alistair Elfick for the use of his lab equipment. This work is funded by an Engineering & Physical Sciences Research Council Doctoral Training Partnership Studentship EP/N509644/1 and MRC grant MR/L012766/1. Further thanks to Alison Macdonald and Stephen Mitchell for helping in imaging.

REFERENCES

Agarwal, S., Wendorff, J. H., & Greiner, A. (2008). Use of electrospinning technique for biomedical applications. *Polymer (Guildf)*, *49*, 5603–5621.

Badylak, S. F., Freytes, D. O., & Gilbert, T. W. (2009). Reprint of: Extracellular matrix as a biological scaffold material: Structure and function. *Acta Biomaterialia*, *5*, 1–13.

Badylak, S. F., & Gilbert, T. W. (2008). Immune response to biologic scaffold materials. *Seminars in Immunology*, *20*, 109–116.

Baldwin, H. S., Shen, H. M., Yan, H. C., DeLisser, H. M., Chung, A., Mickanin, C., … Buck, C. A. (1994). Platelet endothelial-cell adhesion molecule-1 (Pecam-1 Cd31) - alternatively spliced, functionally distinct isoforms expressed during mammalian cardiovascular development. *Development*, *120*, 2539–2553.

Batra, J., Robinson, J., Soares, A. S., Fields, A. P., Radisky, D. C., & Radisky, E. S. (2012). Matrix metalloproteinase-10 (MMP-10) interaction with tissue inhibitors of metalloproteinases TIMP-1 and TIMP-2: Binding studies and crystal structure. *The Journal of Biological Chemistry*, *287*, 15935–15946.

Bédouin, Y., Gordin, D. M., Pellen-Mussi, P., Perez, F., Tricot-Doleux, S., Vasilescu, C., … Gloriant, T. (2018). Enhancement of the biocompatibility by surface nitriding of a low-modulus titanium alloy for dental implant applications. *Journal of Biomedical Materials Research—Part B: Applied Biomaterials*, *107*, 1483–1490.

Bhowmick, S., Rother, S., Zimmermann, H., Lee, P. S., Moeller, S., Schnabelrauch, M., … Scharnweber, D. (2017). Biomimetic electrospun scaffolds from main extracellular matrix components for skin tissue engineering application—The role of chondroitin sulfate and sulfated hyaluronan. *Materials Science and Engineering: C*, *79*, 15–22.

Bhuyan, A. K. (2010). On the mechanism of SDS-induced protein denaturation. *Biopolymers*, *93*, 186–199.

Blanche, C., Blanche, D. A., Kearney, B., Sandhu, M., Czer, L. S. C., Kamlot, A., … Trento, A. (2001). Heart transplantation in patients seventy years of age and older: A comparative analysis of outcome. *The Journal of Thoracic and Cardiovascular Surgery*, *121*, 532–541.

Burton, T. P., & Callanan, A. (2018). A non-woven path: Electrospun polylactic acid scaffolds for kidney tissue engineering. *Journal of Tissue Engineering and Regenerative Medicine*, *15*, 301–310.

Burton, T. P., Corcoran, A., & Callanan, A. (2017). The effect of electrospun polycaprolactone scaffold morphology on human kidney epithelial cells. *Biomedical Materials*, *13*, 015006.

Callanan, A., Davis, N. F., McGloughlin, T. M., & Walsh, M. T. (2014a). The effects of stent interaction on porcine urinary bladder matrix employed as stent-graft materials. *Journal of Biomechanics*, *47*, 1885–1893.

Callanan, A., Davis, N. F., McGloughlin, T. M., & Walsh, M. T. (2014b). Development of a rotational cell-seeding system for tubularized extracellular matrix (ECM) scaffolds in vascular surgery. *Journal of Biomedical Materials Research—Part B: Applied Biomaterials*, *102*, 781–788.

Callanan, A., Davis, N. F., Walsh, M. T., & McGloughlin, T. M. (2012). Mechanical characterisation of unidirectional and cross-directional multilayered urinary bladder matrix (UBM) scaffolds. *Medical Engineering & Physics*, *34*, 1368–1374.

Camacho, N. P., West, P., Torzilli, P. A., & Mendelsohn, R. (2001). FTIR microscopic imaging of collagen and proteoglycan in bovine cartilage. *Biopolymers*, *62*, 1–8.

Carroll, G. T., McGloughlin, T. M., O'Keeffe, L. M., Callanan, A., & Walsh, M. T. (2009). Realistic temporal variations of shear stress modulate MMP-2 and MCP-1 expression in arteriovenous vascular access. *Cellular and Molecular Bioengineering*, *2*, 591–605.

Chakrapani, V. Y., Gnanamani, A., Giridev, V. R., Madhusoothanan, M., & Sekaran, G. (2012). Electrospinning of type I collagen and PCL nanofibers using acetic acid. *Journal of Applied Polymer Science*, *125*, 3221–3227.

Chang, C. W., Dalgliesh, A. J., Lopez, J. E., & Griffiths, L. G. (2016). Cardiac extracellular matrix proteomics: Challenges, techniques, and clinical implications. *Proteomics. Clinical Applications*, *10*, 39–50.

Cheheltani, R., McGoverin, C. M., Rao, J., Vorp, D. A., Kiani, M. F., & Pleshko, N. (2014). Fourier transform infrared spectroscopy to quantify collagen and elastin in an in vitro model of extracellular matrix degradation in aorta. *Analyst*, *139*, 3039–3047.

Choi, B.-H., Choi, Y. S., Kang, D. G., Kim, B. J., Song, Y. H., & Cha, H. J. (2010). Cell behavior on extracellular matrix mimic materials based on mussel adhesive protein fused with functional peptides. *Biomaterials*, *31*, 8980–8988.

Choudhury, D., Tun, H. W., Wang, T., & Naing, M. W. (2018). Organ-derived decellularized extracellular matrix: A game changer for bioink manufacturing? *Trends in Biotechnology*, *36*, 787–805.

Davis, L. M., Callanan, A., Carroll, G. T., Doyle, B. J., Walsh, M. T., & McGloughlin, T. M. (2014). On the potential of hydrated storage for naturally derived ECMs and associated effects on mechanical and cellular performance. *Journal of Biomedical Materials Research—Part B: Applied Biomaterials*, *102*, 89–97.

Dettin, M., Zamuner, A., Roso, M., Iucci, G., Samouillan, V., Danesin, R., … Conconi, M. T. (2015). Facile and selective covalent grafting of an RGD-peptide to electrospun scaffolds improves HUVEC adhesion. *Journal of Peptide Science*, *21*, 786–795.

Dhandayuthapani, B., Yoshida, Y., Maekawa, T., & Kumar, D. S. (2011. Epub ahead of print 2011). Polymeric scaffolds in tissue engineering application: A review. *International Journal of Polymer Science*, *2011*, 1–19. https://doi.org/10.1155/2011/290602

Dowling, D. P., Miller, I. S., Ardhaoui, M., & Gallagher, W. M. (2011). Effect of surface wettability and topography on the adhesion of osteosarcoma cells on plasma-modified polystyrene. *Journal of Biomaterials Applications*, *26*, 327–347.

Dunphy, S., Reid, J. A., Burton, T. P., & Callanan, A. (2018). Mechanical characterisation of directionally frozen polycaprolactone scaffolds using 1,4-dioxane and glacial acetic acid for articular cartilage tissue engineering. *Biomedical Physics & Engineering Express*, *4*, 057004.

Elzein, T., Nasser-Eddine, M., Delaite, C., Bistac, S., & Dumas, P. (2004). FTIR study of polycaprolactone chain organization at interfaces. *Journal of Colloid and Interface Science*, *273*, 381–387.

Eshraghi, S., & Das, S. (2010). Mechanical and microstructural properties of PCL scaffolds with 1-D, 2-D and 3-D orthogonally oriented porous architectures produced by selective laser sintering. *Acta Biomaterialia*, *6*, 2467–2476.

Faucheux, N., Schweiss, R., Lützow, K., Werner, C., & Groth, T. (2004). Self-assembled monolayers with different terminating groups as model substrates for cell adhesion studies. *Biomaterials*, *25*, 2721–2730.

Ferrara, N., Gerber, H. P., & LeCouter, J. (2003). The biology of VEGF and its receptors. *Nature Medicine*, *9*, 669–676.

Fischer, L. J., McIlhenny, S., Tulenko, T., Golesorkhi, N., Zhang, P., Larson, R., … DiMuzio, P. J. (2009). Endothelial differentiation of adipose-derived stem cells: Effects of endothelial cell growth supplement and shear force. *The Journal of Surgical Research*, *152*, 157–166.

Freedman, K. J., Haq, S. R., Edel, J. B., Jemth, P., & Kim, M. J. (2013). Single molecule unfolding and stretching of protein domains inside a solid-state nanopore by electric field. *Scientific Reports*, *3*, 1–8.

Gao, S., Guo, W., Chen, M., Yuan, Z., Wang, M., Zhang, Y., … Guo, Q. (2017). Fabrication and characterization of electrospun nanofibers composed of decellularized meniscus extracellular matrix and polycaprolactone for meniscus tissue engineering. *Journal of Materials Chemistry B*, *5*, 2273–2285.

Garidel, P., & Schott, H. (2006). Fourier-transform Midinfrared spectroscopy for analysis and screening of liquid protein formulations. *BioProcess Tech*, *1*, 48–55.

Garrigues, N. W., Little, D., Sanches-Adams, J., Ruch, D. S., & Guilak, F. (2014). Electrospun cartilage-derived matrix scaffolds for cartilage tissue engineering. *Journal of Biomedical Materials Research—Part A*, *102*, 3998–4008.

Gilbert, T. W., Sellaro, T. L., & Badylak, S. F. (2006). Decellularization of tissues and organs. *Biomaterials*, *27*, 3675–3683.

Grant, R., Hallett, J., Forbes, S., Hay, D., & Callanan, A. (2019). Blended electrospinning with human liver extracellular matrix for engineering new hepatic microenvironments. *Scientific Reports*, *9*, 1–12.

Grant, R., Hay, D. C., & Callanan, A. (2017). A drug-induced hybrid electrospun poly-Capro-lactone: Cell-derived extracellular matrix scaffold for liver tissue engineering. *Tissue Engineering—Part A*, *23*, 650–662.

Guo, F., He, D., Zhang, W., & Walton, R. G. (2012). Trends in prevalence, awareness, management, and control of hypertension among United States adults, 1999 to 2010. *Journal of the American College of Cardiology*, *60*, 599–606.

Han, J., Gerstenhaber, J. A., Lazarovici, P., & Lelkes, P. I. (2013). Tissue factor activity and ECM-related gene expression in human aortic endothelial cells grown on electrospun biohybrid scaffolds. *Biomacromolecules*, *14*, 1338–1348.

Hathout, Y. (2007). Approaches to the study of the cell secretome. *Expert Review of Proteomics*, *4*, 239–248.

He, M., & Callanan, A. (2013). Comparison of methods for whole-organ decellularization in tissue engineering of bioartificial organs. *Tissue Engineering—Part B: Reviews*, *19*, 194–208.

Heron, M. (2017). Deaths: Leading causes for 2015. *National Vital Statistics Reports*, *66*, 1–76.

Herskovits, T. T., Gadegbeku, B., & Jaillet, H. (1970). On the structural stability denaturation of proteins. *The Journal of Biological Chemistry*, *245*, 2588–2598.

Heydarkhan-Hagvall, S., Schenke-Layland, K., Dhanasopon, A. P., Rofail, F., Smith, H., Wu, B. M., … MacLellan, W. R. (2008). Three-dimensional electrospun ECM-based hybrid scaffolds for cardiovascular tissue engineering. *Biomaterials*, *29*, 2907–2914.

Hong, H., Dong, G. N., Shi, W. J., Chen, S., Guo, C., & Hu, P. (2008). Fabrication of biomatrix/polymer hybrid scaffold for heart valve tissue engineering in vitro. *ASAIO Journal*, *54*, 627–632.

Hopwood, D. (1972). Theoretical and practical aspects of glutaraldehyde fixation. *The Histochemical Journal*, *4*, 267–303.

Huber, F., Schnauß, J., Rönicke, S., Rauch, P., Müller, K., Fütterer, C., & Käs, J. (2013). Emergent complexity of the cytoskeleton: From single filaments to tissue. *Advances in Physics*, *62*, 1–112.

Hutmacher, D. W. (2000). Scaffolds in tissue engineering bone and cartilage. *Biomaterials*, *21*, 2529–2543.

Imaizumi, T., Itaya, H., Nasu, S., Yoshida, H., Matsubara, Y., Fujimoto, K., … Satoh, K. (2000). Expression of vascular endothelial growth factor in human umbilical vein endothelial cells stimulated with interleukin-1alpha—An autocrine regulation of angiogenesis and inflammatory reactions. *Thrombosis and Haemostasis*, *83*, 949–955.

Jahnavi, S., Kumary, T. V., Bhuvaneshwar, G. S., Natarajan, T. S., & Verma, R. S. (2015). Engineering of a polymer layered bio-hybrid heart valve scaffold. *Materials Science and Engineering: C*, *51*, 263–273.

Jiang, B., Akgun, B., Lam, R. C., Ameer, G. A., & Wertheim, J. A. (2015). A polymer-extracellular matrix composite with improved thromboresistance and recellularization properties. *Acta Biomaterialia*, *18*, 50–58.

Kang, Y., Kim, S., Khademhosseini, A., & Yang, Y. (2011). Creation of bony microenvironment with CaP and cell-derived ECM to enhance human bone-marrow MSC behavior and delivery of BMP-2. *Biomaterials*, *32*, 6119–6130.

Kasimir, M.-T., Rieder, E., Seebacher, G., Nigisch, A., Dekan, B., Wolner, E., … Simon, P. (2006). Decellularization does not eliminate thrombogenicity and inflammatory stimulation in tissue-engineered porcine heart valves. *The Journal of Heart Valve Disease*, *15*, 278–286 discussion 286.

Kazarian, S. G., & Chan, K. L. A. (2013). ATR-FTIR spectroscopic imaging: Recent advances and applications to biological systems. *Analyst*, *138*, 1940–1951.

Kilic, A., Emani, S., Sai-Sudhakar, C. B., Higgins, R. S., & Whitson, B. A. (2014). Donor selection in heart transplantation. *Journal of Thoracic Disease*, *6*, 1097–1104.

Kumbar, S. G., Nukavarapu, S. P., James, R., Nair, L. S., & Laurencin, C. T. (2008). Electrospun poly(lactic acid-co-glycolic acid) scaffolds for skin tissue engineering. *Biomaterials*, *29*, 4100–4107.

Lawes, C. M., Vander, H. S., & Rodgers, A. (2008). Global burden of blood-pressure-related disease, 2001. *Lancet*, *371*, 1513–1518.

Livak, K. J., & Schmittgen, T. D. (2001). Analysis of relative gene expression data using real-time quantitative PCR and the 2-ΔΔCT method. *Methods*, *25*, 402–408.

Lowery, J. L., Datta, N., & Rutledge, G. C. (2010). Effect of fiber diameter, pore size and seeding method on growth of human dermal fibroblasts in electrospun poly(ε-caprolactone) fibrous mats. *Biomaterials*, *31*, 491–504.

Lu, T. Y., Lin, B., Kim, J., Sullivan, M., Tobita, K., Salama, G., & Yang, L. (2013). Repopulation of decellularized mouse heart with human induced pluripotent stem cell-derived cardiovascular progenitor cells. *Nature Communications*, *4*, 1–11.

Makridakis, S., & DiNicolantonio, J. J. (2014). Hypertension: Empirical evidence and implications in 2014. *Open Hear*, *1*. Epub ahead of print, e000048. https://doi.org/10.1136/openhrt-2014-000048

Marrese, M., Cirillo, V., Guarino, V., & Ambrosio, L. (2018). Short-term degradation of bi-component electrospun fibers: Qualitative and quantitative evaluations via AFM analysis. *Journal of Functional Biomaterials*, *9*, 27.

Masoumi, N., Annabi, N., Assmann, A., Larson, B. L., Hjortnaes, J., Alemdar, N., … Khademhosseini, A. (2014). Tri-layered elastomeric scaffolds for engineering heart valve leaflets. *Biomaterials*, *35*, 7774–7785.

Munir, N., & Callanan, A. (2018). Novel phase separated polycaprolactone/collagen scaffolds for cartilage tissue engineering. *Biomedical Materials*, *13*, 051001.

Munir, N., Larsen, R. S., & Callanan, A. (2018). Fabrication of 3D cryo-printed scaffolds using low-temperature deposition manufacturing for cartilage tissue engineering. *Bioprinting*, *10*, 1–8.

Munir, N., McDonald, A., & Callanan, A. (2019). A combinatorial approach: Cryo-printing and electrospinning hybrid scaffolds for cartilage tissue engineering. *Bioprinting*, *16*, e00056.

Murphy, C. M., Haugh, M. G., & O'Brien, F. J. (2010). The effect of mean pore size on cell attachment, proliferation and migration in collagen-glycosaminoglycan scaffolds for bone tissue engineering. *Biomaterials*, *31*, 461–466.

Nakayama, K. H., Batchelder, C. A., Lee, C. I., & Tarantal, A. F. (2010). Decellularized rhesus monkey kidney as a three-dimensional scaffold for renal tissue engineering. *Tissue Engineering—Part A*, *16*, 2207–2216.

Nayak, N. R., & Brenner, R. M. (2002). Vascular proliferation and vascular endothelial growth factor expression in the rhesus macaque endometrium. *The Journal of Clinical Endocrinology and Metabolism*, *87*, 1845–1855.

Oberwallner, B., Brodarac, A., Choi, Y. H., Saric, T., Anić, P., Morawietz, L., & Stamm, C. (2014). Preparation of cardiac extracellular matrix scaffolds by decellularization of human myocardium. *Journal of Biomedical Materials Research—Part A*, *102*, 3263–3272.

O'Brien, F. J. (2011). Biomaterials & scaffolds for tissue engineering. *Materials Today*, *14*, 88–95.

Ott, H. C., Clippinger, B., Conrad, C., Schuetz, C., Pomerantseva, I., Ikonomou, L., … Vacanti, J. P. (2010). Regeneration and orthotopic transplantation of a bioartificial lung. *Nature Medicine*, *16*, 927–933.

Ott, H. C., Matthiesen, T. S., Goh, S. K., Black, L. D., Kren, S. M., Netoff, T. I., & Taylor, D. A. (2008). Perfusion-decellularized matrix: Using nature's platform to engineer a bioartificial heart. *Nature Medicine*, *14*, 213–221.

Phipps, M. C., Clem, W. C., Grunda, J. M., Clines, G. A., & Bellis, S. L. (2012). Increasing the pore sizes of bone-mimetic electrospun scaffolds comprised of polycaprolactone, collagen I and hydroxyapatite to enhance cell infiltration. *Biomaterials*, *33*, 524–534.

Ravi, S., & Chaikof, E. (2010). Biomaterials for vascular tissue engineering. *Regenerative Medicine*, *5*, 1–21.

Reid, J. A., & Callanan, A. (2019). The influence of aorta extracellular matrix in electrospun polycaprolactone scaffolds. *Journal of Applied Polymer Science*, *136*, 48181.

Ross, E. A., Williams, M. J., & Batich, C. D. (2009). Embryonic stem cells proliferate and differentiate when seeded into kidney scaffolds. *Journal of the American Society of Nephrology*, *20*, 2338–2347.

Saha, K., Pollock, J. F., Schaffer, D. V., & Healy, K. E. (2007). Designing synthetic materials to control stem cell phenotype Krishanu. *Current Opinion in Chemical Biology*, *11*, 381–387.

Sanchez, P., Fernandez-Santos, M., Costanza, S., Climent, A. M., Moscoso, I., Gonzalez-Nicolas, M. A., … Fernandez-Aviles, F. (2015). Acellular human heart matrix: A critical step toward whole heart grafts. *Biomaterials*, *61*, 279–289.

Santoro, R., Venkateswaran, S., Amadeo, F., Zhang, R., Brioschi, M., Callanan, A., … Pesce, M. (2018). Acrylate-based materials for heart valve scaffold engineering. *Biomaterials Science*, *6*, 154–167.

Schoen, B., Avrahami, R., Baruch, L., Efraim, Y., Goldfracht, I., Elul, O., … Machluf, M. (2017). Electrospun extracellular matrix: Paving the way to tailor-made natural scaffolds for cardiac tissue regeneration. *Advanced Functional Materials*, *27*, 1–9.

Sheibani, N., & Frazier, W. A. (1998). Down-regulation of platelet endothelial cell adhesion molecule-1 results in thrombospondin-1 expression and concerted regulation of endothelial cell phenotype. *Molecular Biology of the Cell*, *9*, 701–713.

Stalder, A. F., Melchior, T., Müller, M., Sage, D., Blu, T., & Unser, M. (2010). Low-bond axisymmetric drop shape analysis for surface tension and contact angle measurements of sessile drops. *Colloids and Surfaces A: Physicochemical and Engineering Aspects*, *364*, 72–81.

Sullivan, D. C., Mirmalek-Sani, S. H., Deegan, D. B., Baptista, P. M., Aboushwareb, T., Atala, A., & Yoo, J. J. (2012). Decellularization methods of porcine kidneys for whole organ engineering using a high-throughput system. *Biomaterials*, *33*, 7756–7764.

Sundaramurthi, D., Krishnan, U. M., & Sethuraman, S. (2014). Electrospun nanofibers as scaffolds for skin tissue engineering. *Polymer Reviews*, *54*, 348–376.

Tapias, L., & Ott, H. (2014). Decellularized scaffolds as a platform for bioengineered organs. *Current Opinion in Organ Transplantation*, *19*, 145–152.

Thiery, G., Bernier, J., & Bergeron, M. (1995). A simple technique for staining of cell membranes with imidazole and osmium tetroxide. *The Journal of Histochemistry and Cytochemistry*, *43*, 1079–1084.

United Nations.2015. *World Population Ageing*. Report prepared by United Nations Department of Economic and Social Affairs. Epub ahead of print.

Velidandla, S., Gaikwad, P., Ealla, K. K., Bhorgonde, K. D., Hunsingi, P., & Kumar, A. (2014). Histochemical analysis of polarizing colors of collagen using picrosirius red staining in oral submucous fibrosis. *Journal of International Oral Health*, *6*, 33–38.

Vogels, R. R. M., Lambertz, A., Schuster, P., Jockenhoevel, S., Bouvy, N. D., Disselhorst-Klug, C., … Klink, C. D. (2017). Biocompatibility and biomechanical analysis of elastic TPU threads as new suture material. *Journal of Biomedical Materials Research—Part B: Applied Biomaterials*, *105*, 99–106.

Wang, Z., Lei, L., Cai, X. J., Chen, L. Y., Yuan, M., Yang, G., … Wang, X. (2016). A preliminary study of pamidronic acid downregulation of angiogenic factors IGF-1/ PECAM-1 expression in circulating level in bone metastatic breast cancer patients. *OncoTargets and Therapy*, *9*, 3147–3152.

Wenger, M. P. E., Bozec, L., Horton, M. A., & Mesquida, P. (2007). Mechanical properties of collagen fibrils. *Biophysical Journal*, *93*, 1255–1263.

Weymann, A., Patil, N. P., Sabashnikov, A., Jungebluth, P., Korkmaz, S., Li, S., … Szabo, G. (2014). Bioartificial heart: A human-sized porcine model—The way ahead. *PLoS One*, *9*, 1–8.

Wiseman, B. S., Sternlicht, M. D., Lund, L. R., Alexander, C. M., Mott, J., Bissell, M. J., … Werb, Z. (2003). Site-specific inductive and inhibitory activities of MMP-2 and MMP-3 orchestrate mammary gland branching morphogenesis. *The Journal of Cell Biology*, *162*, 1123–1133.

Woods, T., & Gratzer, P. F. (2005). Effectiveness of three extraction techniques in the development of a decellularized bone-anterior cruciate ligament-bone graft. *Biomaterials*, *26*, 7339–7349.

Wu, J., & Hong, Y. (2016). Enhancing cell infiltration of electrospun fibrous scaffolds in tissue regeneration. *Bioactive Materials*, *1*, 56–64.

Wu, S., Liu, Y. L., Cui, B., Qu, X. H., & Chen, G. Q. (2007). Study on decellularized porcine aortic valve/poly (3-hydroxybutyrate-co-3- hydroxyhexanoate) hybrid heart valve in sheep model. *Artificial Organs*, *31*, 689–697.

Xiao, X., Wang, W., Liu, D., Zhang, H., Gao, P., Geng, L., … Wang, Z. (2015). The promotion of angiogenesis induced by three-dimensional porous beta-tricalcium phosphate scaffold with different interconnection sizes via activation of PI3K/Akt pathways. *Scientific Reports*, *5*, 1–11.

Yang, L., Fitié, C. F. C., van der Werf, K. O., Bennink, M. L., Dijkstra, P. J., & Feijen, J. (2008). Mechanical properties of single electrospun collagen type I fibers. *Biomaterials*, *29*, 955–962.

Zeugolis, D. I., Khew, S. T., Yew, E. S. Y., Ekaputra, A. K., Tong, Y. W., Yung, L. Y. L., … Raghunath, M. (2008). Electro-spinning of pure collagen nano-fibres—Just an expensive way to make gelatin? *Biomaterials*, *29*, 2293–2305.

SUPPORTING INFORMATION

Additional supporting information may be found online in the Supporting Information section at the end of this article.

How to cite this article: Reid JA, Callanan A. Hybrid cardiovascular sourced extracellular matrix scaffolds as possible platforms for vascular tissue engineering. *J Biomed Mater Res*. 2019;1–15. https://doi.org/10.1002/jbm.b.34444